On the Mechanisms of Electrochemical Transport in Polymer Electrolyte Fuel Cells

by

Pratap Rama

A Doctoral Thesis

submitted in partial fulfilment of the requirements for the award of
Degree of Doctor of Philosophy of Loughborough University

15th February 2010

Abstract

The Polymer Electrolyte Fuel Cell (PEFC) is well-poised to play a key role in the portfolio of future energy technologies for civil and military applications. Principally, the PEFC converts part of the chemical energy released during hydrogen-oxidation and oxygen-reduction into electrical energy, generating water a bi-product. It is potentially a zero-emissions technology which can operate silently due to the absence of any moving parts, has quick start-up characteristics and can achieve high thermodynamic efficiency. In order to ensure that the PEFC emerges as a viable option for all applications, it is necessary to ensure that the technology is reliable, capable of delivering performance and cost-effective throughout its life-cycle. To achieve these objectives, a better fundamental understanding of the mechanisms of electrochemical transport in the PEFC is required than is presently available.

The literature identifies that multi-component electrochemical transport within the PEFC plays a central role in fuel cell operation and longevity. Water transport is one of these. It is well-understood that excessive amounts of water within the porous electrodes of the cell can cause flooding, which impedes the supply of reactant gases. It is also well-understood that insufficient water can cause the polymer electrolyte membrane (PEM) to dehydrate, thereby reducing its proton conductivity. Both of these processes can undermine cell performance. Repetitive hydration cycles are also known to precipitate degradation mechanisms which can undermine reliability. However, the mechanisms of multi-component and potentially two-phase transport across the PEFC as a multi-layered assembly which includes the porous electrodes and the PEM are not understood as well: the mechanisms of contaminant transport, fuel crossover and liquid water infiltration particularly through the PEM are important examples.

The modelling literature demonstrates that electrochemical transport in the PEFC is treated either through the use of dilute solution theory or concentrated solution theory. The modelling literature also demonstrates a wide spectrum in the application of modelling assumptions and the formulation of electrochemical equations to simulate transport in the different layers of the PEFC. This thesis

describes research aimed at reconciling the different modelling approaches and philosophies in the literature by developing and applying a unified mechanistic electrochemical treatment to describe multi-component, two-phase transport across the layers of the PEFC.

The approach adopted here is first to construct a multi-component zero-dimensional model for multi-component input gases which is merged with a multi-layer PEFC model to correctly predict the boundary conditions in the gas channels based on the cross-flow of components through the cell. The model is validated using data from the open literature and applied to understand contaminant crossover from anode to cathode. The second step is to develop a unified mechanistic electrochemical treatment to describe multi-component transport across the layers of the PEFC: the general transport equation. This is central to the contribution of this thesis. It is theoretically validated by deriving the key transport equations used in the benchmark fuel cell modelling literature. It is then implemented with the multi-component input model developed previously and validated using data from the open literature. The model is subsequently applied to understand fuel crossover characteristics in the cell. The third and final step is to further-develop the application of the general transport equation to account for two-phase transport across the layers of the PEFC. The resulting model is validated against three different sets of data from the open literature and subsequently applied to understand the effects of PEM thickness, anode gas humidification, cell compression and PEM structural reinforcement on liquid infiltration and two-phase transport across the PEM.

It is demonstrated that the general transport equation developed in this thesis establishes a backbone understanding of the modelling and simulation of transport across the layers of the PEFC. The study successfully reconciles the different modelling philosophies in the fuel cell literature. The progressive validation and application of the general transport equation demonstrates the potential to enhance the scientific understanding of factors affecting PEFC performance and demonstrates its value as a tool for computationally-based cell design, optimisation and diagnostics.

Acknowledgements

The author wishes to express his profound indebtedness first and foremost to Prof. Rui Chen for the opportunity to carry out the research presented here and for the tremendous amount of time, guidance, kind moral support and invaluable advice given wholeheartedly over the years.

The author is also grateful to Prof. Rob Thring and Prof. John Andrews for support and to Dr. Xiao Li for helping with technical matters in chapter 8. The author also wishes to acknowledge his fellow researchers for inspiring him through their own abilities and for making these past few years a doting lifelong memory.

As this manuscript represents the culmination of educational endeavours from childhood, the author wishes to thank all of his teachers and lecturers from Catherine Infants School, Catherine Juniors School, Rushey Mead Secondary School, Wyggeston and Queen Elizabeth I College, and finally Loughborough University for nurturing the means to learn and understand. Thanks are also paid to Harpal Rajput and Pratik Patel for their friendship and laughter throughout these years.

The author would also like to express his gratefulness to his loving, virtuous parents and sister Divya for their selfless patience and unequivocal support throughout; for his fellow researcher and now dear wife Dovilė, the author wishes to express a husband's gratitude for nourishing his life with enduring love, peace and resolve. This thesis would not have been possible without their help.

The author is particularly grateful for and humbled by the graceful virtues of his parents and grandparents, some of whom will never get to see this. For the hardships that they have endured, and for the adversities that they have overcome for the sake of their children, this thesis is dedicated to them.

To

Shri. Munja Vinja & Smt. Manjula Munja Rama

Late Shri. Vinja Rama & Smt. Jasi Vinja Odedra

Late Shri. Narbad Karsan & Late Smt. Nathi Narbad Ranavaya

Contents

1 Introduction **1**

1.1 Basic Principles 1

1.2 Objectives of the Current Research 3

1.3 Outline of Thesis 4

1.4 References 6

2 The Polymer Electrolyte Fuel Cell **7**

2.1 Components of the PEFC 7

2.2 Cell Performance 8

2.2.1 The Thermodynamic Equilibrium Potential 9

2.2.2 Thermodynamic Efficiency 12

2.2.3 Irreversible Voltage Losses 14

2.2.4 Polarisation Curve 18

2.3 References 20

3 A Review of Practical Factors Governing the Performance of Polymer Electrolyte Fuel Cells **21**

3.1 Introduction 21

3.2 Activation Losses 22

3.2.1 Platinum Agglomeration 22

3.2.2 Platinum Migration 22

3.2.3 Exposure to Sub-Zero Operating Conditions 23

3.2.4 Atmospheric Contaminants 23

3.2.5 Fuel Contaminants 24

3.2.6 Carbon Corrosion 24

3.2.7 Chemical Degradation of Silicone Seals 25

3.3 Mass Transportation Losses 26

3.3.1 Cell Flooding 26

3.3.2 Hydrophobicity of Porous Layers 28

3.3.3 Ionomer Loading in Catalyst Layer 29

3.3.4 Impedance to Transportation due to Ice Formation 30

3.3.5 Effects of Compaction on the GDL 31
3.4 Ohmic Losses 32
3.4.1 Resistance to Electron Transfer in the Bi-Polar Plate 32
3.4.2 Resistance to proton transfer in the Polymer Electrolyte Membrane 35
3.5 Efficiency Losses and Catastrophic Cell Failure 38
3.5.1 Mechanical Attack 38
3.5.2 Chemical Attack 40
3.6 Summary 43
3.7 Conclusions 44
3.8 References 48

4 Mathematical Modelling of a PEFC 59
4.1 Mass Transport 59
4.1.1 Concentrated Solution Theory 61
4.1.2 Dilute Solution Theory 64
4.1.3 Knudsen Fluxes 66
4.1.4 Electro-Osmotic Drag 67
4.1.5 Discussions on Mass Transport Processes across the PEM 68
4.2 Ohmic Resistance 69
4.2.1 Resistance to the Flow of Electrons 69
4.2.2 Resistance to the Flow of Protons 69
4.2.3 Discussions on Modelling Resistance to the Flow of Protons PEM across the PEM 71
4.3 Electrode Kinetics 71
4.3.1 Thin Interface Model 72
4.3.2 The Macro-Homogeneous Model 80
4.3.3 The Agglomerate Model 81
4.4.3 Discussions on Fundamental Models for Electrode Kinetics 83
4.4 References 84

5 A Polymer Electrolyte Fuel Cell Model with Multi- Component Input 86
5.1 Introduction 86
5.2 The Basic PEFC Model 89
5.2.1 Thermodynamic Equilibrium Potential and Irreversible Losses 90
5.2.2 Membrane Water Transport Model 90
5.3 The Multi-Component Transportation Model 94
5.3.1 Molar Flux of Oxidised, Reduced and Produced Species 94
5.3.2 Channel Flows 97
5.3.3 Gas Transportation in the Electrode Diffusion Layer 98
5.3.4 Gas Transportation in the Membrane 99
5.3.5 Semi-empirical Carbon Monoxide Degradation Effect. 100
5.4 Results and Discussions 103
5.4.1 Overvoltage 103
5.4.2 Multi-Component Diffusion 107
5.4.3 CO Crossover and Contamination 108
5.5 Conclusions 110
5.6 References 111

6 A Universal Modelling Framework from Fundamental Theory 113
6.1 Introduction 113
6.2 Theoretical Study 118
6.2.1 Driving Force Equation 118
6.2.2 Molecular and Thermal Diffusion Equation 120
6.2.3 The General Transport Equation 121
6.3 Theoretical Validation 123
6.3.1 Dilute Solutions 123
6.3.2 Concentrated Solutions 125
6.4 Model Development 126
6.4.1 Governing Equations 126
6.4.2 Solution Procedure 130
6.5 Results and Discussions 131
6.5.1 Model Validation 131

6.5.2 Hydrogen Crossover: 4-Species System 133
6.6 Conclusions 136
6.7 References 139

7 A Universal Approach to Multi-Layer Two-Phase Modelling through the General Transport Equation. 142
7.1 Introduction 142
7.2 Theoretical Equations for Two-Phase Transport in Porous and Electrolytic Quasi-Porous Media 148
7.2.1 The General Transport Equation 149
7.2.2 Theoretical Equations for Two-Phase Transport in Porous Media 150
7.2.3 Theoretical equations for two-phase flow in quasi-porous media 152
7.3 Sub-Models for the Physical Properties of PEFC Media and Infiltrating Fluids 157
7.3.1 Sub-models for the Inlet and Channel Regions 158
7.3.2 Sub-models for the Porous Layers 158
7.3.3 Sub-models for the Quasi-Porous Layers 161
7.4 Modelling Structure for a One-Dimensional Two-Phase PEFC Model 165
7.5 Experimental Validation 168
7.5.1 Net water transport per proton 168
7.5.2 Ohmic Resistance across the PEM 170
7.5.3 Water Content across the PEM 172
7.6 Conclusions 173
7.7 References 175

8 Water Transport Studies 180
8.1 Introduction 180
8.2 Non-Reinforced Membranes 181
8.2.1 PEM Thickness 182
8.2.2 Anode Humidification 190
8.2.3 PEM Constraint 193

8.2.4 Parameter Effects on PEM Resistance 197
8.3 Structurally-Reinforced Membranes 200
8.3.1 Experimental 202
8.3.2 Results and Discussion 203
8.4 Conclusions 208
8.5 References 210

9 Conclusions and Future Work 211
9.1 Conclusions 211
9.2 Future Work 215
9.2.1 Microscopic Modelling 216
9.2.2 Macroscopic Modelling 218
9.4 References 221

A Appendices 223
A.1 Sub-models for the Inlet and Channel Regions of a PEFC 223
A.2 Key equations for the effects of cell compression on the water uptake and thickness of the quasi-porous PEM 225
A.3 References 227

B List of Publications 228

List of Figures

1-1 Principle reduction-oxidation processes of a hydrogen-fuelled polymer electrolyte fuel cell 2

2-1 The key regions and flows of a PEFC single-cell 8

2-2 An illustration of a PEFC stack showing the bi-polar plate and membrane electrode assemblies of a two-cell PEFC stack 8

2-3 Maximum thermal efficiency of a hydrogen-fuelled low temperature PEFC and the Carnot limit of a heat engine with an exhaust temperature of 45˚C 15

2-4 Basic polarisation curve of a PEFC. 19

2-5 Thermodynamic efficiency of a PEFC as a function of electrical load and cell voltage 20

5-1 Five regions of the polymer electrolyte fuel cell 89

5-2 Third-order polynomial dependence of Θ on current density 101

5-3 Fourth-order polynomial dependence of Θ on current density. 102

5-4 Simulated and measured fuel cell performance at 70˚C. 103

5-5 Effect of varying oxygen composition on the fuel cell performance 104

5-6 Effects of varying temperature on the fuel cell performance; 55˚C (328 K), 70˚C (343 K) and 85˚C (358 K) 104

5-7 Interfacial oxygen mole fractions with 50% and 100% saturation at 85˚C (358 K) 105

5-8 Activation overvoltage with 50% and 100% of saturation at 85˚C (358 K). . . . 106

5-9 Effect of oxygen mole fraction on the fuel cell voltage 106

5-10 Effects of varying hydrogen composition on the fuel cell performance 107

5-11 Interfacial air constituent mole fractions at cathode-membrane interface 108

5-12 CO crossover effects on cathode potential 109

5-13 CO to H_2 flux ratio for inlet fuel feed CO concentrations of 10 ppm, 50 ppm and 100 ppm 109

6-1 Simulation Flowchart 130

6-2 Simulated membrane water content from the general transport equation (6-14), and Springer *et al.*. 132

6-3 Crossover dependence on dry membrane thickness at 1 atm 135
6-4 H_2 Crossover dependence on dry membrane thickness at 3 atm at 80˚C (353 K) and 110˚C (383 K). 135
6-5 H_2 Crossover as function of current density for PEM thicknesses of 50, 100 and 175 µm 136
7-1 PEFC cell structure for the one-dimensional two-phase model. 158
7-2 Simulation flowchart for the object-orientated single-cell, two-phase multi-layer one-dimensional PEFC model 167
7-3 Comparison of simulated and experimental values of net water flux per proton for the 18 test cases 169
7-4 Specific resistance and water content profiles across the PEM for simulated and measured results 171
7-5 Simulated and measured water content profiles as a function of non-dimensional PEM thickness for three levels of supply gas relative humidity; 92%, 80% and 40% 172
8-1 Expanded membrane thickness and percentage change in thickness as a function of the original thickness for five simulated PEM thicknesses 183
8-2 Water content profile as a function of non-dimensional position along the expanded PEM thickness for the five different PEM thicknesses 184
8-3 Liquid intrusion profiles for five different PEM thicknesses as a function of non-dimensional position along the expanded PEM thickness 184
8-4 Depth of liquid water penetration from cathodic PEM boundary for five PEM thicknesses. 185
8-5 Net water transport per proton and average vapour and liquid phase components for five PEM thicknesses 186
8-6 Water flux per proton as a function of non-dimensional position along PEM thickness 187
8-7 Vapour and liquid phase components of net water transport as a function of position along PEM thickness for the 25.4 µm PEM case 189
8-8 PEM water content profile as a function of the non-dimensional membrane position for five PEM thicknesses 190
8-9 Liquid intrusion profiles for five different PEM thicknesses as a function of non-dimensional position along the expanded PEM thickness 191
8-10 Net water transport per proton and average vapour and liquid phase

components for five PEM thicknesses 192
8-11 Vapour and liquid phase components of net water transport as a function of position along PEM thickness with both fuel supplies fully humidified 193
8-12 Change in PEM thickness as a function of degree of constraint 195
8-13 Effect of PEM constraint on PEM water content and liquid infiltration 196
8-14 Resistance maps for different levels of constraint and PEM thicknesses 200
8-15 Applied anode and cathode flow rates in standard litres per minute 203
8-16 Membrane resistance and tuned diffusivity scaling factor as a function of current density 204
8-17 Simulated thickness-averaged water content as a function of current density for case 1 and case 2 as a function of current density 205
8-18 Electro-osmotic drag and diffusive components of net water flux across the PEM as a function of current density 206
8-19 Simulated change in PEM thickness as a function of current density 208
9-1 Single phase multi-component lattice Boltzmann simulation of oxygen permeation through a carbon paper GDL 217
9-2 Multi-Scale PEFC Modelling 219
9-3 Simulated pressure drops within a 25-cell stack using the Hardy-Cross method and the single-phase electrochemical transport model 221

List of Tables

2-1 Changes in free energy and entropy at standard temperature and pressure for hydrogen, oxygen and water 11

2-2 Constants for equation 2-19. 19

3-1 Grades of stainless steel according to composition by weight percentage. 33

3-2 Summary of factors affecting activation, Ohmic and mass transportation losses 46

3-3 Summary of factors affecting efficiency losses and catastrophic cell failure . . . 47

6-1 Governing equations for channel model based on the multi-component input model in chapter 5 127

6-2 Governing equations for electrode model 128

6-3 Governing equations for membrane model 128

6-4 Properties for base case 3-species (water, electrolyte membrane, protons) concentrated solution membrane system 129

6-5 Additional properties for 4-species (water, electrolyte membrane, protons, hydrogen) concentrated solution membrane system 129

6-6 Experimental and simulated hydrogen permeability coefficients for a 50 μm polymer electrolyte membrane 133

7-1 Key equations for the porous regions of the PEFC 160

7-2 Key equations for the quasi-porous region of the PEFC 163

7-3 Test cases for model validation. 169

8-1 Base operating conditions & material properties used in the PEFC model for the water transport studies 181

Nomenclature

a	activity
b	coefficient for compressive strain
C	compressive pressure (bar, ×0.1MPa)
c_i	concentration of species i (mol/cm^3)
d_i	molecular driving force (g/molecule-J)
D_{ij}	diffusion coefficient of species i in species j (cm^2/s)
D_i^T	thermal diffusion coefficient of species i (cm^2/s)
erf	error function
E	potential (V)
$\boldsymbol{E}$	Young's modulus (MPa)
EW	equivalent weight (g/equiv)
f	volume fraction of water in the PEM
F	Faraday constant (96484 C/equiv.)
I	molar flux of water produced at the cathode (mol/cm^2-s)
j	current (A)
J_0	exchange current density (A/cm^2)
J	current density (A/cm^2)
$J(s)$	Leverett J-function
k	Boltzmann constant (J/K)
k_J	relative permeability pre-factor for phase J
ΔF	free energy of activation (kJ/mol)
G	bulk modulus (MPa)
ΔG	change in free energy (kJ/mol)
H	crossover-loss gradient (per ppm)
ΔH	molar change in enthalpy (kJ/mol)
m_i	molecular mass (g/molecule)
M_i	molar mass of species i (g/mol)
n	number of electrons

n_i	molecular concentration of speices *i* (molecules/cm^3)
$\dot{n}_i$	molar flux of species *i* (mol/cm^2-s)
$\dot{N}_i$	molar flow of species *i*, (mol/s)
N_A	Avagadro number (6.022×10^{23} molecules/mol)
p	pressure (Pa)
R	universal gas constant (8.3143 J/mol-K)
$R^{internal}$	internal resistance (Ω)
r^{proton}	area-specific resistance to proton transfer (Ω-cm^2)
s	porous layer saturation
s_{epf}	expanded pore fraction in the quasi-porous layer
$\bar{s}_i$	molar entropy of species *i* (J/mol-K)
S	molar entropy (J/mol-K)
$\overline{\boldsymbol{S}}_{\boldsymbol{i}}$	molecular entropy of species *i* (J/molecule-K)
t	membrane thickness (μm)
T	temperature (K)
$\boldsymbol{v}_{\boldsymbol{i}}$	volumetric flow rate of species *i* (cm^3/s)
V_i	molar volume of species *i* (cm^3/mol)
x	PEM expansion coefficient
$\boldsymbol{X}_{\boldsymbol{i}}$	general molecular force for species *i*, (J/cm-molecule)
X_i	general molar force for species *i* (J/cm-mol)
z	transverse cell co-ordinate
z_i	valence of species *i*

Greek

α	ratio of net water flux to hydrogen flux due to electro-reduction
α_E	charge transfer coefficient for electrode *E*
β	ratio of net water flux to proton flux due to overall redox reaction
$\beta_{X,E}$	parametric coefficient *X* for electrode *E* in the thin-interface treatment
γ	surface tension of water (N/m)
ε	porosity

$\boldsymbol{\varepsilon}$	compressive strain
η	overvoltage (V)
θ	contact angle, degrees
Θ	CO-induced degradation factor
κ_p	absolute permeability, cm^2
κ_ϕ	electrokinetic permeability, cm^2
λ	moles of water per mole of charge site
Λ_i	diffusive flux affinity for species *i* (J/g-cm)
$\boldsymbol{\mu_i}$	molecular electrochemical potential of species *i* (J/molecule)
μ_i	molar electrochemical potential of species *I* (J/mol)
μ_J	viscosity of fluid in phase *J* (Pa-s)
υ_i	stoichiometry of species *i*
ν	Poisson ratio
ξ_i	electro-osmotic drag ratio of species *i*
ρ	density (g/cm^3)
$\boldsymbol{\rho}$	specific resistance (Ω-cm)
ψ_i^{perm}	permeability coefficient of species *i* (mol/cm-atm-s, ×1/101325 mol/cm-Pa-s)
σ	proton conductivity (S/cm)
τ	tortuosity
ϕ	electric potential (V)
Φ_1	diffusive coefficient in the two-phase quasi-porous general transport equation
$\Phi_{2,J}$	protonic coefficient in the two-phase quasi-porous general transport equation
$\Phi_{3,J}$	convective coefficient in the two-phase quasi-porous general transport equation
χ	degree of constraint

Subscripts and superscripts

0	superscript: standard state pressure (1 bar, 0.1MPa)
	subscript: standard temperature (25˚C, 298.15 K)
cap	capillary
comp	compressed
cons	constrained
crit	critical property
epf	fraction of expanded pores
$E-1,2$	interface 1 or 2 of electrode E
fs	free-swelling property
gas	gaseous
H^+	hydrogen ion
i	species *i*
j	species *j*
J	phase J
l	limiting value
liq	liquid
m	exponent for the relative permeability pre-factor
mode	mode of water flux across PEM (i.e., diffusive, convective or protonic)
max	maximum value
mem	membrane
Ox	oxidation process
Red	reduction process
sat	saturated property
T	total value
Th	thermal property
u / c	uncompressed property
vap	vaporous
w	water

1 Introduction

1.1 Basic Principles

The Polymer Electrolyte Fuel Cell (PEFC) is an energy conversion device. It operates under the principle that a proportion of the chemical energy released by oxidising hydrogen and reducing oxygen to produce water can be harnessed as electrical energy. Because the release of electrical energy in a fuel cell is not dependant upon intermediate processes of thermal or mechanical energy conversion, it has the potential to achieve efficiencies in excess of the internal combustion engine.

The PEFC is comprised of two non-consumable electrodes and a separating proton-conducting polymer electrolyte membrane (PEM). The fuel – hydrogen – is supplied to the anode where it is oxidised to produce electrons and protons. The protons are conducted to the cathode through the PEM, while an external electrical circuit which connects the two electrodes conducts electrons to the cathode. The reductant – oxygen – is supplied simultaneously to the cathode where it is reduced to water by combining with the electrons and protons. The anode and cathode both contain catalysts to drive the oxidation and reduction processes respectively.

Due to irreversible losses in the PEFC, a proportion of the chemical energy released from the reduction-oxidation (redox) reactions cannot be harnessed to do useful work. Irreversible losses occur mainly due to the slowness of reactions in the electrodes, limitations in the mass transport of reactant gases and due to finite resistances to ionic and protonic transport in the electron and proton conducting materials of the cell. The remainder of the chemical energy release is carried by the electrons in the external electrical circuit. The amount of energy carried by one mole of electrons gives rise to a cell voltage, while the rate at which the energy carriers move around the electrical circuit gives rise to an electrical current. The product of the cell voltage and the electrical current defines the useful amount of energy released per unit time in electrical form.

For a hydrogen-fuelled PEFC, the overall reaction is;

$$H_2 + \tfrac{1}{2}O_2 \rightarrow H_2O \qquad (1\text{-}1)$$

The hydrogen-oxidation reaction (HOR) that occurs in the anode is;

$$H_2 \rightarrow 2H^+ + 2e^- \qquad (1\text{-}2)$$

The oxygen reduction reaction (ORR) that occurs in the cathode is;

$$2H^+ + 2e^- + \tfrac{1}{2}O_2 \rightarrow H_2O \qquad (1\text{-}3)$$

The principle processes are illustrated in Figure 1-1.

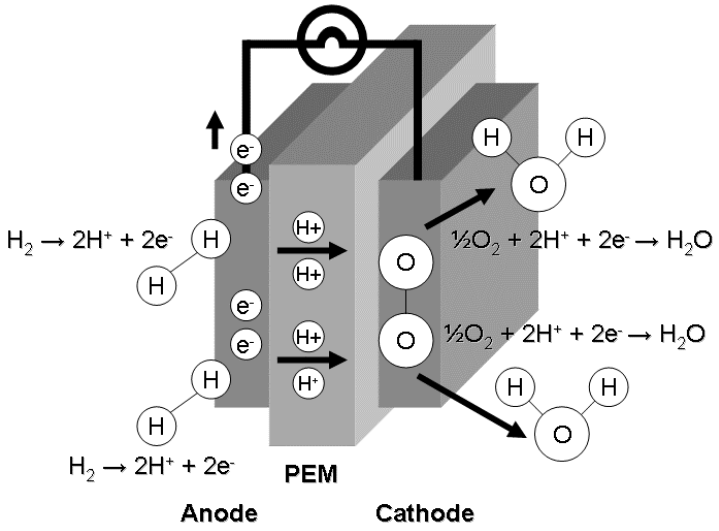

Figure 1-1 Principle reduction-oxidation processes of a hydrogen-fuelled polymer electrolyte fuel cell

The merits, limitations and applications of PEFC technology have been widely discussed in the literature [1,2,3]. In spite of tremendous scientific and engineering progress over the past couple of decades, fuel cell research remains highly geared towards identifying material designs, configurations and operating strategies for better performance, cost reduction and longevity. Due to the small length scales of a PEFC and the micro and nano-scale features of its internal components, *in-situ* measurement can be formidable. As such, it can be advantageous to employ numerical models that can predict the internal

electrochemical state of a PEFC in detail and the species distributions within it based on cell configuration, material composition and operating conditions. In order to do so, it is necessary to have a structured understanding of multi-species, multi-phase electrochemical transport.

The purpose of this thesis is to draw attention to the mechanisms of electrochemical transport in a PEFC. As will be discussed, the literature demonstrates a significant degree of diversity in the selection, manipulation and application of electrochemical theory to model transport within a PEFC, including its multiple layers. This can compound fuel cell development because it does not demonstrate clarity or consistency in the understanding of the internal transport. In order to truly understand internal electrochemical transport in a PEFC, its relationship with the physical properties of the fuel cell materials, infiltrating fluids and the thermodynamic conditions that the cell operates under, it is necessary to structure, demonstrate and apply a unifying mechanistic electrochemical theory.

1.2 Objectives of the Current Research

The aim of the current research is to develop a universal electrochemical theory to describe the mechanisms of electrochemical transport in PEFCs which reconciles the benchmark modelling philosophies in the literature and demonstrably predicts single-phase and two-phase multi-component transport characteristics of a single-cell. The objectives of the current research are as follow:

1. to establish an understanding of the existing theories and modelling philosophies for the PEFC as an electrochemical system;
2. to formulate, numerically validate and apply a multi-component input model for the boundary conditions of a PEFC;
3. to formulate and theoretically validate a universal treatment for multi-component electrochemical transport through the PEFC;
4. to merge, numerically validate and apply (2) and (3) to study factors affecting single-phase multi-component electrochemical transport through the PEFC via multi-layer simulations;

5. to formulate and numerically validate a universal treatment for two-phase multi-component electrochemical transport through the PEFC based on (3) and merged with (2);
6. to apply the above to study factors affecting two-phase water transport through the PEM via multi-layer PEFC simulations.

It is anticipated that the knowledge generated from this research will improve the understanding of the different approaches to modelling transport across the PEFC, how they are fundamentally related and how they can be reconciled under a universal electrochemical theory which can be applied to potentially all layers of the PEFC. It is anticipated that the application of the universal theory developed in this thesis will progressively uncover the phenomenological processes that affect the transport mechanisms within the layers of the PEFC which are formidable to measure *in-situ*, as discussed, and not rigorously captured through existing modelling approaches.

All numerical work for the current study will be carried out in the one-dimensional domain through the thickness of the cell where temperature gradients will be considered as having a negligible influence on transport [4]. In addition, the current study can be limited to non-reactive transport. However it is anticipated that the limitations of the numerical models developed in this research can be addressed in future work by interfacing the electrochemical model formulated in the current work with other highly-developed numerical tools such as computational fluid dynamics and lattice-Boltzmann modelling.

1.3 Outline of Thesis

Chapter 1: Introduction

The first chapter of the thesis has provided a brief introduction to PEFC technology and discussed the aims, objectives and outline of this thesis.

Chapter 2: The Polymer Electrolyte Fuel Cell

The second chapter will provide a discussion on the individual components of the PEFC and will discuss important aspects in respect to the performance of the PEFC. In doing so,

fundamental concepts of fuel cell thermodynamics and irreversible voltage losses will be covered.

Chapter 3: A Review of Practical Factors Governing the Performance of Polymer Electrolyte Fuel Cells

The third chapter will provide an in-depth review of the factors that affect fuel cell performance and longevity and will provide an account of state-of-the-art technological developments that are enhancing the readiness of hydrogen-fuelled PEFCs for market adoption.

Chapter 4: Mathematical Modelling of a Polymer Electrolyte Fuel Cell

The fourth chapter will present and discuss the existing theories for molecular transport and electrode kinetics in the PEFC as an electrochemical system.

Chapter 5: A Polymer Electrolyte Fuel Cell Model with Multi-Component Input

The fifth chapter will provide a complete single-phase model of the PEFC in one-dimension which fully accounts for multi-component input gases. The results obtained will be validated against data obtained from the open literature. The model will also be applied to simulate contaminant transport and its affect on cell performance.

Chapter 6: A Universal Transport Equation from Fundamental Theory

The sixth chapter will discuss the derivation of a single general transport equation (GTE) to describe electrochemical molecular transport through the layers of the PEFC. The electrochemical theory developed in this chapter will be theoretically validated by deriving all benchmark molecular transport equations employed in the PEFC modelling literature. The theory will then be translated into a single-phase one-dimensional multi-component model and numerically validated against data from the open literature. The model will also be applied to elucidate the operational factors that affect hydrogen crossover.

Chapter 7: A Universal Approach to Multi-Layer Two-Phase Modelling through the General Transport Equation

The seventh chapter will further-develop the universal theory developed in the previous chapter to model two-phase flow through the layers of the PEFC. The chapter will provide a description of how liquid water infiltration through porous and quasi-porous layers can be

modelled using the GTE as well as the effects of cell compression. The developed model will be translated into an object-oriented two-phase one-dimensional model and validated against data from the open literature.

Chapter 8: Water Transport Studies

The eighth chapter will present a parametric study to investigate the design and operational factors that can affect liquid water transport through the cell, the bi-modal water content of the PEM, and therefore PEFC performance. Factors considered include PEM thickness, anode humidification, PEM constraint and structural reinforcement.

Chapter 9: Conclusions and Future Work

The final chapter will outline the achievements and conclusions of this thesis and will provide suggestions for further work.

1.4 References

1 **Sammes NM.** *Fuel Cell Technology: reaching towards commercialization*, 2005 (Springer-Verlag, London)

2 **Bengt S.** *Transport phenomena in fuel cells*, 2005 (WIT Press, Southampton)

3 **Barbir F.** *PEM fuel cells: theory and practice*, 2005 (Elsevier Inc., Burlington)

4 **Rowe A, Li X.** Mathematical Modelling of Proton Exchange Membrane Fuel Cells. *J. Power Sources*, 2001, **102,** 82-96

2 The Polymer Electrolyte Fuel Cell

The principal components that form the PEFC are two electrodes (anode and cathode) and a polymer electrolyte membrane (PEM). The electrodes typically contain at least two parts; a relatively thick (~ 250 μm) porous carbon-fibre based gas diffusion layer (GDL), which acts to distribute reactant gases and product water in and out of the cell while providing conductive pathways for the movement of electrons, and a relatively thin (~ 10 μm) carbon-agglomerate based porous catalyst layer (CL) which serves as the reaction bed for the oxygen-reduction or hydrogen-oxidation processes.

2.1 Components of the PEFC

Figures 2-1 provides a description of the physical components of the cell and the potential configuration of a PEFC. A seven-layer assembly is shown which includes anode and cathode GDLs, CLs and a PEM. As commercial products, fuel cell layers can be supplied in a variety of pre-fabricated combinations. The catalyst coated membrane (CCM) is essentially a PEM coated with anode and cathode CLs. A two-layer gas diffusion electrode (GDE) is a GDL with a CL coating on one surface. A three-layer GDE contains an MPL between the GDL and CL. The membrane electrode assembly (MEA) is often a five-layer assembly consisting of anode and cathode GDLs, CLs and a PEM. A seven-layer MEA assembly contains both anode and cathode micro-porous layers (MPL). The MPL is used selectively to control hydration within the cell and therefore does not appear universally in all PEFCs. Figure 2-2 shows a PEFC with repeating components of a single-cell arranged in series.

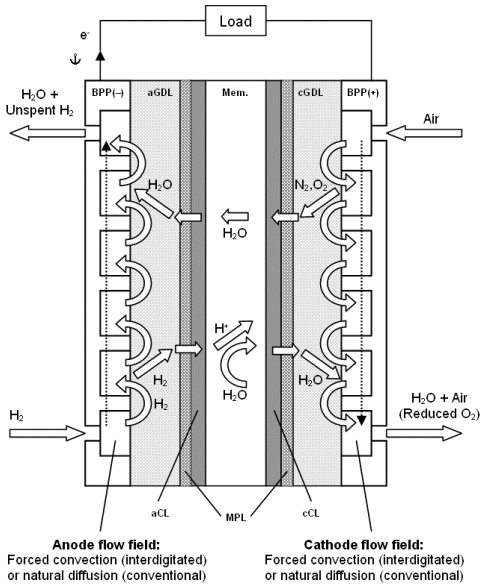

Figure 2-1 The key regions and flows of a PEFC single-cell

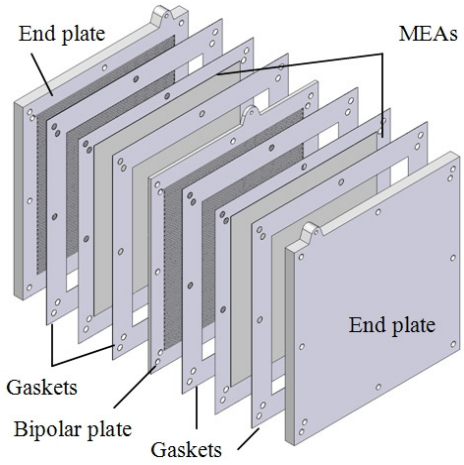

Figure 2-2 An illustration of a PEFC stack showing the bi-polar plate (BPP) and membrane electrode assemblies of a two-cell PEFC stack [1].

2.2 Cell Performance

The performance of a PEFC is indicated by a polarisation curve. Conventionally, this shows the output cell voltage of a single cell as a function of current density, in Amps per square centimetre. Current density is obtained by normalising the total current drawn from the cell to the total footprint area of a cell. This allows the performance of different cells to be compared simultaneously without having to consider the actual footprint area of the cells. Multiplying current density with cell voltage yields power density, in W/cm^2. What is

important is the nature of the cell voltage vs. current density relationship. In general, the output cell voltage deviates from a theoretical maximum potential as current density increases. The purpose of this section is to discuss the ideal output of the cell, the thermodynamic efficiency of a cell and the irreversible losses that typically characterise the polarisation curve.

2.2.1 The Thermodynamic Equilibrium Potential

Consider the following general reversible reaction, which takes place under a state of thermal, chemical and mechanical equilibrium;

$$aA + bB \leftrightarrow mM + nN \tag{2-1}$$

The change in free energy of the forward reaction is given by the Van't Hoff isotherm [2];

$$\Delta G = -RT \ln K + RT \ln \frac{[M]^m [N]^n}{[A]^a [B]^b} \tag{2-2}$$

where

R = universal gas constant

K = equilibrium constant of the reaction at temperature T

$[X]^x$ = activity of species X

The maximum electrical work $W_{el,\max}$ that can be obtained from the cell is equal to the change in free energy at temperature T and can be related to the electromotive force of the reaction E by;

$$\Delta G = W_{el,\max} = -nFE \tag{2-3}$$

where

n = number of moles of electrons

F = Faraday constant

Because by definition the reaction given by equation 2-1 occurs under a state of thermodynamic equilibrium, the electromotive force of the reaction E is more commonly termed the thermodynamic equilibrium potential.

At standard state (1 bar), the change in free energy can be defined as a function of the equilibrium constant K as follows [3];

$$\Delta G^0 = -RT \ln K \tag{2-4}$$

The change in free energy at standard state ΔG^0 can also be defined in terms of the electromotive force at standard-state, also known as the standard-state potential, E^0;

$$\Delta G^0 = -nFE^0 \tag{2-5}$$

Substituting equations 2-3 to 2-5 into 2-2 yields the general form of the Nernst Equation;

$$E = E^0 + \frac{RT}{nF} \ln \frac{[A]^a [B]^b}{[M]^m [N]^n} \tag{2-6}$$

Therefore, for a given system where the reversible reaction given by equation 2-1 occurs under a state of thermodynamic equilibrium, it is possible to determine the thermodynamic equilibrium potential of the forward reaction if the temperature of the system is known, if the activities of the reactants and products are known and if the standard-state potential is known. The thermodynamic equilibrium potential is established when the forward chemical process occurs at the same rate as the reverse reaction and therefore when there is no net charge being drawn from the cell. As such, the thermodynamic equilibrium potential is also commonly known as the open circuit potential, i.e., the electromotive force measured from a cell at zero current.

The standard-state potential can be defined by revisiting the change in free energy of the forward reaction at standard-state. The change in free energy can be defined in terms of the change in enthalpy ΔH^0 and entropy ΔS^0 during the reaction at standard-state, such that ΔG^0 varies according to temperature T;

$$\Delta G^0 = -nFE^0 = \Delta H^0 - T\Delta S^0 \tag{2-7}$$

The standard-state potential is defined using the standard temperature T_0 (25˚C) as [2];

$$E^0 \approx E_0^0 + (T - T_0)\frac{\Delta S_0^0}{nF} \approx -\frac{\Delta G_0^0}{nF} + (T - T_0)\frac{\Delta S_0^0}{nF} \tag{2-8}$$

Here, E_0^0, ΔG_0^0 and ΔS_0^0 are the standard-state potential, free energy change and change in entropy for the forward reaction given in equation 2-1 at standard temperature. This condition is known as standard temperature and pressure (STP). Substituting equation 2-8 into 2-6 yields;

$$E = -\frac{\Delta G_0^0}{nF} + (T - T_0)\frac{\Delta S_0^0}{nF} + \frac{RT}{nF}\ln\frac{[A]^a[B]^b}{[M]^m[N]^n} \tag{2-9}$$

For a hydrogen-fuelled PEFC, the overall reaction involves 2 electrons, hence $n = 2$. The change in free energy and entropy at STP can be calculated using the figures provided in Table 2-1.

	ΔG_0^0	ΔS_0^0
	kJ/mol	*kJ/mol-K*
Gaseous Hydrogen (H_2)	0	130.74
Gaseous Oxygen (O_2)	0	205.25
Liquid Water (H_2O)	-237.35	70.12

Table 2-1 Changes in free energy and entropy at standard temperature and pressure for hydrogen, oxygen and water [2,4]

Assuming that the overall forward reaction of the PEFC can be given as $H_2 + 1/2\,O_2 \rightarrow H_2O$, the change in free energy at STP can be calculated as;

$$\Delta G_0^0 = \sum \Delta G_0^0\Big|_{\text{products}} - \sum \Delta G_0^0\Big|_{\text{reactants}} \tag{2-10}$$

$$\therefore \Delta G_0^0 = \Delta G_0^0\Big|_{water} = -237.35 \text{ kJ/mol}$$

The cell potential at STP is therefore calculated as;

$$E_0^0 = -\frac{\Delta G_0^0}{nF} = \frac{237.35\times10^3}{2\times96484} = 1.229\,V$$

Similarly, the change in entropy at STP can be calculated as;

$$\Delta S_0^0 = \sum \Delta S_0^0\Big|_{\text{products}} - \sum \Delta S_0^0\Big|_{\text{reactants}} \tag{2-11}$$

$$\therefore \Delta S_0^0 = \left(70.12 - 130.74 - \frac{205.25}{2}\right)\times10^3 = -163.25\,\text{kJ/mol-K}$$

such that

$$\frac{\Delta S_0^0}{nF} = \frac{-163.25\times10^3}{2\times96484} = -0.8460\times10^{-3}\ \text{V/K} \tag{2-12}$$

Assuming that the activity of product water is equal to unity, that partial pressures can be defined in bar, i.e., $a_X = p_X / p^0$ where p^0 is the standard pressure, and by substituting equations 2-11 and 2-12 into 2-9 the following form of the Nernst equation can be obtained;

$$E = E^0 + 4.3085\times10^{-5} T \ln\left[p_{H_2} p_{O_2}^{1/2}\right] \tag{2-13a}$$

where

$$E^0 = 1.229 - 0.8460\times10^{-3}(T - 298.15) \tag{2-13b}$$

2.2.2 Thermodynamic Efficiency

The efficiency of an energy conversion device is generally defined as the ratio between the energy delivered by the system and the energy put into the system. In the context

of heat engines, it is usually defined in thermodynamic terms, i.e., the mechanical work done by the system divided by the heat energy input to the system. The heat input corresponds to the heat energy released due to the exothermic reactions during combustion and commonly known as the calorific value or the enthalpy of formation, ΔH_f. The Carnot limit shows that the maximum thermal efficiency of a heat engine is dependant solely on the temperatures of the high and low temperature zones and directly proportional to the temperature of the low temperature zone.

$$\eta_{Carnot,therm} = \frac{W_{mech}}{\Delta H_f} = 1 - \frac{T_C}{T_H} \tag{2-14}$$

where

W_{mech} = mechanical work done

ΔH_f = enthalpy of formation

T_C = temperature of the low temperature zone

T_H = temperature of the high temperature zone

For a PEFC, the efficiency is usually defined similarly in thermodynamic terms. The energy delivered by the PEFC is defined by the electrical energy output W_{elec} while the energy put into the system again corresponds to the heat energy that can be released if the fuel is combusted with an oxidant. This definition allows a relatively straightforward comparison of the PEFC with a heat engine because both efficiencies are defined relative to the amount of heat energy that is released when the fuel is burnt.

$$\eta_{PEFC,therm} = \frac{W_{elec}}{\Delta H_f} \tag{2-15}$$

When hydrogen is burnt below 100 °C, there is a release of what is known as the latent heat of condensation, i.e., the heat released when water vapour is converted into liquid water without a reduction in its temperature. As such, the higher heating value is commonly used for PEFC efficiency calculations, as they typically operate below 100 °C. For the burning of hydrogen, the HHV is -285.84 kJ/mol. Using equations 2-13a and 2-7 it is

possible to determine the standard-state potential and the change in free energy of the PEFC for a range of temperatures. Using equation 2-15 it is then possible to determine the maximum thermodynamic efficiency of the PEFC over this range. Correspondingly, Figure 2-5 compares the maximum thermodynamic efficiency of a PEFC using the HHV against the Carnot limit of a heat engine where the exhaust temperature is 45˚C. Generally speaking, Figure 2-5 demonstrates that the maximum thermodynamic efficiency of a heat engine according to the Carnot limit approaches that of a low-temperature PEFC (<100˚C) when the high temperature zone exceeds 200˚C (473 K).

It is noteworthy from Figure 2-3 that the maximum thermal efficiency of the Carnot limit can exceed the thermal efficiency of a PEFC. Therefore, the PEFC does not always have a higher thermal efficiency than the Carnot limit. In addition, while Figure 2-3 suggests that operating at low temperatures can increase the maximum thermodynamic efficiency of the PEFC, two other issues have to be considered. First of all, it has to be noted that it can be more advantages to operate at higher temperatures as the waste heat is more useful (if the product water takes liquid form, it has already released the latent heat of condensation whereas water vapour contains more heat energy as it retains the latent heat of vaporisation). Second, it has to be noted that the voltage losses that occur when current is drawn from the cell can be greater at low temperatures and therefore it can be more practical to operate at higher temperatures.

2.2.3 Irreversible Voltage Losses

The useful amount of work, the electrical energy, is obtained from the PEFC only when a reasonably large current is drawn. Under such conditions, the cell potential decreases from its thermodynamic equilibrium potential because of irreversible losses. These losses are often referred to as polarisations, overpotentials or overvoltages. The cause of these losses

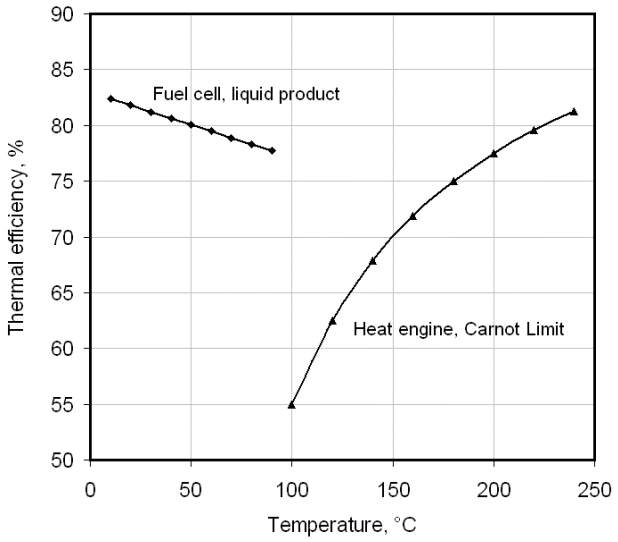

Figure 2-3 Maximum thermal efficiency of a hydrogen-fuelled low temperature PEFC and the Carnot limit of a heat engine with an exhaust temperature of 45˚C.

include slow electrode kinetics, Ohmic resistances of the electrolyte, electrodes and leads, and mass transport limitations.

Activation Losses

At low current densities (1 – 100 mA/cm^2) the activation losses mainly account for the irreversible voltage loss of a PEFC. Activation losses are attributed to the slowness of reactions occurring in the fuel cell electrodes, i.e., the catalyst layers. The anode kinetics are generally much faster than the cathode kinetics and therefore the cathode kinetics largely contributed to the overall activation loss.

Activation losses can be reduced by increasing the temperature of the cell, increasing the electrochemical activity of the electrode with suitable catalysts and by increasing the electrochemically active surface area (EASA) of the electrodes. Activation losses can increase during the course of operation if the EASA reduces in the fuel cell catalyst layers. Other factors significantly affecting performance in the catalyst layers include its material composition and distribution, its geometric structure and the impurity content of the reactant feeds. Assuming that the anode overvoltage is small compared to that of the cathode, the activation loss can be described as follows using the general form of the Tafel equation:

$$\eta_{act} = \frac{RT}{\alpha_c nF} \ln \frac{J_0}{J} \tag{2-16}$$

where

J = current density

α_c = cathodic charge transfer coefficient

The exchange current density J_0 corresponds to the rate at which hydrogen is oxidised and oxygen is reduced according to reversible reaction given by equation 2-1.

Ohmic Losses

At intermediate current densities (100 – 1000mA/cm^2), the irreversible losses are dominated by Ohmic losses in the cell. Ohmic losses can be attributed to the ion conducting properties of the different elements of the cell. The PEM is the central proton conducting part of the cell, which connects the dispersion of electrolyte in the two catalyst layers. Resistance to the flow of protons in the PEM can significantly contribute towards the Ohmic loss of a cell. Resistance to the flow of electrons also contributes towards the Ohmic loss.

The electron conducting parts of the PEFC have finite resistances that are dependant upon cell operating temperature and the compaction force applied to a cell. Charge transfer resistances at the anode and cathode electrode, as well as resistance contributions from any other components in a fuel cell, such as current collectors, all contribute to Ohmic losses. Ohmic losses can be expressed in terms of Ohms law:

$$\eta_{ohmic} = Jr \tag{2-17}$$

where r is the total Ohmic resistance to charge transfer.

Proton conductivity can be improved by improving the hydration of the membrane during operation, by decreasing the thickness of the membrane and improving the ionic conductivity of the membrane. Electrical conductivity can be improved by

selecting/designing components with materials that have high bulk electrical conductivities, and ensuring minimal surface corrosion and maintaining good electrical contact between electron-conducting components of the PEFC.

Mass Transport (Concentration) Losses

At high current densities (> 1000mA/cm^2), mass transportation dominates the irreversible losses. Mass transport losses occur when there is a change in the concentration of a reactant gas on the surface of an electrode, which occurs at high current densities where the hydrogen oxidation and oxygen reduction rates correspondingly hasten. In order to maintain a current for a given potential, the supply of reacting species to the electrode surface has to be sustained. This sustains the electrolytic current due to the movement of ions through the membrane and therefore balances the electric current flowing in the external circuit. This movement cannot be increased indefinitely and a point must be reached where species react at the electrode as fast as they reach it. The amount of current obtained under such a circumstance is known as the limiting current. Mass transport losses can be caused by the slow diffusion of the gas phase through the porous regions, solution/dissolution of the reactants/products into/out of the electrolyte membrane, or diffusion of reactants/products into/out of the electrolyte to/from the electrochemical reaction site. Mass transportation losses can be estimated as;

$$\eta_{conc} = \frac{RT}{nF}\ln\left(1-\frac{J}{J_l}\right) \tag{2-18}$$

where J_l is the limiting current density.

The product water generated inside the PEFC forms at the cathode side and some of it is retained by the PEM, thereby enhancing its proton conductivity. Excess water has to be expelled from the cathode in order to prevent liquid water formation and accumulation, which can subsequently impede pathways for the transport of oxygen to the catalyst sites. At high current densities, the production of water correspondingly hastens. It can become difficult to remove the water from the cathode and can therefore begin to saturate the porous

electrodes. This can slow down the oxygen diffusion, causing a sharp drop in the oxygen concentration resulting in a drastic increase in the mass transport loss.

Fuel Efficiency Losses

As hydrogen passes through the anode GDL and enters the anode catalyst layer, it is possible for some of the hydrogen to permeate straight through the PEM, forgoing the electro-oxidation process. Consequently, it reacts directly with oxygen in the cathode catalyst layer and amounts to a proportion of spent fuel that does not contribute towards the electrical energy harnessed from the cell. This is described as an efficiency loss. Oxygen can also permeate the polymer membrane from the opposite direction through enlarged pores and directly react with hydrogen in the anode catalyst layer. Fuel efficiency losses are highly-dependant on the structure and mechanical state of the PEM; thin PEMs and the formation of pinholes can cause high rates of fuel crossover.

2.2.4 Polarisation Curve

The overall cell output is given by subtracting three of the losses discussed in the preceding section from the open circuit potential of the cell:

$$V = E - Jr - \frac{RT}{\alpha_c nF}\ln\frac{J}{J_0} - \frac{RT}{nF}\ln\left(1 - \frac{J}{J_l}\right) \tag{2-19}$$

Typical parameters for the constants in equation 2-19 are given in Table 2-2. Figure 2-6 demonstrates the typical form of a polarisation curve based on the parameters in Table 2-2.

The thermodynamic efficiency of the PEFC when current is drawn from the cell can be calculated by assuming that the electrical work done by the cell can be equated to the free energy actually delivered by the cell based on the actual cell voltage;

$$W_{elec} = -\Delta G_{act} = nFV \tag{2-20}$$

Equation 2-20 can be applied to 2-15 to determine the thermodynamic efficiency as a function of power density, as shown in Figure 2-7. It is noteworthy that the thermodynamic efficiency increases with decreasing load, unlike the internal combustion engine (ICE). Generally speaking, the PEFC maintains thermodynamic efficiency in the 40% ± 10% band, compared to an average of around 42% and 35% for state-of-the-art diesel and gasoline ICEs respectively.

Parameter		Units	Value
Cell Potential at STP	E_0^0	V	1.229
Open Circuit Potential	E	V	0.95
Cell Temperature	T	K	343
Total area-specific cell Resistance	r	Ohm-cm^2	0.1
Cell Footprint Area	A	cm^2	200
Cathodic Charge Transfer Coefficient	α_c	-	0.5
Exchange Current density	J_0	mA/cm^2	0.067
Limiting Current Density	J_l	A/cm^2	2.0
Universal Gas Constant	R	J/mol-K	8.3143
Faraday Constant	F	C/mol	96484

Table 2-2 Constants for equation 2-19

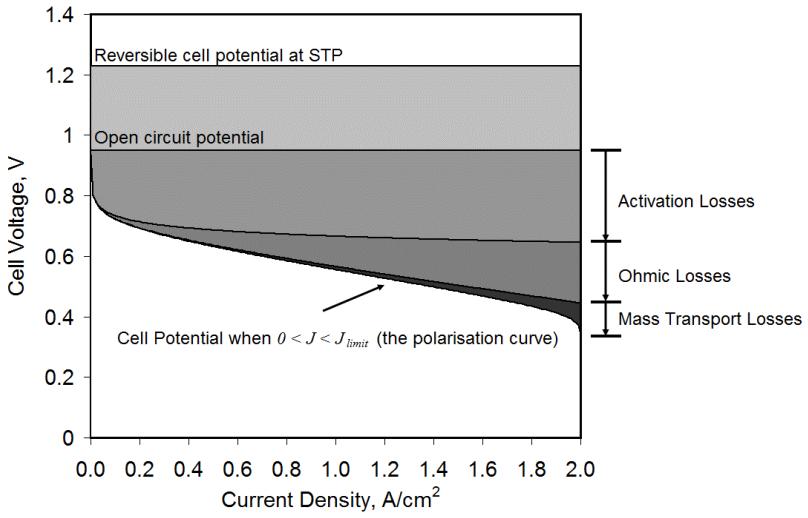

Figure 2-4 Basic polarisation curve of a PEFC

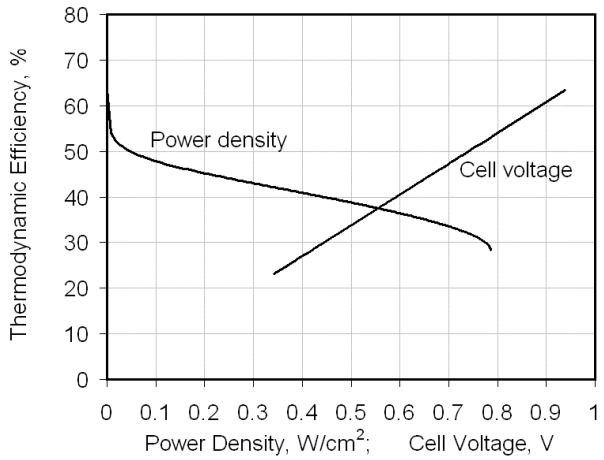

Figure 2-5 Thermodynamic efficiency of a PEFC as a function of electrical load and cell voltage.

2.3 References

1 **Greenwood PS.** *Internal communications, Loughborough University, 2009*.

2 **Berger C.** *Handbook of Fuel Cell Technology*, 1968 (Prentice-Hall, Englewood Cliffs)

3 **Bard AJ, Faulkner LR.** *Electrochemical Methods*, 2001 (John Wiley & Sons, New York)

4 **Hamman CH, Hamnett A, Vielstich W.** *Electrochemistry*, 1998, (Wiley-VCH, New York)

3 *A Review of Practical Factors Governing the Performance of Polymer Electrolyte Fuel Cells*

This chapter presents a comprehensive review that aims to provide a structured understanding of the practical factors that govern the performance of hydrogen-fuelled PEFCs by considering the underlying phenomenological mechanisms that can degrade cell performance and cause failure. As discussed in the preceding chapter, the performance of a PEFC is characterised by one of four loss mechanisms; (1) activation losses; (2) Ohmic losses; (3) mass transportation losses and; (4) fuel efficiency losses. Degradation mechanisms can contribute towards multiple loss mechanisms and can also lead on to the final form of user-detectable loss; (5) catastrophic cell failure.

3.1 Introduction

Research and development in PEFC technology to date has resulted in a vast array of materials, designs, manufacturing techniques and considerations for the different components of the cell [1,2,3]. These variations reflect the fact that there are a multitude of factors that govern the performance of the PEFC, all of which have some element of physical design or operation associated to it that can be altered to improve an aspect of cell performance.

Differences in operating modes and general cell design according to application means that the impact of certain performance degradation and failure mechanisms are also likely to be different from application to application. Automotive fuel cells, for example, are likely to operate with neat hydrogen under load-following or load-levelled modes and be expected to withstand variations in environmental conditions, particularly in terms of temperature, pressure and atmospheric composition. In addition, they are also required to survive over the course of their expected operational lifetimes i.e., around 5,500 hrs, while undergoing as many as 30,000 startup/shutdown cycles [4]. PEFCs for stationary applications would not be subjected to as many startup/shutdown cycles, however, would be expected to survive 10,000 - 40,000 hrs of operation whilst maintaining a tolerance to fuel impurities in the reformate feed. The current review discusses factors that are potentially relevant to all types of applications, and covers all major hardware components in the PEFC.

3.2 Activation Losses

3.2.1 Platinum Agglomeration

In order to maximise the electrochemically active surface area (EASA) in the anodic and cathodic catalyst layers, the catalyst is applied as fine and widely dispersed nano-particles on the surface of a supporting particle [5]. Typically, the catalyst is platinum or platinum alloyed with ruthenium or chromium for example, and the larger supporting particle is carbon-based. Recent studies have shown that within 2000 hrs of operation, it is possible for the metal catalyst to undergo morphological change in the form of catalytic agglomeration and/or ripening [6]. This leads on to a gradual decrease in the EASA. While this phenomenon is observed for both anode and cathode catalyst layers, it is usually the cathodic particles that undergo more extensive agglomeration. This is because the cathode can contain sufficient liquid water to facilitate primary corrosion [7]. Repetitive on/off load cycles for PEFCs can also cause platinum sintering; residual hydrogen can induce a high voltage equivalent to open-circuit voltage to the cathode, causing the sintering to occur [8]. This can be mitigated by purging the anode channel with air. Loss of EASA due to agglomeration has also been observed for un-humidified PEFCs operating at a higher temperature of 150°C in polybenzimidazole (PBI) membranes [9].

3.2.2 Platinum Migration

Another mechanism for the loss of EASA could be attributed to the movement of platinum. When the PEFC is operated through hydrogen-air open circuit to air-air open circuit, platinum can become soluble and could therefore infiltrate adjacent layers [10]. The corresponding loss of platinum can also compromise the EASA. Such phenomenon can also be accompanied by an apparent migration of platinum. Migration of metal catalyst particles in both the anode and cathode catalyst layers in PEFCs has been observed, moving towards the interface between the catalyst layer and the membrane [7]. Platinum migration from the cathode catalyst layer to the anode has also been observed in phosphoric acid fuel cells (PAFC) [11].

3.2.3 Exposure to Sub-Zero Operating Conditions

Exposure to sub-zero operating environments are also known to compromise the EASA. The repetitive freezing and melting of water in the catalyst layer is likely to deform the structure of the catalyst layers by increasing the pore size and reducing the EASA [12].

3.2.4 Atmospheric Contaminants

The effects of reactant contamination and the leaching of contaminants can also significantly contribute towards increases in activation losses at the anode and the cathode; catalytic contamination can occur due to both air pollutants and fuel impurities. The presence of excess liquid water exacerbates the effects of contamination, which can act to transport leached impurities within the cell [13]. Impurities are thereby deposited on the catalyst sites, compromising the EASA on either electrode.

Air impurities such as nitrogen dioxide (NO_2), sulphur dioxide (SO_2) and hydrogen sulfine (H_2S) have been found to have a negative impact on cell performance due to their adsorption on platinum catalyst sites [14]. It has been reported that with low concentrations of NO_2 and SO_2, i.e., 0.4 and 0.5 ppm respectively, the effects of contamination on cell performance can be reversed if the cathode is subsequently fed with neat air [15]. For higher concentrations, i.e., 1-5ppm of either NO_2 or SO_2, cyclic voltammetry is required to fully recover the cathode [14,16]. Exposure to SO_2 and H_2S appear to lead on to the formation of two sulphur species, one of which adsorbs strongly on the platinum sites. In either case, cyclic voltammetry is required to oxidise the sulphur adsorbed [14].

3.2.5 Fuel Contaminants

Operating PEFCs on a hydrocarbon reformate could expose the anode catalyst layer to CO in the concentration range of 10-100ppm [17]. Reformation of methane (CH_4) for example, can yield a hydrogen-rich fuel feed with 80% H_2 and 20% carbon dioxide and carbon monoxide in the mentioned concentrations [18]. The carbon dioxide can lead on to the formation of additional carbin monoxide in the anode catalyst layer either through a

reverse water-gas shift reaction or through the electro-reduction of carbon dioxide [18]. Carbon monoxide is problematic because it can adsorb onto platinum more strongly than hydrogen, which thereby compromises the EASA for hydrogen oxidation. The carbon monoxide in the fuel feed can also cross-over through the membrane to the cathode catalyst layer [19] and can also be present in air. Carbon monoxide contamination can therefore also compromise the EASA for oxygen reduction in the cathode catalyst layer, reducing cathode performance. Carbon monoxide coverage can be reduced if the platinum catalyst is alloyed with ruthenium (Ru) and tin (Sn) to give PtRu and Pt_3Sn [20]. Other methods include ensuring that the saturated vapour pressure of the fuel feed is maintained during operation, by reducing the thickness of the catalyst layer [21], and by elevating the cell temperature from 80°C to around 120°C, which improves the activity of the catalyst layer for hydrogen oxidation [22]. According to another method, oxygen could be bled into the hydrogen feed in order to oxidise carbon monoxide to carbon dioxide before it reaches the anode catalyst layer [23]. A more recent method includes the use of a 'reconfiguration anode', where a catalytic material which uses cobalt, iron and copper is applied to the gas-facing side of the anode gas diffusion layer to oxidise the carbon monoxide in the fuel feed before it permeates into the anode catalyst layer [24]. A comprehensive review of articles discussing PEFC contamination has been carried out by Cheng *et al.* [25].

3.2.6 Carbon Corrosion

Altering the structural composition and material use can improve the performance and stability of the catalyst layers. Nafion and catalyst distributions can be applied non-uniformly to favourably maximise the proton transport and porosity in the opposing regions of greatest ion flux and gaseous flux respectively [26,27,28,29]. Catalytic supports can be favourably chosen for minimised oxidation rates. Carbon corrosion is a significant issue for fuel cells and can occur during fuel starvation, when there is only partial coverage of hydrogen on the catalyst sites and during localised flooding [30,31]. Such conditions can be induced or exacerbated during cyclic operation. If a single cell has insufficient fuel to support the current drawn, carbon can corrode to support the current above that provided by the fuel [30]. The standard potential for the corrosion of carbon is 0.207V. When the anode potential is below 0.207V, fuel is consumed to drive the current. When the anode potential rises above 0.207V, carbon corrosion in the anode catalyst layer occurs to supply protons to support the

current [30]. Platinum agglomeration can also be instigated as a consequence of a loss of catalytic support during carbon corrosion [32]. The chemical equation for carbon corrosion is as follows [30];

$$C + 2H_2O = CO_2 + 4H^+ + 4e^- \quad (3\text{-}1)$$

It has been shown, for example, that while XC72 carbon black reacts more slowly than Black Pearls (BP) 2000, they both become less stable supports under humidified fuel cell operating conditions in comparison to dry conditions [33]. Whilst humidification is necessary for most PEFC designs to reduce the resistance to proton transfer in the polymer membrane, humidifying the cathodic reactant supply up to 60% will also improve catalytic activity due to its impact on the rate-determining step of the oxygen reduction reaction [34]. For low-temperature automotive PEFC stacks, for example, some level of humidification can be unavoidable. Graphitization of carbon supports is suggested as one method to improve thermal stability under such conditions if a high surface area for the supports can be maintained [33]. Operating under fixed current densities and flow rates can also avoid carbon corrosion [31]. One alternative to carbon-black supported platinum catalysts are multi-walled carbon nanotube supported platinum (Pt/CNT) catalysts, which through accelerated durability tests have shown that they are more resistant to platinum sintering. This is due to the stability of CNTs, which possess a higher resistance to electrochemical oxidation than carbon black [35].

3.2.7 Chemical Degradation of Silicone Seals

Another reported form of catalytic contamination can be caused by the chemical degradation of sealing material used in the fuel cell stack. Typically, seals in fuel cell stacks are made of silicone and serve to avoid mixing of hydrogen and oxygen. The acidic character of the polymer electrolyte membrane along with the thermal stressing of the silicone seal can cause it to degrade chemically but without compromising its mechanical functionality [36]. The process is marked by yellow colouration. The products of the silicone reaction occur at both the anode and cathode side, but migrate towards the cathode due to the electric field. PFSA membranes have been found to be impermeable to the products, and so cause the products to accumulate in the catalyst layers. Schulze *et al.* reported that in the cathode

catalyst layer the decomposition products react with catalyst to form particles containing silicone, oxygen and platinum [36].

3.3 Mass Transportation Losses

3.3.1 Cell Flooding

Impedance to the transport of reactants to the catalyst sites results in an increase of mass transportation losses. Impedance to reactant transport can manifest itself in several different ways, but compromise the porous network for gas permeation through the porous layers of the cell. The foremost contributor to the impedance to reactant transport occurs in the cathode side of the cell, due to the formation of liquid water which restricts the transport of oxygen. This compromises the partial pressure hence the local oxygen concentration on the cathode catalyst sites. It propagates from the cathode catalyst layer and can lead to flooding in the GDL and parts of the cathode reactant supply channel. Water management has therefore been the focus of a significant number of research groups and has resulted in a multitude of designs and operating strategies aimed at mitigating mass transportation losses. Liquid water in the flow fields can be carried away if the channel flow rates are sufficiently high. Pressure drops along straight sections and particularly around flow field bends however can lead to water accumulation, subsequently leading to the clogging-up of channels and therefore potentially cell shut-down [37].

Pressure drops along a single channel are governed by the physical characteristics of the channel and the physical characteristics of the fluid. The most relevant physical characteristics of the channel include the length and cross-sectional geometry of the channel, the number, closeness, abruptness and geometry of channel bends and the hydrophobicity of the BPP surface. The characteristics of the fluid are reflected by the Reynolds number (Re) [38,39]. Flows that have low Reynolds numbers ($Re < 50$) are mainly dominated by viscous forces and thereby susceptible to pressure losses induced by skin friction. Flows with higher Reynolds numbers, i.e., $Re > 200$, are susceptible to flow separation particularly when its direction is abruptly changed. Flow separation in the vicinity of sharp corners of flow field bends leads on to the formation of vortices, which also results in pressure losses. Vortices

can also form in the same manner in the vicinity of inlet manifolds [40]. The introduction of finite curvature ratios for 90° bends can assist in maintaining laminar flow [39]. In addition, in order to allow separating flows to become laminar again, it is necessary to optimise the length of the straight section immediately downstream of the bend.

In the general case, pressure losses along single channels can be minimised if the overall flow field path length is kept short and if the number and abruptness of bends are minimised. Recent studies have highlighted that uniform flows with typically small pressure drops can be established particularly for flow fields with straight, parallel channels [41] and for serpentine channels that have shorter path lengths and larger numbers of multiple channels rather than longer path lengths and fewer channels within the same cell area [42]. Such measures can ensure that the channels remain pressurised along their entire lengths and reduce the chance of flooding whereby high upstream pressures and low downstream pressures are established causing liquid water to be pushed down and accumulate in downstream regions of the flow fields [43]. In general, liquid water has a tendency to accumulate in regions where the gas-phase flow becomes stagnant, particularly in abrupt 180° bends often seen in serpentine flow fields [44,45,46].

Interdigitated flow fields could be used over conventional gas distributors to improve oxygen distribution to the cathode catalyst layer and water removal by adding forced convection to gas diffusion to drive transport in the porous layers [47]. Forced convection is induced by decoupling the direct path between inlet and exit flow fields on one or both sides of the bi-polar plate design. Under certain conditions, interdigitated flow fields can also yield reductions in fuel consumption rates without loss in performance compared to conventional flow field designs [48]. In the context of PEFC stacks, interdigitated flow fields can also induce unbalanced pressure drops between cells. The concept is still undergoing development [49,50,51,52,53,54,55, 56,57,58,59, 60,61].

Counterflow configurations have shown that orienting the reactant flows to pass through opposite-sided inlets can allow for better internal humidification of the cell [62,63]. The high water content in the anode inlet feed can be used to humidify the membrane when water molecules are electro-osmotically dragged from the anode to the dry cathode by migrating protons, whereas the cathode inlet is adjacent to the drier anode exit feed which allows for membrane hydration through diffusion and convection, driven from the cathode

side. Counterflow configurations appear in automotive fuel cell stacks [64] and depending upon the operating strategy it can be possible to delay the onset of flooding.

If water can be generated within the membrane for humidification, it could be possible to reduce the extent to which the inlet reactant gases need to be humidified. This could naturally suppress the onset of two-phase flow and cell flooding, and could assist in simplifying the system design. As such, the dispersion of platinum particles within the membrane has been explored [65,66]. Here, water would be generated within the membrane by virtue of the recombination of hydrogen and oxygen on catalyst sites. The concept therefore relies upon the permeation of hydrogen and oxygen through the membrane region. The limitation of this method is that the platinum dispersions are susceptible to forming electron-conducting networks that could cause short circuits [67]. Recent re-developments have focused on membranes consisting of one middle layer of Nafion containing dispersions of Pt/CNT with two outer layers of Nafion [67]. The entire membrane assembly can be as thin as 25 microns. Reported results show that up to 90% of the performance obtained with humidified reactants can be obtained by such self-humidifying membranes with dry reactants [67]. Another example is of silicone oxide-supported platinum catalyst dispersed within protected three-layer sulfonated poly(ether ether ketone) (SPEEK)/PTFE/Nafion matrix membranes [68]. At present, though, self-humidification is not a standard concept.

Along with the literature reported above on the various means of mitigating mass transportation losses, numerous patents have been filed related to improved water management schemes [69,70,71,72,73,74].

3.3.2 Hydrophobicity of Porous Layers

Liquid water transportation and removal can be facilitated by treating porous layers with hydrophobic material, commonly polytetrafluoroethylene (PTFE) or fluorinated ethylene propylene (FEP). The hydrophobicity of a surface is reflected through the contact angle that a water droplet makes on the surface of the material; a contact angle less than 90° reflects a hydrophilic surface, while that greater than 90° reflects a hydrophobic surface.

Water transport can be managed through the use of the MPL. Because it is highly hydrophobic, it can act to transport liquid water away from the cathode GDL in the direction of the anode via the membrane, thereby delaying flooding effects in the cathode and simultaneously hydrating the membrane layer [75,76,77,78,79]. The use of an MPL also lessens the sensitivity of the catalyst layer to flooding, allowing thinner catalyst layers to be used [80]. A bi-functional hydrophobic and hydrophilic porous structure can simultaneously facilitate both gas-phase and liquid-phase transport respectively. Such pore structures can be achieved with composite carbon black loaded to around 0.5mg/cm^2 with a PTFE content of 30 wt.% [81].

The GDL is also usually treated with PTFE. A higher PTFE content can also help to preserve the porous structure of the GDL by increasing the material rigidity [82], however it can also compromise the electrical conductivity of the GDL [83] and excessive coating can lead to high levels of flooding [80]. Also, it has been shown that for GDLs that are made up of graphite fibres, the hydrophobic polymer tends to localise on the surface regions on treatment; large numbers of surface pores made by intersecting fibres will be blocked by thin polymer films, rendering the bulk of the interior less hydrophobic [84]. It has also been shown that the contact angle of treated GDLs can reduce with temperature [84].

Mechanical and electrochemical degradation of PTFE in GDLs has also been reported [84,85]. Operating conditions that induce thermal cycles in the fuel cell stack which result in a loss of hydrophobicity can therefore make water removal more difficult. It can also cause the polymer to delaminate, thereby deteriorating the hydrophobic property of the GDL and compromising the ability to remove water with respect to operational life. It is arguable that the MPL, which has a comparable material composition to the GDL and is also porous in nature, is susceptible to the same degradation mechanisms. Damage to PTFE coatings can also be induced when GDLs are exposed to sub-zero operating conditions [86].

3.3.3 Ionomer Loading in Catalyst Layer

The PFSA ionomer loading in the catalyst layer can also have an effect on the transport of reactants to active sites in the catalyst layer. The material is placed in the anode and cathode catalyst layers in order to provide pathways for proton transport [87,88]. Water

uptake in the polymer electrolyte material could cause it to correspondingly expand, thereby reducing the pore sizes in the catalyst layer [89] which impedes reactant supply. The effect is usually reversible since the polymer electrolyte material will also contract when the cell is not in operation, or when liquid water production reduces at lower operating cell current densities for example. Excessive ionomer loading for a given platinum loading will also inherently impede reactant supply; higher mass transportation losses have been reported due to the impedance to oxygen transportation in the catalyst layer [90]. Ionomer skins can also form on the outer surface of the catalyst layer of the completed MEA, however this can be limited to certain fabrication techniques [91]. In general, the fabrication processes for the catalyst layer such as spraying, painting rolling and screen printing all possess a limited degree of precision and ultimately therefore the degree of control over the composite structure of the fabricated MEA [92]. Navessin *et al.* reported that decreasing the ion exchange capacity (IEC) of the ionomer, which is the equivalent to increasing the equivalent weight (EW), results in an increase in hydropobicity, decrease in water content, increase in oxygen solubility and an increase in the ORR current. The EW reflects the ratio of the atomic weight of an element to the valence it assumes in a chemical compound. A low IEC (or high EW) could improve the cell performance by facilitating water management.

3.3.4 Impedance to Transportation due to Ice Formation

The effects of sub-zero operating conditions significantly influence mass transportation losses. The operating temperature of the cell has to be brought up to above freezing before ice formation completely fills the pores of the cathode catalyst layer [93]. The instantaneous effect of ice formation is to impede oxygen transport to the catalyst sites and can render entire cells inactive. Freezing conditions are known to weaken the MPL structurally to an extent that renders it prone to material loss from air flow through the GDL [94]. In practice, ice formation can occur in any region of the fuel cell where water resides and so it is important to remove excess water from the cell prior to start-up, and to operate the cell on start-up such that water generated in the cathode catalyst layer is not allowed to freeze. Gas-purging has been identified as a mechanism by which excess water can be removed [95]. In one reported method, gas-purging is done before the cell temperature falls below 0°C using dry gases such as nitrogen and oxygen for the anode and cathode respectively, optionally using 30% methanol or 35% ethylene glycol as antifreeze additives

[96]. Another reported method involves purging using gases with a limited degree of relative humidity to ensure that the provision of adequate water content in the proton conducting membrane is not completely compromised [97].

3.3.5 Effects of Compaction on the GDL

The porous structure and thickness of the GDL also influences two-phase water and reactant transport [98]. Reactant transport can be enhanced when the GDL porosity is in the region of around 0.3-0.6 [99,100] and liquid water removal to the gas channel can be enhanced with a linearly-graded porosity [99]. The use of thinner GDLs can also improve performance by allowing for greater liquid water mass transfer under steady-state conditions [99,101] and greater reactant mass transfer towards the catalyst layer [100]. The permeability of a GDL is another relevant parameter, which varies according to the carbon type [82]; woven and non-woven GDLs have exhibited slightly higher permeability than carbon fibre paper GDLs with similar solid volume fractions [102].

A fuel cell stack is held together by compacting together single cells. The corresponding compression can result a non-uniform pressure distribution across the active area of the cell, which can affect the structural properties of the GDL. Over-compression is argued to be a common occurrence in most fuel cells [103] which causes pores in the GDL to collapse, thereby reducing the porosity, increasing flooding [104] and reducing gas permeability [105]. The deforming over-compression can be less significant under channel regions and occurs mainly between mating surfaces that transmit compaction forces, for example land areas in the bi-polar plates and under rib areas where the cell is sealed with gasket material [105,106,107]. It has been observed that increased compression initially improves the performance of the cell by reducing the interfacial resistance between the bi-polar plate and the GDL up to an optimal threshold, whereas further compression thereafter narrows the diffusion path for mass transfer from the gas channels to the catalyst layers [108,109]. The effects of stress due to over-compression are more pronounced at high current and low pressure [110]. Chang *et al*. [109] identified the threshold clamping pressure to be in the region of 0.5MPa. The damage to GDLs is manifested through a break-up of fibres and a deterioration of hydrophibic coating, thereby compromising the ability to remove water from the cell [111].

3.4 Ohmic Losses

3.4.1 Resistance to Electron Transfer in the Bi-Polar Plate

Both resistance to electron transfer and proton transfer contribute towards the overall Ohmic losses incurred in PEFCs. Elements of the cell where electron transfer occurs includes the carbon support in the catalyst layers, the GDL and the BPP. Proton transfer occurs in the polymer electrolyte matrix dispersed in the catalyst layers and the PEM.

While the bipolar plate provides the bulk of the mechanical strength of the stack, it also serves as a current collector, as a thermally conductive medium to remove excess heat energy from single cells, and as a device to supply reactants and to remove water via flow fields on both faces of the plate. However, they must withstand the acidic and humid conditions within the stack. Corrosion is a significant issue for BPPs, which leads on to the loss of electrical conductivity. While the BPP must have high mechanical strength, low susceptibility to material dissolution, low susceptibility to the release of metal ions and high corrosion resistance, the bulk electrical conductivity must be high and the interfacial contact resistance (ICR) must be kept low [112]. As an indication, targets set for mechanical strength and electrical conductivity are 44.26 MPa and 100 S/cm respectively [113]. These attributes have to be achieved with materials and processes that are compatible with the concept of low cost and high volume manufacturability. As such, an array of different chemical compositions and synthesising processes have been investigated to identify how these requirements can be simultaneously met.

Graphitic Bi-Polar Plates

Graphite is conventionally regarded as the standard material for BPPs because of its high conductivity (300 S/cm) [113] and high corrosion resistance [114]. However, graphite BPPs are susceptible to fracturing due to shock and mechanical vibration, are permeable to gases and can be costly to machine in high volumes [112].

Stainless-Steel Bi-Polar Plates

While corrosion-resistant metals have better mechanical properties and are cheaper to machine in high volumes than graphite plates, the chemical process that provides corrosion resistance can also compromise its electrical conductivity. Stainless steel (SS), for example, develops a chromium (III) oxide (Cr_2O_3) passivating layer on the surface which prevents the bulk metal from corrosion. This thin film however impedes electron transfer and therefore raises the ICR. The consequent Ohmic heating thereby compromises the electrical energy that can be harnessed from single cells. The bulk resistivity is however insignificant in relation to the surface resistance due to this film [115].

Stainless steel is the standard alloy for metallic BPPs, and has the major constituents of iron (Fe), chromium (Cr) and nickel (Ni). There are mainly six relevant grades of SS for BPPs, distinguishable by their chemical compositions. These are provided in table 3-1.

	Chromium (Cr)	**Nickel (Ni)**
SS316L	16.20 - 16.80	10.10 - 10.30
SS317L	18.10 – 18.60	12.45 – 12.75
SS904L	20.48	24.95
SS349™	23	14.5
SS310	25	20
AISI446	28.367	2.958

Table 3-1 Grades of stainless steel according to composition by weight percentage [115] [116] [117]

The conductivity of SS316 is, for example, around 51 S/cm [113]. It has been shown that those grades of SS with a higher content of chromium and nickel, SS904L for example, result in the formation of thinner passive oxide films with low ICR. Raising chromium content alone, however, can improve corrosion resistance and it is possible to attain a low ICR if a clean, stable and integral surface is developed [115,116,117,118,119]. The effect of chromium content on corrosion resistance is also evident in amorphous iron-based alloys such as $Fe_{50}Cr_{18}Mo_8Al_2Y_2C_{14}B_6$ [120]. Amorphous alloys intrinsically possess high corrosion resistance and high strength (around 2GPa) due to the absence of defects such as grain boundaries and dislocations [120]. In addition, surface treatment of SS in the form of a selective dissolution processes can improve the metallurgical surface structure, ensuring that

it is defect-free, solid and integral [118]. Smoother surfaces can also result in reduced interfacial contact resistances.

Coating of Stainless-Steel Substrate

Corrosion resistance can be improved if stainless steel is coated as a substrate. When coated with titanium nitride (TiN), if coating defects such as micro-cracks and pinholes can be minimised, a higher corrosion resistance and electrical conductivity for SS316 can be achieved [121]. Stainless steel can also be coated with conducting polymers such as polypyrrole (PPY) and polyaniline (PANI) [122,123,124]. The interfacial contact resistance however is five times that of graphite at a compaction force of 200N/cm^2, and reduced to one-two times that of graphite at 400N/cm^2 [122]. The number of deposition cycles that the substrate is subjected to during the electro-polymerisation process dictates the thickness of the polymer film; the coating is known to degenerate with time, and coating compositions need to be modified in order to maintain the protective properties of the polymer surface [124]. SS304 coated with nitride layers using the physical vapour deposition (PVD) method has also been reported, which results in interfacial contact resistances less than that of uncoated SS904L [125]. Coating does generally however add to the cost of the final product [113].

Other forms of metallic bipolar plates include copper alloys such as C-17200 copper-beryllium, which form electrically conductive oxides [126] and nickel-based alloys with lower amounts of [Fe + Cr], resulting in oxides with reduced ICR [125].

Moulded Bi-Polar Plates

Injection and compression moulding as low-cost, high-volume manufacturing processes could arguably mitigate the high production costs associated with machined graphite and stainless steel bipolar plates. The process requires the synthesis of a mouldable compound. In general, polymer-based compounds can be susceptible to shrinkage after the moulding process and could warp with time. Also, inhomogeneous pre-mixing of the carbon-polymer compound can give rise to the formation of polymer-rich boundaries in the mould,

compromising the electrical conductivity closer to the surface. Two reported compounds include carbon–polymer [127], for example graphite powder (80-60 wt.%) with vinyl ester (20-40 wt.%) [128], and Nylon-6 with SS316L alloy fibres [129]. The bulk conductivities of the resulting materials are 5-150 S/cm and 60 S/cm for the carbon-polymer [127] and Nylon-6–SS316L compounds respectively. Commercially available carbon-based bi-polar plates and bi-polar plate materials include those based on phenolic resin and other polymers such as polyvinylidene difluoride (PVDF) and polypropylene (PP) [130,131,132,133]. The conductivity of these materials range from around 30 S/cm to 200 S/cm with flexural strength in the region of 40-50 MPa. Other compounds constituting of vinyl ester resin, graphite powder with organoclay have been reported with bulk conductivities in the region of 260-312 S/cm [134]. The organoclay is prepared by ionic exchange of montmorillonite (MMT) with poly(oxypropylene)-backboned diamine intercalating agents. Higher MMT content improves flexural strength, impact strength and anticorrosive protection, but slightly reduces the electrical conductivity.

3.4.2 Resistance to proton transfer in the Polymer Electrolyte Membrane

Impurity Ions

Resistance to proton transfer in the polymer electrolyte material is characterised by the interplay between absorbed water, cations and fixed charge ionic clusters of the membrane electrolyte. Cations in the form of foreign impurity ions can displace protons and enter the electrolyte membrane, decreasing the proton conductivity in proportion to the ionic charge of the cation [13]. Foreign ions reported in literature include the alkali metals Li^+, Na^+, K^+, Rb^+ and Cs^+ [135,136,137,138,139,140,141], the alkaline earths Mg^{2+}, Ca^{2+}, Sr^{2+} and Ba^{2+} [142,143,145], the transition elements Ag^+, Ni^{2+}, Mn^{2+}, Cu^{2+}, Zn^{2+}, Cr^{3+}, Fe^{3+} [144,145,146,147], rare earths La^{3+} [145] and Al^{3+} [147], and ammonium derivatives $R_nNH_{4-n}^+$ (where R = H, CH_3, C_2H_5, C_3H_7, C_4H_9 and n = 1 to 4) [148,149]. Sources of impurity ions include impure gas feeds, corroded materials in the fuel cell stack or reactant supply system, i.e., transition metal ion contaminants such as Cu^{2+}, Ni^{2+} and Fe^{3+} [144], fittings, tubing or indeed ions in the water or coolant supply [141].

As discussed, compromising the hydrated state of the membrane results in the loss of proton conductivity. Water transport through the cell governs how well the membrane is hydrated, and water transport itself is characterised by its diffusivity and its transfer coefficient in the different regions of the cell. For the general case of operation under uncontaminated conditions, the water content of the membrane decreases non-linearly through the membrane thickness towards the anode with increasing current density, thereby resulting in an decrease in proton conductivity. This reflects the rise in electro-osmotic drag with increasing current density, resulting in a comparably large amount of water moving away from the anode to the cathode in relation to that diffusing through the PFSA-based membrane from the cathode to the anode [17]. Membrane contamination can increase the non-uniformity in water content and decrease the overall water content profile. The literature reports that the penetration of impurity ions into the membrane induces; (1) a decrease in the diffusion coefficient of water, and; (2) an increase in the water-transfer coefficient [13].

The literature suggests that water can reside in the membrane in the form of one of three possible population groups [137]; (1) Henry or Flory-Huggins type populations where water molecules are sorbed by an ordinary dissolution mechanism; (2) Langmuir type populations where water molecules reside in a hydration layer around cations and sulfonic charge groups due to the strong interactions caused by hydrogen bonds, and; (3) water cluster populations. Water clusters can be distinguished from Langmuir-type populations and are known to become dominant populations when the water activity in the membrane is greater than around 0.6. Clustering can change depending upon the type of cation penetrating the membrane; it is known to increase in the order of $Cs^+ > Li^+ > H^+$. Legras *et al.* reported that the water clusters compromise the mobility of water overall which correspondingly results in a decrease in water diffusivity [137]. Shi *et al.* reported that the replacement of protons by impurity ions can induce electro-static cross-linking of ionic domains or the formation of sulfonate salts, causing the membrane to contract and expel water [145]. This can also result in the loss of water diffusivity [13]. Kundu *et al.* reported that physical cross-linking of ionic domains alters the mechanical properties of the membrane, causing an increase in membrane stiffness [141]. Young's Modulus is shown to increase by one order of magnitude with increasing ionic radius, in the order $Ni^{2+} > Cu^{2+} > Na^+ > K^+$.

The transport of protons through the polymer electrolyte from the anode to the cathode is known to induce the aforementioned electro-osmotic drag flux [150]. For other

ions, the magnitude of each contributory transport mode depends upon the existence of hydrophilic and hydrophobic parts of the ion. Through the investigation of ammonium derivatives, Xie *et al.* reported that such ions with hydrophobic skeletons tended not to have peripherally bound water molecules and instead cause hydrodynamic pumping [149]. Other cations, including fully hydrophilic cations, with a high charge density and a high enthalpy of hydration tend to carry more water molecules during transport by the electro-osmotic drag, which increases with water content [142,149,151]. Overall this illustrates that while the transfer of protons across the polymer electrolyte material induces an electro-osmotic drag, overall water transfer can indeed be unfavourably magnified as water interacts with impurity ions. The duration over which the degradation is prolonged depends upon the concentration of the impurity ions [138] and the length of time that the impurity ions reside within the polymer electrolyte membrane. Impurities with large diameters can penetrate the membrane and induce a plugging effect, compromising hydration and thus proton conductivity [149]. Therefore in general, water transport due to the presence of impurity ions can indeed hasten membrane dehydration, and the adverse effect on membrane performance is exacerbated when the impurity ions are concentrated closer to the anode and cathode catalyst layers [152,153].

Anisotropic Expansion

The swelling phenomenon experienced in fuel cells that use PFSA-based materials due to the uptake of water can lead on to anisotropic expansion. Casciola *et al.* reported that through-plane conductivity could decay when such swelling occurs, precipitated by high operating temperatures (120°C) and high relative humidity (>90%) [154].

Membrane expansion could be restrained by the compaction of the cell. However, it has already been argued that the stresses actually experienced in operating fuel cells are likely to be less than those required to sufficiently constrain the membrane [155]. Reinforcing the membrane structurally however provides a more robust method. Methods include dispersing PTFE fibrils within membranes (fibril content of 2.7 wt.%) [156], dispersing carbon nanotubes within Nafion membranes (CNT content of 1 wt.%) [157] and the use of porous, expanded PTFE sheets that are bonded with membrane resins on both sides [158,159,160]. A 50 micron thick membrane made of recast Nafion has a tensile strength of

22.08MPa. Dispersing 1 wt.% CNT within the membrane can increase this by 68.8% [157]. The use of a PTFE porous sheet for reinforcement can increase the tensile strength by 87.5% [157]. The dimensional change for recast Nafion in water at 80°C is 25% [159]. For Nafion reinforced with dispersed CNT, the dimensional change is decreased to 12.4% [157] and for PTFE reinforced Nafion this is decreased to 10% [159]. At 90% RH, expanded PTFE reinforcement can suppress in-plane dimensional change from 12% down to 2.5% [161].

3.5 Efficiency Losses and Catastrophic Cell Failure

Loss of efficiency and catastrophic cell failure can be induced when the strength and stability of the fuel cell materials are degraded irreversibly by mechanical or chemical attack. Rigid elements such as the bipolar plate are susceptible to cracking under mechanical stress and vibration. Seals are susceptible to oxidation [162], which compromises its functionality and can therefore rupture.

The electrolyte material has to survive under various cyclic loads and through chemically-induced structural degradation whilst serving its primary role as a proton conductor. Efficiency losses in the electrolyte membrane can result as an inherent consequence of employing thin membranes [163] or by *in-situ* membrane thinning, allowing hydrogen to diffuse through the electrolyte from anode to cathode. Membrane thinning largely reflects a loss of chemical structure, primarily induced by peroxide radical attack. Pinhole formation is a precursor to catastrophic cell failure, propagating from localised regions where temperature extremes exist which mechanically degrade the fuel cell materials. This includes regions exposed to thermal hot-spots or ice formation. The purpose of this section is to discuss the irreversible degradation mechanisms caused by mechanical and chemical attack.

3.5.1 Mechanical attack

The impedance to transport in the porous layers of the cell due to ice formation was discussed previously. It has also been reported that ice formation caused as a consequence of operation at sub-zero conditions down to -20°C can cause the catalyst layer to delaminate

from both the membrane and the gas diffusion layer [86]. The surface of the electrolyte membrane has also been observed to become rough at sub-zero conditions, leading to the formation of cracks and eventual pinholes [86].

The formation of thermal hot-spots has also been reported in the literature, as instigated through different mechanisms [164,165]. Hottinen *et al.* reported that a significant portion of the heat generated under the channel sections of the bipolar plate has to flow in the in-plane direction [165]. This could result in the formation of hot-spots below the channel. The beginning of rib areas where current enters the GDL from the bipolar plate could also be regions of high Ohmic heating, giving rise to other hot-spots, and the effect of heat transfer can be magnified when superimposed with inhomogeneous compression. Stanic *et al.* [164] reported evidence of the formation of pinholes in regions where carbon fibres at the MEA-GDL interface created spots of high compression, accelerating membrane creep. High reaction rates in the vicinity of highly compressed membrane regions can raise the amount of heat energy generated, and therefore the local temperature. Overall, the local strength of the membrane at these higher-temperature, high-compression hot-spots can reduce and so can cause the electrolyte membrane to collapse. Membrane durability is also affected by repeated swelling and contraction induced by variations in relative humidity (RH) [166]. Kusolgu *et al.* [167] investigated in-plane stresses caused by in-plane membrane swelling and found that swelling as a phenomenon can have a more dominant impact on fatigue stresses than clamping conditions or the membrane thickness. Thermal hotspots can also develop in regions where hydrogen and oxygen combine exothermically on platinum catalyst sites, causing a cycle of increasing crossover and continual propagation of pinholes [168]. In general, hygro-thermal stressing can significantly affect the durability of PFSA-based membranes [161, 169, 170, 171]. However dimensional change due to hygro-thermal stressing can be restrained by reinforcing PFSA membranes with expandable PTFE, as discussed [161].

It is possible that irregularities in the electrolyte membrane or MEA could be induced during manufacture. Ensuring the absence of contaminants and uniformity in the thickness of membrane batches depends upon quality control during the manufacturing process. Curtin *et al.* reported DuPont's manufacturing techniques for PFSA membranes, which includes two inspection points for membrane film thickness and one inspection point for defects [172].

In general, greater control over manufacturing quality could be granted by adopting manufacturing processes and quality control practices that have become highly-developed in similar industries. Relevant examples include the recoding media, semiconductor, battery and photovoltaic industries [173] and well-established standards for manufacture and test [174,175,176].

3.5.2 Chemical Attack

Chemical attack in PFSA-based membrane can occur due to the presence of defects in the polymer group. The defects exist as groups in the polymer that can interact with active radicals, resulting in the chemical degeneration of the PFSA-based material.

The PFSA polymer is synthesised from a copolymer of tetraflouroethylene (TFE) and perfluoro(4-methyl-3,6-dioxa-7-octene-1-sulfonyl fluoride) by chemically converting the pendant SO_2F sulfonyl fluoride groups to sulfonic acid SO_3H [172,177]. The SO_3H is ionically bonded such that the end of the side chain contains an SO_3^- and an H^+ ion [5].

Formation of Defective End Groups

End group defects can be generated during polymer synthesis as a consequence of chemical or mechanical processes; initiators, transfer agents, solvents or contaminants could induce defects during chemical processing, while ageing, heating or extrusion could also induce defects during the handling of the polymer [178]. Pianca *et al.* [178] identified the following end groups; carboxylic acid ($–CF_2–COOH$), amide ($–CF_2–CONH_2$), perfluorovinyl ($–CF_2–CF=CF_2$), acyl fluoride ($–CF_2–COF$), difluoromethyl ($–CF_2–CF_2H$) and ethyl ($–CF_2–CH_2–CH_3$). Alentiev *et al.* [179] identified other end groups including $–CF_2–CF=O$ and $–CF_2–CF=O$ and residual C–H bonds in the main chain such as $R_f–CFH-R_f´$. It is primarily the H containing end groups that are of particular interest for PFSA membranes in fuel cell environments, which can undergo aggressive chemical attack in the presence of peroxide radicals at low relative humidity conditions and temperatures in excess of 90°C [172].

Formation of Hydrogen Peroxide

Hydrogen peroxide can be formed through three reported processes. The first occurs as a consequence of oxygen reduction at the cathode [180];

$$O_2 + 2H^+ + 2e^- \rightarrow H_2O_2 \quad (3\text{-}2)$$

The second occurs as a consequence of oxygen crossover from the cathode to the anode, or when air is bleed to the anode side [180,181,182];

$$Pt + 1/2\, H_2 \rightarrow PtH \quad (3\text{-}3)$$

$$2H^* + O_2 \rightarrow H_2O_2 \quad (3\text{-}4)$$

La Conti *et al.* identified the intermediate formation of hydroperoxy ($HO_2^\bullet$) [183];

$$H_2 \rightarrow 2H^\bullet \text{ (on Pt or Pt - alloy catalyst)} \quad (3\text{-}5)$$

$$H^\bullet + O_2 \rightarrow HO_2^\bullet \quad (3\text{-}6)$$

$$HO_2^\bullet + H^+ \rightarrow H_2O_2 \quad (3\text{-}7)$$

The third occurs due to the crossover of hydrogen from the anode to the cathode, making it possible for hydrogen peroxide to form in the cathode catalyst layer [184,185]. It has been reported that hydrogen peroxide formation can be hastened by the presence of chloride ions which act as site-blocking species, reducing the number of active sites for the ORR and reducing the number of pairs of platinum sites required to break the O-O bond [186]. Chloride anions can originate from the fuel cell catalyst synthesising process and can be present as a water contaminant in the humidified reactant supplies.

Formation of Peroxide Radicals

Highly-oxidative peroxide radicals can subsequently form from the decomposition of hydrogen peroxide and as active species can decompose PFSA-based membranes [177]. Transition metals such as Cu^{2+} and Fe^{2+} are known to be catalysts for the decomposition of

hydrogen peroxide [177] and can originating from piping tubes and tanks of fuel cell systems. The Haber-Weiss mechanism details the formation of reactive oxygen hydroxyl ($HO^{\bullet}$) and hydroperoxyl radicals for Fe^{2+} [177];

$$H_2O_2 + Fe^{2+} \rightarrow HO^{\bullet} + OH^{-} + Fe^{3+} \quad (3\text{-}8)$$

$$Fe^{2+} + HO^{\bullet} \rightarrow Fe^{3+} + OH^{-} \quad (3\text{-}9)$$

$$H_2O_2 + HO^{\bullet} \rightarrow HO_2^{\bullet} + H_2O \quad (3\text{-}10)$$

$$Fe^{2+} + HO_2^{\bullet} \rightarrow Fe^{3+} + HO_2^{-} \quad (3\text{-}11)$$

$$Fe^{3+} + HO_2^{\bullet} \rightarrow Fe^{2+} + H^{+} + O_2 \quad (3\text{-}12)$$

Steps (3-8) and (3-10) result in the formation of hydroxyl and hydroperoxyl radicals, respectively. For bivalent transition metals in general (M^{2+}), radical formation can be generalised by the following mechanism [183];

$$H_2O_2 + M^{2+} \rightarrow HO^{\bullet} + OH^{-} + M^{3+} \quad (3\text{-}13)$$

$$H_2O_2 + HO^{\bullet} \rightarrow HO_2^{\bullet} + H_2O \quad (3\text{-}14)$$

Mechanism of Peroxide Attack on Defective End Groups

Peroxide radicals in the presence of defective polymer end groups proceed to decompose the polymer structure. Curtin *et al.* detail the following three-step mechanism whereby hydroxyl radicals attack carboxylic acid end groups [172];

Step 1: Abstraction of hydrogen from an acid end group

$$R_f - CF_2 - COOH + HO^{\bullet} \rightarrow R_f - CF_2^{\bullet} + CO_2 + H_2O \quad (3\text{-}15)$$

Step 2: Reaction of perfluorocarbon radical with hydroxyl radical

$$R_f - CF_2^{\bullet} + HO^{\bullet} \rightarrow R_f - CF_2OH \rightarrow R_f - COF + HF \quad (3\text{-}16)$$

Step 3: Hydrolysis of acid fluoride

$$R_f - COF + H_2O \rightarrow R_f - COOH + HF \tag{3-17}$$

The release of fluoride therefore reflects the decomposition of the PFSA membrane. Fluoride emission rates (FER) can be determined by sampling the fluoride content of water in the anode and cathode exhaust [187]. Assuming a zero-order reaction for the production of fluoride ions, it is possible to postulate the following relationship to determine the rate at which Nafion decomposed [188];

$$r_d = \frac{\Delta M_{\overline{F}}}{M_{F-Nafion}\Delta t} \tag{3-18}$$

where $\Delta M_{\overline{F}}$ is the change in the amount of F^- released in μmol, $M_{F-Nafion}$ is the total amount of F in the Nafion and Δt is the timestep in hours. The literature demonstrates that the FER technique is being increasingly applied to determine ionomer degradation [181,187,188,189].

Effect of Membrane Degradation due to Peroxide Attack

The effect of peroxide attack is to alter the membrane structure and the chemical properties of the PFSA membrane. Loss of sulfonic end groups results in the loss of proton conductivity, thereby increasing the Ohmic resistance. Continual membrane degradation due to peroxide radical attack and subsequent fluoride release results in membrane thinning. This increases the diffusion of oxygen and hydrogen in opposing directions from the cathode and anode respectively. Primarily, it is the crossover of hydrogen that increases because of the high effective diffusivity of hydrogen molecules [6].

3.6 Summary

The performance degradation, failure modes and the associated causes discussed in the above are summarised in Tables 3-2 and 3-3. Faults are listed according to the physical component of the PEFC assembly where they originate or reside. The information presented

in these tables have been used to construct a systematic set of fault trees for the PEFC, which has been reported elsewhere [190].

3.7 Conclusions

The review given in this chapter provides a qualitative account of performance degradation and failure in hydrogen-fuelled PEFCs and discusses some of the state-of-the-art concepts aimed at overcoming these limitations. The purpose of the review is to establish a backbone understanding of the phenomenological processes that occur within the PEFC, how they are influenced through elements of design, manufacturing and operation and ultimately how they can affect the performance of the PEFC. The conclusions from this chapter are as follows;

- Performance degradation or failure can occur as a consequence of gradual processes, where certain operating conditions or operating routines cause a systematic degradation of structural and electrokinetic properties of PEFC components. Latent flaws in component design and manufacture can also lead to performance degradation or failure.
- The identified phenomenological processes that lead on to performance degradation can be organised in terms of potentially irreversible increases in activation losses, Ohmic losses, mass transportation losses and efficiency losses
- The performance degradation and failure modes identified through the literature pertain to the following PEFC components:
    - PFSA-based membrane
    - Catalyst layer
        - Carbon support
        - PFSA-based ionomer matrix
        - Catalyst particles
        - Porous structure of the catalyst layer
    - Gas diffusion media
        - Hydrophobic treatment material in the GDL
        - Porous structure of the GDL
    - Bipolar Plate
        - Stainless Steel BPPs

        - Polymer-based BPPs
    - Sealing material
        - Silicone-based seals
- In reviewing the performance degradation and failure modes, twenty-two common faults can be identified
- The twenty-two common faults are induced by forty-eight general causes.

As mentioned, the review also discusses newer aspects of fuel cell design, manufacture and operation as remedial measures that limit performance degradation and failure. In terms of MEA development, there is emphasis on attaining high mechanical strength, dimensional stability and an understanding of the mechanisms that govern internal transport and water management. For BPP and GDL development there is emphasis on improving the homogeneity of multi-phase flows through channels and porous media and on establishing materials, material preparation, material treatment and fabrication processes for high mechanical strength, high electrical conductivity and low susceptibility to chemical attack. Manufacturing and quality control are also critical areas for PEFC development which depend on the adoption of scalable manufacturing processes and practices from similar established industries, establishing repeatable precision processes and by adopting quality control practices.

The review demonstrates that internal electrochemical transport and water management in particular is a key phenomenological process that affects performance and longevity, and therefore cost. Understanding the mechanisms of electrochemical transport and how they can be theoretically simulated is therefore fundamental to fuel cell research and development.

Performance Loss Mechanism	Fuel Cell Component	Fault/Process	Cause
Increase of Activation Losses	Platinum catalyst	(1) Platinum agglomeration causing loss of EASA	(1) Repetitive on/off load cycling (2) High voltage induce at cathode equivalent to OCV due to residual hydrogen (3) Loss of carbon support
		(2) Platinum migration causing loss of catalyst material	(4) Solubility of platinum when cell is operated through hydrogen-air open circuit to air-air open circuit
		(3) Adsorption of atmospheric contaminants on platinum causing loss of EASA	(5) Air impurities such as NO_2, SO_2 and H_2S
		(4) Adsorption of fuel impurities on platinum causing loss of EASA	(6) Fuel impurities such as CO and CO_2
		(5) Loss of catalyst due to chemical attack and formation of silicone/oxygen/platinum particles	(7) Chemical degradation of silicone sealant
	Geometric structure of the catalyst layer	(6) Deformation of catalyst structure by freezing and melting water, resulting in increased pore size and reduced EASA	(8) Residual water in catalyst layers
	Carbon support in catalyst layer	(7) Corrosion of carbon to support the current above that provided by the fuel when the cell is supplied with insufficient fuel to support the current drawn	(9) Fuel starvation (10) Partial coverage of hydrogen on catalyst sites (11) Localised flooding
Increase of Mass Transportation Losses	Porous and void regions of the cell; catalyst layers, GDLs, BPP flow fields	(8) Flooding caused by the accumulation and condensation of water vapour to induce two-phase flow	(12) Low flow rate of channel gases (13) Low pressure in gas flow channels (14) Flow-field geometry (15) Degradation of polymer electrolyte in catalyst layer due to impurity ions
		(9) Loss of hydrophobicity in porous regions of the cell treated with hydrophobic material	(16) Loss of material/material properties due to repeated thermal cycling / high operating temperature (17) Delamination caused by repeated thermal cycling (18) Damage to material caused by exposure to sub-zero conditions (19) Cell over-compression, impacting the GDL
	Geometric structure of catalyst layer	(10) Impedance to transport attributable to presence of ionomer	(20) Ionomer expansion on water uptake causing pores to collapse (21) Excessive ionomer loading (22) Formation of ionomer skins on catalyst layers (23) Lack of control during MEA processing
		(11) Impedance to transport attributable to ice formation	(24) Presence of residual water from previous shut-down (25) Operation at sub-zero temperatures
	GDL	(12) Loss of porosity, increased flooding and reduced gas permeability	(26) Over-compression and inhomogeneous compression, induced during cell assembly or by warping of moulded BPPs

Table 3-2 Summary of factors affecting activation, Ohmic and mass transportation losses

Performance Loss Mechanism	Fuel Cell Component	Fault/Process	Cause
Increase of Ohmic Losses	Stainless-steel BPP	(13) Loss of surface electrical conductivity	(27) Impedance to electron transfer due to passivating layer on SS surface
	Coated stainless-steel BPP	(-) Loss of surface electrical conductivity	(28) Coating defects such as pinholes and micro-cracks when coated with TiN (29) Degradation of conductive coating (30) Degradation of conductive polymer coating
	Injection-moulded BPP	(14) Low electrical conductivity	(31) Formation of polymer-rich boundary during injection-moulding process
	Polymer Electrolyte Membrane	(15) Loss of proton conductivity	(32) Loss of membrane hydration (33) Replacement of protons by impurity ions causing decrease in the water diffusion coefficient and increase in water transfer coefficient (34) Anisotropic swelling of membrane causing the water diffusion coefficient to decrease
Increase of Efficiency Loss, potentially leading to Catastrophic Cell Failure	Polymer electrolyte membrane	(16) Formation of cracks and pinholes	(35) Increased roughness of electrolyte membrane surface, inducing by sub-zero operating conditions (36) Mechanical stresses induced by thermal hotspots in regions of strong electrical contact (i.e., GDL and BPP shoulder), high compression, and high reaction rates (37) Defects during the manufacturing process (38) Peroxide and peroxide radical attack of polymer end groups (39 Repetitive swelling/contraction due to hygro-thermal stresses (40) Excessive pressure differential between anode and cathode gas supply
Catastrophic Cell Failure	GDL/catalyst layer/membrane	(17) Delamination of layers	(41)Thermal cycling including exposure to sub-zero conditions
	Catalyst layer	(18) Excessive adsorption of atmospheric and fuel impurities	(42) Loss of tolerance to contaminants
	BPP	(19) Cracking	(43) Inhomogeneous compression (44) Mechanical shock/vibration (45) Irregularities in cell/stack construction
		(20) Warping	(46) Low initial rigidity of polymer matrix
	Seal	(21) Gas leakage	(47) Oxidation of seals
	Polymer electrolyte membrane	(22) Short circuit	(48) Formation of electrical network due to mal-distribution of platinum within (self-humidifying) membrane

Table 3-3 Summary of factors affecting efficiency losses and catastrophic cell failure

3.8 References

1 **Mehta V, Cooper JS.** Review and analysis of PEM fuel cell design and manufacturing. *J. Power Sources*, 2003, **114**, 32-53

2 **Haile SM.** Fuel cell materials and components. *Acta Mater.*, 2003, **51**, 5981-6000

3 **Cooper JS.** Design analysis of PEMFC bipolar plates considering stack manufacturing and environmental impact. *J. Power Sources*, 2004, **129**, 152-169

4 **Yu PT, Gu W, Makharia R, Wagner FT, Gasteiger A.** The Impact of Carbon Stability on PEM Fuel Cell Startup and Shutdown Voltage Degradation. *210th ECS Meeting, Cancun, Mexico, Durability – Fuel Starvation and Start/Stop Degradation*, October 29-November 3 2006

5 **Larminie J, Dicks A.** *Fuel Cell Systems Explained*, 2003 (John Wiley & Sons, Chichester)

6 **Xie J, Wood III DL, Wayne DM, Zawodzinski TA, Atanassov P, Borup RL.** Durability of PEFCs at High Humidity Conditions. *J. Electrochem. Soc.*, 2005, **152**(1), A104-A113

7 **Xie J, Wood III DL, More KL, Atanassov P, Borup RL.** Mictrostructural Changes of membrane Electrode Assemblies during PEFC Durability Testing at High Humidity Conditions. *J. Electrochem. Soc.*, 2005, **152**(5), A1011-A1020

8 **Lee S-Y, Cho E, Lee J-H, Kim H-J, Lim T-H, Oh I-H, Won J.** Effects of Purging on the Degradation of PEMFCs Operating with Repetitive On/Off Cycles. *J. Electrochem. Soc.*, 2007, **154**(2), B194-B200

9 **Zhai Y, Zhang H, Liu G, Hu J, Yi B.** Degradation Study on MEA in H3PO4/PBI High-Temperature PEMFC Life Test. *J. Electrochem. Soc.*, 2007, **154**(1), B72-B76

10 **Darling RM, Meyers JP.** Mathematical Model of Platinum Movement in PEM Fuel Cells. *J. Electrochem. Soc.*, 2005, 152(1), A242-A247

11 **Aragane J, Murahashi T, Okada T.** Change of Pt Distribution in the Active Components of Phosphoric Acid Fuel Cell. *J. Electrochem. Soc.*, 1988, 135(4), 844-850

12 **Cho EA, Ko J-J, Ha HY, Hong S-A, Lee K-Y, Lim T-W, Oh I-H.** Characteristics of the PEMFC Repetitively Brought to Temperatures below 0°C. *J. Electrochem. Soc.*, 2003, **150**(12), A1667-A1670

13 **St-Pierre J, Wilkinson DP, Knights S, Bos M.** Relationship between water management, contamination and lifetime degradation in PEFC. *J. New Mat. Elect. Syst.*, 2000, **3**, 99-106

14 **Mohtadi R, Lee W-K, Van Zee JW.** Assessing durability of cathodes exposed to common air impurities. *J. Power Sources*, 2004, **138**, 216-225

15 **Moore JM, Adcock PL, Lakeman JB, Mepsted GO.** The effect of battlefield contaminants on PEMFC performance. *J. Power Sources*, 2000, **85**, 254-260

16 **Jing F, Hou M, Shi W, Fu J, Yu H, Ming P, Yi B.** The effect of ambient contamination of PEMFC performance. *J. Power Sources*, 2007, **166**, 172-176

17 **Springer TE, Rockward T, Zawodzinski TA, Gottesfeld S.** Model for Polymer Electrolyte Fuel Cell Operation on Reformate Feed. *J. Electrochem. Soc.*, 2001, **148**(1), A11-A23

18 **Sishtla C, Koncar G, Platon R, Gamburzev S, Appleby AJ, Velev O.** Performance and endurance of a PEMFC operated with synthetic reformate fuel feed. *J. Power Sources*, 1998, **71**, 249-255

19 **Qi, Z., He, C., and Kaufman.** A. Effect of CO in the anode fuel on the performance of PEM fuel cell cathode. *J. Power Sources*, 2002, **111**, 239–274.

20 **Liu P, Logadottir A, Norskov JK.** Modeling the electro-oxidation of CO and H2/CO on Pt, Ru, PtRu and Pt3Sn. *Electrochim. Acta*, 2003, **48**, 3731-3742

21 **Isono T, Suzuki S, Kaneko M, Akiyama Y, Miyake Y, Yonezu I.** Development of a high-performance PEFC module operated by reformed gas. *J. Power Sources*, 2000, **86**, 269-273

22 **Si Y, Jiang R, Lin J-C, Kunz R, Fenton JM.** CO Tolerance of Carbon-Supported Platinum-Ruthenium Catalysts at Elevated Temperature and Atmospheric Pressure in a PEM Fuel Cell. *J. Electrochem. Soc.*, 2004, **151**(11), A1820-A1824

23 **Gottesfled S, Pafford J.** A New Approach to the Problem of Carbon Monoxide Poisoning in Fuel Cells Operating at Low Temperatures. *J. Electrochem. Soc.*, 1988, 135(10), 2651-2652

24 **Adcock PA, Pacheco SV, Norman KM, Uribe FA.** Transition Metal Oxides as Reconfigured Fuel Cell Anode Catalysts for Improved CO Tolerance, Polarization Data. *J. Electrochem. Soc.*, 2005, **152**(2), A459-A466

25 **Cheng X, Shi Z, Glass N, Zhang L, Zhang J, Song D, Liu Z-S, Wang H, Shen J.** A review of PEM hydrogen fuel cell contamination, Impacts, mechanisms, and mitigation. *J. Power Sources*, 2007, **165**, 739-756

26 **Marr C, Li X.** Composition and performance modelling of catalyst layer in a proton exchange membrane fuel cell. *J. Power Sources*, 1999, **77**, 17-27

27 **Wang Q, Eikerling M, Song D, Liu Z, Navessin T, Xie Z, Holdcroft S.** Functionally Graded Cathode Catalyst Layers for Polymer Electrolyte Fuel Cells. I Theoretical Modelling. *J. Electrochem. Soc.*, 2004, **151**(7), A950-A957

28 **Xie Z, Navessin T, Shi K, Chow R, Wang Q, Song D, Andreaus B, Eikerling M, Liu Z, Holdcroft S.** Functionally Graded Cathode Catalyst Layers for Polymer Electrolyte Fuel Cells. II Experimental Study of the Effect of Nafion Distribution. *J. Electrochem. Soc.*, 2005, **152**(6), A1171-A1179

29 **Frost JC, Gascoyne JM, Hards GA, Wilkinson DP, Prater KB.** Manufacture of Electrodes. *United States Patent*, 1997, 5,702,839

30 **Fuller T, Gray G.** Carbon Corrosion Induced by Partial Hydrogen Coverage. *208th ECS Meeting, Durability and Reliability of Low-Temperature Fuel Cells Systems*, Los Angeles, California, October 16-October 21 2005, **1**(8)

31 **Meyers JP, Darling RM.** Model of Carbon Corrosion in PEM Fuel Cells. *J. Electrochem. Soc.*, 2006, **153**(8), A1432-A1442

32 **Merzougui B, Swathirajan S.** Rotating Disk Electrode Investigations of Fuel Cell Catalyst Degradation Due to Potential Cycling in Acid Electrolyte. *J. Electrochem. Soc.*, 2006, **153**(12), A2220-A2226

33 **Stevens DA, Hicks MT, Haugen GM, Dahn JR.** Ex Situ and In Situ Stability Studies of PEMFC Catalysts. Effect of Carbon Type and Humidification on Degradation of the Cathode. *J. Electrochem. Soc.*, 2005, **152**(12), A2309-A2315

34 **Xu H, Song Y, Kunz HR, Fenton JM.** Effect of Elevated Temperature and Reduced Relative Humidity on ORR Kinetics for PEM Fuel Cells. *J. Electrochem. Soc.*, 2005, **152**(9), A1828-A1836

35 **Shao Y, Yon G, Shi P.** Durability Study of Pt/C and Pt/CNTs Catalysts under Simulated PEM Fuel Cell Conditions. *J. Electrochem. Soc.*, 2006, **153**(6), A1093-A1097

36 **Schulze M, Knori T, Schneider A, Gülzow.** Degradation of sealings for PEFC test cells during fuel cell operation. *J. Power Sources*, 2004, **127**, 222-229

37 **Zhang FY, Yang XG, Wang CY.** Liquid Water Removal from a Polymer Electrolyte Fuel Cell. *J. Electrochem. Soc.*, 2006, **153**(2), A225-A232

38 **Maharudrayya S, Jayanti S, Deshpande AP.** Pressure drop and flow distribution in multiple parallel-channel configurations used in proton-exchange membrane fuel cell stacks. *J. Power Sources*, 2005, **157**, 358-367

39 **Maharudrayya S, Jayanti S, Desphande AP.** Pressure losses in laminar flow through serpentine channels in fuel cell stacks. *J. Power Sources*, 2004, **138**, 1-13

40 **Berraras F, Lozano A, Valino L, Marin C, Pasau A.** Flow distribution in a bipolar plate of a proton exchange membrane fuel cell, experiments and numerical simulation studies. *J. Power Sources*, 2005, **144**, 54-66

41 **Karvonen S, Hottinen T, Saarinen J, Himanen O.** Modeling of flow field in polymer electrolyte membrane fuel cell. *J. Power Sources*, 2006, **161**, 876-887

42 **Shimpalee S, Greenway S, Van Zee JW.** The impact of channel path length on PEMFC flow-field design. *J. Power Sources*, 2006, 398-406

43 **Su A, Weng F-B, Hsu C-Y, Chen Y-M.** Studies on flooding in PEM fuel cell cathode channels. *Int. J. Hydrogen Energ.,* 2006, **31**, 1031-1039

44 **Trabold TA, Owejan JP, Jacobson DL, Arif M, Huffman.** In situ investigation of water transport in an operating PEM fuel cell using neutron radiography, Part 1 – Experimental method and serpentine flow field results. *Int. J. Heat Mass. Trans.,* 2006, **49**, 4712-4720

45 **Trabold TA, Owejan JP, Jacobson DL, Arif M, Huffman.** In situ investigation of water transport in an operating PEM fuel cell using neutron radiography, Part 2 – Transient water accumulation in an interdigitated cathode flow field. *Int. J. Heat Mass. Trans.*, 2006, **49**, 4721-4731

46 **Liu X, Guo H, Ye F, Ma CH.** Water flooding and pressure drop characteristics in flow channels of proton exchange membrane fuel cells. *Electrochim. Acta*, 2007, **52**, 3607-3614

47 **Yi JS, Nguyen TV.** Multicomponent Transport in Porous Electrodes of Proton Exchange Membrane Fuel Cells Using the Interdigitated Gas Distributors. *J. Electrochem. Soc.*, 1999, **146**(1), 38-45

48 **Yan W-M, Yang C-H, Soong C-Y, Chen F, Mei S-C.** Experimental studies on optimal operating conditions for different flow field designs of PEM fuel cells. *J. Power Sources*, 2006, **160**, 284-292

49 **Grujicic M, Zhao CL, Chittajallu KM, Ocherbeck JM.** Cathode and interdigitated air distributor geometry optimization in polymer electrolyte membrane (PEM) fuel cells. *Mater. Sci. Eng. B-Adv.,*, 2004, **108**, 241-252

50 **Wang L, Liu H.** Performance studies of PEM fuel cells with interdigitated flow fields. *J. Power Sources*, 2004, **134**, 185-196

51 **Cheng B, Minggao O, Baolian YI.** Analysis of Water Management in Proton Exchange Membrane Fuel Cells. *Tsinghua Science and Technology*, 2006, **11**(1), 54-64

52 **Hwang JJ, Chao CH, Ho WY, Chang CL, Wang DY.** Effect of flow orientation on thermal-electrochemical transports in a PEM fuel cell. *J. Power Sources*, 2006, **157**, 85-97

53 **Su A, Weng F-B, Hsu C-Y, Chen Y-M.** Studies on flooding in PEM fuel cell cathode channels. *Int. J. Hydrogen Energ.*, 2006, **31**, 1031-1039

54 **Arati E, Pinna M, Costa P.** Gas-phase mass-transfer resistance at PEMFC electrodes. Part 2. Effects of the flow geometry and the related pressure field. *J. Power Sources*, 2006, **158**, 206-212

55 **Hsieh S-S, Yang S-H, Kuo J-K, Huang C-F, Tsai H-H.** Study of operational parameters on the performance of micro PEMFCs with different flow fields. *Energ. Convers. Manage,*, 2006, **47**, 1868-1878

56 **Shyam Prasad KB, Maharudrayya S, Jayanti S.** Flow maldistribution in interdigitated channels used in PEM fuel cells. *J. Power Sources*, 2006, **159**, 595-604

57 **Zou J, Peng X-F, Yan W-M.** Dynamic analysis of gas transport in cathode side of PEM fuel cell with interdigitated flow field. *J. Power Sources*, 2006, **159**, 514-523

58 **Yan W-M, Mei S-C, Soong C-Y, Liu Z-S, Song D.** Experimental study on the performance of PEM fuel cells with interdigitated flow channels. *J. Power Sources*, 2066, **160**, 116-122

59 **Yan W-M, Chen C-Y, Mei S-C, Soong C-Y, Chen F.** Effects of operating conditions on cell performance of PEM fuel cells with conventional or interdigitated flow field. *J. Power Sources*, 2006, **162**, 1157-1164

60 **Owejan JP, Trabold TA, Jacobson DL, Baker DR, Hussey DS, Arif M**. In situ investigation of water transport in an operating PEM fuel cell using neutron radiography, Part 2 – Transient water accumulation in an interdigitated cathode flow field. *Int. J. Heat Mass Trans.*, 2006, **49**, 4921-4931

61 **Hwang JJ, Chao CH, Wu W.** Thermal-fluid transports in a five-layer membrane-electrode assembly of a PEM fuel cell. *J. Power Sources*, 2006, **163**, 450-459

62 **Ge S-H, Yi B-L.** A mathematical model for PEMFC in different flow modes. *J. Power Sources*, 2003, 142, 1-11

63 **Hwang JJ, Chao CH, Ho WY, Chang CL, Wang DY.** Effect of flow orientation on thermal-electrochemical transports in a PEM fuel cell. *J. Power Sources*, 2006, **157**, 85-97

64 **Lou GL, Ju H, Wang C-Y.** Prediction of Dry-Wet-Dry Transition in Polymer Electrolyte Fuel Cells. *J. Electrochem. Soc.*, 2007, **154**(3), B316-B321

65 **Watanabe M, Uchida H, Seki Y, Emori M.** Self-Humidifying Polymer Electrolyte Membranes for Fuel Cells. *J. Electrochem. Soc.*, 1996, **143**(12), 3847-3852

66 **Watanabe M, Uchida H, Emori M.** Analysis of Self-Humidification and Suppression of Gas Crossover in Pt-Dispersed Polymer Electrolyte Membranes for Fuel Cells. *J. Electrochem. Soc.*, 1998, **145**(4), 1137-1141

67 **Liu Y-H, Yi B, Shao Z-G, Wang L, Xing D, Zhang H.** Pt/CNTs-Nafion reinforced and self-humidifying composite membrane for PEMFC applications. *J. Power Sources*, 2007, **163**, 807-813

68 **Zhang Y, Zhang H, Zhu X, Gang L, Bi C, Liang Y.** Fabrication and characterisation of a PTFE-reinforced integral composite membrane for self-humidifying PEMFC. *J. Power Sources*, 2007, **165**, 786-792

69 **Watanabe M.** Structure for wetting diaphragm of solid polymer electrolyte electrochemical cell and process of preparing same. *United States Patent*, 1996, 5,529,855

70 **Watanabe M.** Fuel cell, electrolytic cell and process of cooling and/or rehumidifying same. *United States Patent*, 1998, 5,846,668

71 **Voss HH, Wilkinson DP, Watkins DS.** Method and apparatus for removing water from electrochemical fuel cells. *United States Patent*, 1993, 5,260,143

72 **Voss HH, Wilkinson DP, Watkins DS.** Method and apparatus for removing water from electrochemical fuel cells by controlling the temperature and pressure of the reactant streams. *United States Patent*, 1995, 5,441,819

73 **Wilkinson DP, Voss HH, Fletcher NJ, Johnson MC, Pow EG.** Electrochemical fuel cell stack with concurrent flow of coolant and oxidant streams and countercurrent flow of fuel and oxidant streams. *United States Patent*, 1998, 5,773,160

74 **Fletcher NJ, Chow CY, Pow EG, Wozniczka BM, Voss HH, Hornburg G.** Electrochemical fuel cell stack with concurrently flowing coolant and oxidant streams. *United States Patent*, 1996, 5,547,776

75 **Qi Z, Kauffman A.** Improvement of water management by a microporous sublayer for PEM fuel cells. *J. Power Sources*, 2002, **109**, 38-46

76 **Weber AZ, Newman J.** Effects of Microporous Layers in Polymer Electrolyte Fuel Cells. *J. Electrochem. Soc.*, 2005, **152**(4), A677-A688

77 **Pasaogullari U, Wang C-Y.** Two-phase transport and the role of micro-porous layer in polymer electrolyte fuel cells. *Electrochim. Acta*, 2004, **49**, 4359-4369

78 **Pasaogullari U, Wang C-Y, Chen KS.** Two-Phase Transport in Polymer Electrolyte Fuel Cells with Bilayer Cathode Gas Diffusion Media. *J. Electrochem. Soc.*, 2005, **152**(8), A1574-A1582

79 **Gostick JT, Fowler MW, Ioannidis MA, Protzker MD, Volfkovich YM, Sakars A.** Capillary pressure and hydrophilic porosity in gas diffusion layers for polymer electrolyte fuel cells. *J. Power Sources*, 2006, **156**, 375-387

80 **Lin G, Van Nguyen T.** Effect of Thickness and Hydrophobic Polymer Content of the Gas Diffusion Layer on Electrode Flooding Level in a PEMFC. *J. Electrochem. Soc.*, 2005, **152**(1), A1942-A1948

81 **Wang XL, Zhang HM, Zhang JL, Xu HF, Tian ZQ, Chen J, Zhong HX, Liang YM, Yi BL.** Micro-porous layer with composition carbon black for PEM fuel cells. *Electrochim. Acta* 2006, **51**, 4909-4915

82 **Gurau V, Bluemle MJ, De Castro ES, Tsou Y-M, Zawodzinski Jr TA, Mann Jr A.** Characterisation of transport properties in gas diffusion layers for proton exchange membrane fuel cells. 2. Absolute permeability. *J. Power Sources*, 2007, **165**, 793-802

83 **Bevers D, Rogers R, von Bradke M.** Examination of the influence of PTFE coating on the properties of carbon papers in polymer electrolyte fuel cells. *J. Power Sources*, 1996, **63**, 193-201

84 **Lim C, Wang CY.** Effects of hydrophobic polymer content in GDL on power performance of a PEM fuel cell. *Electrochim. Acta*, 2004, **49**, 4149-4156

85 **Thoben B, Siebke A.** Influence of Different Gas Diffusion Layers on the Water management of the PEFC Cathode. *J. New Mat. Elect. Syst.*, 2004, **7**, 13-20

86 **Yan Q, Toghiani H, Lee Y-W, Liang K, Causey H.** Effect of sub-freezing temperatures on a PEM fuel cell performance, startup and fuel cell components. *J. Power Sources*, 2006, **160**, 1242-1250

87 **Bernardi DM, Verbrugge MW.** Mathematical Model of a Gas Diffusion Electrode Bonded to a Polymer Electrolyte. *AIChE Journal,* 1991, **37**(8), 1151-1163

88 **Bernardi DM, Verbrugge MW.** A Mathematical Model of the Solid-Polymer-Electrolyte Fuel Cell. *J. Electrochem. Soc.*, 1992, **139**(9), 2477-2491

89 **Fowler MW, Mann RF, Amphlett JC, Peppley BA, Roberge PR.** Incorporation of voltage degradation into a generalised steady state electrochemical model for a PEM fuel cell. *J. Power Sources*, 2002, **106**, 274-283

90 **Yin K-M.** Parametric Study of Proton-Exchange-Membrane Fuel Cell Cathode Using an Agglomerate Model. *J. Electrochem. Soc.*, 2005, **152**(3), A583-A593

91 **Xie J, Garzon F, Zawodzinski T, Smith W.** Ionomer Degregation in Composite MEAs and Its Effect on Polymer Electrolyte Fuel Cell Performance. *J. Electrochem. Soc.*, 2004, **151**(7), A1084-A1093

92 **Rajalakshmi N, Dhathathreyan KS.** Catalyst layer in PEMFC electrodes – Fabrication, characterisation and analysis. *Chem. Eng. J.*, 2007, **129**, 31-40

93 **Mao L, Wang C-Y.** Analysis of Cold Start in Polymer Electrolyte Fuel Cells. *J. Electrochem. Soc.*, 2007, **154**(2), AB139-B146

94 **Lee C, Merida W.** Gas diffusion layer durability under steady-state and freezing conditions. *J. Power Sources*, 2007, **164**, 141-153

95 **Mao L, Wang C-Y.** Analysis of Cold Start in Polymer Electrolyte Fuel Cells. *J. Electrochem. Soc.*, 2007, **154**(2), B139-B146

96 **Cho EA, Ko J-J, Ha HY, Hong S-A, Lee K-Y, Lim T-W, Oh I-H.** Efeects of Water Removal on the Performance Degradation of PEMFCs Repetitively Brought to <0°C. *J. Electrochem. Soc.*, 2004, **151**(5), A661-A665

97 **Hou J, Yu H, Zhang S, Sun S, Wang H, Yi B, Ming P.** Analysis of PEMFC freeze degradation at -20°C after gas purging. *J. Power Sources*, 2006, **162**, 513-520

98 **Chang M-H, Chen F, Teng H-S.** Effects of two-phase transport in the cathode gas diffusion layer on the performance of a PEMFC. *J. Power Sources*, 2006, **160**, 268-276

99 **Zhan Z, Xiao J, Li D, Pan D, Yuan R.** Effects of porosity distribution variation on the liquid water flux through gas diffusion layers of PEM fuel cells. *J. Power Sources*, 2006, **160**, 1041-1048

100 **Jang J-H, Yan W-M, Shih C-C.** Effects of the gas diffusion-layer parameters on cell performance of PEM fuel cells. *J. Power Sources*, 2006, **161**, 323-332

101 **Eikerling M.** Water management in Cathode Catalyst Layers of PEM Fuel Cells. *J. Electrochem. Soc.*, 2006, **153**(3), E58-E70

102 **Feser JP, Prasad AK, Advani SG.** Experimental characterisation of in-plane permeability of gas diffusion layers. *J. Power Sources*, 2006, **162**, 1226-1231

103 **Ge J, Higier A, Liu H.** Effect of gas diffusion layer compression on PEM fuel cell performance. *J. Power Sources*, 2006, **159**, 922-927

104 **Ihonen J, Mikkola M, Lindbergh.** Flooding of Gas Diffusion Backing in PEFCs. *J. Electrochem. Soc.*, 2004, **151**(8), A1152-A1161

105 **Nitta I, Hottinen T, Hilmanen O, Mikkola M.** Inhomogeneous compression of PEMFC gas diffusion layer. Part I. Experimental. *J. Power Sources*, 2007, **171**, 26-36

106 **Sui PC, Djilali N.** Analysis of coupled electron and mass transport in the gas diffusion layer of a PEM fuel cell. *J. Power Sources*, 2006, **161**, 294-300

107 **Matsuura T, Kato M, Hori M.** Study on metallic bipolar plate for proton exchange membrane fuel cell. *J. Power Sources*, 2006, **161**, 74-78

108 **Zhou P, Wu CW, Ma GJ.** Influence of clamping force on the performance of PEMFCs. *J. Power Sources*, 2007, 163, 874-881

109 **Chang WR, Hwang JJ, Weng FB, Chan SH.** Effect of clamping pressure on the performance of a PEM fuel cell. *J. Power Sources*, 2007, **166**, 149-154

110 **Escribano S, Blachot J-F, Ethiève J, Morin A, Mosdale R.** Characterisation of PEMFCs gas diffusion layers properties. *J. Power Sources*, 2006, **156**, 8-13

111 **Bazylak A, Sinton D, Liu Z-S, Djilali N.** Effects of compression on liquid water transport and microstructure of PEMFC gas distribution layers. *J. Power Sources*, 2007, **163**, 784-792

112 **Tawfik H, Hung Y, Mahajan D.** Metal bipolar plates for PEM fuel cell – a review. *J. Power Sources*, 2007, **163**, 755-767

113 **Greenwood P, Chen R, Thring, RH.** Polyethylene-Carbon Material for PEM Fuel Cell Bi-Polar Plates. *Proc. IMechE Part L: J. Materials*, 2008, ***222****(3), 197-208*

114 **Scholta J, Rohland B, Trapp V, Focken U.** Investigations on novel low-cost graphite composite bipolar plates. *J. Power Sources*, 1999, **84**, 231-234

115 **Davies DP, Adcock PL, Turpin M, Rowen SJ.** Stainless steel as a bipolar plate material for solid polymer fuel cells. *J. Power Sources*, 2000, **86**, 237-242

116 **Wang H, Sweikart A, Turner JA.** Stainless steel as bipolar plate material for polymer electrolyte membrane fuel cells. *J. Power Sources*, 2003, **115**, 243-251

117 **Wang H, Turner JA.** Ferratic stainless steel as bipolar plate material for polymer electrolyte membrane fuel cells. *J. Power Sources*, 2004, **128**, 193-200

118 **Lee S-J, Huang C-H, Lai J-J, Chen Y-P.** Corrosion-resistant component for PEM fuel cells. *J. Power Sources*, 2004, **131**, 162-168

119 **Lee S-J, Lai J-J, Huang C-H.** Stainless steel bipolar plates. *J. Power Sources*, 2005, **145**, 362-368

120 **Jayaraj J, Kim YC, Kim KB, Seok HK, Fleury E.** Corrosion studies on Fe-based amorphous alloys in simulated PEM fuel cell environment. *Sci. Technol. Adv. Mat,*, 2005, **6**, 282-289

121 **Cho EA, Jeon U-S, Hong S-A, Oh I-H, Kang S-G.** Performance of a 1kW-class PEMFC stack using TiN-coated 316 stainless steel bipolar plates. *J. Power Sources*, 2005, **142**, 177-183

122 **Joseph S, McClure JC, Chianelli R, Pich P, Sebastian PJ.** Conducting polymer-coated stainless steel bipolar plates for proton exchange membrane fuel cells (PEMFC). *Int. J. Hydrogen Energ.*, 2005, **30**, 1339-1344

123 **Wang Y, Northwood DO.** An investigation into polypyrrole-coated 316L stainless steel as a bipolar plate material for PEM fuel cells. *J. Power Sources*, 2006, **163**, 500-508

124 **Garcia MAL, Smit MA.** Study of electrodeposited polypyrrole coatings for the corrosion protection of stainless steel bipolar plates for the PEM fuel cell. *J. Power Sources*, 2006, 397-402

125 **Silva RF, Fracnhi D, Leone A, Pilloni L, Masci A, Pozio A.** Surface conductivity and stability of metallic bipolar plate materials for polymer electrolyte fuel cells. *Electrochim. Acta*, 2006, **51**, 3592-3598

126 **Nikam VV, Reddy RG.** Copper alloy bipolar plates for polymer electrolyte membrane fuel cell. *Electrochim. Acta*, 2006, **51**, 6338-6345

127 **Heinzel A, Mahlendorf F, Niemzig O, Kreuz C.** Injection moulded low cost bipolar plates for PEM fuel cells. *J. Power Sources*, 2004, **131**, 35-40

128 **Kuan H-C, Ma C-CM, Chen KH, Chen S-M.** Preparation, electrical, mechanical and thermal properties of composite bipolar plate for a fuel cell. *J. Power Sources*, 2004, **134**, 7-17

129 **Kuo J-K, Chen C-K.** A novel Nylon-6–S316L fiber compound material for injection molded fuel cell bipolar plates. *J. Power Sources*, 2006, **162**, 207-214

130 **Schunk Kohlenstofftechnik GmbH**. *Schunk Moulded Bipolar Plate Datasheet*, 2006, available from http://www.schunk-fuelcells.com/sixcms/media.php/1722/ 08_02e.pdf

131 **Eisenhuth**. *Eisenhuth Sigracet Bipolar Plate Datasheet*, available from http://www.eisenhuth.de/pdf /SIGRACET_Datenblaetter.pdf

132 **Kehr D, Rin G, Banhardt V.** Bipolar Plate Press Device and Method for Production Thereof. Schunk Kohlenstofftechnik GmbH. *World Intellectual Property Organisation*, 2003, Patent Number - WO03047016

133 **SGL Carbon AG.** *Bipolar Plate For Fuel Cell Stacks*, 2004. US Patent No - 6706437

134 **Yen C-Y, Liao S-H, Lin Y-F, Hung C-H, Lin Y-Y, Ma C-CM.** Preparation and properties of high performance nanocomposite bipolar plate for fuel cell. *J. Power Sources*, 2006, **162**, 309-315

135 **Tricoli V.** Proton and Methanol Transport in Poly(perfluorosulfonate) Membranes Containing Cs+ and H+ Cations. *J. Electrochem. Soc.*, 1998, **145**(11), 3798-3801

136 **Samec Z, Trojanek A, Langmaier J.** Diffusion Coefficients of Alkali Metal Cations in Nafion form Ion-Exchange Measurements. *J. Electrochem. Soc.*, 1997, **144**(12), 4236-4242

137 **Legras M, Hirata Y, Nguyen QT, Langevin D, Métayer M.** Sorption and diffusion behaviours of water in Nafion 117 membranes with different counter ions. *Desalination*, 2002, **147**, 351-357

138 **Stenina IA, Sistat P, Rebrov AI, Pourcelly G, Yaroslavstev AB.** Ion mobility in Nafion-117 membranes. *Desalination* 2004, **170**, 49-57

139 **Koter S, Piotrowski P, Kerres J.** Comparative investigations of ion-exchange membranes. *J. Membrane Sci.*, 1999, **153**, 83-90

140 **Okada T, Møller-Holst S, Gorseth O, Kjelstrup S.** Transport and equilibrium properties of Nafion membranes with H+ and Na+ ions. *J. Electroanal. Chem.*, 1998, **442**, 137-145

141 **Kundu S, Simon LC, Fowler M, Grot S.** Mechanical properties of Nafion electrolyte membranes under hydrated conditions. *Polymer*, 2005, **46**, 11707-11715

142 **Xie G, Okada T.** Water Transport Behavior in Nafion 117 Membranes. *J. Electrochem. Soc.*, 1995, **142**(9), 3057-3062

143 **Okada T, Nakamura N, Yuasa M, Sekine I.** Ion and Water Transport Characteristics in Membranes for Polymer Electrolyte Fuel Cells Containing H+ and Ca2+ Cations. *J. Electrochem. Soc.*, 1997, **144**(8), 2744-2750

144 **Kelly MJ, Falfilek G, Besenhard JO, Kronberger H, Nauer GE.** Contaminant absorption and conductivity in polymer electrolyte membranes. *J. Power Sources*, 2005, **145**, 249-252

145 **Shi M, Anson FC.** Dehydration of protonated Nafion coatings induced by cation exchange and monitored by quartz crystal microgravimetry. *J. Electroanal. Chem.*, 1997, **425**, 117-123

146 **Suresh G, Scinida YM, Pandey AK, Goswami A.** Self-diffusion coefficient of water in Nafion-117 membrane with different monovalent counterions, a radiotracer study. *J. Membrane Sci.*, 2005, 250, 39-45

147 **Pourcelly G, Oikonomou A, Gavach C, Hurwitz HD.** Influence of the water content on the kinetics of counter-ion transport in perflourosulphonic membranes. *J. Electroanal. Chem.*, 1990, **287**, 43-59

148 **Okada T, Xie G, Gorseth O, Kjelstrup S, Nakamura N, Arimura T.** Ion and water transport characteristics of Nafion membranes as electrolytes. *Electrochim. Acta*, 1998, **43**(24), 3741-3747

149 **Xie G, Okada T.** Characteristics of water transport in relation to microscopic structure in Nafion membranes. *J. Chem. Soc., Faraday T.*, 1996, **94**(4), 663-669

150 **Springer TE, Zawodzinski TA, Gottesfeld S.** Polymer Electrolyte Fuel Cell Model. *J. Electrochem. Soc.*, 1991, **138**, 2334-2342

151 **Xie G, Okada T.** Pumping effects in water movement accompanying cation transport across Nafion 117 membranes. *Electrochim. Acta*, 1996, **41**(9), 1569-1571

152 **Okada T.** Theory for water management in membranes for polymer electrolyte fuel cells. Part 1. The effect of impurity ions at the anode side on the membrane performances. *J. Electroanal. Chem.*, 1999, **465**, 1-17

153 **Okada T.** Theory for water management in membranes for polymer electrolyte fuel cells. Part 2. The effect of impurity ions at the cathode side on the membrane performances. *J. Electroanal. Chem.*, 1999, **465**, 18-29

154 **Casciola M, Albertu G, Sganappa M, Narducci R.** On the decay of Nafion proton conductivity at high temperature and relative humidity. *J. Power Sources*, 2006, **162**, 141-145

155 **Weber AZ, Newman J.** Transport in Polymer-Electrolyte Membranes, Part II. Mathematical Model. *J. Electrochem. Soc.*, 2004, **151**(2), A311-A325

156 **Hommura S, Kunisa Y, Terada I, Yoshitake M.** Characterisation of fibril reinforced membranes for fuel cells. *J. Fluorine Chem.*, 2003, **120**, 151-155

157 **Liu Y-H, Yi B, Shao Z-G, Xing D, Zhang H.** Carbon Nanotubes Reinforced Nafion Composite Membrane for Fuel Cell Applications. *Electrochem. Solid. St.*, 2006, **9**(7), A356-A359

158 **Ahn S-Y, Lee Y-C, Ha HY, Hong S-A, Oh I-H.** Properties of the reinforced composite membranes formbed by melt soluble ion conducting polymer resins for PEMFCs. *Electrichim. Acta*, 2004, **50**, 571-575

159 **Zhang Y, Zhang H, Zhu X, Gang L, Bi C, Liang Y.** Fabrication and characterisation of a PTFE-reinforced integral composite membrane for self-humidifying PEMFC. *J. Power Sources*, 2007, **165**, 786-792

160 **Wang L, Yi BL, Zhang HM, Liu YH, Xing DM, Shao Z-G, Cai YH.** Sulfonated polyimide/PTFE reinforced membrane for PEMFCs. *J. Power Sources*, 2007, **167**, 47-52

161 **Tang Y, Karlsson AM, Santare MH, Gilbert M, Cleghorn S, Johnson WB.** An experimental investigation of humidity and temperature effects on the mechanical properties of perfluorsulfonic acid membranes. *Mat. Sci. Eng. A-Struct.*, 2006, **425**, 297-304

162 **St-Pierre J, Jia N.** Successful Demonstration of Ballard PEMFCS for Space Shuttle Applications. *J. New Mater. Elect. Syst.*, 2002, **5**, 263-271

163 **Seddiq M, Khaleghi H, Mirzaei M.** Numerical analysis of gas cross-over through the membrane in a proton exchange membrane fuel cell. *J. Power Sources*, 2006, **161**, 371-379

164 **Stanic V, Braun J, Hoberecht M.** Durability of Membrane Electrode Assemblies (MEAs) in PEM Fuel Cells Operated on Pure Hydrogen and Oxygen. *AIAA J.*, 2003, **21**(1), 468-475

165 **Hottinen T, Himanen O, Karbonen S, Nitta I.** Inhomogeneous compression of PEMFC gas diffusion layer, Part II. Modeling the effect. *J. Power Sources*, 2007, **171**: 113-121

166 **Huang X, Solasi R, Zou Y, Feshler M, Reifsnider K, Condit D, Burlatsky S, Madden T.** Mechanical Endurance of Polymer Electrolyte Membrane and PEM Fuel Cell Durability. *J. Polym. Sci., Part B, Polymer Physics*, 2006, **44**, 2346-2357

167 **Kusoglu A, Karlsson AM, Santare MH, Cleghorn S Johnson WB.** Mechanical behaviour of fuel cell membranes under humidity cycles and effect of swelling anisotropy on the fatigue stresses. *J. Power Sources*, 2007, **170**, 345-358

168 **Zhang J, Xie Z, Zhang J, Tang Y, Song C, Navessin T, Shi Z, Song D, Wang H, Wilkinson DP, Liu Z-S, Holdcroft S.** High temperature PEM fuel cells. *J. Power Sources*, 2006, **160**, 872-891

169 **Kusolgu A, Karlsson AM, Santare MH, Cleghorn S, Johnson WB.** Mechanical response of fuel cell membranes subjected to a hygro-thermal cycle. *J. Power Sources*, 2006, **161**, 987-996

170 **Liu D, Case S.** Durability of proton exchange membrane fuel cells under dynamic testing conditions with cyclic current profile. *J. Power Sources*, 2006, **162**, 521-531

171 **MAR Sadiq Al-Baghdadi, HAK Shahad Al-Janabi.** Prediction of hygro-thermal stress distribution in proton exchange membranes using a three-dimensional multi-phase computation fluid dynamics model. *Proc. IMechE Pt. A: J. Power and Energy*, 2007, **221**, 941-953

172 **Curtin DE, Lousenberg RD, Henry TJ, Tangeman PC, Tisack ME.** Advanced materials for improved PEMFC performance and life. *J. Power Sources*, 2004, **131**, 41-48

173 **U. S. Department of Energy**. *Manufacturing research & development of PEM fuel cell systems for transportation applications*, 2006, available from http:// www1.eere.energy.gov/hydrogenandfuelcells/pdfs/mfg_wkshp_fuelcell.pdf

174 **US Department of Defence**. *MIL-STD-2164: Environmental Stress Screening Process for Electronic Equipment,* 1985, available from http://www.weibull. com/mil_std/ mil_std_2164.pdf

175 **US Department of Defence.** *MIL-STD-2165: Testability Program for Electronic Systems and Equipments*, 1985, available from http://www.weibull. com/mil_std/mil_std_2165.pdf

176 **US Department of Defence.** *MIL-STD-2035: Nondestructive Testing Acceptance Criteria*, 1991, available from http://www.weibull.com/mil_std/ mil_hdbk_2035.pdf

177 **Kinumoto T, Inaba M, Nakayama Y, Ogata K, Umebayashi R, Taksaka A, Iriyama Y, Abe T, Ogumi Z.** Durability of perfluorinated ionomer membrane against hydrogen peroxide. *J. Power Sources*, 2006, **158**, 1222-1228

178 **Pianca M, Barchiesi E, Esposto G, Radice S.** End groups in fluoropolymers. *J. Fluorine Chem.*, 1999, **95**, 71-84

179 **Alentiev A, Kostina J, Bondarenko G.** Chemical aging of Nafion, FTIR study. *Desalination*, 2006, **200**, 32-33

180 **Qiao J, Saito M, Hayamizu K, Okada T.** Degradation of Perfluorinated Ionomer Membranes for PEM Fuel Cells during Processing with H2O2. *J. Electrochem. Soc.*, 2006, **153**(6), A967-A974

181 **Inaba M, Kinumoto T, Kiriake M, Umebayashi R, Tasks A, Ogumi Z.** Gas crossover and membrane degradation in polymer electrolyte fuel cells. *Electrochim. Acta*, 2006, **51**, 5746-5753

182 **Liu W, Zuckerbrod D.** *In Situ* Detection of Hydrogen Peroxide in PEM Fuel Cells. *J. Electrochem. Soc.*, 2005, **152**(6), A1165-A1170

183 **LaConti AB, Hamdan M, McDonald RC.** *Handbook of Fuel Cells, Fundamentals, Technology and Applications, Volume 3*, 2003. Vielstich W, Lamm A, Gaseiger HA, Editors. (Wiley, New York)

184 **Inaba M.** Degradation Mechanisms for Polymer Electrolyte Fuel Cells. *14th International Conference on the Properties of Water and Steam, Kyoto*, 2004

185 **Endoh E, Terazono S, Widjaja H, Takimoto Y.** Degradation Study of MEA for PEMFCs under Low Humidity Conditions. *Electrochem. Solid St.*, 2004, **7**(7), A209-A211

186 **Schmidt TJ, Paulus UA, Gasteiger HA, Behm.** The oxygen reduction reaction on a Pt/carbon fuel cell catalyst in the presence of chloring anions. *J. Electroanal. Chem.*, 2001, **508**, 41-47

187 **Healy J, Hayden C, Xie T, Olson K, Waldo R, Brundage M, Gasteiger H, Abbott J.** Aspects of the Chemical Degradation of PFSA Ionomers used in PEM Fuel Cells. *Fuel Cells*, 2005, **5**(2), 302-308

188 **Aoki M, Uchida H, Watanabe M.** Novel evaluation method for degradation rate of polymer electrolytes in fuel cells. *Electrochem. Commun.*, 2005, **7**, 1434-1438

189 **Mittal V, Kunz HR, Fenton JM.** Effect of Catalyst Properties on Membrane Degradation Rate and the Underlying Degradation Mechanism in PEMFCs. *J. Electrochem. Soc.*, 2006, **153**(9), A1755-A1759

190 **Rama P, Chen R, Andrews J.** Failure Analysis of Polymer Electrolyte Fuel Cells. *SAE*, **2008**, 2008-01-0634

4 Mathematical Modelling of a PEFC

In this chapter, the electrochemical theory that describes the processes of the PEFC are discussed in greater detail. The discussion is presented in three parts, first focusing on the central topic of mass transport, followed by Ohmic losses and finally electrode kinetics.

4.1 Mass Transport

Molecular transport is a key process that directly affects the irreversible losses in an operating fuel cell at practical operating current densities. Mass transport losses occur when the concentration of oxygen at the cathode catalyst site falls, particularly at high current densities. Ohmic losses occur when the water content of the PEM is below a matrix threshold, which causes the resistance to proton transport across it to increase. A clearer insight into the mechanics of phenomenological cell processes and therefore irreversible voltage losses can be obtained by considering and applying the theory of molecular transport in electrochemical systems.

Mass transport can be broken down into two fundamental components: the thermo-fluidic and electrochemical state within a confined system and the transport that occurs as a consequence. The two most rudimentary thermo-fluidic conditions that can induce transport are spatial pressure gradients and temperature gradients. As an electrochemical system, transport in the PEFC can also be induced by spatial concentration gradients and by an electric field.

Molecular Diffusion

The molecules of a given species within a defined enclosed system will distribute through random motion from a region of high concentration to a region of low concentration. This process is known as molecular diffusion, or simply diffusion. The diffusive flux can be defined as the net molecular flux of the species from the region of high concentration to the region of low concentration. For an open system, a reference volume can be taken which

travels at a reference velocity. Within this volume, if there is a concentration gradient of a constituent species, then there will be a net molecular flux of that species from the region of high concentration to the region of low concentration. If the velocity of the species is different to the reference velocity, then the molecules of the species are said to be diffusing and the diffusion velocity can be defined as the average velocity of the species with respect to the reference velocity.

Convection

In convective or viscous flux, the molecules surrounding a wall particle loose their initial relatively high velocity, causing them to slow down. This leads to a dampening effect that continues until the boundary layer reaches the same velocity as the wall particle. The convective flux itself corresponds to that portion of flow that occurs in the laminar regime, which is driven by a pressure gradient. Convective flow can occur in gas-phases and liquid-phases. Since convection is a form of bulk flow, it does not have a tendency to separate constituent species of like-phase mixtures and so a mixture of different constituents in a single phase can be treated as a single phase.

Knudsen Flux

The Knudsen regime describes a type of flow that occurs when the likelihood of molecule-molecule collisions is low in relation to molecule-wall collisions. As such, molecules colliding off walls do not collide with other molecules. Therefore, the mean distance between two molecular collisions is much greater than the average distance between two neighbouring particles.

Thermal Diffusion

Thermal diffusion (also known as the Soret Effect) is the tendency of a mixture of two or more components of a fluid to separate as a result of a spatial temperature gradient. It is possible for the mixture to partially separate into components with the heavier larger

molecules concentrating at the lower temperature and lighter smaller molecules at the higher temperature as a result of thermal diffusion. The spatial temperature gradients that develop inside a working PEFC are usually not considered to be sufficiently large to induce molecular separation amongst the components of the fluids that infiltrate the cell. Thermal diffusion is therefore not explicitly considered in the current work.

Electro-Osmotic Drag

In a PEFC, electro-osmotic drag is the process by which water molecules are forcibly moved under an electric field through the polymer electrolyte. The process can be attributed to the interaction between the protons that migrate from the anode catalyst layer through to the cathode via the PEM and the water (a polar liquid) that infiltrates the solid polymer electrolyte. The interaction is commonly described as a drag process; a number of water molecules are said to be dragged per proton that migrates due to the electric field.

4.1.1 Concentrated Solution Theory

Concentrated solution theory can often be traced as the fundamental starting point for many of the key transport equations in the fuel cell modelling literature. For a multi-component electrochemical system, it can be assumed that intermolecular transport is driven by a spatial gradient in electrochemical potential. The gradient in electrochemical potential itself reflects a spatial gradient of electric potential and chemical concentration. The flux equation for this type of system can be expressed as [1]:

$$c_i \nabla \mu_i = \sum_j K_{ij} \left(v_j - v_i \right) \tag{4-1}$$

where

c_i = concentration of species *i*

$\nabla \mu_i$ = gradient in electrochemical potential of species *i*

K_{ij} = frictional coefficient of species pair *i,j*

v_i = velocity of species i

The frictional coefficient accounts for the local concentrations of pairs of constituent species and the diffusion coefficient of the species pair;

$$K_{ij} = \frac{RTc_i c_j}{c_T D_{ij}} \tag{4-2}$$

Substituting equation 4-2 into 4-1 yields

$$\frac{c_i \nabla \mu_i}{RT} = \sum_{i \neq j}^{n} \frac{c_i c_j}{c_T D_{ij}} \left(v_j - v_i \right) \tag{4-3}$$

The molar flux of a given species can be defined in terms of its concentration and velocity as:

$$\dot{n}_i = c_i \left(v_i - v_{ref} \right) \tag{4-4}$$

where the reference velocity accounts for the bulk fluid motion.

Substituting equation 4-4 into the flux equation 4-3 yields;

$$\frac{c_i \nabla \mu_i}{RT} = \sum_{i \neq j}^{n} \frac{c_i \dot{n}_j - c_j \dot{n}_i}{c_T D_{ij}} \tag{4-5}$$

This is the common form of the flux equation for concentrated solution theory and forms the basis of a number of PEFC models [2,3,4,5]. It has been applied to model transport across the PEM by treating it as a ternary system composed of water, electrolyte and protons. In doing so, the electrochemical potential gradient can be expressed as;

$$\nabla \mu_i = z_i F \nabla \phi + RT \frac{\nabla c_i}{c_i} \tag{4-6}$$

The Stefan-Maxwell Equation

For multi-component transport that does not involve species which have a positive or negative valance ($z_i = 0$), the electrochemical potential gradient can be expressed as:

$$\nabla \mu_i = RT \frac{\nabla c_i}{c_i} \tag{4-7}$$

Substituting into the flux equation yields

$$\nabla c_i = \sum_{i \neq j}^{n} \frac{c_i \dot{n}_j - c_j \dot{n}_i}{c_T D_{ij}} \tag{4-8}$$

By the ideal gas law

$$c_T = \frac{p}{RT} \tag{4-9}$$

Substituting equation 4-9 into 4-8 yields what is more commonly known as the Stefan-Maxwell equation:

$$\nabla c_i = \sum_{i \neq j}^{n} \frac{RT}{pD_{ij}} \left(c_i \dot{n}_j - c_j \dot{n}_i \right) \tag{4-10a}$$

Using the identity $c_i = y_i c_T$ and assuming that $\nabla c_T = 0$, equation 4-10a can be rewritten in terms of mole fractions as:

$$\nabla y_i = \sum_{i \neq j}^{n} \frac{RT}{pD_{ij}} \left(y_i \dot{n}_j - y_j \dot{n}_i \right) \tag{4-10b}$$

The Stefan-Maxwell equation can be applied to simulate multi-component diffusion in a chemical system. When diffusion occurs in a porous medium such as the GDL or MPL, the binary diffusion coefficient of species pair *ij* has to be adjusted to account for its

tortuosity, porosity and pore saturation, particularly if liquid water can infiltrate its porous network. Generally speaking, therefore, D_{ij} is replaced with a recalculated value D_{ij}^{eff} such that $D_{ij}^{eff} < D_{ij}$. The effective diffusivity can be calculated as:

$$D_{ij}^{eff} = D_{ij} \frac{\varepsilon}{\tau}(1-s)^m \tag{4-11}$$

In the context of PEFC modelling, the Stefan-Maxwell equation can be applied to determine the distribution of oxygen through the cathodic porous layers (GDL, MPL) and through the pores of the cathodic catalyst layer. The Stefan-Maxwell equation can be applied to calculate the change in the concentration of a reactant through a porous medium as a function of thickness when the reactant is a part of a multi-component system and the flux rate of each species through the medium is known. Therefore, the Stefan-Maxwell equation is critical in characterising the effects of mass transport limitations.

4.1.2 Dilute Solution Theory

Dilute solution theory can be derived from concentrated solution theory. The fundamental difference between the two approaches is that it is assumed that for a dilute system, the concentration of the solvent is much greater than the concentration of the solutes. Consequently, each solvent species can be considered in relation to the solvent and not in relation to each other because solvent interactions are assumed to be insignificant. If the solute species is *j* then $c_i << c_j$ and $c_j \approx c_T$. Hence, equation 4-5 can be expressed as

$$\dot{n}_i = -\frac{c_i \nabla \mu_i}{RT} D_{ij} + c_i v_j \tag{4-12}$$

This is sometimes known as the diffusion equation in fuel cell modelling. Equation 4-12 can be applied to simulate the transport of water across the PEM. In this case, the velocity of the polymer electrolyte is zero $(v_j = 0)$ and so equation 4-12 reduces to

$$\dot{n}_i = -\frac{c_i \nabla \mu_i}{RT} D_{ij} \tag{4-13}$$

where D_{ij} becomes the diffusion coefficient of water in the polymer electrolyte and should take into account the fact that it can swell during water uptake.

The Nernst-Planck Equation

For the transport of a charged species through a solute according to dilute solution theory, equation 4-6 can be substituted into equation 4-12 to yield:

$$\dot{n}_i = -z_i \frac{D_{ij}}{RT} F c_i \nabla \phi - D_{ij} \nabla c_i + c_i v_j \tag{4-14}$$

The mobility of the species *i* can be defined as;

$$u_i = \frac{D_{ij}}{RT} \tag{4- 15}$$

which can be substituted into equation 4-14 to yield the Nernst-Planck equation:

$$\dot{n}_i = -z_i u_i F c_i \nabla \phi - D_{ij} \nabla c_i + c_i v_j \tag{4-16}$$

The Nernst-Planck equation therefore describes the transport of a solute species *i* in a solvent species *j* due to:

- migration due to a gradient in electric potential
- diffusion due to a gradient in the chemical concentration of species *i*
- convection (due to a pressure gradient)

Convection is not implicitly linked to a pressure gradient in equation 4-16. Bernardi and Verbrugge [6] apply equation 4-16 to model the transport of protons across the PEM by treating it as a liquid water and electrolyte membrane composite solvent. They assume that the electrolyte is uniformly hydrated, which as a general assumption could be plausible for

very thin membranes (<50 microns in this case). The convective flux becomes the superficial pore-water flux in the membrane that is driven by a hydraulic pressure gradient. Generally, this can be given by Darcy's law:

$$v_j = -\frac{\kappa_p}{\mu}\nabla p \tag{4-17}$$

However if it is assumed that the pore water velocity is also affected by the gradient in electric potential, then Darcy's law has to be modified into a form that is known as Schlogl's velocity equation [6]:

$$v_j = \frac{\kappa_\phi}{\mu} z_j c_j F_j \nabla\phi - \frac{\kappa_p}{\mu}\nabla p \tag{4-18}$$

Fick's Law

For the transport of a species that has no net charge, substitution of equation 4-7 into 4-13 yields Fick's law of diffusion:

$$\dot{n}_i = -D_{ij}\nabla c_i \tag{4-19}$$

Here, D_{ij} becomes the diffusion coefficient of species *i* in the solute *j*, both of which by definition should be electro-neutral substances. Fick's law is often used instead of the Stefan-Maxwell equation for simplicity to describe multi-component transport across the GDL and the MPL; Ficks law forgoes the need to consider cross-species interactions. When applying Ficks law to model transport across a material that has a tortuous, porous network, the same considerations discussed previously regarding the use of D_{ij}^{eff} instead of D_{ij} would apply.

4.1.3 Knudsen Fluxes

Typically, Knudsen fluxes occur as free-molecular transport in porous structures where the characteristic pore radii are less than 10nm. As such, this type of flow can occur in

the catalyst layers of a PEFC. The Knudsen flux for a given species is calculated as a function of its concentration gradient, such that:

$$\dot{n}_i^K = -D_i^K \nabla c_i \tag{4-20}$$

The effective Knudsen diffusivity D_i^K accounts for the molar mass of the species i and the geometry of the pore in which the Knudsen flux occurs. It can be calculated as [7]:

$$D_i^K = r_K \sqrt{\frac{RT}{M_i}} \tag{4-21}$$

where

r_K = the Knudsen radius

M_i = the molar mass of species i

The total Knudsen flux for a multi-component system is calculated as:

$$n_{tot}^K = \sum_i \dot{n}_i^K \tag{4-22}$$

Although Knudsen flux is a form of diffusive flux, it does not explicitly appear in concentrated solution theory or dilute solution theory and is therefore often appended on to the relevant flux equation for a given species i.

4.1.4 Electro-Osmotic Drag

The electro-osmotic drag flux indicates in molar terms the rate at which water molecules are dragged by protons that migrate due to an electric field from the anode catalyst layer through the PEM to the cathode catalyst layer. For water it can be defined as:

$$\dot{n}_{w,drag} = \frac{J}{F}\xi_w \tag{4-23}$$

where

ξ_w = electro-osmotic drag coefficient of water

The electro-osmotic drag coefficient varies according to the local hydration of the PEM and temperature, and usually determined by experimental means [8,9]. For Nafion, the drag coefficient is typically between 1.5 to 2.8 [9].

Water flux due to electro-osmotic drag can be accommodated for by appending equation 4-23 on to the end of the flux equation from either concentrated or dilute solution theory. In their standard forms as given above, neither concentrated or dilute solution theory explicitly account for electro-osmotic drag when applied to describe the transport of water in solid polymer electrolytes.

4.1.5 Discussions on Mass Transport Processes across the PEM

The discussions above highlight the standard electrochemical equations to mechanistically describe the different types of transport that occur in the PEFC. Diffusion and convection can potentially occur in all layers of the PEFC. Knudsen flux is likely to develop in structures where the characteristic pore radii are in the order of 10 nm, for example, the catalyst layers. Electro-osmotic drag occurs through electrolytic regions of the cell, which therefore includes the catalyst layer and PEM.

The discussion demonstrates that there are largely two treatments that can be used to describing molecular transport in electrochemical systems; concentrated solution theory and dilute solution theory. As shown, the second can be obtained from the first if it is assumed that the concentration of the solute is much less than that of the solvent, i.e., the dilute solution assumption. For a multi-component concentrated system, concentrated solution theory can be applied. If it is assumed that cross-component interactions can be neglected according to the dilute solution assumption, dilute solution theory can be applied. In order to capture convection, Knudsen flux and electro-osmotic drag, it is necessary to introduce equations 4-17 or 4-18, 4-20 and 4-23 respectively into both concentrated and dilute solution theory.

4.2 Ohmic Resistance

4.2.1 Resistance to the Flow of Electrons

The total Ohmic resistance of a single cell is composed of two components; a resistance to the flow of electrons and a resistance to the flow of protons. Resistance to the flow of electrons is manifested in the electron-conducting parts of the cell, such as the catalyst layers, the carbon substrates of the GDL and MPL, and the bipolar plate. The compaction force applied to a PEFC assembly can force carbon fibrils within the GDL closer together, which can reduce the internal resistance to electron flow. Cell compaction can also decrease the contact resistance in the interface between electron-conducting layers (i.e., between the GDL and BPP, the MPL and the CL or the GDL and CL). Overall resistance to electron flow can be measured directly *ex-situ* as a function of compaction force for compressible layers and usually do not change *in-situ* according to the operating conditions of the cell. This is because the electron-conducting properties of the relevant materials such as carbon are unaffected by thermo-fluidic variables such as temperature, pressure and mass transport under fuel cell operating conditions.

4.2.2 Resistance to the Flow of Protons

The resistance to proton flow in the cell is characterised by two components; most significantly that which occurs across the proton-conducting PEM but also that which occurs in the polymer electrolyte in the catalyst layers. As such, the resistance to proton flow depends mainly upon the concentration of water across the PEM and can be calculated as

$$r^{proton} = \int_0^{t_{mem}} \frac{1}{\sigma} . dz \tag{4-24}$$

where

σ = proton conductivity of the PEM

t_{mem} = thickness of the PEM

It is possible to determine the proton conductivity of the PEM through *ex-situ* experimental tests based upon the uptake of water over a range of temperatures. As such, the experimental expression can be substituted directly into equation 4-24 where the proton conductivity becomes $\sigma(\lambda,T)$ and λ is the water content per sulphonic side chain.

A mechanistic description of resistance to the flow of protons across the PEM invokes a more detailed understanding of the diffusivity, concentration and convective velocity of protons. The movement of protons across the PEM is governed by Ohms law:

$$J = -\sigma \nabla \phi \tag{4-25}$$

Substituting 4-25 into 4-24 yields:

$$r^{proton} = -\int_0^{t_m} \frac{\nabla \phi}{J}.dz \tag{4-26}$$

The right hand side of equation 4-26 can be determined by recalling the form of the Nernst-Planck equation as given by 4-14 and applying it to determine the transport of protons across the PEM:

$$\dot{n}_{H^+} = -z_{H^+} \frac{D_{H^+}}{RT} F c_{H^+} \nabla \phi - D_{H^+} \nabla c_{H^+} + c_{H^+} v \tag{4-27}$$

where

v = the pore water velocity

D_{H^+} = the diffusion coefficient of protons in the PEM

If the flow of electrolytic charge across the membrane is related to the current density, then the current density can be given by:

$$J = F z_{H^+} \dot{n}_{H^+} \tag{4-28}$$

Substituting equation 4-27 into 4-28 yields:

$$J = -z_{H_2}^2 \frac{F^2}{RT} D_{H^+} c_{H^+} \nabla\phi - z_{H^+} F D_{H^+} \nabla c_{H^+} + z_{H^+} c_{H^+} F v \tag{4-29}$$

Given that z_{H^+}=1, equation 4-29 can be rearranged to give:

$$\nabla\phi = -\frac{JRT}{D_{H^+} c_{H^+} F^2} - \frac{RT}{F c_{H^+}} \nabla c_{H^+} + \frac{RT}{F D_{H^+}} v \tag{4-30}$$

Substituting 4-30 into 4-26 and integrating yields:

$$r^{proton} = \frac{RT}{F^2} \int_0^{t_m} \frac{1}{D_{H^+} c_{H^+}} dz + \frac{RT}{JF} \int_0^{t_m} \frac{1}{c_{H^+}} \cdot \frac{dc_{H^+}}{dz} dz - \frac{RT}{JF} \int_0^{t_m} \frac{v}{D_{H^+}} dz \tag{4-31}$$

4.2.3 Discussions on Modelling Resistance to the Flow of Protons across the PEM

Because the PEM is at least a ternary system, the interaction of migration, diffusion and convection processes can have an overall affect on water content and distribution. The challenge in employing equation 4-31 is that it is does not capture how the three proton transport processes interact with the various forms of water transport in the membrane. Therefore, equation 4-24 is commonly applied with experimental expressions for conductivity determined from *ex-situ* tests instead, i.e., $\sigma(\lambda, T)$. The interaction between protons due to migration and water in the PEM can be simply accounted for by considering the electro-osmotic drag flux, which is a function of the experimental electro-osmotic drag coefficient and the distribution of water across the PEM simulated through dilute or concentrated solution theory.

4.3 Electrode Kinetics

Activation losses occur in the anode and the cathode catalyst layers. This section considers three techniques by which the catalyst layer can be modelled to estimate the activation losses. The first method calculates the overall activation overvoltage of both

catalyst layers combined, treating each as a thin interface. The two methods that subsequently follow, namely the macro-homogeneous and agglomerate methods, are macroscopic treatments where the catalyst layer is treated as a region of finite thickness.

4.3.1 Thin Interface Model

Butler-Volmer Kinetics

Consider the following reaction which describes the reduction and oxidation processes for a reaction;

$$\text{Red} \leftrightarrow Ox + e^{-} \tag{4-32}$$

The rate of a reaction is the rate constant multiplied by the concentration of reactants raised to the orders of reaction, which is usually first order [10]. Therefore, the rates of the reduction and oxidation processes can be expressed in terms of an Arhennius equation such that;

$$\upsilon_{\text{Red}} = K_{\text{Red}}[c_{\text{Red}}]\exp\left[-\frac{\Delta G_{\text{Red}}}{RT}\right] \tag{4-33}$$

$$\upsilon_{\text{Ox}} = K_{\text{Ox}}[c_{\text{Ox}}]\exp\left[-\frac{\Delta G_{\text{Ox}}}{RT}\right] \tag{4-34}$$

where the subscripts ‘Red’ and ‘Ox’ refer to the reduction and oxidation processes respectively, K_{Red} and K_{Ox} are the corresponding rate constants, $[c_{\text{Red}}]$ and $[c_{\text{Ox}}]$ are the concentrations of the reactant molecule and ions, and ΔG_{Red} and ΔG_{Ox} are the activation energy change for the reduction and oxidation reactions respectively. In an irreversible system, there is no perceptible reaction at equilibrium. Current is generated only by the application of extra potential, the overpotential η. Therefore, the magnitude of ΔG_{Red} and ΔG_{Ox} become

$$\Delta G_{\text{Red}} = (\Delta G_{\text{Red}})^0 + \alpha nF\eta \tag{4-35}$$

$$\Delta G_{\text{Ox}} = (\Delta G_{\text{Ox}})^0 - (1-\alpha)nF\eta \tag{4-36}$$

The overpotential serves two purposes; a proportion of it (a fraction given by α) assists in the reduction process while the remaining slows down the oxidation process. The parameter α in the theory of electrode kinetics is known as the charge transfer coefficient and ranges between 0 and 1. The rates of the reduction and oxidation processes now become;

$$\upsilon_{\text{Red}} = K_{\text{Red}}[c_{\text{Red}}]\exp\left[-\frac{\Delta G_{\text{Red}} - \alpha nF\eta}{RT}\right] \tag{4-37}$$

$$\upsilon_{\text{Ox}} = K_{\text{Ox}}[c_{\text{Ox}}]\exp\left[-\frac{\Delta G_{\text{Ox}} + (1-\alpha)nF\eta}{RT}\right] \tag{4-38}$$

These can also be expressed in terms of the reduction and oxidation current densities as follows using Faradays law:

$$\upsilon_{\text{Red}} = \frac{J_{\text{Red}}}{nF} \tag{4-39}$$

$$\upsilon_{\text{Ox}} = \frac{J_{\text{Ox}}}{nF} \tag{4-40}$$

Therefore,

$$J_{\text{Red}} = nFK_{\text{Red}}[c_{\text{Red}}]\exp\left[-\frac{(\Delta G_{\text{Red}})^0}{RT}\right]\exp\left[-\frac{\alpha nF\eta}{RT}\right] \tag{4-41}$$

$$J_{\text{Ox}} = nFK_{\text{Ox}}[c_{\text{Ox}}]\exp\left[-\frac{(\Delta G_{\text{Ox}})^0}{RT}\right]\exp\left[-\frac{(1-\alpha)nF\eta}{RT}\right] \tag{4-42}$$

The forms of equations 4-41 and 4-42 can be simplified to;

$$J_{\text{Red}} = J_0 \exp\left[-\frac{\alpha nF\eta}{RT}\right] \tag{4-43}$$

$$J_{\text{Ox}} = J_0 \exp\left[\frac{(1-\alpha)nF\eta}{RT}\right] \tag{4-44}$$

were the J_0 is the exchange current density. The net current density $J = J_{\text{Red}} - J_{\text{Ox}}$ is given by:

$$J = J_o\left[\exp\left[-\frac{\alpha nF\eta}{RT}\right] - \exp\left[\frac{(1-\alpha nF\eta)}{RT}\right]\right] \tag{4-45}$$

The above equation is known as the Butler-Volmer equation. Because it is thought that only one electron can be transferred at a time, the expression strictly holds in the above form for processes involving a single electron. Reactions that involve multiple electron transfers, therefore, should be expressed as a number of one-electron reactions. Under such a circumstance, it is more rigorous to replace α with α_{Red} and to replace $(1-\alpha)$ with α_{Ox} because $\alpha_{\text{Red}} + \alpha_{\text{Ox}} \neq 1$ except for when $n = 1$;

$$J = J_o\left[\exp\left[-\frac{\alpha_{Red} nF\eta}{RT}\right] - \exp\left[\frac{(\alpha_{Ox} nF\eta)}{RT}\right]\right] \tag{4-46}$$

The Tafel Equation

In fuel cell modelling the overpotential at the anode electron is often neglected because it is usually at least an order of magnitude smaller than that of the overpotential at the cathode electrode. Amphlett *et al.* [11] suggest that the activation overvoltage for hydrogen oxidation at 298.15 K and at a current density of 0.11 A/cm^2 is 0.009 V compared to 0.35 V for oxygen reduction. In addition, when considering the overpotential at the cathode electrode, the second term on the right hand side of equation 4-46 is insignificant compared to the first term. Therefore, the net current density produced by the cell can be

obtained from the following reduced Butler-Volmer equation, where the subscript 'c' refers to the reduction process at the cathode,

$$J = J_0 \exp\left[-\frac{\alpha_c nF\eta}{RT}\right] \tag{4-47}$$

Based on the reduced Bulter-Volmer equation, the dependence of cathodic current density on overpotential is given by;

$$\ln J = \ln J_0 - \frac{\alpha_c nF\eta}{RT} \tag{4-48}$$

For a large overpotential to the cathodic reaction, η can be expressed by

$$\eta_{act,cathodic} = \frac{RT}{\alpha_c nF}\ln J_0 - \frac{RT}{\alpha_c nF}\ln J \tag{4-49}$$

Conversely, for a large overpotential to the anodic reaction, only the second term of equation 4-49 is of significance, and

$$\eta_{act,anodic} = \frac{RT}{\alpha_a nF}\ln J_0 - \frac{RT}{\alpha_a nF}\ln J \tag{4-50}$$

The two equations above are known as the Tafel equation, which can be generally expressed in the form

$$\eta = d + e\log J \tag{4-51}$$

In general terms, therefore, the activation overvoltage can be given as follows;

$$\eta_{act} = \frac{RT}{\alpha nF}\ln\frac{J_0}{J} \tag{4-52}$$

The Thin Interface Treatment

The thin interface treatment considers the activation overvoltage separately at both electrodes in terms of the exchange current density. The total activation overvoltage is then determined as the sum of the two components. The analysis starts by defining the exchange current density of the oxygen reduction process at the cathode using surface concentrations [12];

$$J_0 = nFK_b\left(c_{H^+}\right)^{(1-\alpha_c)}\left(c_{O_2}\right)^{(1-\alpha_c)}\left(c_{H_2O}\right)^{(\alpha_c)} \tag{4-53}$$

where

$$K_b = \frac{k_B TS}{h\gamma^{++}}\exp\left(\frac{-\Delta F_e^{++}}{RT}\right) \tag{4-54}$$

and where

k_B = Boltzmann constant

S = standard state of surface concentration

h = Planck constant

γ^{++} = transfer coefficient at the transition state

ΔF_e^{++} = standard state free energy of activation from going directly from gas-state and active electrode site to the activation complex of ionisation

The transition state refers to a position from the electrode surface where an electrolyte species can become associated with either the electrolyte solution by gaining a positive charge to become M^+ or can just as easily become associated with the metal of the electrode surface to become M. Substituting K_B into the exchange current density yields:

$$J_0 = nF\frac{k_B TS}{h\gamma^{++}}\exp\left(\frac{-\Delta F_e^{++}}{RT}\right)\left(c^*_{H^+}\right)^{(1-\alpha_c)}\left(c^*_{O_2}\right)^{(1-\alpha_c)}\left(c^*_{H_2O}\right)^{(\alpha_c)} \tag{4-55}$$

Substituting the cathodic exchange current density into the Tafel equation for the cathode activation overpotential yields:

$$\eta_{act,cathodic} = \frac{RT}{\alpha_c nF}\left[\ln\left(nF\frac{k_B TS}{h\gamma^{++}}\exp\left(\frac{-\Delta F_e^{++}}{RT}\right)\left(c_{H^+}^*\right)^{(1-\alpha_c)}\left(c_{O_2}^*\right)^{(1-\alpha_c)}\left(c_{H_2O}^*\right)^{(\alpha_c)}\right) - \ln J\right] \tag{4-56}$$

The law of electroneutrality requires that:

$$z_m c_m + \sum_i z_i c_i = 0 \tag{4-57}$$

where $z_m c_m$ is the total charge on the PEM and $\sum_i z_i c_i$ is the total charge on mobile species in the PEM. When there are no ionic contaminants permeating the PEM, protons are the only ionic species and the sulfonic end groups are the only charged membrane species. Given that z_m and z_i are both constants, being -1 and +1 respectively, yields $c_m = c_i$.

It can be assumed that the part of the PEM that is in closest contact with the cathode will have an approximately constant concentration of water and protons. It is as also assumed that all other terms will be constant apart from the surface concentration of oxygen at the catalyst layer, the current and the temperature. . Therefore, the constants in equation 4-56 can be grouped together and the cathodic activation overvoltage can be expressed in parametric form as;

$$\eta_{act,cathodic} = \beta_{1,c} + \beta_{2,c}T + \beta_{3,c}T\ln\left(c_{O_2}^*\right) + \beta_{4,c}\ln(J) \tag{4-58}$$

where

$$\beta_{1,c} = \left(\frac{-\Delta F_e^{++}}{\alpha_c nF}\right)$$

$$\beta_{2,c} = \frac{R}{\alpha_c nF}\ln\left[nF\frac{k_B TS}{h\gamma^{++}}\left(c_{H^+}^*\right)^{(1-\alpha_c)}\left(c_{H_2O}^*\right)^{(\alpha_c)}\right]$$

$$\beta_{3,c} = \frac{R}{\alpha_c nF}(1-\alpha_c)$$

$$\beta_{4,c} = -\frac{R}{\alpha_c nF}$$

For the anode, it is suggested that the process that controls the reaction rate is the chemisorption of hydrogen [12], i.e., the process whereby a valence bond is formed between a molecule of hydrogen and the surface of the catalyst-loaded anode. The exchange current density for strong chemisorption at the anode can be defined as:

$$J_0 = nFK_a \exp\left(\frac{(1-\gamma)\Delta F_c}{RT}\right) \tag{4-59}$$

where

$$K_a = \frac{k_B T}{h\gamma^{++}}\left(c^*_{H_2}\right)\exp\left(\frac{-\left(\Delta F^{++} - \gamma\Delta F_c\right)}{RT}\right) \tag{4-60}$$

and where

$\gamma = 1 - \alpha_a$

ΔF^{++} = standard-state free energy of activation for chemisorption

ΔF_c = standard-state free energy of chemisorption from gas state per mole of H_2

The exchange current density can therefore be expressed as

$$J_0 = nF\frac{k_B T}{h\gamma^{++}}\left(c^*_{H_2}\right)\exp\left(\frac{-\left(\Delta F^{++} - \gamma\Delta F_c\right)}{RT}\right)\exp\left(\frac{(1-\gamma)\Delta F_c}{RT}\right) \tag{4-61}$$

Substituting the anodic exchange current density into the Tafel equation for the anodic overvoltage yields:

$$\eta_{act,cathodic} = \frac{RT}{\alpha_c nF}\left[\ln\left(nF\frac{k_B T}{h\gamma^{++}}\left(c^*_{H_2}\right)\exp\left(\frac{-\left(\Delta F^{++} - \gamma\Delta F_c\right)}{RT}\right)\exp\left(\frac{(1-\gamma)\Delta F_c}{RT}\right)\right) - \ln J\right] \tag{4-62}$$

Because hydrogen is usually supplied neat to a PEFC or through a hydrogen-rich reformate feed with a mole fraction in excess of 0.7, it can be assumed that the variation in its

concentration for most low-pressure fuel cell applications is likely to be negligible. Therefore, the hydrogen concentration at the reaction sites for the above equation can be approximated as a constant, along with all other terms apart from temperature and current. In parametric form, therefore, the above equation can be expressed as

$$\eta_{act,anodic} = \beta_{1,a} + \beta_{2,a}T + \beta_{4,a}\ln(J) \tag{4-63}$$

where

$$\beta_{1,a} = \frac{-\Delta F^{++}}{\alpha_a nF}$$

$$\beta_{2,a} = \frac{R}{\alpha_a nF}\ln\left(nF\frac{k_B}{h\gamma^{++}}\right)\left(c^*_{H_2}\right)$$

$$\beta_{4,a} = -\frac{R}{\alpha_a nF}$$

The total activation overvoltage is given by

$$\eta_{act} = \eta_{act,cathodic} + \eta_{act,anodic} \tag{4-64}$$

such that

$$\eta_{act} = \beta_1 + \beta_2 T + \beta_3 T\ln\left(c^*_{O_2}\right) + \beta_4\ln(J) \tag{4-65}$$

where

$$\beta_1 = \beta_{1,c} + \beta_{1,a}$$

$$\beta_2 = \beta_{2,c} + \beta_{2,a}$$

$$\beta_3 = \beta_{3,c}$$

$$\beta_4 = \beta_{4,c} + \beta_{4,a}$$

Therefore, by using the thin interface treatment, it is possible to define the total activation overvoltage of a PEFC in parametric form. The parametric constants can be statistically evaluated from empirical analysis and applied to estimate the activation

overvoltage at a given current, temperature and predetermined oxygen concentration at the catalyst sites.

4.3.2 The Macro-Homogeneous Model

Fundamentally, macroscopic models such as the macro-homogeneous and agglomerate models consider the catalyst layer to be a matrix structure that contains three principal components;

- a porous network for the supply of oxygen to the reaction sites and the removal of excess water;
- a solid interconnected carbon-phase which serves as a network for the supply of electrons;
- an electrolytic phase which provides a network for the supply of protons.

The macro-homogeneous (MH) model considers the catalyst later to be a homogeneous phase and calculates its performance according to the bulk properties of the catalyst layer structure [13,14].

It is possible for molecular diffusion, convection and Knudsen diffusion to occur within the catalyst layer. Two-phase flow can also propagate through the catalyst layer, particularly in the cathode catalyst layer due to the product water being formed there. For the current discussion, the simplest case is taken, where Fick's law of diffusion is applied to describe material balance of oxygen;

$$\frac{dc_{O_2}}{dz} = -\frac{J - J(z)}{nFD_{O_2}^{eff}} \tag{4-66}$$

where $J(z)$ is the local current density. Ohms law can be used to define the increase in phase potential in the solid and the electrolyte with respect to channel depth [13]:

$$\frac{d\eta}{dx} = \frac{1}{\kappa_s^{eff}} I - \left(\frac{1}{\kappa_m^{eff}} + \frac{1}{\kappa_s^{eff}} \right) J(z) \tag{4-67}$$

The total activation overvoltage of the cathode catalyst layer can then be calculated with known boundary conditions.

4.3.3 The Agglomerate Model

The agglomerate model assumes that the catalyst layer can be approximately modelled as a collection of carbon-supported catalyst agglomerates that are coated by a thin layer of polymer electrolyte [15,16,17,18]. The agglomerates are all assumed to be identical in geometry and organised in an artificial manner.

The agglomerate model was initially used by Iczkowski and Cutlip to determine the performance of the cathode catalyst layer in a PAFC [19]. In general, like the macro-homogeneous model, it is assumed that oxygen is reduced as it diffuses through the catalyst layer;

$$\frac{dn_{o_2}(z)}{dz} = -n_R \tag{4-68}$$

where

n_{o_2} = diffusive flux of oxygen past any point in the catalyst layer (kmol/m^2-s)

n_R = rate of reaction of oxygen per m^3 of electrode at a given point (kmol/m^3-s)

First, oxygen diffuses into the catalyst layer, where it permeates through the porous network. The oxygen then dissolves in the outer layer of the film of electrolyte which covers the agglomerates. The dissolved oxygen then diffuses across the film and diffuses into the pores of the agglomerates. The rate of reaction per unit volume in the catalyst layer is calculated as

$$n_R = aD_{O_2,mem}\frac{p_{O_2}(z)c^0_{O_2} - c_{O_2}(r_a, z)}{\delta} \tag{4-69}$$

where

a = the area of the film per unit volume of the electrode

$D_{O_2,mem}$ = the diffusion coefficient of oxygen in the electrolyte

$p_{O_2}(z)$ = the partial pressure of oxygen in the gas pores

$c_{O_2}^0$ = the solubility of oxygen in the electrolyte

δ = the thickness of the film

r_a = the radius of the agglomerate

Using identities for the concentration of dissolved oxygen at the surface of the agglomerate $c_{O_2}(r_a, z)$, the above equations can be equated and rearranged to yield an expression for the change in oxygen flux rate across the catalyst layer:

$$\frac{dn_{O_2}}{dz} = -\frac{p_{O_2}(z)}{\frac{\delta}{aD_{O_2,mem}c_{O_2}^0} + \frac{1}{\varsigma_c K_e c_{O_2}^0}} \tag{4-70}$$

where the effectiveness factor for the diffusion and reaction of oxygen ς_c can generally be defined as the actual reaction rate for a given quantity of catalytic agglomerates to the reaction rate if the oxygen concentration throughout it was the same as at the surface [20].

The rate constant can be defined in terms of the current density assuming that the only source of voltage loss is activation, $J_T(E)$:

$$K_e = \frac{J_T(E)}{4Fz_{O_2}p_{O_2,gas}c_{O_2}^0} \tag{4-71}$$

where

z_{O_2} = thickness of the catalyst layer

$p_{O_2,gas}$ = partial pressure of oxygen in the gas stream

Finally, $J_T(E)$ can be related to potential through the equation;

$$J(E) = J(E_{Ref})\exp_{10}\left[\frac{E_{Ref} - E}{T_s}\right] \tag{4-72}$$

4.4.3 Discussions on the Fundamental Models for Electrode Kinetics

The three types of models discussed above clearly have different applications and in terms of fuel cell modelling. The most pertinent difference between the thin interface and two macroscopic treatments is that former deals with the reaction kinetics in great detail but does not afford any consideration to structural aspects of the catalyst layer. Therefore, in terms of generating polarisation curves considering the dependence of activation overvoltage on parameters that are controllable from an operational point of view (i.e., cell temperature, air/oxygen supply pressure and composition, current density), the thin interface model can suffice. However, in order to elucidate certain effects of catalyst layer design on the reactive flow through it, macroscopic treatments would appear to be more relevant.

Ridge *et al.* [21] took the same fundamental approach described for the agglomerate model described above, but also considered the transport of protons through the electrolyte phase by considering the Nernst-Planck equation and determined that proton transport limitations can have a large effect on electrode performance. It was also found that electrode performance can be improved by minimising the agglomerate radii. For a given catalytic loading, smaller agglomerates would have the effect of increasing the accessible surface area of the active sites. Broka and Ekdunge [22] found that the macro-homogeneous model can predict that thicker catalyst layers can induce higher overpotentials due to a corresponding increase in the barrier to mass transport and limited proton conductivity, while the agglomerate model predicts that the limiting current density is proportional to the total accessible surface area of the active sites, such that increasing the thickness of the later increases the limiting current. It is argued in the same work that the macro-homogeneous model does not simulate the polarisation as well as the agglomerate model in relation to experimental data.

It is evident that the two different macroscopic modelling treatments can generate conflicting results, though the predictions of the agglomerate treatment do appear to follow predicted polarisation data more closely than the macro-homogeneous treatment. However, it has to be acknowledged that not all of the requisite constants for either of the macroscopic treatments can be readily determined, and that neither inherently reflects the true

heterogeneous nature of catalyst layer structures, which can influence the actual performance of the catalyst layer.

For the purposes of the current research, the thin interface model is applied when required to determine the activation overvoltage of the cell. Reactive flow across the catalyst layer is not treated rigorously in the present work. It is assumed that the polymer electrolyte which penetrates the catalyst layer acts as an infinitely thin continuum to the PEM and therefore has the same water content in the electrolytic phase throughout its thickness as the PEM at the catalyst layer/PEM interface. In reality the total thickness of the catalyst layers could contribute towards 5% of the total thickness of a complete seven-layer assembly assuming that the total thickness of the assembly is ~ 500 μm (aGDL/aMPL/aCL/PEM/cCL/cMPL/cGDL). It is acknowledged that reactive flow simulation in electrochemical systems is a separate branch of fuel cell modelling and simulation that requires dedicated focus, which is beyond the scope of the current thesis. However, using the fundamental electrochemical theory discussed in this chapter, it is possible to construct the foundations of a simple fuel cell model that handles multi-component inlet gases to the anode and cathode.

4.4 References

1 **Newman J.** *Electrochemical Systems*, 1991 (Prentice Hall, Englewood Cliffs)

2 **Fuller TF, Newman J.** A Concentrated Solution Theory Model of Transport in Solid-Polymer-Electrolyte Fuel Cells. *The Electrochemical Society Proceedings Series*, 1989, **PV 89-14**, 25-38

3 **Fuller TF, Newman J.** Water and Thermal Management in Solid-Polymer-Electrolyte Fuel Cells. *J. Electrochem. Soc.*, 1993, **140**(5), 1218-1225

4 **Weber AZ, Newman J.** Transport in Polymer-Electrolyte Membranes, II Mathematical Model. *J. Electrochem. Soc.*, 2004, **151**(2),A311-A325

5 **Janssen GJM.** A Phenomenological Model of Water Transport in a Proton Exchange Membrane Fuel Cell. *J. Electrochem. Soc.*, 2001, **148**(12),A1313-A1323

6 **Bernardi DM, Verbrugge MW.** A Mathematical model of the Solid-Polymer-Electrolyte Fuel Cell. *J. Electrochem. Soc.*, 1992, **139**, 2477-2491

7 **Cunningham RE, Williams RJJ.** *Diffusion in Gases and Porous Media,* 1980 (Plenum Press., New York)

8 **Fuller TF, Newman J.** Experimental Determination of the Transport Number of Water in Nafion 117 Membranes. *J. Electrochem. Soc.*, 1992, **139**(5), A1332-A1337

9 **Pivovar BS.** An Overview of Electro-Osmosis in Fuel Cell Polymer Electrolytes. *Polymer*, 2006, **47**, 4194-4202

10 **Hibbert DB.** *Introduction to Electrochemistry*, 1993 (Macmillan Press, Basingstoke)

11 **Amphlett JC, Baumert RM, Mann RF, Peppley BA, Roberge PR.** Performance Modelling of the Ballard Mark IV Solid Polymer Fuel Cell, I. Mechanistic Model Development. *J. Electrochem. Soc.*, 1995, **142**(1), 1-8

12 **Berger C.** *Handbook of Fuel Cell Technology*, 1968 (Prentice-Hall, Englewood Cliffs)

13 **Eikerling M, Kornyshev AA.** Modelling the Performance of the Cathode Catalyst Layer of Polymer Electrolyte Fuel Cells. *J. Electroanal. Chem.*, 1998, **453**, 89-106

14 **Jeng KT, Kuo CP, Lee SF.** Modelling the Catalyst Layer of a PEM Fuel Cell Cathode using a Dimensionless Approach. *J. Power Sources*, 2003, **128**(2), 145-151

15 **Giner J, Hunter C.** The Mechanism of Operation of the Teflon-Bonded Gas Diffusion Electrode, A Mathematical Model. *J. Electrochem. Soc.*, 1969, **116**, 1124-1130

16 **Viitanen M, Lampinen MJ.** A Mathematical model and optimization of the structure for porous air electrodes. *J. Power Sources*, 1990, **32**, 207-231

17 **Cutlip MB.** An approximate model for mass transfer with reaction in porous gas diffusion electrodes. *Electrochim. Acta*, 1975, **20**, 767-773

18 **Yang SC, Cutlip MB. Stonehart P.** Simulation and optimization of porous gas-diffusion electrodes used in hydrogen/oxygen phosphoric acid fuel cell - I. optimization to PAFC cathode development. *Electrochim. Acta*, 1990, **35**, 869-878

19 **Iczkowski RP, Cutlip MB.** Voltage Losses in Fuel Cell Cathodes. *J. Electrochem. Soc.*, 1980, **127**(7), 1433-1436

20 **Winterbottom JM, King MB** (*eds.*)**.** *Reactor Design for Chemical Engineers*, 1999 (Stanley Thornes Ltd., Cheltenham)

21 **Ridge SJ, White RE, Tsou Y, Beaver RN, Eisman GA.** Oxygen Reduction in a Proton Exchange Membrane Test Cell. *J. Electrochem. Soc.*, 1989, **136**(7), 1902-1909

22 **Broka K, Ekdunge P. Modelling the PEM Fuel Cell Cathode.** *J. Applied Electrochem.*, 1997, **24**, 3767-3772

5 A Polymer Electrolyte Fuel Cell Model with Multi-Component Input

Many models have been successfully developed over the last couple of decades to simulate the processes of the PEFC. One of the limitations of these models is that typically only two constituent species are considered in the dry pre-humidified anode and cathode inlet gases, namely oxygen and nitrogen for the cathode, and hydrogen and carbon dioxide for the anode. Another limitation is that they do not systematically consider the effects of cross-flow through the cell on the composition of gases in the channels as this in turn affects the boundary conditions during simulation. In order to extend the potential of theoretical studies and to bring PEFC simulation closer towards reality, in this chapter, a simple one-dimensional steady-state, low temperature, isothermal, isobaric PEFC model is developed which accommodates multi-component inlet gases and accounts for the effect of cross-flow through the cell on the composition of gases in the channels. The model determines the actual cross-flow through the cell for a given set of cell conditions. The model is validated and applied to investigate the effects of carbon monoxide infiltration and crossover on the performance of the cathode catalyst layer.

5.1 Introduction

The critical element of a model is the founding theory, and for a PEFC this encompasses electrochemistry, thermodynamics, and fluid mechanics. While the founding theory for different models may well be common, the manipulation of the theory can lead to different systems of equations and different assumptions as discussed in the preceding chapter. In addition, models based largely on theory may consider the principal phenomenological processes but can also be difficult to solve with an abundance of parametric constants that are not necessarily easy to define. Alternatively, empirical models based upon experimental data could provide more accurate results within a certain operating range for specific cell designs, but would not necessarily be universal in applicability and may not reflect a full understanding of the processes involved. The intermediate solution would therefore lie in a semi-empirical model that identifies the key processes but uses

experimental results to assist in solving the key equations without over-computation. There are a number of key historical models that have been developed.

Fuller and Newman [1] introduced concentrated solution theory to describe species flux in the membrane. Three species were considered in the model: polymer with acid end groups, hydrogen ions, and water. Mass transportation was considered in 1D across the cell, while thermal management was introduced in the transverse along-the-gas-channel direction via energy balance. Each channel gas was treated as a heat removal medium, and the effects of different thermal conductivities of these gases were analysed with respect to cell performance. It was found that the hydration of the membrane was sensitive to the rate of heat removal, such that low rates of heat removal, i.e., low thermal conductivity of channel gases, would result in poor cell performance.

Bernardi and Verbrugge [2,3] developed a mathematical model which divided the cell into seven regions: gas flow channels, gas diffusers and catalyst layers for cathode and anode, and a membrane region in between. Species flux within these regions was described using dilute solution theory, where the Nernst-Planck equation was used to describe the flux due to migration, diffusion and convection. Cell operation was assumed to be isothermal, and gas-phase pressures were assumed to be constant due to the low gas-phase viscosity. Liquid-phase pressures were assumed to be variable, and pressure gradients were introduced to the model via Schlogl's velocity equation. The model assumed that the membrane was fully and uniformly hydrated.

Springer *et al.* [4] developed a semi-empirical model. Dilute solution theory was used to described water flux in the membrane. The form of the flux equation employed however coupled the flux due to migration and diffusion as a function of the chemical potential of water. The cell was assumed to be isobaric and so pressure-driven convective fluxes were not considered. In the PEM, since water is produced in the cathode, the greatest concentration of water is likely to reside in the region of the PEM that is the closest to the cathode catalyst layer. Diffusion therefore is likely to occur through the PEM in the direction of the anode. However, because water molecules interact with protons which migrate from anode to cathode, water is also electro-osmotically dragged back to the cathode. This phenomenon was mathematically simulated in the model in part using experimental data. The fundamental argument presented by the model was that the counter-acting water fluxes caused a gradient

in water content to build up across the membrane, such that the membrane was not always uniformly hydrated. This gradient from anode to cathode increased with respect to operating current density causing the membrane to loose its proton-conductivity, which increased the overall cell resistance and reduced the output cell voltage.

Amphlett *et al.* [**5**] developed a different semi-empirical model using experimental performance data from the Ballard Mark IV fuel cell. The model assumed isobaric and isothermal operation. Electrode transport was described using the Stefan-Maxwell equation and the activation and Ohmic overvotlages were defined by applying linear regression to experimental data. Membrane transport was not mathematically modelled. However, the calculated polarisation curves correlated well with experimental results.

One of the fundamental limitations among these benchmark models is that only up to two constituent species were considered in the dry pre-humidified anode and cathode inlet gases. This limitation extends to other computational models where multi-component transport is considered but restricted to the inclusion of oxygen, nitrogen and water in the inlet cathode feed after humidification [6,7]. This reflects only the ideal case. Tropospheric air would have at least ten constituents while reformed fuel supplies would typically contain carbon dioxide and carbon monoxide.

Carbon monoxide is important since its molecules will, for example, adsorb more readily onto platinum-based catalyst sites than hydrogen. With its presence, the surface fraction available for hydrogen chemisorption is compromised [8,9,10,11,12]. Correspondingly, the activation energy increases for the hydrogen oxidation process, which increases the anodic activation overvoltage. Although it has received little attention, carbon monoxide is known to permeate the membrane and consequently degrade the performance of the cathode catalyst [13].

In this research, an one-dimensional isothermal, steady-state PEFC model based on a number of key publications in the area has been developed. In the model, the fuel cell consists of five regions, as illustrated in Figure 5-1. Gas chambers for anode and cathode transport humidified fuel and air respectively and also remove unused gases and water. The catalyst is treated as an infinitely thin interfacial layer. The model introduces the capability to handle multi-component input gases and couples this with the multi-component diffusion

mechanism of the Stefan-Maxwell equation to describe gas transport in the electrodes. The mass transport model of the cell is completed by considering water transport in the membrane region. The transport processes in the two electrodes and the membrane were assumed to be simultaneous and inter-dependent. The transport of carbon monoxide across the cell from the anode inlet has been studied due to its impact on cell performance. The simulated overvoltages by the model are validated against experimental data obtained from the Ballard Mark IV fuel cell [5].

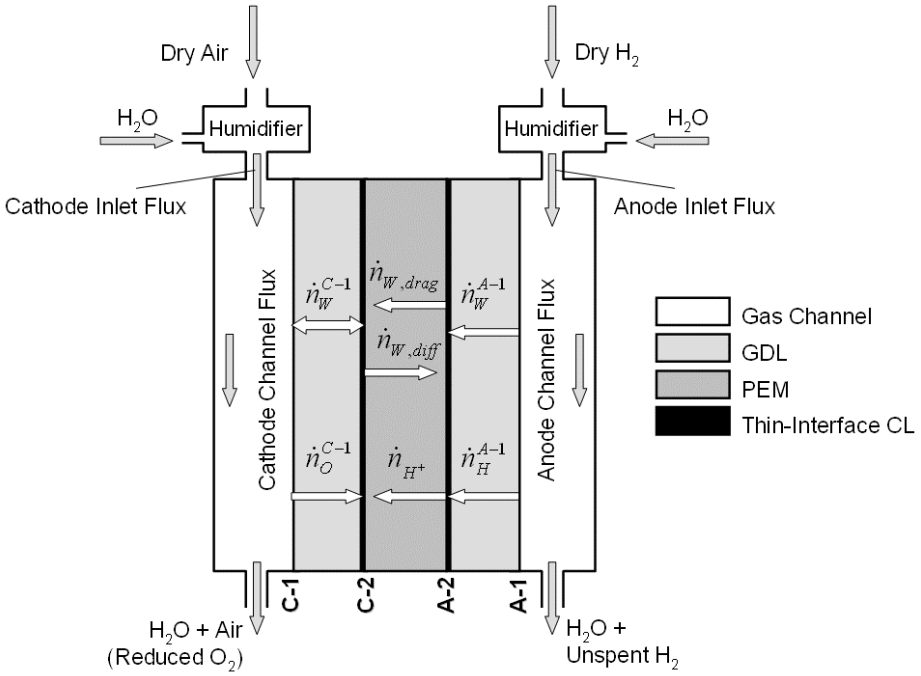

Figure 5-1 Five regions of the polymer electrolyte fuel cell

5.2 The Basic PEFC Model

The current PEFC model can be divided into two parts; the basic model and the multi-species mass transportation model. The assumptions applied in developing the model are as follow:

- the total pressures in the channels are constant and equal
- both anode and cathode streams are saturated with water vapour at their given gas inlet temperatures
- the fuel cell operates under isothermal steady-state conditions
- the heat conduction by channel flows is negligible

- the gas mixtures behave as ideal gases
- the water exists in vapour form
- when the local water activity exceeds unity, the excess liquid water exists as small droplets of negligible volume
- the diffusion coefficient of water in the membrane is a function of the water content
- the water drag is a function of the local water content
- there is zero crossover of hydrogen and oxygen across the membrane region
- the only species that travels through the hydrated PEM are the protons due to electric field, water vapour due to diffusion and electro-osmotic drag, and potentially carbon monoxide due to diffusion
- the concentration of water in the membrane is much less than the electrolyte concentration.

5.2.1 Thermodynamic Equilibrium Potential and Irreversible Losses

The thermodynamic equilibrium potential can be calculated using the Nernst equation, as derived in chapter 2, resulting in equation 2-13. In this chapter, it is assumed that activation (η_{act}) and Ohmic (η_{ohm}) losses decrease the cell potential from its equilibrium potential when a reasonably large current is drawn up to a maximum of 1.0 A/cm^2.

Activation losses are described using the thin interface treatment described in chapter 4. The total activation overvoltage is calculated using equation 4-65. It is assumed that the parametric coefficients in equation 4-65 can be treated as constants for a given fuel cell system and determined by applying linear regression to measured test data. As such, the total activation overvoltage for the Ballard Mark IV PEFC, can be expressed as [5];

$$\eta_{act} = -0.9514 + 0.00312T - 0.000187T\left[\ln(j)\right] + 7.4\times10^{-5}T\left[\ln(c_{O_2}^{C-2})\right] \tag{5-1}$$

The concentration of oxygen is defined by Henry's law [5];

$$c_{O_2}^{C-2} = \frac{p_{O_2}^{C-2}}{5.08\times10^6 \exp\left(\frac{-498}{T}\right)} \tag{5-2}$$

The total drop in the cell potential due to Ohmic resistance consists of the combined resistance to electron and proton transport and defined by Ohm's law in the model:

$$\eta_{ohmic}^{total} = \eta_{ohmic}^{eletronic} + \eta_{ohmic}^{protons} = -jR^{internal} \tag{5-3}$$

For the purpose of this chapter, the internal resistance is defined in terms of cell temperature and cell current based on the active cell area. It is assumed that this relationship can be determined again by applying linear regression to test data. As such, the following expression determined by Amplett *et al.* is adopted [5];

$$R^{internal} = 0.01605 - 3.5\times10^{-5}T + 8.0\times10^{-5}\, j \tag{5-4}$$

5.2.2 Water Transport Model for the PEM

The activation overvoltage is defined by the concentration of oxygen at the cathode to membrane interface, which is dependant upon the water flux in the electrodes and the membrane. While transport in the electrodes is dealt with later in section 5.3.3, consideration is given here to transport within the membrane region.

By assuming the membrane mixture to be moderately dilute, the flux of a species *i* can be obtained as follows from equation 4-12;

$$\dot{n}_i = -\frac{D_i}{RT} c_i \nabla \mu_i + v_j c_i \tag{5-5}$$

The first term explains that the gradient in chemical potential is the driving force behind migration and diffusion. The second term represents the convection due to the bulk motion of the solvent species. In the case of a membrane under isobaric conditions, it reduces to [4];

$$\dot{n}_i = -\frac{D_i}{RT} c_i \nabla \mu_i \tag{5-6}$$

The chemical potential can be defined in terms of absolute activity [14];

$$\mu_i = RT \ln a_i \tag{5-7}$$

which leads to a definition of water flux due to diffusion in the membrane;

$$\dot{n}_{W,diff} = -\frac{D_i}{RT} c_W \nabla \left(RT \ln a_W \right) \tag{5-8}$$

The spatial distribution of water across the PEM can often be expressed in terms of water content per charge site. Therefore, the diffusive flux of water can be described as

$$\dot{n}_{W,diff} = -D' c_W \frac{d(\ln a)}{d\lambda} \frac{d\lambda}{dz'} \tag{5-9}$$

The concentration parameter c_w and laboratory coordinate z' are not fixed to the membrane coordinates and need to be modified to prevent the need to track membrane swelling. It is possible to convert from the laboratory coordinate z' to the dry membrane coordinate z using an extension parameter x such that;

$$z' = (1 + x\lambda) z \tag{5-10}$$

The concentration of water can also be defined as follows, noting that the density of the PEM will decrease when it is expanded;

$$c_W = \lambda \frac{\rho_{dry}}{(1 + x\lambda) M_m} \tag{5-11}$$

Using the following mathematical identity:

$$\frac{d(\ln a)}{d\lambda} = \frac{d(\ln a)}{da} \frac{da}{d\lambda} = \frac{1}{a} \frac{da}{d\lambda} \tag{5-12}$$

it is possible to redefine the diffusive flux of water across the PEM as;

$$\dot{n}_{W,diff} = -\frac{\rho_{dry}}{M_m}\left[D' \frac{\lambda}{a(1+x\lambda)^2} \frac{da}{d\lambda} \right] \frac{d\lambda}{dz} \tag{5-13}$$

The term in the square bracket is the intra-diffusion coefficient of the water in the membrane and can be experimentally obtained as [4];

$$D_{\lambda>4} = 10^{-6} \exp\left[2416\left(\frac{1}{303} - \frac{1}{T} \right) \right] \left(2.563 - 0.33\lambda + 0.0264\lambda^2 - 0.000671\lambda^3 \right) \tag{5-14}$$

The value of λ at the boundary of a PEM can be determined using the local water vapour activity. At 30˚C (303 K), it has been experimental obtained as [4],

$$\lambda_{303K} = 0.043 + 17.81a - 39.85a^2 + 36.0a^3 \tag{5-15}$$

in which a is the local water activity and is defined as the ratio of the local water partial pressure to the saturation vapour pressure.

In addition to the diffusive water flux, there is a reverse water flux flowing in the membrane from anode to cathode due to electro-osmotic drag. It is therefore a function of the local water content and the flux of hydrogen ions. It can be related to the molar flux of hydrogen to the membrane I as [4],

$$\dot{n}_{W,drag} = \frac{5\lambda}{22} I \tag{5-16}$$

Therefore the net water flux across the membrane is the difference between the diffusive flux of water and the flux due to electro-osmotic drag,

$$\dot{n}_W = \frac{5\lambda}{22} I - \frac{\rho_{dry}}{M_m} D_\lambda \frac{d\lambda}{dz} \tag{5-17}$$

To mathematically link the processes of water flux across electrodes to the process of net water flux across membrane, it is necessary to introduce the ratio of net water flux to molar hydrogen flux in the anode, α_W^A, into the model. Its value is determined through iteration and is not assumed or fixed *a-priori*. The correct value is obtained when the activity of water as a function of λ from equation 5-18 is equal to that determined at interface C2 from the diffusion layer model, which will be discussed in section 5.3.3. This is a key feature of this model as it directly couples the composition and transportation of species in the anode and cathode sides of the cell and can vary according to the simulated operating conditions (temperature, current density, gas pressure, humidification) and design features of the cell (layer thicknesses, PEM equivalent weight).

Rearranging equation 5-17 gives the water distribution in the membrane;

$$\frac{d\lambda}{dz} = \frac{M_m I}{\rho_{dry}} \frac{1}{D_\lambda} \left[\frac{5\lambda}{22} - \alpha_W^A \right] \tag{5-18}$$

5.3 The Multi-Component Input Model

Mass transportation characterises the availability of reactant gases at the catalyst sites and the transport of water in and out of the cell.

5.3.1 Molar Flux of Oxidised, Reduced and Produced Species

Consider the overall fuel cell reaction $H_2 + 1/2O_2 \Rightarrow H_2O$. It consists of two electrode processes, the hydrogen oxidation in the active catalyst region of the anode $H_2 \Rightarrow 2H^+ + 2e^-$, and the oxygen reduction process that takes place to produce water in catalyst region of the cathode $1/2O_2 + 2H^+ + 2e^- \Rightarrow H_2O$.

It is assumed that hydrogen does not crossover through the membrane. Any hydrogen flux through the anode diffuser corresponds exactly to the amount of hydrogen required to induce a constant steady-state cell current density J through the oxidation process. For the anode;

$$\dot{n}_H^{A-1} = I = \frac{J}{2F} \tag{5-19}$$

For the cathode, the oxygen flux also corresponds exactly to current flow with zero crossover;

$$\dot{n}_O^{C-1} = \frac{I}{2} \tag{5-20}$$

A flux ratio of a species i in the electrode E denoted α_i^E is defined as the molar flux of species i over the molar flux of oxygen or hydrogen for the cathode or anode denoted as n, respectively.

$$\alpha_i^E = \frac{\dot{n}_i^E}{\dot{n}_n^E} \tag{5-21}$$

Ideally, the rate at which water is generated, $\dot{n}_W^{Gen}$, at the cathode equals the molar flux of oxidised hydrogen. The water flux in the cathode is the sum of the water flux from the anode and the water generated by the cell reaction. Therefore, the fluxes of oxidized and reduced species as well as water fluxes can be related as;

$$I = \dot{n}_H^{A-1} = 2\dot{n}_O^{C-1} = \dot{n}_W^{Gen} = \frac{\dot{n}_W^{C-1}}{1+\alpha_W^A} \tag{5-22}$$

The water flux ratio in the cathode can be related to that for the anode by:

$$\alpha_W^C = -2\left(1+\alpha_W^A\right) \tag{5-23}$$

In the model, both inlet anode and cathode gas streams have been assumed to be saturated with water vapour at a given humidification temperature. The mole fractions of water in the anode and cathode inlet gas streams are given by;

$$y_W^{E-IN} = \frac{p_E^{sat}}{p_E} \tag{5-24}$$

The saturation vapour pressure of water is calculated as [4];

$$\log_{10} p_E^{sat} = -2.1794 + 0.02953T - 9.1837 \cdot 10^{-5} T^2 + 1.4454 \cdot 10^{-7} T^3 \tag{5-25}$$

When the dry inlet gases each with a species molar fraction of y_i^o are humidified with a mole fraction of water, y_W^{E-IN}, the dry mole fractions of the constituent species change, but their ratios relative to hydrogen or oxygen in the anode or cathode, respectively, remain the same,

$$\frac{y_i^\circ}{y_n^\circ} = \frac{y_i^{E-IN}}{y_n^{E-IN}} \tag{5-26}$$

Upon humidification, the new mole fractions still add up to unity for each electrode;

$$y_W^{E-IN} + y_n^{E-IN} + \sum_{i=1}^{n-1} y_i^{E-IN} = 1 \tag{5-27}$$

Rearranging equation 5-27 and substituting it into equation 5-26 yields the humidified mole fraction of a species after the gas is humidified is;

$$y_i^{E-IN} = y_i^\circ \left(1 - y_W^{E-IN}\right) \tag{5-28}$$

For a humidified gas, the ratio of molar flux equals the ratio of mole fractions of different species,

$$\frac{\dot{n}_i^{E-IN}}{\dot{n}_n^{E-IN}} = \frac{y_i^{E-IN}}{y_n^{E-IN}} \tag{5-29}$$

The water fluxes across the electrodes can then obtained as;

$$\dot{n}_W^{E-IN} = \dot{n}_n^{E-IN} \frac{y_W^{E-IN}}{y_n^{\circ}\left(1 - y_W^{E-IN}\right)} \tag{5-30}$$

and for any other species, i,

$$\dot{n}_i^{E-IN} = \dot{n}_n^{E-IN} \frac{y_i^{\circ}}{y_n^{\circ}} \tag{5-31}$$

Stoichiometric ratios can be defined as the ratio of the oxidant or the reductant flux in the inlet to the flux of the oxidant or reductant required to support the current density *J*; $\upsilon_H = \left(\dot{n}_H^{A-IN}\right)/I$ for the anode; $\upsilon_O = \left(\dot{n}_O^{C-IN}\right)/(I/2)$ for the cathode. The inlet flux of species i to the anode is,

$$\dot{n}_i^{A-IN} = I\upsilon_H \frac{y_i^{\circ}}{y_H^{\circ}} \tag{5-32}$$

and to the cathode

$$\dot{n}_i^{C-IN} = \frac{1}{2} I\upsilon_O \frac{y_i^{\circ}}{y_O^{\circ}} \tag{5-33}$$

5.3.2 Channel Flows

The inlet flux of a species to either anode or cathode is equal to the flux of that species through the channel and the flux of that species through the electrode.

$$\dot{n}_i^{E-IN} = \dot{n}_i^{E-CH} + \dot{n}_i^{E-1} \tag{5-34}$$

Substituting equation 5-21 and equations 5-32 and 5-33 respectively into equation 5-34, gives the species flux in the anode as;

$$\dot{n}_i^{A-CH} = I\left(\upsilon_H \frac{y_i^{\circ}}{y_H^{\circ}} - \alpha_i^A\right) \tag{5-35}$$

and in the cathode channel as;

$$\dot{n}_i^{C-CH} = \frac{I}{2}\left(\upsilon_O \frac{y_i^{\circ}}{y_O^{\circ}} - \alpha_i^C \right) \tag{5-36}$$

The total flux in the channel is the sum of that for all species including water, plus the flux of any additional species through the PEM from the opposite electrode (OE);

$$\dot{n}_T^{E-CH} = \dot{n}_W^{E-CH} + \sum_{i=1}^{n} \dot{n}_i^{E-CH} + \sum_{i=1}^{n_{OE}} \dot{n}_i^{OE-1} \tag{5-37}$$

In the current model, if an inert species is assumed not to permeate the membrane, the flux ratio of this species can be reduced to zero, i.e., $\alpha_i^A = 0$ or $\alpha_i^C = 0$, which reduces the additional flux from the opposite.

The mole fraction of a species in the channel can be obtained as

$$y_i^{E-CH} = \frac{\dot{n}_i^{E-CH}}{\dot{n}_T^{E-CH}} \tag{5-38}$$

5.3.3 Gas Transportation in the Electrode Diffusion Layer

It is expected that a gradient in mole fraction across the electrode diffusion layer for all species exists. Diffusion in the diffusion layers is described by the Stefan-Maxwell equation in the model,

$$\frac{dy_i^E}{dz} = RT \sum_i \frac{y_i^E \dot{n}_j^{E-1} - y_j^E \dot{n}_i^{E-1}}{pD_{ij}} \tag{5-39}$$

The species mole fraction at the electrode to membrane interface can be obtained by analytically integrating the equation across the electrode using channel mole fractions. The

pressure-diffusivity term for species pair i and j in the equation can be defined using the Slattery-Bird equation [15],

$$pD_{ij} = a\left(\frac{T}{T_{c,ij}}\right)^{b}\left(M_{ij}\right)^{-1/2}\left(P_{c,ij}\right)^{2/3}\left(T_{c,ij}\right)^{5/6} \tag{5-40}$$

where $M_{ij} = \frac{2M_iM_j}{M_i + M_j}$. $T_{c,ij} = \left(T_{c,i}T_{c,j}\right)^{1/2}$ and $p_{c,ij} = \left(p_{c,i}p_{c,j}\right)^{1/2}$ are the critical properties of the constituent species. In this model,. the pressure-diffusivity product is modified simply by the Bruggeman correction factor $\in$ to account for the porosity and tortuosity of the electrodes in the model [4].

5.3.4 Gas Transportation in the Membrane

To simulate a gas species permeating through the membrane, it is assumed that a diffusive flux of the species across the membrane is driven by a concentration gradient and therefore modelled using Fick's law of diffusion [16]. Carbon monoxide can have a serious degradation effect on the catalyst in an electrode. Its flux is simulated in the model using the binary diffusivity D_{CO-H_2O} of carbon monoxide and water vapour. Applying equation 5-21 to Fick's law, the flux ratio of carbon monoxide to hydrogen in the anode is given as;

$$\alpha_{CO}^{A} = -\frac{pD_{CO-H_2O}}{RT}\frac{1}{\dot{n}_{H_2}^{A}}\nabla y_{CO} \tag{5-41}$$

The variable α_{CO}^{A} is also refined via iteration. The correct value is obtained when the carbon monoxide mole fraction at cathode to membrane interface calculated from membrane side using equation 5-41 equals the carbon monoxide mole fraction calculated from cathode side using equation 5-39.

5.3.5 Semi-empirical Carbon Monoxide Degradation Effect

Although it has received little attention, carbon moxide is known to permeate through the membrane and to consequently degrade the performance of the cathode catalyst layer [13]. Using the model of carbon monoxide transportation in the membrane, the effect on cathode performance is simulated in the model by using a carbon monoxide induced degradation factor, Θ defined as

$$\Theta = \frac{\eta_{act,cath}^{pure} - \eta_{act,cath}^{pois}}{\eta_{act,cath}^{pure}} \tag{5-42}$$

where $\eta_{act,cath}^{pure}$ is the cathodic activation overvoltage with pure hydrogen, and $\eta_{act,cath}^{pois}$ is the activation overvoltage with carbon monoxide contamination.

In a previous experimental study by Qi *et al.* [13], the cathode potential was measured using three different anode feeds; pure H_2, 70% H_2 30% CO_2 with 10 ppm CO, and 70% H_2 30% CO_2 with 50 ppm CO. The cathode potential reflects the sum of the thermodynamic equilibrium potential, the Ohmic overvoltage and the cathodic activation overvoltage. The thermodynamic equilibrium potential and the Ohmic overvoltage are not functions of carbon monoxide contamination. They can be calculated and taken away from the measured value to obtain the cathode activation overvoltage.

The carbon monoxide induced degradation factor is assumed to be a linear function of the interfacial carbon monoxide concentration at any given current density. This is simply due to the fact that the experimental data covered two contaminated fuel feeds only. The first tested fuel was pure H_2 and was only used to determine the cathodic activation overvoltage $\eta_{act,cath}^{pure}$. However, it cannot be used to determine the degradation factor. This is because the carbon dioxide contained in the fuel feed could have some degradation effect on cathode performance due to the water-gas shift reaction at the anode [17]. Such effect in the model is assumed to be constant for any given current density and independent of the carbon monoxide transport due to fuel feed carbon monoxide contamination. The relationship between the cathode-membrane interfacial carbon monoxide concentration and the degradation factor was modelled as;

$$\Theta = \Theta_0 + \mathrm{H} y_{CO}^{\prime C-2} \tag{5-43}$$

where Θ_0 is the water-gas shift induced degradation factor, $y_{CO}^{\prime C-2}$ is the carbon monoxide concentration at cathode to membrane interface in ppm, and H is the gradient of the change in degradation factor with respect to the change in carbon monoxide interfacial concentration.

The gradient H is obtained from the experimental data [13]. It is found to be non-linear with respect to current density as shown in Figure 5-2. The polynomial fit of equation 5-44 was deduced.

$$\mathrm{H} = -0.2056J^3 + 0.3956J^2 - 0.1194J + 0.0430 \tag{5-44}$$

For the straight-line relationship postulated in equation 5-43, the carbon monoxide degradation factor attributable to the water-gas shift reaction Θ_0 is derived from the published results [13] and shown in Figure 5-3. Again, it is found to be non-linear with respect to current density, and the polynomial fit is given in equation 5-45.

$$\Theta_0 = 0.4551J^4 - 1.1161J^3 + 1.2495J^2 - 0.6145J + 0.11 \tag{5-45}$$

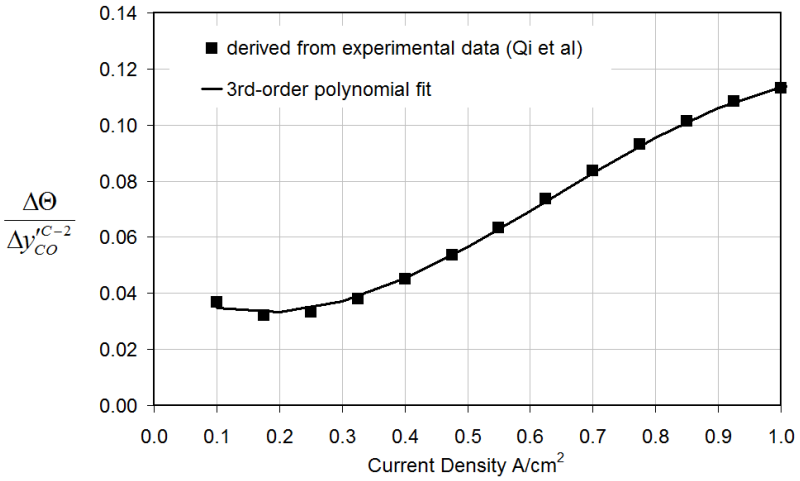

Figure 5-2 Third-order polynomial dependence of H on current density, J

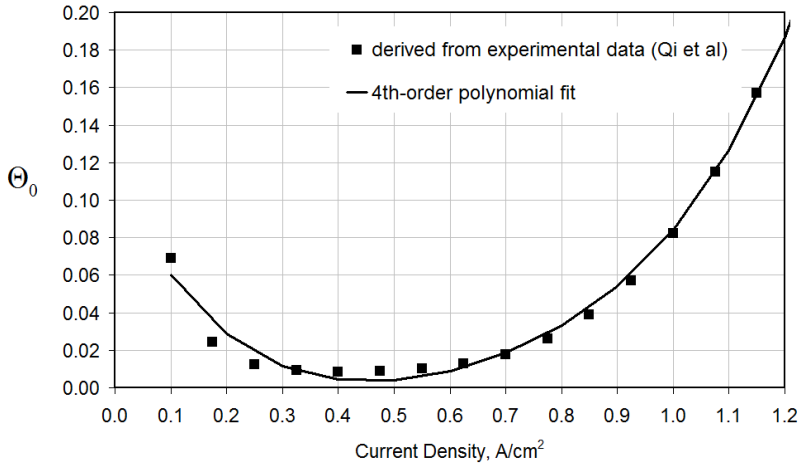

Figure 5-3 Fourth-order polynomial dependence of Θ_0 on current density, J

The total activation overvoltage given by equation 5-1 includes both anode and cathode activation overvoltage, and cannot be decomposed into individual contributions. As such, the Tafel equation given by equation 5-46 was employed to solely simulate the cathode activation overvoltage with a pure H_2 fuel feed, as derived in Chapter 4;

$$\eta_{act,cath}^{pure} = \frac{RT}{\alpha n F} \ln\left(\frac{J_0}{J}\right) \tag{5-46}$$

where the exchange current density J_0 was estimated to be 0.8 mA/cm^2 for the cell from the experimental data obtained by Qi *et al.* [13].

For a 70% H_2 30% CO_2 pre-humidified fuel feed with any level of carbon monoxide contamination, the cathodic activation overvoltage is;

$$\eta_{act,cath}^{pois} = \eta_{act,cath}^{pure}(1+\Theta) \tag{5-47}$$

5.4 Results and Discussions

5.4.1 Overvoltage

Figure 5-4 shows a comparison of calculated cell voltage at varying current density with published experimental results obtained from the Ballard Mark IV [5]. The cell conditions during test and the inputs into the model were as follow; air with 21% of O_2 and 79% of N_2, pure hydrogen fuel supply, 70˚C operating temperature, and 310 kPa operation pressure. The diffusivity correction factor was set to 0.3 and the thickness of both electrodes were set to 250 µm. Oxygen stoichiometry was set to 1.75, and hydrogen stoichiometry set to 1.3. The membrane thickness was 180 µm, while the dry membrane density was assumed to be 1.98 g/cm^3, and its equivalent weight 1100 g/mol. The active cell area was taken to be 50.56 cm^2. The results show that the model prediction agrees well with the experimental results. There is a slight overprediction at 0.4 and 0.5 A/cm^2 which could be due to mass transport limits caused by liquid water accumulation, which is not covered in the current model.

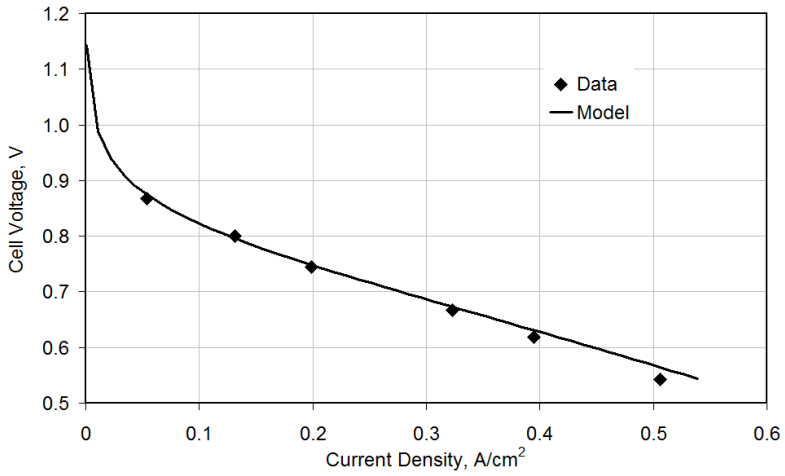

Figure 5-4 Simulated and measured fuel cell performance at 70˚C

Figure 5-5 shows the measured and calculated effects of varying oxygen composition from 21% to 46% and 100% on the cell voltage. The results show that the cell voltage decreases as oxygen composition reduces. This is because the activation overvoltage, which is dominated by cell operation temperature, current density and oxygen concentration at the

membrane to cathode interface, decreases as the availability of oxygen in the supply increases. Such effect has been included in equation 5-1.

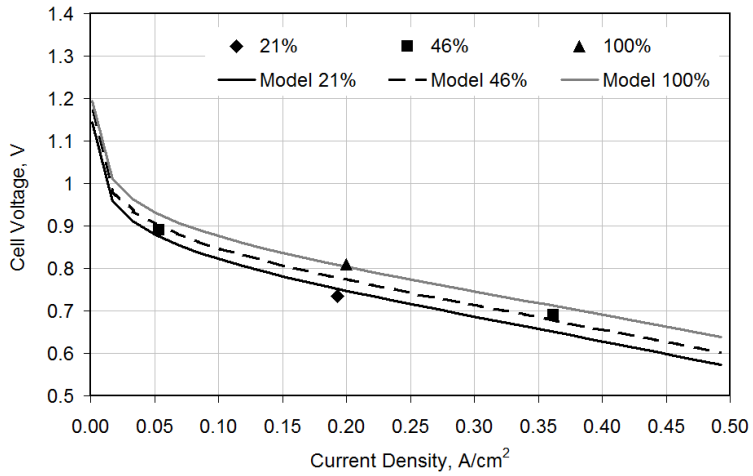

Figure 5-5 Effect of varying oxygen composition on the fuel cell performance

Figure 5-6 shows the measured and calculated effects of different cell operation temperatures on the cell voltage as a function of current density. The figure shows that the cell voltage increases with temperature. The reason of such increase is largely due to the fact that both cell internal electric resistance and activation overvoltage are dependant on cell operation temperature as shown in equation 5-1 and 5-4, respectively. As cell operation temperature increases, both the internal resistance and the activation overvoltage decrease.

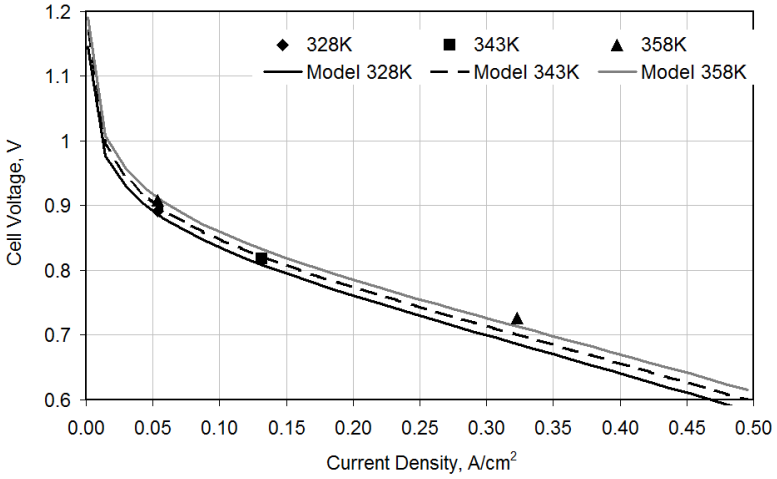

Figure 5-6 Effects of varying temperature on the fuel cell performance; 55˚C (328 K), 70˚C (343 K) and 85˚C (358 K)

There is a noticeable discrepancy between simulated and measured results at the operation temperature of 85˚C; the simulated cell voltage is lower than the measured value. This may be due to the fact that a saturated inlet gas has been used in the model while during the test, the same condition may have been difficult to maintain at the high humidifying temperature [18]. The saturation, hence the relative humidity, has a significant influence towards interfacial oxygen mole fractions and cell activation overvoltage. Figure 5-7 shows the simulated interfacial oxygen mole fractions with 50% and 100% of saturating vapour pressure at 85˚C in the cathode inlet stream. It shows that the oxygen molar fraction at the cathode to membrane interface increases as humidity decreases. Figure 5-8 shows the calculated activation overvoltage as a function of current density with 50% and 100% of saturation pressure achieved at 85˚C. The figure shows that the absolute value of cell activation overvoltage increases as humidification increases. In other words, the effect of less humidification is to decrease the impact of activation overvoltage on the thermodynamic cell voltage.

It is consequently possible to compare the simulated cell voltage under this condition to that obtained from test. Figure 5-9 shows the comparison between the measured and the recalculated overvoltage curve. Compared to the discrepancy in the previous result shown in Figure 5-6, the agreement at 50% saturation vapour pressure is noticeably better.

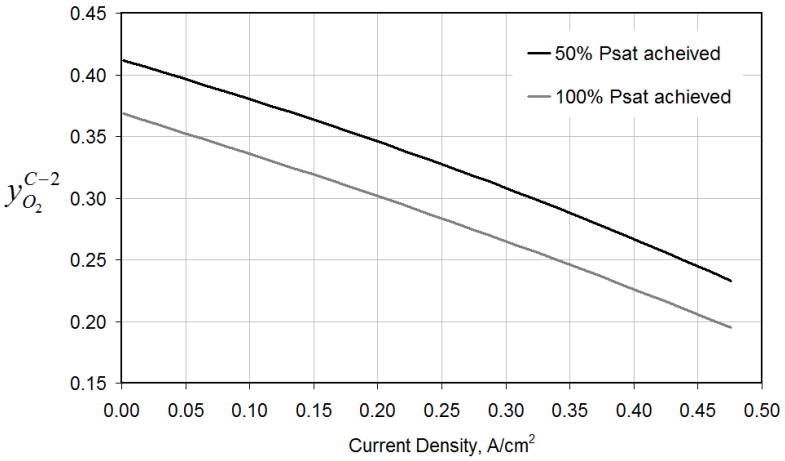

Figure 5-7 Interfacial oxygen mole fractions with 50% and 100% saturation at 85˚C (358 K)

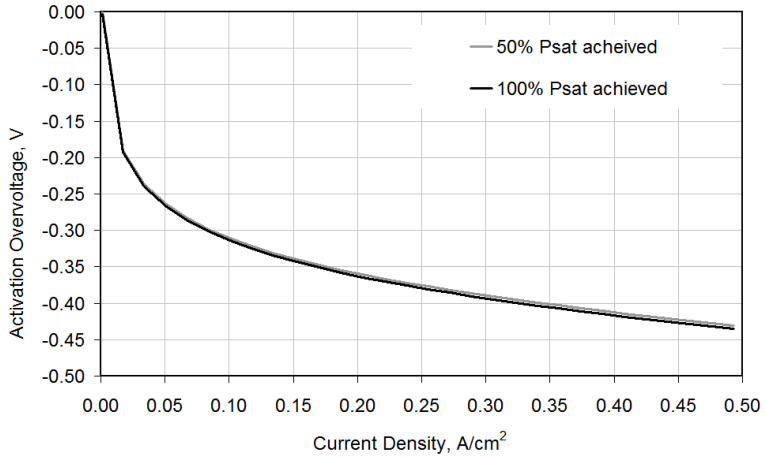

Figure 5-8 Activation overvoltage with 50% and 100% of saturation at 85˚C (358 K)

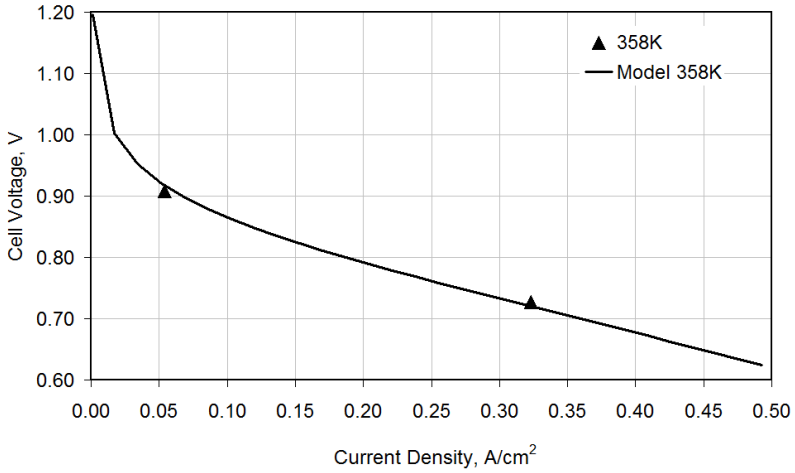

Figure 5-9 Effect of oxygen mole fraction on the fuel cell voltage

Figure 5-10 shows the effects of varying hydrogen composition, 65%, 81% and 100% on cell voltage. Similar to the effect of oxygen variation, the cell voltage decreases with hydrogen composition. This is due to two reasons. First, the thermodynamic equilibrium potential is modelled as a directly proportional function of the square of the hydrogen partial pressure. Correspondingly, any increase in the hydrogen inlet composition results in an increase of the thermodynamic equilibrium. This is because the hydrogen mole fraction gradient is positive through the electrode thickness leading to higher interfacial values.

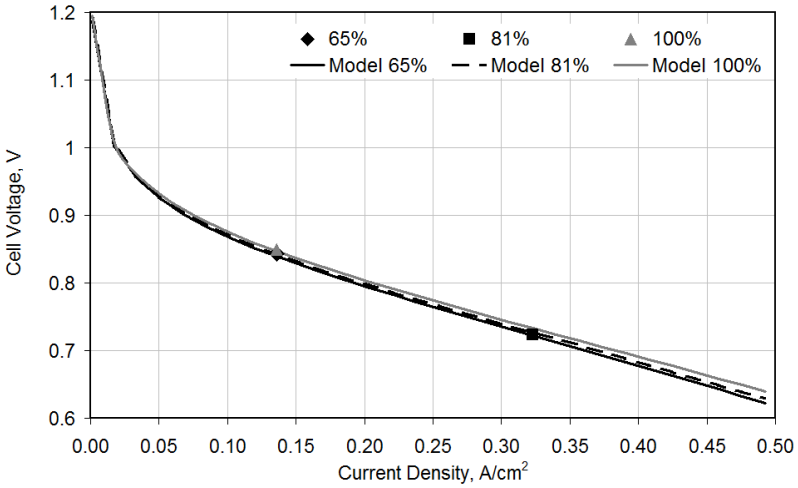

Figure 5-10 Effects of varying hydrogen composition on the fuel cell performance

As discussed in the preceding chapter, the total activation overvoltage is largely characterised by the cathodic oxygen reduction which is slower than the anodic hydrogen oxidation process. The relative insignificance of the anodic activation overvoltage due to fast electrode kinetics verifies the assumption of a constant anodic activation overvoltage, as implied in equation 5-1 for the current density range of interest in Figure 5-8. As such, an increase in the interracial hydrogen partial pressure induces no change in calculations from equation 5-1.

5.4.2 Multi-Component Diffusion

Experimental research on transient performance published by Moore *et al.* [20] indicated that atmospheric concentrations of contaminant gases can degrade the cell performance. Figure 5-11 shows the calculated cathode to membrane interfacial mole fractions at varying current density when the cathode inlet is supplied with dry atmospheric air which contains O_2, N_2, Ar, CO_2, Ne, He, Kr, CH_4, H_2, and N_2O. It shows that the multi-component diffusion model has the potential to take any number of chemical constituents in the atmosphere into account simultaneously.

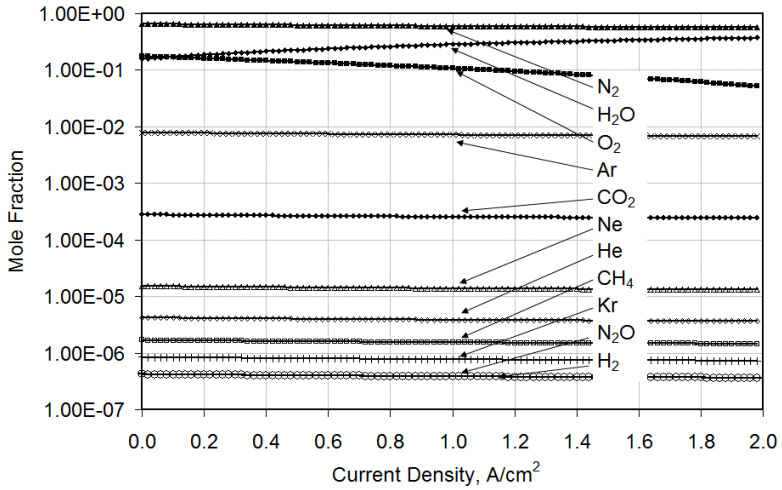

Figure 5-11 Interfacial air constituent mole fractions at cathode-membrane interface

5.4.3 CO Crossover and Contamination

Figure 5-12 shows the calculated cathode potential for fuel feeds with different inlet carbon monoxide concentrations and the experimental results obtained by Qi *et al.* [13]. Both experimental and simulated results were based on a thin 25 µm PEM. The anode catalyst was a platinum-ruthenium alloy applied with a loading of 0.6 mg/cm^2. The cathode catalyst was pure platinum applied with a loading of 0.4 mg/cm^2. The simulated and measured results agree well with pre-humidified fuel feeds of pure H_2, H_2 mixed with 30% CO_2 and 10 ppm CO, and 50 ppm CO. Model predictions with high CO concentrations in the fuel feed are also presented in the figure. The cathode is supplied with pre-humidified air containing 21% O_2 and 79% N_2. It shows the significant losses on the cathode potential with fuel feeds contaminated with high carbon monoxide concentrations.

Figure 5-13 shows the flux ratio of CO to the H_2 across the anode and PEM and current density. The results show that the flux ratio profile increases for all current densities with increasing carbon monoxide content in the inlet gas. This increases the interfacial carbon monoxide concentration at the cathode-membrane interface and results in the greater activation losses observed in Figure 5-12. In general, each curve in Figure 5-13 shows that the CO to H_2 flux ratio decreases with increasing current density.

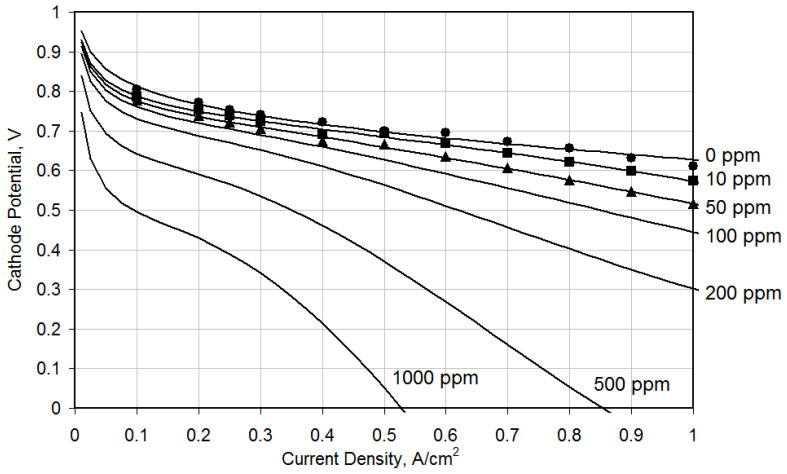

Figure 5-12 CO crossover effects on cathode potential; line: simulated; (●) 0 ppm, measured; (■) 10 ppm, measured; (▲) 50 ppm, measured. For uncontaminated feeds, the pre-humidified anode supply is neat H_2. For contaminated feeds, the pre-humidified anode supply is 30% CO_2/70% H_2.

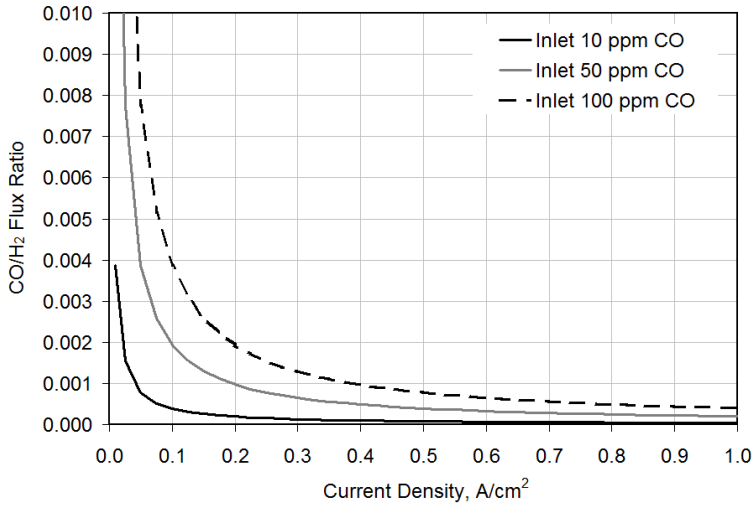

Figure 5-13 CO to H_2 flux ratio for inlet fuel feed CO concentrations of 10 ppm, 50 ppm and 100 ppm.

The experimental results obtained by Qi *et al.* [13] showed that the anode overvoltage was linear and relatively small in relation to the cathode potential. The cathode potential therefore closely characterises the cell potential. Oetjen *et al.* [18], for example, investigated the effect of carbon monoxide poisoning on the overall cell potential with H_2 feeds contaminated up to 250 ppm of carbon monoxide. The experimental results for an anode loaded with platinum-ruthenium catalyst exhibited the similar linear current density to

overvoltage relationships above 0.2 A/cm^2 as those presented in Figure 5-12. However, the overvoltages predicted by the model in Figure 5-12 are generally lower than the experimental results of Oetjen *et al*. This may partially be attributed to the differences in catalytic loading, fuel feed and oxidant supply. The cathode and anode catalysts loadings were 1 mg/cm^2 of pure platinum and platinum-ruthenium, respectively. This is 150% and 67% higher than the catalyst loadings used in the experiments and cited by the model. In addition, Oetjen [2] *et al.* did not use fuel feeds containing carbon dioxide, and the cathode feed was pure oxygen. Both conditions would serve to increase the availability of hydrogen and oxygen at the anode and cathode catalyst sites, and therefore reduce the activation overvoltages.

5.5 Conclusions

A one-dimensional steady-state, low temperature, isothermal, isobaric PEFC model has been developed and applied in this chapter. The model accommodates multi-component diffusion in the porous electrodes and therefore offers the potential to further investigate effects of multi-component transport on cell performance. In this model:

- channel flows were determined using mass balance and algebraic manipulation and derived from predefined initial inlet conditions.
- electrode fluxes are determined by hydrogen oxidation and oxygen reduction with zero reactant crossover.
- gas diffusion through the electrodes is modelled using the Stefan-Maxwell equation.
- catalyst layers were considered as fine dispersion of platinum and platinum-ruthenium at the cathode-membrane and anode-membrane interfaces.
- electrode kinetics have been described using the Butler-Volmer equation. It is assumed that oxygen reduction and hydrogen chemisorption are the rate controlling steps for activation [15].
- membrane transportation in the model considered the water flux in the membrane due to both diffusion and electro-osmotic drag due to proton migration based on the dilute solution treatment proposed by Springer *et al.* [4].
- semi-empirical expressions for activation and Ohmic losses developed by Amphlett *et al.* [5] have been adopted in the model to simulate the overvoltages.

- experimental results published by Qi *et al.* [13] were used to determine the change in cathodic activation overvoltage with carbon monoxide crossover across the membrane.

The simulated results agree well with experimental results of the Ballard Mark IV fuel cell obtained by Amphlett *et al*. Model predictions for fuel feeds contaminated with carbon monoxide agree well with experimental results of Qi *et al.* [13]. The simulated results also showed that the current multi-component PEFC model has the potential to take all chemical constituents in the atmosphere into account simultaneously. The composition of the multi-component gases in each channel can be calculated based on the humidification temperature and the magnitude of the cross-flow that occurs within the cell.

The theoretical framework is at present limited to simulating isobaric and isothermal conditions in a fuel cell. Transport equations based on concentrated solution theory and dilute solution theory are selectively applied in order to determine the distribution of species within the different layers of the PEFC. The next step is to focus on the fundamental modelling theory for electrochemical transport and attempt to demonstrate a common approach to characterise multi-component flows through the different layers of a PEFC. It is acknowledged that liquid water transport has not been systematically considered in the theoretical treatment thus far, but will be addressed later on in the thesis.

5.6 References

1 **Fuller TF, Newman J.** Water and Thermal Management in Solid-Polymer-Electrolyte Fuel Cells. *J. Electrochem. Soc.*, 1993, **140**, 1218-1224

2 **Bernardi DM, Verbrugge MW.** Mathematical Model of a Gas-Diffusion Electrode Bonded to a Polymer Electrolyte. *AIChE J.*, 1991, **37**, 1151-1163

3 **Bernardi DM, Verbrugge MW.** A Mathematical Model of the Solid-Polymer-Electrolyte Fuel Cell. *J. Electrochem. Soc.*, 1992, **139**, 2477-2491

4 **Springer TE, Zawodzinksi TA, Gottesfeld S.** Polymer Electrolyte Fuel Cell Model. *J. Electrochem. Soc.*, 1991, **138**, 2334

5 **Amphlett JC, Baumert RM, Mann RF, Peppley BA, Roberge PR, Harris TJ.** Performance Modeling of the Ballard Mark IV Solid Polymer Electrolyte Fuel Cell. *J. Electrochem. Soc.*, 1995, **142**, 1-8

6 **Yi JS, Nguyen TV.** Multicomponent Transport in Porous Electrodes of Polymer electrolyte fuel cells Using the Interdigitated Gas Distributors. *J. Electrochem. Soc.*, 1999, **146**(1), 38-45

7 **Bradean R, Promislow K.** Transport Phenomena in the Porous Cathode of a Polymer electrolyte fuel cell. *Numer. Heat Transfer*, 2002, **Part A** (42), 121-138

8 **Dhar HP, Christner LG, Kush AK, Maru HC.** Performance Study of Fuel Cell Pt-on-C Anode in Presence of CO and CO2, and calculation of Adsorption Parameters for CO. *J. Electrochem. Soc.*, 1986, **133**(8), 1574-1582

9 **Vogel W, Lundquist L, Ross P, Stonehart P.** The Rate Controlling Step for Electrochemical Oxidation of Hydrogen on Pt in Acid and Poisoning of the Reaction by CO. *Electrochim. Acta*, 1975, **20**, 79-93

10 **Wang J-T, Savinell RF.** Simulation Studies on the Fuel Electrode of a H2-O2 Electrolyte Fuel Cell. *Electrochim. Acta*, 1992, **37**(15), 2737-2745

11 **Springer TE, Rockward T, Zawonzinski TA, Gottesfeld S.** Model for polymer Electrolyte Fuel Cell Operation on Reformate Feed. *J. Electrochem. Soc.*, 2001, **148**(1), A11-A23

12 **Liu P, Logadottir A, Nørskov JK.** Modelling the electro-oxidation of CO and H2/CO on Pt, Ru, PtRu and Pt3Sn. *Electrochim. Acta*, 2003, **48**, 3731-3742

13 **Qi Z, He C, Kaufman A.** Effect of CO in the Anode Fuel on the Performance of PEM Fuel Cell Anode. *J. Power Sources,* 2002, **111**, 239-274

14 **Newman J.** *Electrochemical Systems*, 1991 (Prentice Hall, Englewood Cliffs)

15 **Slattery JC, Bird RB.** Calculation of the Diffusion Coefficient of Dilute Gases and of the Self-diffusion Coefficient of Dense Gases. *AIChE J.*, 1958, **4**, 137-141

16 **Cunningham RE, Williams RJJ.** *Diffusion in Gases and Porous Media*, 1980 (Plenum Press)

17 **de Bruijn FA, Papageorgopoulos DC, Sitters EF, Janssen GJM.** The influence of carbon dioxide on PEM fuel cell anodes. *J. Power Sources*, 2002, **110**, 117-124

18 **Oetjen H-F, Schmidt VM, Stimming U, Trila F.** Performance Data of a Polymer electrolyte fuel cell Using H2/CO as Fuel Gas. *J. Electrochem. Soc.*, 1996, **143**(12), 3838-3842

19 **Davis M W.** *Development and evaluation of a test apparatus for fuel cells.* M.Sc. thesis, Virginia Polytechnic Institute and State University, 2000.

20 **Moore JM., Adcock PL., Lakeman B., Mepsted GO.** The effects of battlefield contaminants on PEMFC performance. *J. Power Sources*, 2000, **85**, 254–260.

6 A Universal Modelling Framework from Fundamental Theory

In this chapter, a mathematical multi-component modelling approach for PEFCs is presented based upon fundamental molecular theory. The aim of this chapter is to demonstrably reconcile the key transport equations used by the historically prominent PEFC models under a single simple universal mechanistic equation. The general transport equation developed here as such describes transport in concentrated solutions without further assumptions and explicitly accommodates multi-species electro-osmotic drag. The objective of the general transport equation is to universally simulate multi-species transport across PFSA and other types of PEMs such as high-temperature polybenzimidazole (PBI) membranes, as well as non-reactive porous fuel cell materials such as the GDL and MPL. To test the developed theory, simulated results are generated using widely available relations for lower-temperature PEFCs (< 120°C) in the literature.

This chapter is presented in five parts. The introduction provides a review of the benchmark modelling philosophies and how they have been applied for PEFC development. The second part presents the newly-developed general transport equation from the theory of molecular transport. The third part establishes the direct links between the developed general transport equation and the key transport equations in the benchmark literature. The fourth part merges the multi-component input model described in the previous chapter and requisite closure relations with the general transport equation for multi-layer PEFC modelling. Finally, the model is applied for numerical validation and to examine the phenomenon of hydrogen crossover.

6.1 Introduction

The literature identifies three common modelling groups that can be classed according to the form of the transport equation applied to model the membrane region. First, we have the models based on the use of the Nernst-Planck equation to describe the transport of hydrogen ions in the membrane. To recall, this equation describes the flux of a single

species due to migration, diffusion and convection. An early example of this was in the model of Ridge *et al.* [1], although they excluded convective fluxes. The most significant use of the Nernst-Planck equation was made by Bernardi and Verbrugge (BV) a few years later [2,3]. Bernardi first presented a relatively simple study identifying the required operating conditions to achieve water balance [4]. Following work first focused on a 1D half-cell model comprising of cathode diffuser, catalyst layer and membrane region [2], and was subsequently extended to a complete 1D fuel cell model [3]. They also make use of the Nernst-Planck equation to model dissolved hydrogen and oxygen transport in the membrane region, and consider the effects of applying back-pressure on the cathode side to maintain water balance. Parallel two-phase flow was also considered, with the liquid-phase velocity in the membrane pores defined using Schlogl's velocity equation. In their work however, they consider the membrane to be thin and assume it to be uniformly hydrated. In reality, competing water transport mechanisms would cause non-uniformity in the water distribution across the membrane region limiting the applicability of this type of model. Cross-interactions between species are also neglected when using the Nernst-Planck equation. Incorporation of structural parameters however allowed their model to make significant predictions; they found that reactions across the cathode catalyst layer were likely to be non-uniform, implying that cost-savings were possible by concentrating catalyst material closer towards the cathode gas diffuser.

The Nernst-Planck approach has been adopted by Pisani *et al.* [5,6,7]. Initially they adopted the BV model and successfully improved the model predictions at higher current densities [5]; the initial BV models did not predict the polarisations at higher current densities caused by cathode flooding very well. Subsequent studies used the improved BV model to analyse the effect of the porous structure of the catalyst layer on cell performance [6], and later work focused on optimising the BV model for faster computation by eliminating non-linear terms [7].

The NP-based BV models have also been adopted by Djilali *et al.* [8,9]. They developed the model to include the effects of heat transfer and included Knudsen diffusion in the electrodes [8]. This research group then used the BV model to conduct a 3D computational analysis of a section of the PEFC. Their model and other such models allowed the effects of geometric parameters of the gas diffusion layer on cell performance to be quantified [9].

The publication of the half-cell BV model [2] coincided with the publication of another significant model presented by Springer *et al.* [10]. The Nernst-Planck equation is a derivative of Dilute Solution Theory (DST) as shown in chapter 4. Another form of DST given by equation 4-13 was used by Springer *et al.* [10] who applied it to describe in part the transport of water across the membrane, assuming that the gradient in chemical potential of water drives a diffusive flux of water across the membrane from cathode to anode. The commonality between the Nernst-Planck based BV models and the Springer *et al.* models is the fact that their key transport equations both belong to DST. The difference is that they both use the derivatives of DST to model the transport of different primary species; hydrogen ions for BV and water for Springer *et al.* [10]. Springer *et al.* modify the DST equation such that the gradient in the chemical potential of water is translated into a gradient in water content per membrane charge site, λ (i.e., per sulphonic end group). The other significant difference is the explicit inclusion of electro-osmotic water drag in the model of Springer *et al.*; an extra term is appended to account for the drag of water by hydrogen ions across the membrane from anode to cathode, as shown in chapter 4. The net result is a counter-directional flux of dragged water and diffusing water in the membrane, setting up a non-uniform water distribution across the membrane thickness. This forms the basis of many 'diffusion' models.

In 1993, Van Nguyen and White adopted the model of Springer *et al.* to simulate heat and mass transfer in 2D [11], acknowledging the counter-directional diffusive and drag fluxes of water across the membrane in 1D. They found that the back-diffusion of water across the cell from cathode to anode was insufficient to keep the membrane well hydrated and therefore optimally conductive, and consequently concluded that anode humidification was necessary under certain operating conditions. Similar studies were conducted by Okada *et al.* [12]. In later work, the basic diffusion-based transport equation 4-13 was modified to account for a pressure-driven convective water flux in the membrane [13]. By this point, the DST-derived diffusion term is reduced to Fick's law and the appended convective term is simply Darcy's law. The resulting transport equation can therefore be classed as being 'semi-composite'. Later modelling efforts by Van Nguyen *et al.* investigated the improvements in cell performance when interdigitated gas distributors were used to separate gas channels into inlet and exit channels and therefore to force flow though the porous electrodes [14]. Following work focused more on improving the modelling of liquid water and considering liquid water saturation explicitly [15]. These studies of Van Nguyen *et al.* have directly

influenced cell design by identifying the regions of the cell where flooding is most likely to occur first.

The water diffusion and drag-based transport equation based on DST has commonly formed the basis of transient models [16,17,18]. Applications have attempted to address again the issues of thermal and water management [19]. The 'semi-composite' approach has also been widely used in the literature [20,21,22,23,24]. Kulikovsky [21] in particular considered the non-linear diffusion of water in the membrane, leading to the identification of co-existing dry and wet regions. Later work has been orientated around determining cell performance under co- and counter-flow configurations with two-phase water, acknowledging counter-flow configurations allow for better internal humidification under certain conditions [22,23].

A few years following the publication of the BV [2-4] and Springer *et al.* [10] models, Fuller and Newman presented an alternative model that used Concentrated Solution Theory (CST) to describe transport in the membrane [25]. This was based upon earlier work where it was illustrated that a multi-component form of CST could be used to describe the transport of a three-species system; water, hydrogen ions and electrolyte membrane [26]. Their model assumed that temperature can change along the length of the gas channel and illustrated that the rate of heat removal from the cell was critical in preventing membrane dehydration. A key aspect of their work was the application of CST to simultaneously model the transport of multiple species without decomposing the transport equation into independent constituents, as done by the DST treatments of BV [2,3] and Springer *et al.* [10], and their derivatives. Also, they illustrated that it was possible to model the membrane system without making the assumption that the system is dilute.

The application of CST for fuel cell modelling has been developed over several lines. Janssen [27] used CST to model the effect of two-phase water transport in the electrodes on the electro-osmotic drag coefficient in the membrane. More recently, two-phase water transport in the membrane was modelled by Weber and Newman, accounting for both liquid and vapour phase water boundary conditions for the membrane [28,29,30]. In both the work of Janssen [27] and Weber and Newman [28-30], the expansion of the key transport equations yields frictional coefficients which account for interactions between species. These coefficients are related to water-phase dependant transport properties such as the electro-

osmotic drag coefficient. While proving useful to predict the water flux in the membrane under two-phase conditions, the models are not able to predict H_2 or oxygen crossover using CST without resorting to Fick's Law. Indeed, Weber and Newman [29] illustrated that Fick's law would be superimposed on to the CST-based two-phase water flux equations to define H_2 and O_2 permeation through the membrane. This eludes the utility of the multi-component nature of CST. Meyers and Newman [31,32,33] however maintained the multi-component nature of CST to model the DMFC, for which fuel crossover is a significant issue.

Other studies have also made use of CST. Wohr *et al.* [34] used it to develop a dynamic model with energy balance. They suggested several ways to improve membrane humidity as a result, including raising the humidifier temperature, increasing GDL porosity and GDL thickness, and finally suggested the use of cooling plates to improve heat removal. Futerko and Hsing applied forms of CST to model water transport in the membrane, focusing more on 2D effects [35,36]. They considered the effect of humidity on membrane resistance [35], and operation without reactant feed humidification [36]. Thampan *et al.* [37] developed a model with a similar approach to Janssen [27] and Weber and Newman [29], concentrating on the conductivity of the membrane at different operating temperatures when the membrane is in contact with water in either liquid or vapour phase.

Other significant models that do not strictly pertain to the categorisations above are mentioned here. Eikerling *et al.* [38] proposed a model based on the assumption that water flux in the membrane is characterised by convection due to capillary pressure and electro-osmotic drag. Key to their model was the use of pore-size distribution data to determine local conductivity and permeability. Meier *et al.* [39] also used the capillary pressure argument to propose a convective flux of water in the membrane and attributed it to causing the non-uniform distribution of water across the membrane. Both these models make use of Darcys law to describe the convective water flux. Baschuk and Li [40] proposed a BV-based model that was orientated to defining equivalent resistances throughout the thickness of the cell. Finally we have the semi-empirical based models of Amphlett *et al.* [41,42]. As discussed, the activation and Ohmic overvoltages are defined initially in these models on a theoretical basis, with characteristic constants grouped and defined using experimental data. These models focus squarely on producing performance curves and exhibit generally good correlation with experimental data. These models provide quick cell performance predictions without applying a systematic treatment of cell-level transport phenomenon.

The above is by no means an exhaustive list of modelling efforts, but aims to identify the Nernst-Planck based BV approach [2,3], the diffusion-based approach of Springer *et al.* [10] and the CST-based approach of Newman *et al.* [25, 26, 28-33]. Further discussions into modelling approaches are given by Weber and Newman [43] and Wang [44].

The purpose of this work is to illustrate that all these three prominent modelling approaches can be related by a multi-species general transport equation, which can be applied to the layers of the PEFC to describe electrochemical transport. In this chapter, a general transport equation is derived and its validity is demonstrated by deriving all three key transport equations in literature (Dilute Solution-based Nernst-Planck, Dilute Solution-based diffusion equation and Concentrated Solution Theory). The general transport equation is then applied to a simple PEFC model. Calculated water content curves obtained using the general transport equation are compared to published data. Finally, the multi-species aspect of the model is used to predict hydrogen crossover through the membrane.

6.2 Theoretical Study

6.2.1 Driving Force Equation

The common form of Concentrated Solution Theory can be traced back to the work of Hirschfelder *et al.* [45]. The total driving force of a general species *i* was defined as

$$d_i = \frac{n_i m_i}{n_T kT}\left[\Lambda_i - \frac{1}{\rho}\nabla p + \frac{1}{\rho}\sum_j n_j \boldsymbol{X}_j\right] \tag{6-1}$$

where

n_i = molecular concentration of species *i*

m_i = molecular mass of species *i*

n_T = total molecular concentration

k = Boltzman constant

T = local temperature

ρ = total density

Λ_i = diffusive flux affinity

$\boldsymbol{X}_j$ = general molecular force acting on species *j*.

The first term in the bracket of equation 6-1 reflects the flux due to diffusion; the second reflects convective flux due to a gradient in total pressure; the final term reflects the interactive flux that is induced because of external fields acting upon the other species in the multi-species system.

Hirschfelder *et al.* [45] suggested that there are three physical contributors to the diffusive flux of a general species *i*; a gradient in electrochemical potential; a gradient in temperature and an additional general flux caused by an external field

$$\Lambda_i = \frac{1}{m_i}\nabla\boldsymbol{\mu}_i + \frac{\overline{\boldsymbol{S}}_i}{m_i}\nabla T - \frac{1}{m_i}\boldsymbol{X}_i \tag{6-2}$$

where

$\nabla\boldsymbol{\mu}_i$ = the gradient in molecular electrochemical potential of the general species *i*

$\overline{\boldsymbol{S}}_i$ = the molecular entropy of the general species *i*.

Substituting equation 6-2 into equation 6-1 yields

$$d_i = \frac{n_i}{n_T kT}\left[\nabla\boldsymbol{\mu}_i + \overline{\boldsymbol{S}_i}\nabla T - \frac{m_i}{\rho}\nabla p - \left(\boldsymbol{X}_i - \frac{m_i}{\rho}\sum_{j=1}^{v} n_j \boldsymbol{X}_j\right)\right] \tag{6-3}$$

The molecular concentration of a general species *i* is defined as $n_i = N_A c_i$ where c_i is the molar concentration, and N_A is the number of molecules per mol of substance, i.e., the Avagadro Number . The total molar concentration is defined as $c_T = n_T / N_A$ and the definition of the Boltzmann constant is $k = R / N_A$ where R is the universal gas constant.

Since the above treatment considers particle-level properties, it is recast into more convenient molar terms by using the Avagadro number. Substitution of these definitions into equation 6-3 gives the total driving force term for a general species *i*;

$$d_i = \frac{c_i}{c_T}\frac{1}{RT}\left[\nabla\mu_i + \overline{S_i}\nabla T - \frac{M_i}{\rho}\nabla p - \left(X_i - \frac{M_i}{\rho}\sum_{j=1}^{v} c_j X_j\right)\right] \tag{6-4}$$

This is the general driving force equation and accounts for the physical conditions that drive overall intermolecular transport including effects due to

- a gradient in electrochemical potential, composed of
  - a gradient in concentration, and
  - a gradient in electric potential
- an overall temperature gradient
- a gradient in total pressure
- a force induced by an external field

6.2.2 Molecular and Thermal Diffusion Equation

From the same work of Hirshfelder *et al.* [45] it is possible to define the general driving force as being the sum of the forces driving molecular diffusion and thermal diffusion

$$d_i = \sum_j \frac{n_i n_j}{n_T^2 D_{ij}}\left(v_j - v_i\right) + \nabla \ln T \sum_j \frac{n_i n_j}{n_T^2 D_{ij}}\left(\frac{D_j^{Th}}{n_j m_j} - \frac{D_i^{Th}}{n_i m_i}\right) \tag{6-5}$$

where

D_{ij} = diffusion coefficient of species *i* in species *j*

v_i = velocity of species *i*

D_i^{Th} = thermal diffusion coefficient of species *i*.

Equation 6-5 is converted from molecular values to molar values using $n_i m_i = \rho_i$ and $n_i = N_A c_i$, giving

$$d_i = \sum_j \frac{c_i c_j}{{c_T}^2 D_{ij}} \left[v_j - v_i + \left(\frac{D_j^{Th}}{\rho_j} - \frac{D_i^{Th}}{\rho_i} \right) \nabla \ln T \right] \tag{6-6}$$

6.2.3 The General Transport Equation

Equation 6-4 describes the physical conditions that induce molecular transport and equation 6-6 reflects the transport that occurs due to the physical drivers. Equating the two equations gives the general transport equation for concentrated solutions.

$$\begin{aligned} & c_i \left[\nabla \mu_i + \overline{S_i} \nabla T - \frac{M_i}{\rho} \nabla p - \left(X_i - \frac{M_i}{\rho} \sum_{j \neq i}^{v} c_j X_j \right) \right] \\ & \quad = RT \sum_j \frac{c_i c_j}{c_T D_{ij}} \left[v_j - v_i + \left(\frac{D_j^{Th}}{\rho_j} - \frac{D_i^{Th}}{\rho_i} \right) \nabla \ln T \right] \end{aligned} \tag{6-7}$$

A species with zero valence can be affected by an external field, for example a field in electric potential set up by an electric current can cause a species with zero valence to be dragged by electro-osmosis due to the flux of hydrogen ions.

The molar flux of a species *i*, $\dot{n}_i$ is defined as $\dot{n}_i = v_i c_i$. When $\nabla P = \nabla T = 0$, equation 6-7 can be simplified and rearranged to give;

$$\dot{n}_i = -\frac{c_T}{c_j} \frac{D_{ij}}{RT} c_i \nabla \mu_i + \frac{c_T}{c_j} \frac{D_{ij}}{RT} c_i \left(X_i - \frac{M_i}{\rho} c_j X_j \right) + c_i v_j \tag{6-8}$$

The first and last terms on the right hand side define diffusion and convection. The middle term is related to electro-osmotic drag flux. When considering the flux of water (species *i*) in the electrolytic membrane (species *j*) where the electrolyte experiences no drag, the electro-osmotic drag flux of water equates to

$$\dot{n}_{w,drag} = \frac{c_w}{c_{mem}} \frac{c_T}{RT} D_{w,mem} X_w \tag{6-9}$$

The electro-osmotic drag ratio ξ_i is now introduced which is the number of molecules of species *i* dragged per hydrogen ion, i.e.,

$$\xi_i = \frac{n_{i,drag}}{n_{H+}} = \frac{c_{i,drag}}{c_{H+}} \tag{6-10}$$

Since the velocity with which water is dragged is equal to the velocity of hydrogen ions that are transported due to the electric field, i.e., $v_{w,drag} = v_{H+}$, this gives;

$$\xi_i = \frac{\dot{n}_{i,drag}}{\dot{n}_{H+}} \qquad \xi_w = \frac{\dot{n}_{w,drag}}{\dot{n}_{H+}} \tag{6-11a,b}$$

Substitution of equation 6-11a,b into equation 6-9 and rearranging provides the general molar force in relation to the electro-osmotic drag ratio of any species *i* and of water as;

$$X_i = \xi_i \dot{n}_{H+} \frac{RT}{D_{i,mem}} \frac{c_m}{c_T c_i} \qquad X_w = \xi_w \dot{n}_{H+} \frac{RT}{D_{w,mem}} \frac{c_m}{c_T c_w} \tag{6-12a,b}$$

Generally, equation 6-12a,b can be applied equally to a multi-species concentrated system because;

- it is derived from a general concentrated solution system
- the electro-osmotic drag characteristics of species *i* alone in the membrane is dependant only upon its transport properties in the membrane (accounted for by $D_{i,mem}$) and the magnitude of the hydrogen ion flux (accounted for by $\dot{n}_{H+}$). The overall electro-osmotic drag induced flux for a species *i* including interactions with other electro-osmotically dragged species is accounted for by the $\frac{M_i}{\rho} \sum_{j \neq i} c_j X_j$ term in equation 6-7.
- electro-osmotic drag is assumed to occur independently of temperature and pressure gradients

Using the derived expression for X_i, the general transport equation, equation 6-7, for concentrated solutions becomes

$$c_i\left[\nabla\mu_i + \overline{S}_i\nabla T - \frac{M_i}{\rho}\nabla p\right] = RT\sum_j \frac{c_i c_j}{c_T D_{ij}}\left[v_j - v_i + \left(\frac{D_j^{Th}}{\rho_j} - \frac{D_i^{Th}}{\rho_i}\right)\nabla \ln T\right] + RT\dot{n}_{H+}\frac{c_m}{c_T}\left(\frac{\xi_i}{D_{i,m}} - \frac{\rho_i}{\rho}\sum_{j\neq i,mem}^{v}\frac{\xi_j}{D_{j,mem}}\right) \tag{6-13}$$

6.3 Theoretical Validation

In both key dilute solution models [2,3,10] and key concentrated solution model [26], 1D temperature effects across the cell were neglected $(\nabla T = 0)$.

$$c_i\left[\nabla\mu_i - \frac{M_i}{\rho}\nabla p\right] = RT\sum_j \frac{c_i c_j}{c_T D_{ij}}\left[v_j - v_i\right] + RT\dot{n}_{H+}\frac{c_m}{c_T}\left(\frac{\xi_i}{D_{i,m}} - \frac{\rho_i}{\rho}\sum_{j\neq i,mem}^{v}\frac{\xi_j}{D_{j,mem}}\right) \tag{6-14}$$

Also, none of these explicitly consider the effect of the overall pressure gradient, hence $\nabla p = 0$.

6.3.1 Dilute Solutions

Fundamentally for a dilute solution the concentration of a general minor solute species *i* is assumed to be significantly lower than that of the solvent species *j*, $c_i << c_j$ and $c_j \approx c_T$. Also, the solvent species experiences no drag, hence $\xi_j = 0$. By substituting these conditions into the equation 6-14 the general transport equation can be reduced to the following for the solute species *i*,

$$\dot{n}_i = -\frac{D_{i,j}}{RT}c_i\nabla\mu_i + \xi_i\dot{n}_{H+} + v_j \tag{6-15}$$

This is the key transport equation for dilute solutions which includes flux due to electro-osmotic drag.

Model of Springer *et al.*

Springer *et al.* [10] consider the transport of water (solute species *i*) in the electrolyte membrane (solvent species *j*). Since the electrolytic membrane is static, $v_m = 0$ and the general transport equation 6-15 can be rearranged to yield the net water flux across the membrane

$$\dot{n}_w = -\frac{D_{w,mem}}{RT} c_w \nabla \mu_w + \xi_w \dot{n}_{H+} \tag{6-16}$$

where the first term on the right hand side describes diffusive flux and is consistent with equation 19 which appears in the work of Springer *et al.* [10]. The second term describes electro-osmotic drag flux and is consistent with equation 18 in that work.

Model of Bernardi and Verbrugge

In the BV models [2,3], the key transport equation is the Nernst-Planck equation and is applied to describe the transport of dissolved hydrogen ions (solute species *i*) in a bulk system consisting of water and electrolytic membrane (solvent species pair *j*) where $\xi_i = 0$. The electrochemical potential of a species is defined as [46]

$$\nabla \mu_i = RT \frac{\nabla c_i}{c_i} + z_i F \nabla \phi \tag{6-17}$$

where F is the Faraday constant, z_i is the valence of species *i* and $\nabla \phi$ is the gradient in electric potential ($V.cm^{-1}$). Substitution into the dilute solution transport equation (6-15) yields the familiar Nernst-Planck equation

$$\dot{n}_i = -\frac{D_{i,j}}{RT} z_i F c_i \nabla\phi - D_{i,j}\nabla c_i + v_j \tag{6-18}$$

where v_j becomes the pore-water velocity in the membrane, which is defined using Schlogl's velocity equation

$$v_j = \frac{\kappa_\phi}{\mu} z_j c_j F \nabla\phi - \frac{\kappa_p}{\mu}\nabla p \tag{6-19}$$

Here, κ_ϕ and κ_p are the electrokinetic and absolute (hydraulic) permeabilities respectively and μ is the viscosity ($g.cm^{-1}.s^{-1}$), not to be confused with the electrochemical potential and ∇p is specifically the hydraulic pressure gradient.

6.3.2 Concentrated Solutions

Newman stated that for a three-species system it is more rigorous to use concentrated solution theory to describe transport [46]. In the treatment of Weber and Newman [29], electro-osmotic drag is implicitly absorbed into frictional coefficients which are related to the diffusion coefficients D_{ij}. Because of this treatment, which is based upon assumptions of marginal currents and marginal chemical potential gradients for water through the membrane, the explicit electro-osmotic drag terms in equation 6-14 reduce to zero $\xi_i = 0$. Consequently substitution into the general transport equation 6-14 leaves the common form of CST which is comparable to the Stefan-Maxwell equation

$$c_i \nabla\mu_i = RT \sum_j \frac{c_i c_j}{c_T D_{ij}} \left[v_j - v_i\right] \tag{6-20}$$

6.4 Model Development

6.4.1 Governing Equations

The validity of the general transport equation given by equation 6-14 can be examined by applying it to model multi-species transport in 1D across the PEFC. This is done in the context of an isothermal model. Equation 6-14 is applied directly to simulate electrochemical transport across the PEM. It is also applied to simulate transport across the GDL without deriving the Stefan-Maxwell equation. In doing so, the ξ_i term reduces to zero as electro-osmotic drag does not occur in the GDL (all species have zero valence). The conditions in the channels of the cell are determined by the multi-component input model presented in the previous chapter. The assumptions of the new model are different to the previous model in the following aspects;

1. the membrane region is characterised as a concentrated solution system with at least three constituent species; water, electrolyte membrane and protons
2. the flux of any additional species can be treated as part of the concentrated solution system, without superimposing an independent flux equation based on Fick's law
3. the diffusion coefficient of protons in the concentrated solution system is characterised solely by its dissolution in water
   - diffusivity in the dry membrane is zero, i.e., $D_{H^+,mem} \cong 0$
   - diffusivity in the water contained in a humidified membrane is non-zero and given by the value determined by Bernardi and Verbrugge [3] $D_{H^+,w} = 4.5\times10^{-5} cm^2/s$
4. for the four species system including hydrogen, the binary diffusion coefficient of the species pair of protons in hydrogen in the membrane region is negligible, $D_{H^+,H_2} \cong 0$
5. Capillary forces in the electrodes are assumed to be negligible and water is assumed to exist in vapour form [47].

A summary of the key equations for the channel, electrode and membrane regions of the cell are given in Tables 6-1, 6-2 and 6-3 respectively. The conditions for the base case are given in Table 6-4. The base case reflects isobaric cell operation at 80˚C where it is assumed that both air and H_2 feeds are fully humidified to the same temperature, with 3-species in the membrane system. The additional case given in Table 5 reflects a 4-species concentrated

solution system with the addition of hydrogen crossover. The $D_{i,mem}$ diffusion coefficients should be regarded as the intra-diffusion coefficient of species *i* in the membrane.

For the four component system, it is assumed that hydrogen crossover leads to the formation of additional water at the cathode catalyst site. Such reaction would produce only heat energy, and not both heat and electrical energy. From a transport perspective, the magnitude of water and oxygen fluxes in the cathode increases, which in the model is reflected by changes in the cathode flux ratios α_i^C; $\alpha_w^C = -2\left(1+\alpha_w^A+\alpha_{H_2,X}\right)$ and $\alpha_O^C = 1+\alpha_{H_2X}$. Similarly, the hydrogen flux in the anode increases $\alpha_{H_2}^A = 1+\alpha_{H_2X}$.

To validate the model against experimental data, calculated hydrogen permeability coefficients for a four-species system are compared to calculations based on *in-situ* measurements of hydrogen crossover. The H_2 permeability coefficients can be calculated as

$$\psi_{H_2}^{perm} = \frac{I_{H_2,X}\, t_{mem}}{p_{H_2}^{CH-A}} \tag{6-21}$$

where the flux rate of hydrogen crossover is calculated as

$$I_{H_2,X} = \frac{J\alpha_{H_2,X}}{2F} \tag{6-22}$$

Species flux in channel *(mol/cm²-s)*	$\dot{n}_i^{E-CH} = \dot{n}_i^{E-IN} - \dot{n}_i^{E-1}$
Species flux through electrode *(mol/cm²-s)*	$\dot{n}_i^E = \alpha_i^E \dot{n}_n^E$ anode: $\dot{n}_H^{A-1} = I$ cathode: $\dot{n}_O^{C-1} = I/2$
Total channel flux *(mol/cm²-s)*	$\dot{n}_{total}^{E-CH} = \sum_{i=1}^{n} \dot{n}_i^{E-CH}$
Channel mole fraction *(-)*	$y_i^{E-CH} = \frac{\dot{n}_i^{E-CH}}{\dot{n}_{total}^{E-CH}}$
Channel concentration *(mol/cm³)*	$c_i^{E-CH} = \frac{p}{RT} y_i^{E-CH}$ -

Table 6-1 Governing equations for channel model based on the multi-component input model in chapter 5

		Reference
Transport Equation	$c_i\left[\nabla\mu_i - \frac{M_i}{\rho}\nabla p\right] = RT\sum_j \frac{1}{c_T D_{ij}}\left[c_i\dot{n}_j - c_j\dot{n}_i\right]$	Equation 6-14
Total concentration *(mol/cm³)*	$c_T = \sum_i c_i$	-
Total pressure *(Pa)*	$p = c_T RT$	-
Pressure-Diffusivity product *(Pa-cm²/s)*	$pD_{ij} = a\left(\frac{T}{T_{c,ij}}\right)^b \left(M_{ij}\right)^{-1/2}\left(P_{c,ij}\right)^{2/3}\left(T_{c,ij}\right)^{5/6}\varepsilon^{3/2}$	[10], [48]

Table 6-2 Governing equations for electrode model

		Reference
Transport Equation	$c_i\left[\nabla\mu_i - \frac{M_i}{\rho}\nabla p\right] = RT\sum_j \frac{c_i c_j}{c_T D_{ij}}\left[v_j - v_i\right] + RT\dot{n}_{H+}\frac{c_m}{c_T}\left(\frac{\xi_i}{D_{i,m}} - \frac{\rho_i}{\rho}\sum_{j\neq i,mem}^{v}\frac{\xi_j}{D_{j,m}}\right)$	Equation 6-14
Molar Volume *(cm³/mol)*	$V = V_{mem} + \lambda V_w$	[29]
Total Concentration *(mol/cm³)*	$c_T = \frac{1}{V} + \sum_{i\neq w,mem} c_i$	-
Partial molar volume of dry membrane *(cm³/mol)*	$V_m = \frac{EW}{\rho_{mem,dry}}$	[29]
Water content per charge site *(-)*	$\lambda = c_w V_{mem}$	-
Water volume fraction in membrane *(-)*	$f_v = \frac{\lambda V_w}{V_{mem} + \lambda V_w}$	[29]
Expanded membrane thickness *(μm)*	$t_{mem} = t_{mem,dry}\left(1 + 0.36\times\frac{\overline{\lambda}V_w}{V_m}\right)$	[29]

Table 6-3 Governing equations for membrane model

		Reference
Temperatures *(K)*	$T_A^{sat} = T_C^{sat} = T_{cell} = 353K$	[10]
PEM Equivalent Weight *(mol/equiv)*	$EW = 1155$	[10]
Dry PEM density *(g/cm^3)*	$\rho_{m,dry} = 1.98$	
Diffusivities *(cm^2/s)*	$D_{w,mem} = 10^{-6}\exp\left[2416\left(\frac{1}{303}-\frac{1}{T}\right)\right] \times\left(2.563-0.33\lambda+0.0264\lambda^2-0.000671\lambda^3\right)$	[10] [3]
	$D_{w,H+} = 4.5\times10^{-5}$	-
	$D_{H+,mem} = 0$	
Electro-osmotic drag ratio *(-)*	$\xi_w = \frac{2.5}{22}\lambda$	[10]
	$\xi_m = 0$	-
	$\xi_{H+} = 0$	-
Dry PEM thickness *(μm)*	$t_m = 175$	[10]
Temperature gradient *(K/cm)*	$\nabla T = 0$	-
Applied pressure gradient *(Pa/cm)*	$\nabla p = 0$	-
Channel pressures	$p^{A-CH} = p^{C-CH} = 303.975kPa$	[10]

Table 6-4 Properties for base-case 3-species (water, electrolyte membrane, protons) concentrated solution membrane system

		Reference
Hydrogen dffusivities *(cm^2/s)*	$D_{H_2,m} = \left(2.2\times10^{-11}f_v + 2.9\times10^{-12}\right) \times\exp\left[\frac{21000}{R}\left(\frac{1}{303.15}-\frac{1}{T}\right)\right] \times45.596\times10^3$	[29], [10]
	$D_{H_2,w} = \frac{24.70\times10^3}{p}\left(\frac{T}{146.55}\right)^{2.334}$	[29]
	$D_{H_2,H+} = 0$	-
Electro-osmotic drag ratio	$\xi_{H_2} = 0$	-
Channel pressures		
(Fig. 3)	$p^{A-CH} = p^{C-CH} = 101.325kPa$	[53]
(Fig. 4, 5)	$p^{A-CH} = p^{C-CH} = 303.975kPa$	-

Table 6-5 Additional properties for 4-species (water, electrolyte membrane, protons, hydrogen) concentrated solution membrane system

6.4.2 Solution Procedure

The diagram below illustrates the solution procedure applied to the overall model for the 4-species concentrated solution system in the membrane region. In the case of the 3-species system, the procedure is simplified as α_{H_2} does not need to be determined. Each iterative step is repeated five times in order to determine the correct thickness of the expanded membrane. The differential transport equations in the three regions of the cell are solved using a Runge-Kutta algorithm.

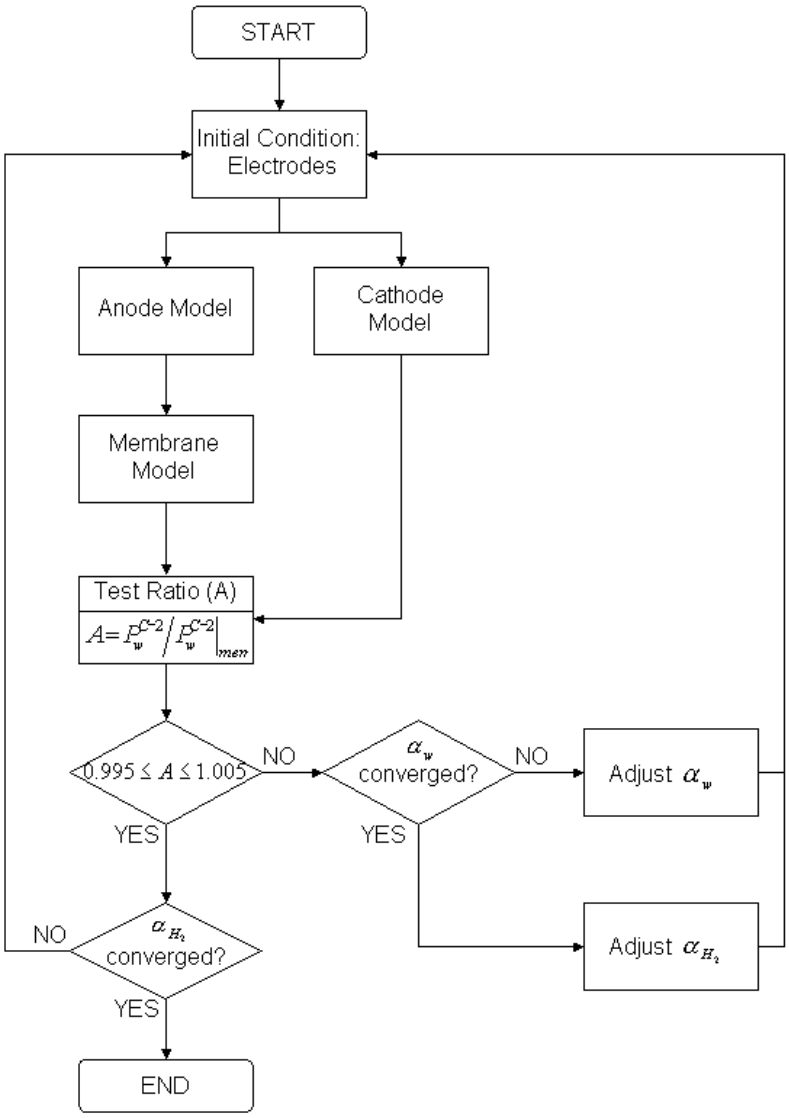

Figure 6-1 Simulation Flowchart

6.5 Results and Discussions

6.5.1 Model Validation

Model-to-Model Validation: 3-Species System

The validity of the multi-species universal transport equation can be tested by comparing simulated water content curves for a 3-species concentrated solution to existing published results. Formation of water at the cathode sets up a concentration gradient across the membrane, allowing for molecular transport from cathode to anode. This is opposed by an electro-osmotic drag flux of water from anode to cathode. Because the electro-osmotic drag flux is directly proportional to current density, the water content at lower current densities is much more uniform. This was illustrated by Springer *et al.* [10]. Although their work only considered the flux of water in a dilute solution, the multi-species model presented here for concentrated solutions should principally predict the same phenomenon.

Figure 6-2 shows simulated water content curves using equation 6-14 for the base condition at four different current densities. The model predicts a relatively uniform water distribution at 0.1 A/cm^2, with a linear fall in water content from 14 molecules per charge site to 11 molecules per charge site. At 0.8 A/cm^2, the water content profile becomes non-linear. At this current density the cathode has 14.8 water molecules per charge site whereas the anode is much drier with less than 3 molecules per charge site.

The water content characteristics are generally consistent with the published results of Springer *et al.* [10]. The concentrated solution theory based approach of equation 6-14 suggests larger gradients in water content than the dilution solution theory approach of equation 6-15 at higher current densities (> 0.2 A/cm^2). The difference is due to the dilute solution theory assumption that the concentration of any minor species is much less than that of the solute. As a consequence, a c_j/c_T factor is missing in the key equation 6-15 for dilute solutions and assumed to be unity, whereas for concentrated solutions it would be less than unity. The effect is to reduce the dominance of c_i in the context of equation 6-15 particularly

at low water contents ($\lambda < 6$), thereby reducing the overall water content throughout the membrane at any position. Overall Figure 6-2 illustrates that the new approach correctly predicts the expected water content profiles at various current densities.

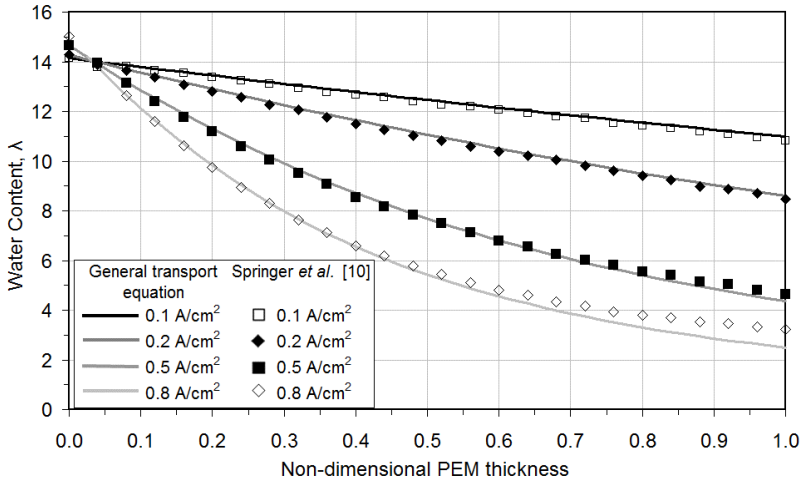

Figure 6-2 Model-to-model validation: simulated membrane water content from the general transport equation (6-14), and from the work of Springer *et al.* [10]

Model-to-Measurement Validation: 4-Species System

The data of Cheng *et al.* [49] is employed in order to validate the model against experimental data. They measured the hydrogen crossover rate in a 4.4 cm^2 experimental fuel cell employing a 50 µm thick PEM operated with fully humidified reactant supplies as 80, 100 and 120˚C and anode back-pressures of 2.02 atm and 3.04 atm. In their work, the hydrogen permeability coefficient is calculated using equation 6-21 where the crossover current I_x is determined directly from the measurement. In the current work, the coefficient is calculated using equations 6-21 and 6-22. This is fundamentally similar to that employed by Cheng *et al*, but modified to be a function of the hydrogen crossover ratio, which is determined by the simulation. The hydrogen partial pressure can be calculated as a function of the anode back-pressure using;

$$p_{H_2}^{CH-A} = \left(\frac{p_{H_2}^{IN-A}}{p_{total}^{IN-A}} \right) \left(\frac{p_{total}^{IN-A} + p_{back-pressure}}{2} \right) \tag{6-23}$$

The data in Table 6-6 compares the calculated hydrogen permeability coefficients obtained from the general transport equation to the experimental data [49]. Hydrogen diffusivities used in the calculation are given in Table 6-5. The calculated hydrogen permeability coefficients are generally within the same order of magnitude as the experimentally-derived values. Table 1 demonstrates that the hydrogen permeability coefficient increases with increasing humidification temperature. This observation can be confirmed from the work reported previously by Weber *et al.* [29]; their data fit suggests that for a PEM with a water volume fraction of 50%, raising the cell temperature from 80 to 120˚C will have the effect of increasing the hydrogen permeability coefficient from 4.52×10^{-11} to 9.36×10^{-11} mol/cm-atm-s.

Humidification Temperature (˚C)		Hydrogen Permeability Coefficient (mol/cm-atm-s)	
		Anode back-pressure	
		3.04 atm	2.02 atm
80	Cheng *et al*	3.87E-11	3.71E-11
	General Transport Equation	1.91E-12	1.15E-11
100	Cheng *et al*	6.13E-11	5.24E-11
	General Transport Equation	1.90E-11	6.38E-11
120	Cheng *et al*	1.04E-10	1.08E-10
	General Transport Equation	1.36E-10	4.23E-10

Table 6-6 Experimental [49] and simulated hydrogen permeability coefficients for a 50 μm polymer electrolyte membrane

6.5.2 Hydrogen Crossover: 4-Species System

The use of thinner membranes in fuel cells can allow for better performance because the uniformity in water content is improved at all current densities. This owes to the shorter molecular transport path for water from cathode to anode and has the overall effect of increasing the proton conductivity of the membrane region [10,50]. With better internal humidification, the need to provide external humidification especially through the anode side can be somewhat mitigated [51]. On the same principal however, the shorter transport path exacerbates the phenomenon of crossover across the membrane. Due to its small molecular

diameter, hydrogen crossover is specifically an important issue in PEFCs. In general such crossover can be impeded by using thicker membranes [52]. The increase in crossover for thinner membranes amounts to unutilised fuel and so reduces the overall cell efficiency. The unused fuel corresponds to an equivalent crossover current density, and the target for future fuel cell vehicles for this is 5 mA/cm^2 or less at 1 atm [53].

To model crossover through the membrane, the conditions of Table 6-5 were applied in addition to the base conditions of Table 6-4 to simulate a four-component concentrated solution system in the membrane region. In the absence of suitable data in the literature, it was assumed that the electro-osmotic drag of hydrogen is negligible.

Figures 6-3 and 6-4 show the relationship between membrane thickness and the net flux ratio of hydrogen across the membrane to oxidised hydrogen at 1 A/cm^2 for 80˚C and 110˚C; 1 A/cm^2 is chosen because it is a typical operation point on the performance curve, and allows for easy translation into an equivalent current density $I_X = \alpha^A_{H_2-X} I$, $J_X = 2FI_X$ and $J = 2FI$. Hence, $\alpha^A_{H_2-X}$ should be 0.005 or less at 1 A/cm^2 when operated at 1 atm.

Figure 6-3 considers the crossover for different thickness at 1 atm. Large stacks ($\geq 10kW$) are likely to operate at higher pressures, and this is considered in Figures 6-4 and 6-5. Figure 6-3 illustrates that the flux ratio drops below 0.005 (crossover current density of 5 mA/cm^2) for membranes thicker than around 30 µm. The flux ratio can be reduced further below 0.001 (1 mA/cm^2) for membranes thicker than 175 µm.

Figure 6-4 shows the crossover for different membrane thicknesses when the cell is operated at 3 atm. For a cell operated at 80˚C, the results show that an increase in thickness from 25 µm to 50 µm yields a 60% drop in the net hydrogen crossover flux ratio and is equivalent to a reduction in the crossover current density of 21.2 mA/cm^2. Increasing the thickness further by a factor of 3.5 from 50 µm to 175 µm yields a 72% drop in the net hydrogen crossover flux ratio, but the magnitude of the drop in the crossover current density is less, at 10.3 mA/cm^2. The results also show that for the given base conditions, the crossover current density only drops below 5 mA/cm^2 above 150 µm for operation at 80˚C.

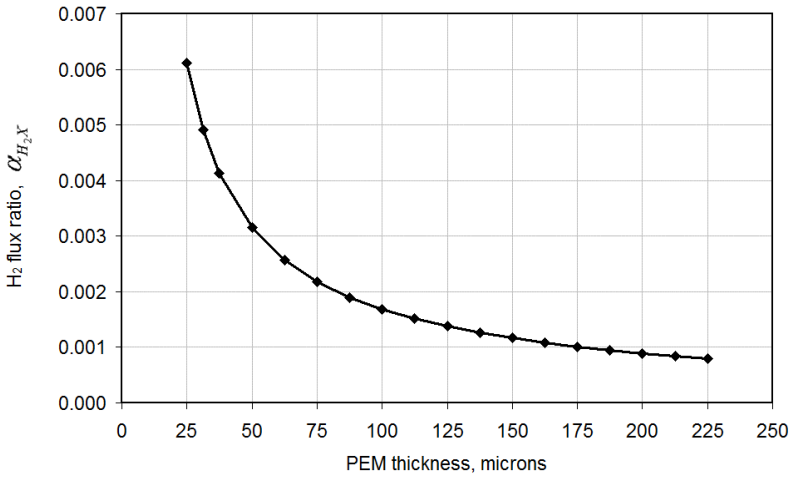

Figure 6-3 Crossover dependence on dry membrane thickness at 1 *atm*

Raising the operating temperature to 110˚C at the same inlet pressures of 3 *atm* induces an increase in crossover. The increase is relatively small for the thin 25 µm membrane at 7% and increases to 32% for a 225 µm membrane. The increase in crossover with temperature can be attributed to the dependence of the hydrogen diffusion coefficient on temperature. When $f_v = 0.5$ in the membrane region, $D_{H_2,mem}$ increases from $2.07\times10^{-6} cm^2/s$ at 80˚C to $6.98\times10^{-5} cm^2/s$ at 110˚C and $D_{H_2,W}$ increases from 0.641 cm^2/s at 353*K* to 0.776 cm^2/s at 110˚C. Due to the increase in H_2 crossover with temperature, the crossover current density only falls below 5 mA/cm^2 when the thickness exceeds 175 µm.

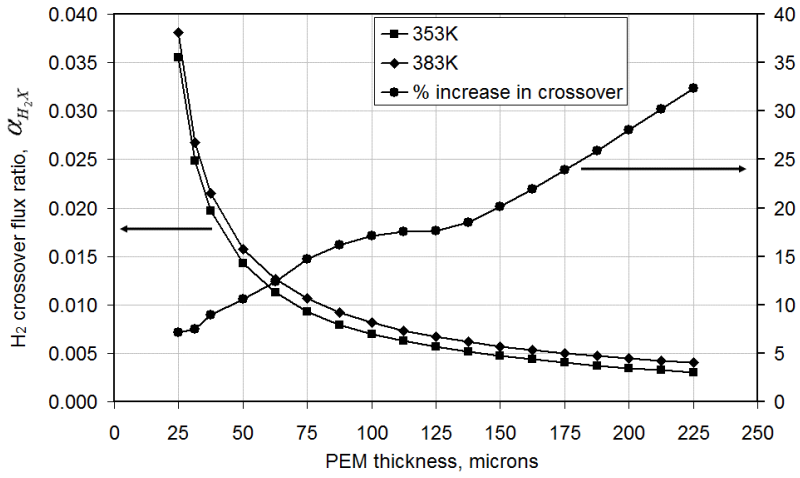

Figure 6-4 H_2 Crossover dependence on dry membrane thickness at 3 *atm* at 80˚C (353 K) and 110˚C (383 K)

Figure 6-5 considers the crossover at all practical current densities for three typical membrane thicknesses. In general, operation at low current densities induces a high rate of hydrogen crossover. As current density increases, the crossover rate decays for all three membrane thicknesses considered. A similar phenomenon was observed in the previous chapter for carbon monoxide crossover through the membrane. The thinner membranes exhibit consistently higher H_2 crossover with respect to current density. The H_2 flux ratio drops below 0.05 after 80 mA/cm^2 for the 175 µm membrane, 150 mA/cm^2 for the 100 µm membrane and 300 mA/cm^2 for the 50 µm membrane. At 1 A/cm^2, the 175 µm membrane exhibits a reduction in the flux ratio below 0.005. The 100 µm membrane is still allowing a hydrogen crossover ratio of 0.007 and the 50 µm membrane allows double that at 0.014.

6.6 Conclusions

The literature identifies three prominent equations to model electrochemical transport across the cell; the Nernst-Planck equation [2,3]; the diffusion equation in terms of chemical potential with an appended term for electro-osmotic drag [10]; and the Stefan-Maxwell type equation from Concentrated Solution Theory [25,26]. The first two pertain to Dilute Solution

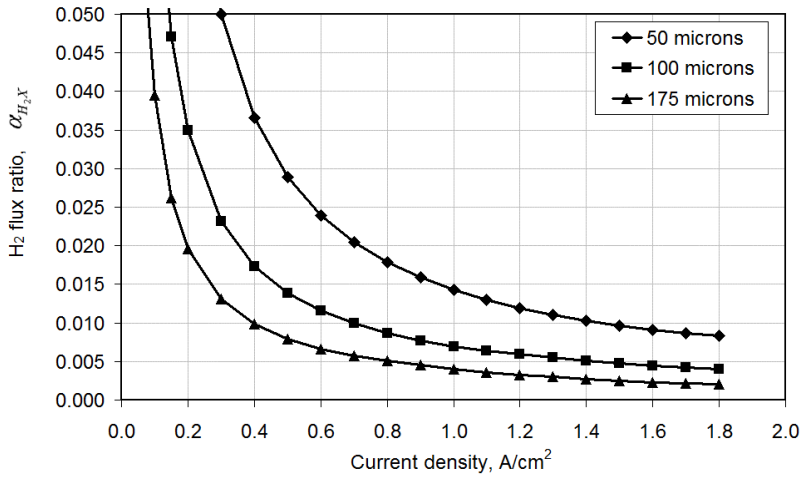

Figure 6-5 H_2 Crossover as function of current density for PEM thicknesses of 50, 100 and 175 µm

Theory and are generally applicable for a solute species when its concentration is assumed to be much less than the solvent concentration. The third directly pertains to Concentrated Solution Theory.

Using founding principals presented by Hirschfelder *et al.* [45], a general transport equation for concentrated solutions has been developed in this work which includes a term for flux due to external fields.

In the context of a fuel cell membrane, it is argued that it is a field in electric potential which causes electro-osmotic drag of constituent species with zero valence due to the hydrogen ion flux that occurs across it. Relative to a constituent species with zero valence, the field in electric potential is effectively an external field, and on this basis is included in the general transport equation to model multi-species electro-osmotic drag.

Theoretical validation has shown that the developed expression is consistent with all three existing key transport equations. This proves that the developed general transport equation can be reduced to the two forms of Dilute Solution Theory (Nernst-Planck equation [2,3] and the diffusion equation with explicit electro-osmotic drag [26]) for fuel cell membrane systems, and to the Stefan-Maxwell form of Concentrated Solution Theory [25,26]. Thus, the work in this chapter is the first to bridge the gap that exists between the different modelling philosophies for transport in the literature.

In the context of a simple fuel cell model, the calculated results using the general transport equation for a three-species system (water, electrolyte membrane, protons) correctly predicts water content profiles that are consistent with published data. The calculated results predict that the water content is marginally less using the developed general transport equation in comparison to the results of Springer *et al.* obtained from Dilute Solution Theory [10]. This is attributed to the dilute solution assumption that $c_{mem} \approx c_T$. Overall, the consistency with the published data shows that the general transport equation correctly predicts the molecular transport of water including electro-osmotic drag flux.

Calculated results for a simple 1D fuel cell with a four-component concentrated solution membrane system (water, electrolyte membrane, protons, hydrogen) give important

results in relation to the crossover of hydrogen across the PEM. The general trend shows an increase in crossover for thinner membranes, and for a fixed membrane thickness a higher crossover at lower current densities.

The results show at 80˚C, 1 *atm* and 1 A/cm^2, the nominal membrane thickness for less than 5 mA/cm^2 equivalent crossover current density is 30 µm. At 3 *atm* and 80˚C, the nominal membrane thickness for the same equivalent crossover current density is about 150 µm, and increases further to 175 µm at 110˚C. At 110˚C, the diffusion coefficient of hydrogen in the membrane and in water increases, facilitating a marginal increase in crossover for all membrane thicknesses. The simulation results also show that at 3 *atm* and 80˚C, a 60% drop in crossover can be achieved by doubling the membrane thickness from 25 µm to 50 µm at 80˚C. A further 72% drop is observed when increasing the membrane thickness further to 175 µm at the same temperature. Thin membranes exhibit consistently higher crossover at all practical current densities compared to thicker membranes. At least a 50% decrease in crossover is achieved at all practical current densities when the membrane thickness is doubled from 50 to 100 µm.

Finally the results for three different membrane thicknesses showed a significant reduction in crossover at all practical current densities for thicker membranes. The calculated results suggest that from the three thicknesses considered, the 175 µm membrane is the most likely to offer equivalent crossover current densities of 5 mA/cm^2 or less in the practical operating range.

Overall, it has been shown that the general transport equation, equation (6-14), can be used to model multi-species transport without the need to superimpose independent transport equations based on dilute solution relations such as Fick's law. It has been shown that this can be done in multi-component form while being able to accommodate electro-osmotic drag flux explicitly. The next step is to apply the general transport equation to simulate two-phase electrochemical transport through the multiple layers of the PEFC.

6.7 References

1 **Ridge SJ, White RE, Tsou Y, Beaver RN, Eisman GA.** Oxygen Reduction in a Proton Exchange Membrane Test Cell. *J. Electrochem. Soc.*, 1989, **136**, 1902-1909

2 **Bernardi DM, Verbrugge MW.** Mathematical Model of a Gas-Diffusion Electrode Bonded to a Polymer Electrolyte. *AIChE J.*, 1991, 37, 1151-1163

3 **Bernardi DM, Verbrugge MW.** A Mathematical Model of the Solid-Polymer-Electrolyte Fuel Cell. *J. Electrochem. Soc.*, 1992, **139**, 2477-2491

4 **Berndardi DM.** Water-Balance Calculations for Solid-Polymer-Electrolyte Fuel Cells. *J. Electrochem. Soc.*, 1990, **137**, 3344-3350

5 **Pisani L, Murgia G, Valentini M, D'Aguanno B.** A Working Model of Polymer Electrolyte Fuel Cells. *J. Electrochem. Soc.*, 2002, **149**, A898-A904

6 **Pisani L, Murgia G, Valentini M, D'Aguanno B.** Analytical Pore Scale Modelling of the Reactive Regions of Polymer Electrolyte Fuel Cells. *J. Electrochem. Soc.*, 2003, **150**, A1549-A1559

7 **Murgia G, Pisani L, Valentini M, D'Aguanno B.** Electrochemistry and Mass Transport in Polymer Electrolyte Fuel Cells, I. Model. *J. Electrochem. Soc.*, 2002, **149**, A31-A38

8 **Djilali N, Lu D.** Infuence of heat transfer on gas and water transport in fuel cells. *Int. J. Therm. Sci.*, 2002, **41**, 29-40

9 **Berning T, Djilali N.** Three-dimensional computational analysis of transport phenomena in a PEM fuel cell – a parametric study. *J. Power Sources*, 2003, **124**, 440-452

10 **Springer TE, Zawodzinski TA, Gottesfeld S.** Polymer Electrolyte Fuel Cell Model. *J. Electrochem. Soc.*, 1991, **138**, 2334-2342

11 **Nguyen TV, White RE.** A Water and Heat Management Model for Proton-Exchange-Membrane Fuel Cells. *J. Electrochem. Soc.*, 1993, **140**, 2178-2186

12 **Okada T, Xie G, Meeg M.** Simulation for water management in membranes for polymer electrolye fuel cells. *Electrochim. Acta*, 1998, **43**, 2141-2155

13 **Yi JS, Nguyen TV.** An Along-the-channel Model for Proton Exchange Membrane Fuel Cells. *J. Electrochem. Soc.*, 1998, **145**, 1149-1159

14 **Nataranjan D, Nguyen TV.** A Two-Dimensional, Two-Phase, Multicomponent, Transient Model for the Cathode of a Proton Exchange Membrane Fuel Cell Using Conventional Gas Distributors. *J. Electrochem. Soc.*, 2001, **148**, A1324-A1335

15 **Nataranja D, Nguyen TV.** Three-dimensional effects of liquid water flooding in the cathode of a PEM fuel cell. *J. Power Sources*, 2003, **115**, 66-80

16 **van Bussel HPLH, Koene FGH, Mallant RKAM.** Dynamic model of solid polymer fuel cell water management. *J. Power Sources*, 1998, **71**, 218-222

17 **Siegel NP, Ellis MW, Nelson DJ, von Sparkovsky MR.** A two-dimensional computational model of a PEMFC with liquid water transport. *J. Power Sources*, 2004, **128**, 173-184

18 **Chen F, Su Y-G, Soong C-Y, Yan W-M, Chu H-S.** Transient Behaviour of water transport in the membrane of a PEM fuel cell. *J. Electroanal. Chem.*, 2004, **566**, 85-93

19 **Yan W-M, Chen F, Wu H-Y, Soong C-Y, Chu H-S.** Analysis of thermal and water management with temperature-dependant diffusion effects in membrane of proton exchange membrane fuel cells. *J. Power Sources*, 2004, **566**, 85-93

20 **Rowe A, Li X.** Mathematical modelling of proton exchange membrane fuel cells. *J. Power Sources*, 2001, **102**, 82-96

21 **Kulikovsky AA.** Quasi-3D Modeling of Water Transport in Polymer Electrolyte Fuel Cells. *J. Electrochem. Soc.*, 2003, **150**, A1432-A1439

22 **Ge S-H, Yi B-L.** A mathematical model for PEMFC in different flow modes. *J. Power Sources*, 2003, **124**, 1-11

23 **Sun H, Liu D, Guo L-J.** PEM fuel cell performance and its two-phase mass transport. *J. Power Sources*, 2005, **143**, 125-135

24 **Yu X, Xhou B, Sobiesiak A.** Water and thermal management for Ballard PEM fuel cell stack. *J. Power Sources*, *2005, **147**, 184-195*

25 **Fuller TF, Newman J.** Water and Thermal Management in Solid-Polymer-Electrolyte Fuel Cells. *J. Electrochem. Soc.*, 1993, **140**, 1218-1225

26 **Fuller TF, Newman J.** A Concentrated Solution Theory Model of Transport in Solid-Polymer-Electrolyte Fuel Cells. *The Electrochemical Society Proceeding Series* 1989, **PV 89-14**, 25-38

27 **Janssen GJM.** A Phenomenological Model of Water Transport in a Proton Exchange Membrane Fuel Cell. *J. Electrochem. Soc.*, 2001, **148**, A1313-A1323

28 **Weber AZ, Newman J.** Transport in Polymer-Electrolyte Membranes, I. Physical Model. *J. Electrochem. Soc.* 2003, **150**, A1008-A1015

29 **Weber AZ, Newman J.** Transport in Polymer-Electrolyte Membranes, II. Mathematical Model. *J. Electrochem. Soc.*, 2004, **151**, A311-A325

30 **Weber AZ, Newman J.** Transport in Polymer-Electrolyte Membranes, III. Model Validation in a Simple Fuel-Cell Model. *J. Electrochem. Soc.*, 2004, **151**, A326-A339

31 **Meyers JP, Newman J.** Simulation of the Direct Methanol Fuel Cell, I. Thermodynamic Framework for a Multicomponent Membrane. *J. Electrochem. Soc.*, 2002, **149**, A710-A717

32 **Meyers JP, Newman J.** Simulation of the Direct Methanol Fuel Cell, II. Modelling and Data Analysis of Transport and Kinetic Phenomenon. *J. Electrochem. Soc.*, 2002, **149**, A718-A728

33 **Meyers JP, Newman J.** Simulation of the Direct Methanol Fuel Cell, III. Design and Optimisation. *J. Electrochem. Soc.*, 2002, **149**, A729-A735

34 **Wohr M, Bolwin K, Schnurnberger W, Fischer M, Neubrand W, Eigenberger G.** Dynamic Modelling and Simulation of a Polymer Membrane Fuel Cell including Mass Transport Limitation. *Int. J. Hydrogen Energ.*, 1998, **23**, 213-218

35 **Futerko P, Hsing I-M.** Two-dimensional finite-element method study of the resistance of membranes in polymer electrolyte fuel cells. *Electrochim. Acta*, 2000, **45**, 1741-1751

36 **Hsing I-M, Futerko P.** Two-dimensional simulation of water transport in polymer electrolyte fuel cells. *Chem. Eng. Sci.*, 2000, **55**, 4209-4218

37 **Thampan T, Malhotra S, Tang H, Datta R.** Modelling of Conductive Transport in Proton-Exchange Membranes for Fuel Cells. *J. Electrochem. Soc.*, 2000, **149**, 3242-3250

38 **Eikerling M, Kharkats YI, Kornyshev AA, Volfkovich YM.** Phenomenological Theory of Electro-osmotic Effect and Water Management in Polymer Electrolyte Proton-Conducting Membranes. *J. Electrochem. Soc.*, 1998, **145**, 2684-2699

39 **Meier F, Eignerberger G.** Transport Properties for the modelling of water transport in ionomer membranes for PEM-fuel cells. *Electrochim. Acta,* 2004, **49**, 1731-1742

40 **Baschuk JJ, Li X.** Modelling of polymer electrolyte membrane fuel cells with variable degrees of water flooding. *J. Power Sources*, 2000, **86**, 181-196

41 **Amphlett JC, Baumert RM, Mann RF, Peppley BA, Roberge PR.** Performance Modelling of the Ballard mark IV Solid Polymer Electrolyte Fuel Cell. *J. Electrochem. Soc.*, 1995, **142**, 1-8

42 **Mann RF, Amphlett JC, Hooper MAI, Jensen HM, Peppley BA, Roberge PR.** Development and application of a generalised steady-state electrochemical model for a PEM fuel cell. *J. Power Sources*, 2000, **86**, 173-180

43 **Weber AZ, Newman J.** Modelling in Polymer-Electrolyte Fuel Cells. *Chem. Rev.*, 2004, **104**, 4679-4726

44 **Wang CY.** Fundamental Models for Fuel Cell Engineering. *Chem. Rev.,* 2004, **104**, 4727-4766

45 **Hirschfelder JO, Curtiss CF, Bird RB.** *Molecular Theory of Gases and Liquids*, 1964 (John Wiley & Sons, Inc., New York)

46 **Newman J.** *Electrochemical Systems*, 1973 (Prentice-Hall, Inc., Englewood Cliffs, New Jersey)

47 **Wang ZH, Wang CY, Chen KS.** Two-phase flow and transport in the air cathode of proton exchange membrane fuel cells. *J. Power Sources*, 2001, **94**, 40-50

48 **Slattery JC, Bird RB.** Calculation of the Diffusion Coefficient of Dilute Gases and of the Self-diffusion Coefficient of Dense Gases. *AIChE J.*, 1958, **4**, 137-141

49 **Cheng X, Zhang J, Tang Y, Song C, Shen J, Song D, Zhang J.** Hydrogen Crossover in High-Temperature PEM Fuel Cells. *J. Power Sources*, 2007, **167**, 25-31

50 **Freire TJP, Gonzalez ER.** Effect of membrane characteristics and humidification conditions on the impedence response of polymer electrolyte fuel cells. *J. Electroanal. Chem.*, 2001, **503**, 57-68

51 **Sena DR, Ticianelli EA, Paganin VA, Gonzalez ER.** Effect of water transport in a PEFC at low temperatures operating with dry hydrogen. *J. Electranal. Chem.*, 1999, 477, 164-170

52 **Matsuyama H, Matsui K, Kitamura Y, Maki T, Teramoto M.** Effect of membrane thickness and membrane preparation condition on facilitated transport of CO2 through ionomer membrane. *Sep. Purif. Technol.*, 1999, **17**, 235-241

53 **US Department of Energy.** *Hydrogen, Fuel Cells & Infrastructure Technologies Program*, 2005

7 A Universal Approach to Multi-Layer Two-Phase Modelling through the General Transport Equation

A mathematical multi-layer, multi-species two-phase modelling framework for polymer electrolyte fuel cells (PEFCs) is presented in this chapter using the general transport equation. The general transport equation was developed in the previous chapter and applied to bridge the gap that exists between the benchmark modelling philosophies in the literature for transport across the PEFC. In this chapter, the general transport equation is applied with Darcy's law to characterise water transport and water uptake through the porous and quasi-porous layers of a PEFC under single- and two-phase operating conditions. The characteristic transport equations and available material properties from the literature are then translated into a single-cell fuel cell model which is implemented using the Object Modelling Technique (OMT). The PEFC model is applied to predict and validate the net water transport ratio and water content under a range of operating conditions. The numerical model exhibits good agreement with experimental data under both vapour- and liquid-equilibrated conditions.

This chapter is presented in five parts. The first provides a general review of the treatment of two-phase flow in the fuel cell modelling literature and a discussion of the key concepts. The second part presents the developed system of equations for multi-component two-phase flow based on the general transport equation and Darcy's law. The third part discusses the auxiliary equations adopted to simulate two-phase transport while the fourth describes the structure of the model, programmed using the OMT concept. The fifth part presents the results of the model validation, which is carried out against data from three independent experimental test cases from the literature.

7.1 Introduction

The different layers of a complete fuel cell assembly can be classed as being either porous or quasi-porous media. The gas diffusion layer (GDL), the micro-porous layer (MPL) and to an extent the catalyst layer (CL) can all be classed as porous media while the PEM can

be classed as a quasi-porous medium. The GDL, MPL and CL exihibit definite porous structures under dry or liquid-infiltrated conditions whereas the PEM is generally impermeable to bulk gas flow yet can behave like a porous material when liquid water infiltrates its polymer structure. Since two-phase conditions can potentially affect both types of media under fuel cell operating conditions, it is possible to consider two-phase transport as a common fundamental process that is theoretically governed by modes of diffusion, convection and in the case of the PEM by electro-osmotic drag. The physical differences between porous and quasi-porous media and the mechanisms by which two-phase flow can propagate within them are important and have to be considered as well to fully understand water transport in a PEFC.

A great deal of effort has already been spent to model transport phenomenon in PEFCs [1,2]. The earlier benchmark models developed around the early 1990's focused mainly on establishing a fundamental understanding of the internal transport mechanisms in the GDLs and the PEM [3,4,5]. In essence, these models selectively modelled diffusion, convection or electro-osmotic drag as the main modes of water transport using forms of concentrated solution theory or dilute solution theory, as discussed in the previous chapter. These were single-phase models that did not rigorously account for the effect that the simultaneous presence of water vapour and liquid water can have on water transport across a layer, water uptake in the PEM and therefore cell performance.

Within a working cell, there are actually a multitude of interdependent phenomenological processes that occur which govern cell performance. Fuel cell models over the years have been developed and adapted accordingly but in doing so have had to apply simplifying assumptions and/or spatial limits to the modelling treatment. Without some of these assumptions, developers run the risk of creating models that are difficult to solve numerically, computationally expensive and therefore impractical to use for proper fuel cell development. However, the assumptions that are made and the way in which they are applied are quite often different and as such have resulted in a multitude of numerical models. The following brief review focuses on how two-phase transport has been handled in the fuel cell modelling literature and the underlying assumptions that have been made. Models for the porous media are discussed first (GDL, MPL, CL), followed by quasi-porous media (PEM).

Fuel cell models explicitly dealing with two-phase transport phenomenon began to appear around the late 1990's [1,2]. In modelling terms, the problem of two-phase transport was mainly prescribed to the cathode CL and the cathode GDL because of the fact that it is these regions where product water forms first and has to be removed from to prevent cell flooding. In order to model two-phase water transport in porous fuel cell media, it is assumed that the internal porous network can be approximately treated as a collection of non-connected tortuous capillary tubes, where capillary-driven flow is governed by the difference between gas and liquid phase pressures. The principal modes of transport are still diffusion and convection but a material-specific relationship is also required to define the level of liquid-phase saturation within a pore as a function of the capillary pressure.

One prominent method that established a two-phase treatment based on the capillary-tube scheme is now commonly known as the multi-phase mixture model, developed by Wang and co-workers [6,7,8,9,10,11,12,13]. The multi-phase mixture approach is based on conservation equations for mass, energy, charge, momentum and species, the latter two of which accommodate convection and single-species diffusion respectively through Darcy's law and Fick's law. The physical properties of the multi-phase flow infiltrating the porous medium such as density, concentration, velocity and viscosity are calculated based on the assumption that the flow can be treated as a chemical mixture. As such, the mixture properties and the effective diffusion coefficients are calculated based on the local level of saturation [7]. This method has been translated into a three-dimensional model and has progressively elucidated the potential effects of operating parameters on two-phase transport in porous fuel cell media such as reactant stoichiometry and humidification [10,13]. Other subsequent multi-dimensional models reported by Birgersson *et al.* [14] and Djilali and co-workers [15,16] have been based on the same fundamental principals of mass, energy, charge, momentum and species conservation but treat the gas phase and liquid phase separately and describe multi-component diffusion for gas-phase transport in Stefan-Maxwell forms. Acosta *et al.* focused on the functional form of the capillary pressure-saturation relationship, noting a hysteresis in water retention characteristics of GDLs during drainage and imbibition [17]. Their multi-dimensional model treats gas and liquid phases separately, accounting for convection using an extended form of Darcy's law and Fick's law to describe diffusion for each gas component individually.

Treatments based on Darcy's law and Fick's law appear elsewhere too. It is known through experimental studies that two-phase transport can occur as a transient phenomenon within a working cell; the level of saturation within a fuel cell GDL for example can change with respect to time under constant current conditions [18]. In order to model two-phase transients, Ziegler *et al.* focused on simulating cyclo-voltammograms and demonstrated that mass transport limitations can increase because of the time-dependant accumulation of water on the cathode side of a working cell [19]. Their modelling treatment is one-dimensional and multi-component diffusion and gas-phase pressure drops in the GDLs are neglected. Single-component gas-phase diffusion and liquid-phase convection in the GDL are described using Fick's law and Darcy's law respectively.

Natarajan and Van Nguyen [20] and Nam and Kaviany [21] applied another approach to model two-phase transport. They assumed that liquid phase flow across the GDL is driven by a gradient in liquid saturation rather than the phase pressure gradient directly. This treatment is based on a previous modelling-based study of steam injection in dry porous media [22]. Here, Darcy's law is modified to become a function of the gradient in liquid saturation. The capillary pressure-saturation relationship is translated into a differential form and applied through a capillary diffusivity term. Diffusion in vapour-phase is either modelled in single-component form using Fick's law [21,27] or in multi-component form using the Stefan-Maxwell equation [20]. Mazumader and Cole [23,24] and Van Nguyen and co-workers [25,26] have applied the concept of capillary-driven flow in multi-dimensional modelling frameworks based on the continuity equations by using an additional relationship for the conservation of liquid water. The method has also been adopted by McKay *et al.* to predict the transients of liquid water accumulation in the GDLs of a fuel cell stack for embedded real time control [27].

The relationship between liquid-phase saturation and capillary pressure is an important one for fuel cell modelling and varies from material to material. It depends upon a number of physical factors including the porosity of the material, its absolute permeability, the hydrophobicity of internal surfaces, internal pore radii, material compression and also the viscosity of the infiltrating fluid. Because this relationship was not defined in the past for porous fuel cell materials the Leverett J-function was often adopted, which was originally developed in petroleum engineering as a generic technique to characterise saturation in isotropic soil beds with uniform wettability [28]. In fact the Leverett-based approach has

been widely adopted in many of the two-phase models above and is still commonly applied because it is simple to use and provides a superficial indication of the level of saturation in the porous layers of a fuel cell. To address the lack of rigour in the Leverett-based approach for fuel cell modelling purposes, other semi-empirical fits have been developed in recent years for specific commercially-available porous fuel cell media [17,25,26,29,30]. These studies have focused more on understanding the physical characteristics of modern porous fuel cell layers [29], analysing the effect of the true functional form of the capillary pressure-saturation relationship on two-phase transport [25,26] and the hysteresis during and drainage and imbibition [17,31]. GDLs are treated with polytetrafluoroethylene (PTFE) or fluorinated ethylene propylene (FEP) to ensure that its internal pores are hydrophobic, thereby mobilising any liquid water that enters or accumulates within it. However, the hysteresis demonstrates that the hydrophobising agent is heterogeneously dispersed within the GDL, leaving a porous network which is partially hydrophobic and partially hydrophilic. As such, once a GDL is infiltrated with liquid water it may not be easily removed from certain hydrophilic pores. On a similar note, experiment-based studies of commercial GDLs conducted by Van Nguyen and co-workers have concluded that low hydrophilic porosity is indeed a desirable property for high fuel cell performance [26] but that some hydrophilic porosity has to exist to effectively conduct liquid water away from regions that are already flooded [32]. Overall, these observations illustrate that internally the GDL can be a heterogeneous material with complex water transport characteristics.

Modern fuel cells employ a bi-layer assembly on either side of the catalyst-coated membrane (CCM) which contains both the GDL and the MPL. Fundamentally, the MPL and GDL can have a common carbon-based substrate; the difference is that the MPL is usually treated with a higher level of hydrophobising agent. In a working cell the MPL sits between the GDL and CL and can help control the direction in which liquid water within the cell is transported under certain operating conditions [11]. The MPL can therefore help improve cell performance by reducing the liquid water saturation in the cathode GDL [33]. In terms of modelling, because the MPL is a porous medium two-phase transport can be treated in the same manner as the GDL, but consideration has to be given to the fact that capillary flow will affect its saturation characteristics differently because its physical properties will be different.

The treatment of the CL is complex because there are two phenomenological processes occurring simultaneously; potentially two-phase transport and electro-reduction in

the cathode CL or electro-oxidation in the anode CL. The detailed mathematical models that have been generated to consider these processes have usually focused on just the cathode side of the cell [26,34,35,36,37,38]. In multi-layer fuel cell models the CL is often treated as a thin interface.

The PEM plays a central role in water transport and is also affected by two phase phenomenon. Most models assume that the PEM operates under a vapour-equilibrated mode and do not systematically consider the effect of liquid water coming into contact with a boundary. This treatment has not changed significantly in the modelling literature as evident in almost all multi-layer fuel cell models referenced above and others [39,40,41,42]. Water transport is predominantly modelled by adopting one of three equations; the Nernst-Planck equation as established by Verbrugge and co-workers, [4,43,44,45,46]; the diffusion equation in terms of chemical potential with an appended term for electro-osmotic drag, as established by Springer *et al*. [3]; and the multi-component Stefan-Maxwell equation as established by Fuller and Newman [5]. As discussed in the previous chapter, the first two pertain to dilute solution theory and are generally applicable for a solute species when its concentration is assumed to be much less than the solvent concentration, while the third directly pertains to concentrated solution theory. The most commonly adopted method is the dilute solution approach of Springer *et al*, while the dilute solute approach of Verbrugge and co-workers and the concentrated solution approach of Fuller and Newman appear much more rarely [47,48,49]. In practice, it is well understood that the charged end groups within the polymer electrolyte matrix hold up to a maximum of around 14 water molecules when equilibrated in water vapour. It is also known that if the PEM is equilibrated with liquid water the charged end groups can hold up to around 22 water molecules. This behaviour at unit activity is commonly attributed to Schroeder's paradox [50,51]. In terms of modelling because liquid water in the PEM can affect all modes of transport and therefore the proton conductivity across it, it also needs to be considered. Generally, this has not been the case mainly because unlike the GDL and MPL, the PEM does not have a definite rigid porous structure and therefore difficult to structurally characterise and model using the conservation equations mentioned above or the dilute or concentrated solution theories in their standard forms. However, it has been proposed that the presence and infiltration of liquid water can forcibly create a pore network within the PEM, and this idea has formed the foundation of one notable modelling approach based on concentrated solution theory which departs from the traditional treatment of the PEM [52,53,54,55,56].

Although the above review is not completely exhaustive, it provides a reasonable understanding of the mainstream modelling efforts in two-phase fuel cell simulation and the physical phenomenon that occur under two-phase conditions. What becomes clear, though, is that while each piece of work is fundamentally focused on describing two phase flow, the manner in which fundamental transport theory and experimentally-obtained relations are applied is not universally consistent.

The purpose of the current work is to apply the general transport equation (GTE) from fundamental transport theory to model two-phase flow in the porous and quasi-porous layers of the PEFC. In the previous chapter, the theoretical validity of the GTE was proven by deriving all the benchmark transport equations used in the modelling literature. The GTE was then translated into a simple single-phase model and simulated results were validated against published data. In the current study, the established understanding is extended by demonstrating a simple yet theoretically consistent method by which two-phase transport can be modelled in the porous and quasi-porous layers of the cell using the GTE. This common root has not been demonstrated in the literature to date. The theoretical framework is then translated into a working one-dimensional multi-layer, two-phase fuel cell model which incorporates recent semi-empirical data fits to characterise the physical properties of modern fuel cell materials. The model is applied in two parts. First, it is applied to simulate a set of experimental test cases; the modelling results are validated against experimental data to verify the predicted water transport and water uptake characteristics inside a working cell. Second, the model is applied to study the effects of PEM thickness, anode humidification and cell compression on liquid water infiltration, water transport and water uptake characteristics across the PEM when two-phase operating conditions are established inside the PEFC. The second part is presented in chapter 8.

7.2 Theoretical Equations for Two-Phase Transport in Porous and Electrolytic Quasi-Porous Media

All the transport layers of a fuel cell can be treated as fundamentally being porous or quasi-porous. For both types of media, internal transport under two-phase conditions is in general a common phenomenological process and can therefore be treated as a common

process in modelling terms. As such, transport under two-phase conditions can be described for both types of fuel cell media using the GTE. This section focuses on deriving the functional form of the theoretical equations for two-phase-driven transport in porous and quasi-porous fuel cell media.

7.2.1 The General Transport Equation

The GTE is taken from the previous study of PEFC transport mechanisms and derived from the molecular theory of gases and liquids as presented in chapter 6. It describes the movement of a species as part of a multi-species concentrated solution system due to the following modes of transport;

- diffusion due to concentration gradients
- convection due to pressure gradients
- thermal diffusion due to temperature gradients
- electro-osmotic drag due to an electric field

In its generalised form, the GTE appears as follows;

$$c_i\left[\nabla\mu_i + \bar{s}_i\nabla T - \frac{M_i}{\rho}\nabla p\right] - RT\dot{n}_{H+}\frac{c_m}{c_T}\left(\frac{\xi_i}{D_{i,m}} - \frac{\rho_i}{\rho}\sum_{j\neq i,mem}^{v}\frac{\xi_j}{D_{j,mem}}\right) = RT\sum_j\frac{c_i c_j}{c_T D_{ij}}\left[v_j - v_i + \left(\frac{D_j^{Th}}{\rho_j} - \frac{D_i^{Th}}{\rho_i}\right)\nabla\ln T\right] \tag{7-1}$$

In the current modelling framework, the effects of temperature gradients are neglected $(\nabla T = 0)$, leading to the following reduced form of the GTE;

$$c_i\left[\nabla\mu_i - \frac{M_i}{\rho}\nabla p\right] - RT\dot{n}_{H+}\frac{c_m}{c_T}\left(\frac{\xi_i}{D_{i,m}} - \frac{\rho_i}{\rho}\sum_{j\neq i,mem}^{v}\frac{\xi_j}{D_{j,mem}}\right) = RT\sum_j\frac{c_i c_j}{c_T D_{ij}}\left[v_j - v_i\right] \tag{7-2}$$

The second term of the left hand side of equation 7-2 accounts for electro-osmotic drag and does not occur in electro-neutral materials such as the GDL or MPL.

Two indeterminate gradients appear in equation 7-2; first, the electrochemical potential gradient and second the phase pressure gradient. In order to solve the phase

pressure gradients, therefore, an additional relationship based on the fluid dynamics of the system is required, i.e., Darcy's law:

$$v_J = -\frac{k_J \kappa}{\mu_J} \nabla p_J ; J = liq, gas \tag{7-3}$$

where

κ = absolute permeability of the material,

k_J = relative permeability pre-factor,

μ_J = viscosity of the fluid

∇P_J = pressure gradient in the phase J .

The following sub-sections describe how the GTE and Darcy's law are applied to solve the two characteristic gradients for two-phase flow in porous and quasi-porous fuel cell media.

7.2.2 Theoretical Equations for Two-Phase Transport in Porous Media

Concentration gradients

The electrochemical potential of a species can be defined as [57];

$$\nabla \mu_i = RT \frac{\nabla c_i}{c_i} + z_i F \nabla \phi \tag{7-4}$$

Substituting this into 7-2 for porous media where electro-osmotic drag does not occur ($\xi_i = 0$) and assuming that the water vapour behaves as an ideal gas yields;

$$\nabla c_i = \frac{\nabla p_{gas}}{RT}\left(\frac{\rho_i}{\rho} - 1\right) + \sum_j \frac{RT}{p_{gas} D_{ij}}\left(\dot{n}_j c_i - \dot{n}_i c_j\right) \tag{7-5}$$

where the molar flux of species i is defined as $\dot{n}_i = c_i v_i$. The total water flux across the cell can be related to the proton flux by;

$$I = \frac{J}{2F} = \dot{n}_{H^+} = \frac{\dot{n}_w}{\alpha} \tag{7-6}$$

It is assumed that water vapour travels along that proportion of the porous network of a given layer which is not saturated by liquid water. The local saturation, s, is calculated using the local capillary pressure:

$$P_{cap} = P_{gas} - P_{liq} \tag{7-7}$$

As such, it is assumed that the proportion of the total amount of water that travels through the porous network in vapour form can be determined by the fraction $(1-s)$, whereas that which occurs in liquid form through the saturated pores can be determined by s. The flux of water vapour can now be defined as

$$n_{w,vap} = (1-s) I \alpha_E \tag{7-8}$$

where $\alpha_A = \alpha$ for anodic porous layers

$\alpha_C = -2(1+\alpha)$ for cathodic porous layers

The density of the gas-phase mixture is calculated as;

$$\rho_{gas} = \sum_i c_i M_i \tag{7-9}$$

Pressure Gradients

Pressure gradients are accounted for using Darcys law, as given by equation 7-3. The relative permeability pre-factor k_j for liquid and gas phases respectively is calculated as;

$$k_{liq} = s^m \tag{7-10}$$

$$k_{gas} = (1-s)^m$$

The velocity of phase J is converted to flux rates using $\dot{n}_J = v_J c_J$ which yields;

$$\nabla p_J = -\frac{\dot{n}_J \mu_J}{c_J k_J \kappa} \tag{7-11}$$

The flux of water vapour is calculated using equation 7-8 while that of liquid water is calculated as;

$$n_{i,liq} = sI\alpha_E \tag{7-12}$$

It is assumed that multi-component transport occurs in the vapour phase while water alone constitutes the liquid phase.

7.2.3 Theoretical equations for two-phase flow in quasi-porous media

Concentration gradients

The general transport equation given by equation 7-2 can be applied for a three-species polymer electrolyte system where water is the primary species i, and hydrogen ions and the solid polymer electrolyte respectively become the secondary species j. For such system, the GTE becomes:

$$c_w\left(\nabla\mu_w - \frac{M_i}{\rho}\nabla p\right) = \frac{RT}{c_T}\left[\frac{1}{D_{w,H+}}\left(c_w\dot{n}_{H+} - c_{H+}\dot{n}_w\right) + \frac{1}{D_{w,mem}}\left(c_w\dot{n}_{mem} - c_{mem}\dot{n}_w\right)\right] + RT\dot{n}_{H+}\frac{c_m}{c_T}\frac{\xi_w}{D_{w,mem}} \tag{7-13}$$

Given that water within the PEM has no net charge, i.e., $z_w = 0$, the electrochemical potential of water can be defined as follows using equation 7-4;

$$\nabla \mu_w = RT \frac{\nabla c_w}{c_w} \tag{7-14}$$

By grouping terms and noting that the flux of the membrane phase is zero, i.e., $\dot{n}_{mem} = 0$ yields

$$RT\nabla c_w - \frac{\rho_w}{\rho}\nabla p = \frac{RT}{c_T}\left[\frac{c_w \dot{n}_{H+}}{D_{w,H+}} - \left(\frac{c_{H+}\dot{n}_w}{D_{w,H+}} + \frac{c_{mem}\dot{n}_w}{D_{w,mem}}\right)\right] + RT\dot{n}_{H+}\frac{c_m}{c_T}\frac{\xi_w}{D_{w,mem}} \tag{7-15}$$

Rearranging equation 7-15 to describe the net water flux across the PEM yields;

$$\dot{n}_w = \left[\frac{c_{H+}}{D_{w,H+}} + \frac{c_{mem}}{D_{w,mem}}\right]^{-1}\left[\dot{n}_{H+}\left(\frac{c_w}{D_{w,H+}} + \frac{c_m \xi_w}{D_{w,mem}}\right) - c_T \nabla c_w + \frac{c_T \rho_w}{RT\rho}\nabla p\right] \tag{7-16}$$

Equation 7-16 describes the total molar flux of water across the PEM. In the present state, 7-16 does not explicate the difference between water transport in vapour-equilibrated and liquid-equilibrated states. However, it is possible to postulate a physical model for the PEM system based on a previous treatment [52] in order to do this.

The PEM is characterised by hydrophilic sulfonic acid sites which are tethered to a hydrophobic fluorocarbon backbone. The PEM essentially contains a myriad of these polymer chains and the resulting structure is often referred to as a polymer matrix. It is assumed that on the surface of the PEM, the polymer chains are orientated in a way that exposes the fluorocarbon backbone, resulting in a highly-hydrophobic surface.

In the physical model, it is primarily assumed that the polymer matrix is quasi-porous in nature and contains internal hydrophobic pathways that can be forcibly expanded by capillary action. During initial hydration, it is assumed that water molecules become strongly associated to the charged end groups. As hydration continues, the charged end groups begin to form inverted micelles which contain water. As hydration continues further, these water clusters grow larger and synonymously create weak water networks between them in the collapsed hydrophobic pathways. When the boundaries of the PEM are in contact with

saturated water vapour, the individual channels between water clusters are well-established and definite.

When liquid water comes into contact with one of the boundaries, it is assumed that the hydrophobic skin which initially covers the outer surface is forced to re-orientate, exposing the hydrophilic charged end groups instead. This can subsequently allow liquid water to infiltrate the PEM along the channels in the water network and depending upon the liquid pressure at the boundary can forcibly expand them via capillary action. As the liquid water infiltrates the PEM, the water clusters enlarge further. When all the boundaries of the PEM are in contact with liquid water, the water clusters enlarge to their maximum permissible thermodynamic states and all the initially-collapsed hydrophobic channels are forcibly expanded and completely filled with liquid water.

According to the description above, there are as such two polar states that the PEM can operate under; firstly, a collapsed state where the PEM is equilibrated with water vapour and secondly a fully expanded state where the PEM is equilibrated with liquid water. It is possible for the PEM to equilibrate with water vapour and liquid water simultaneously, creating a transitional regime where a fraction of expandable pores are actually expanded. This may occur when the cathodic bondary is in contact with liquid water while the anodic boundary is not. Under this regime, it is possible for two transport modes to co-exist; a vapour-equilibrated transport mode in the collapsed region of the PEM, and a liquid-equilibrated transport mode in the liquid-filled network of expanded pores within the PEM. In terms of water content, denoted λ, this transitional regime describes the increase of water content from its maximum value for a fully vapour-equilibrated state (around 14) to its fully liquid-equilibrated state (around 22).

It is assumed that the magnitude of the capillary pressure in the expanded liquid-filled pore network is directly related to and therefore defines the fraction of pores that are actually expanded. The expanded pore fraction is denoted s_{epf}. Conceptually, the pore expansion fraction is similar to saturation in the capillary pressure-saturation relationship for GDLs but with the notable difference that the pore expansion fraction represents the fraction of pores between water clusters which are initially collapsed that are forcibly expanded by infiltrating

liquid water whereas saturation represents the fraction of pre-existing open pores which become completely filled with the infiltrating liquid water.

By assuming the physical model above, equation 7-16 can be recast to consist of two parts; one part relating to the vapour-equilibrated mode and the other to the liquid-equilibrated mode. Assuming that the expanded pore fraction determines the proportion of flow occurring in liquid- and vapour-equilibrated networks in an identical manner to pore saturation in equations 7-8 and 7-12, and grouping coefficient terms for vapour-equilibrated and liquid-equilibrated phases yields;

$$\nabla c_w = \frac{1}{c_T}\left(s_{epf}\left(I\Phi_{2,liq} + \Phi_{3,liq}\right) + \left(1 - s_{epf}\right)\left(I\Phi_{2,vap} + \Phi_{3,vap}\right) - I\Phi_1\alpha\right) \tag{7-17}$$

where

$$\Phi_1 = \left[\frac{c_{H+}}{D_{w,H+}} + \frac{c_{mem}}{D_{w,mem}}\right]; \tag{7-18}$$

$$\Phi_{2,J} = \frac{c_w}{D_{w,H+}} + \frac{c_m \xi_{w,J}}{D_{w,mem}};$$

$$\Phi_{3,J} = \frac{c_T \rho_w}{RT\rho}\nabla p_J$$

The gradient in water content, where water content is defined as the number of water molecules per charge site is calculated as;

$$\nabla\lambda = \nabla\left(\frac{c_w}{c_{mem}}\right) \tag{7-19}$$

where

$$c_{mem} = \frac{\rho_{dry}}{M_{mem}} \tag{7-20}$$

Pressure Gradients

Pressure gradients across the quasi-porous PEM region can be calculated using Darcy's law, as given in equation 7-9. The permeability pre-factor k_J is calculated here differently as a function of the volume fraction of water that occupies the PEM, f. The general definition of the volume fraction of water in the PEM is;

$$f = \frac{\lambda V_w}{V_{mem} + \lambda V_w} \tag{7-21}$$

where the partial molar volume of species i is calculated as;

$$V_i = \frac{M_i}{\rho_i} \tag{7-22}$$

In the case of the PEM, the density is taken as the dry value. Based on statistical arguments, the effective hydraulic permeability of the PEM is defined as [53]

$$k_{liq} = \left(\frac{f}{f_{liq}} \right)^2 \tag{7-23}$$

where f_{liq} corresponds to the maximum liquid-phase water content;

$$f_{liq} = \frac{\lambda_{liq,\max} V_w}{V_{mem} - \lambda_{liq,\max} V_w} \tag{7-24}$$

It is assumed that $\lambda_{liq,\max} = 22$ based on literature values [58,59].

7.3 Sub-Models for the Physical Properties of PEFC Media and Infiltrating Fluids

The validity of the theoretical equations for two-phase transport described in the preceding section can be tested by applying them through a one-dimensional modelling framework for the PEFC. In the current work, this is done through an isothermal model which treats the fuel cell has having seven regions of potential interest. The anode and cathode sides of the cell can each contain a supply channel, a GDL and an MPL. The central layer is the PEM.

The purpose of this section is to discuss the sub-models that are required to supplement the two-phase transport equations described in the preceding section. These sub-models are mainly adopted from the literature and account for the operating conditions, the physical properties of the fuel cell layers and the physical properties of the working fluids that infiltrate the cell.

The main assumptions of the current model are as follow;

1. the fuel cell operates under steady-state conditions
2. two-phase flow in the channel can be treated as mist flow
3. thermal diffusion due to temperature gradients can be neglected
4. gravitational effects on two-phase transport can be neglected
5. the catalyst layers can be treated as a thin interface
6. convective flow across the PEM only occurs in the intruding liquid water network

Figure 7-1 illustrates the potential modelling domain; since the MPL is used selectively in practice, the modelling structure will treat the MPL as an optional layer. If the MPL is disregarded, interface A-2b or C-2b would disappear and interface A-2 or C-2 would represent the interface between the GDL and the PEM. The CL is shown in Figure 7-1 for illustration purposes.

The composition of the reactant supplies to the anode and cathode channel regions of the cell are determined using the multi-species input model developed in chapter 5. The composition within each channel is determined as a function of reactant humidification temperature, dry gas composition, stoichiometry, the net water transport ratio and current

density. The model inherently accommodates conditions where one or neither of the inlet gases are partially/fully humidified.

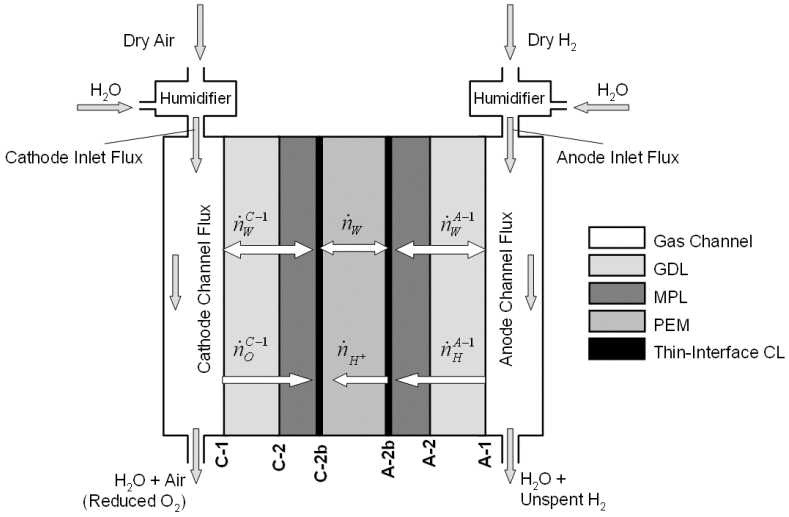

Figure 7-1 PEFC cell structure for the one-dimensional two-phase model

7.3.1 Sub-models for the Inlet and Channel Regions

The existing multi-species input model is improved in two regards. First, a simple thermodynamic sub-model is devised which calculates anode and cathode supply stoichiometries directly from the flow rates of the supply gases. This is useful for model validation/application purposes when flow rates are provided from experiment rather than stoichiometry. Second, another simple sub-model is devised to calculate the boundary pressures and concentrations of the gas-phase constituents for the side of the GDL that interfaces with the channel. The key equations are discussed in more detail in the appendix.

7.3.2 Sub-models for the Porous Layers

The equations given in Table 7-1 describe the local pressure-diffusivity product, viscosity, liquid phase saturation and compression effects in GDL and the MPL. Local values are calculated by taking into account the effective porosity of the layer and local level of saturation. It is assumed that the effective porosity depends upon the level of cell compression.

The pressure-diffusivity product is defined by the Slattery-Bird equation, as discussed in the previous chapter, but modified to account for the tortuosity of the porous network, its effective porosity and liquid saturation. The phase viscosity is required in equation 7-9 to calculate the phase pressure drop. The viscosity of water vapour and liquid water are calculated as functions of temperature, while that of air and hydrogen are taken as fixed values. The viscosity of the vapour-phase mixture is calculated using the mole fractions of the constituent species.

Two-phase fuel cell models typically adopt the Leverett approach to macroscopically characterise the level of saturation in a porous diffusion layer as a function of the local capillary pressure using equation 7-7. For a given capillary pressure, it is possible to calculate the level of saturation using the standard Leverett J-function as given by equations 7-29 and 7-30. While this method is readily adoptable, there are two main drawbacks to its use: (1) because of the stochastic nature and heterogeneous hydrophobicity of a GDL or MPL, it is difficult to obtain a meaningful contact angle for equation 7-29, and; (2) the local porosity and permeability are likely to change according to the compression pressure exerted onto the working cell.

The current model includes a unified semi-empirical approach which is specifically developed for the PTFE-treated porous carbon paper fuel cell layers manufactured by SGL [60]. This method is based on the Leverett function, but modified to take into account key physical characteristics associated to fuel cell media, which are not experienced in soil bed systems such as the level of hydrophobic fill, the cell compression pressure and the compressed porosity of the material. In the current framework, the standard Leverett method is applied when the specific form of the capillary pressure-saturation relationship is unknown or undefined for the porous material in question, and the validated Leverett method is applied specifically when SGL-manufactured porous materials are used.

The recent literature identifies a hysteresis in the capillary pressure-saturation relationship of GDLs during water drainage and imbibition [17,31,61], a phenomenon that has been encountered in petroleum engineering [62]. The experimental data suggests that the heterogeneous distribution of the hydrophobising agent through the porous layer creates hydrophilic and hydrophobic domains which result in different capillary pressure-saturation profiles according to whether water is being removed from or infiltrating in to the porous

Pressure-Diffusivity

$$p_{gas}D_{ij}^{eff} = p_{gas}D_{ij} \times \frac{\varepsilon}{\tau}(1-s)^{3/2} \tag{7-25}$$

Viscosity

$$\ln \mu_{\mathrm{w,vap}} = -1.0373\times10^{1} - 8.6737\times10^{-1}\left(\frac{T_{crit}}{T}-1\right)^{1/3} - 2.9699\times10^{-1}\left(\frac{T_{crit}}{T}-1\right)^{4/3} + 9.0510\times10^{-1}\left(\frac{T_{crit}}{T}-1\right)^{7/3} \tag{7-26}$$

$T_{crit} = 647.25\mathrm{K}$

$\mu_{0.21O_2/0.79N_2} = 17.2\times10^{-6}$ Pa-s

$\mu_{H_2} = 8.42\times10^{-6}$ Pa-s

$$\mu_{vap} = \sum_i x_i \mu_i \tag{7-27}$$

$$\ln\mu_{\mathrm{w,liq}} = -1.01083\times10^{1} + 1.39621\left(\frac{T_{crit}}{T}-1\right)^{1/3} + 4.8431\times10^{-1}\left(\frac{T_{crit}}{T}-1\right)^{4/3} + 7.1019\times10^{-1}\left(\frac{T_{crit}}{T}-1\right)^{7/3} \tag{7-28}$$

Saturation vs. Capillary Pressure: Standard Leverett J-Function

$$p_{cap} = \gamma\cos\theta\left(\frac{\varepsilon}{K}\right)^{1/2} J(s) \tag{7-29}$$

$$J(s) = \begin{cases} 1.417(1-s) - 2.120(1-s)^2 + 1.263(1-s)^3 & \text{if } \theta < 90^\circ \\ 1.417s - 2.120s^2 + 1.263s^3 & \text{if } \theta > 90^\circ \end{cases} \tag{7-30}$$

Saturation vs. Capillary Pressure: Validated Leverett J-Function

$$p_{cap} = \left(\frac{293}{T}\right)^6 \gamma(T) 2^{0.4C}\left(\frac{\varepsilon_{comp}}{K}\right)^{1/2} J(s_{nwp}) \tag{7-31}$$

$$J(s_{nwp}) = \begin{cases} wt\%\left(0.0469 - 0.00152wt\% - 0.0406s_{nwp}^2 + 0.143s_{nwp}^3\right) + 0.0561\ln s_{nwp} & 0.00 < s_{nwp} \le 0.50 \\ wt\%\left(1.534 - 0.0293wt\% - 12.68s_{nwp}^2 + 18.824s_{nwp}^3\right) + 3.416\ln s_{nwp} & 0.50 \le s_{nwp} \le 0.65 \\ wt\%\left(1.7 - 0.0324wt\% - 14.1s_{nwp}^2 + 20.9s_{nwp}^3\right) + 3.79\ln s_{nwp} & 0.65 < s_{nwp} < 1.00 \end{cases} \tag{7-32}$$

Surface tension of water

$$\gamma = -1.78T\times10^{-4} + 0.1247 \text{ N/m} \tag{7-33}$$

Compression Effects

$$Y_{comp} = Y_{u/c}\left(\frac{0.9}{1+\boldsymbol{\varepsilon}} + 0.1\right) \tag{7-34}$$

$$\boldsymbol{\varepsilon} = -b_1C^2 + b_2C \qquad \text{where } \begin{cases} b_1 = -0.0083; b_2 = 0.0911 & \text{SGL 24-Series} \\ b_1 = 0.0046; b_3 = 0.0843 & \text{SGL10BB} \end{cases} \tag{7-35}$$

Table 7-1 Key equations for the porous regions of the PEFC

layer. While the current work does not make a distinction between water drainage or imbibition, it is anticipated that these newer profiles will be adopted into the current modelling framework in due course as more becomes clear about the phenomenon in fuel cell materials.

As discussed previously, it is assumed that cell compression affects the porosity and the thickness of the porous layers. It is assumed that the change in thickness and porosity can be calculated using a common semi-empirical relationship as given by equation 7-34 where Y denotes either porosity ε or layer thickness t_{layer} and the substripts $comp$ and u/c denote compressed and uncompressed states respectively. The compressive strain depends upon the specific structural properties of the porous layer in question and will therefore vary from material to material. In the current study, the relationship given by equation 7-35 is employed where C is the compressive pressure with units of MPa.

7.3.3 Sub-models for the Quasi-Porous Layers

In the current treatment, the quasi-porous PEM is treated as a ternary system consisting of water, protons and polymer electrolyte where water transport can occur in liquid- or vapour-equilibrated networks. The equations given in Table 7-2 describe the physical properties of the quasi-porous ternary system including diffusivity, electro-osmotic drag, hydraulic permeability, viscosity, pore expansion, molar volumes, Ohmic resistance and proton conductivity. Compression effects on water uptake and dimensional changes are taken into account through the mechanical properties of the polymer electrolyte.

In order to solve equation 7-17, the diffusion coefficient of water in the PEM must be known. The diffusion coefficient of water depends upon the water content of the PEM. For an unconstrained Nafion-based PEM system, the well-known experimentally-derived expression given by equation 7-36 is used [3]. For Nafion-based composite membranes there is a penalty to pay in the water diffusion coefficient because of the internal structural reinforcement. In essence, structurally reinforced membranes contain an inert matrix which is impregnated with Nafion. As such, the general form of the above equation applies but has to be modified by a pre-factor k_{diff} to account for the loss of diffusivity, where $0.00 < k_{diff} < 1.00$. This results in equation 7-37. The literature demonstrates a wide scatter in

the value of k_{diff} at all values of λ [63] and an understanding of the dependence of k_{diff} on λ has not been demonstrated yet.

The magnitude of the electro-osmotic drag coefficient is assumed to change according to whether the transport occurs in the liquid- or vapour- equilibrated network. For the vapour-equilibrated mode, the electro-osmotic drag coefficient is taken as unity. For the liquid-equilibrated mode, the temperature-dependency of 7-38 is adopted [53].

Hydraulic permeability and the viscosity of liquid water are required to calculate the hydraulic pressure gradient across the PEM. There is a scatter in the range of values for Nafion in the literature with respect to hydraulic permeability. Meier *et al*. calculate 2×10^{-16} to 1.4×10^{-15} cm^2 depending upon the local water content using experimental measurements [64,65]. Verburgge and Hill initially adopt a value of 1.58×10^{-13} cm^2 [43] while Bernardi and Verbrugge later report a value of 1.8×10^{-14} cm^2 based on a water-balance measurements [4]. The latter is adopted in the current model, which sits within the range of these values. The viscosity of liquid water is calculated simply using equation 7-27.

In order to determine the contribution of vapour- and liquid-equilibrated transport modes on the net water transport across the PEM as given in equation 7-17, it is necessary to calculate the fraction of pores in the PEM that are forcibly expanded by the intruding liquid water. In the adopted physical model for the quasi-porous PEM region, it is assumed that pore expansion is driven by capillary action when a boundary of the PEM comes into contact with liquid water [53]. For a given capillary pressure, it is possible to calculate the corresponding pore radius of the local capillary tube using the Young-Laplace equation, as given by equation 7-39. This radius represents a critical dimensional threshold; all pores with a radius larger than the critical radius will be collapsed whereas those with a smaller radius will be expanded and completely filled with liquid water. Using pore-size distribution data for Nafion measured using standard contact porosimetry [66,67] and assuming that the measured micropores correspond to the channels in the PEM, it is possible to calculate the fraction of channels that are expanded by liquid water using equation 7-40 [53].

Diffusivity of water in polymer electrolyte; non-reinforced Nafion-based PEMs

$$D_{w,mem(Nafion)} = \left(2.5630 - 0.330\lambda + 0.02640\lambda^2 - 0.0006710\lambda^3\right) \times \exp\left[2416\left(\frac{1}{303} - \frac{1}{T}\right)\right] \times 10^{-6} \tag{7-36}$$

Diffusivity of water in polymer electrolyte; structurally-reinforced, Nafion-impregnated PEMs

$$D_{w,mem(GORE)} = k_{diff}\, D_{w,mem(Nafion)} \tag{7-37}$$

Diffusivity of protons in water

$$D_{H^+,w} = 4.5 \times 10^{-5}\ cm^2/s$$

Electro-osmotic drag coefficient

$$\xi_{vap} = 1$$

$$\xi_{liq} = 2.55 \exp\left[\frac{4000}{R}\left(\frac{1}{303.15} - \frac{1}{T}\right)\right] \tag{7-38}$$

Pore expansion

$$r_{crit} = -\frac{2\gamma\cos\theta}{p_{liq}} \tag{7-39}$$

$$s_{epf} = \frac{1}{2}\left[1 - erf\left(\frac{\ln r_{crit} - \ln(1.25)}{0.3\sqrt{2}}\right)\right] \tag{7-40}$$

Molar volume – free-swelling PEM

$$V_{tot} = V_w\lambda + V_{mem} \tag{7-41}$$

$$c_w = \frac{\lambda}{V_{tot}} \tag{7-42}$$

$$c_{mem} = \frac{1}{V_{mem}} \tag{7-43}$$

Proton conductivity across the PEM

$$\sigma = \sigma_o\left(f - f_o\right)^{1.5} \exp\left[\frac{E_a}{R}\left(\frac{1}{T_{ref}} - \frac{1}{T}\right)\right] \tag{7-44}$$

Local water content and activity

$$\lambda = 0.043 + 17.81a - 39.85a^2 + 36a^3;\ 0 < a \le 1 \tag{7-45}$$

$$a = c_6\left(-c_1 + c_2\lambda^2 + 216\left(c_3 - c_4\lambda + c_5\lambda^2\right)^{1/2}\right)^{1/3} - c_7\left(-c_1 + c_2\lambda^2 + 216\left(c_3 - c_4\lambda + c_5\lambda^2\right)^{1/2}\right)^{-1/3} + c_8 \tag{7-46}$$

where $\begin{cases} c_1 = 419565187;\ c_2 = 139968000;\ c_3 = 3824822562051; c_4 = 2517391122000; \\ c_5 = 419904000000;\ c_6 = 1/2160;\ c_7 = 134183/2160;\ c_8 = 797/2160 \end{cases}$

Local activity as a function of water pressure

$$a = \frac{p_{w,vap}}{p_w^{sat}} \tag{7-47}$$

Table 7-2 Key equations for the quasi-porous region of the PEFC

In the case of a compressed PEFC, the effect of PEM constraint on the water uptake across the PEM is calculated based on the mechanical properties of the PEM. A full explanation of the assumptions adopted and equations applied for this mechanical sub-model is provided in the appendix. In the complete PEFC model, the manner in which the effect of compression on PEM thickness is accounted for requires some explanation. In the first instance, the model is allowed to calculate the water content at the anodic and cathodic boundaries assuming a free-swelling state. These boundary conditions are then modified according to the level of compression, which in return automatically modifies the intermediate water content profile within the PEM and also allows the actual thickness of the membrane to be calculated as a function of its free-swelling equivalent state. Because the calculation of PEM thickness requires the average water content across the membrane to be known, a small number of iterations have to be carried out within the quasi-porous layer sub-model. The iterations allow the average water content to converge to a stable value, which corresponds to the actual thickness of the PEM.

The proton conductivity for Nafion-based PEMs is calculated using percolation theory [68], as given by equation 7-44, where σ_o is the critical conductivity of Nafion and f_o is the threshold volume fraction at which the insulator-to-conductor transition occurs [53]. It is assumed that the critical conductivity can be set to 0.5 S/cm [53] based on the measured conductivity of Nafion under vapour-equilibrated [69] and liquid-equilibrated conditions [70]. It is assumed that the insulator-to-conductor transition occurs in Nafion when $\lambda = 2$ which translates to $f = 0.06$ [53]. The activation energy E_a reflects the Arrhenius dependence of conductivity on temperature and assumed to equal 11 kJ/mol [53]. Equation 7-44 is applied with these parameters to calculate the local conductivity based on the local volume fraction of water and temperature. It is assumed that conductivity increases as a function of f until a second threshold for the volume fraction of water is reached. If more water is added beyond this point, the effect on improving the continuity of pathways for proton conduction across the PEM becomes negligible. The literature suggests that this second threshold occurs when $f = 0.45$ [53]. Therefore, for calculation purposes it is assumed that $f = 0.45$ when $f > 0.45$. In the case of structurally-reinforced PEMs that are impregnated with Nafion, it is assumed that equation 7-44 can be applied equally.

In order to translate the interfacial vapour pressures between the appropriate anode porous layer and the PEM for the quasi-porous layer model, a relationship is needed to calculate water content as a function of activity. An inverse relationship is also required to covert water content into activity to define the boundary pressures for the porous layers of the cathode side of the cell. Traditionally, these relationships have been derived from a semi-empirical fit for data at 30˚C [58] first used by Springer *et al.* [3]. Since then other chemical models have been proposed in the modelling literature [53,70]. The chemical model of Weber and Newman is directly dependant on temperature [53] while the Brunauer-Emmett-Teller (BET) approach of Thampan *et al.* is a function of the relative humidity at the CL-PEM interface [70]. In the current model, the semi-empirical fit of Zawodzinski *et al.* [58] given by equation 7-45 and its rearranged form of 7-46 are applied because they capture the functional form and magnitude of the relationship relatively well and are simple to apply.

7.4 Modelling Structure for a One-Dimensional Two-Phase PEFC Model

The modelling framework for the single-cell, one-dimensional multi-phase fuel cell model is implemented using the object modelling technique (OMT) [71,72]. The modelling framework comprises of three repeating object-orientated models, namely; (a) the channel model: this includes the multi-species input model given in the appendix; (b) the porous layer model: this includes the transport equations 7-4 to 7-10 and the auxiliary equations in Table 7-1, and (c) the quasi-porous layer model: this includes the transport equations 7-17 to 7-24 and the auxiliary equations in Table 7-2. The object-orientated approach is adopted because it enables the modelling framework to be adaptable and much less sensitive to massive restructuring during further development. The approach also eliminates repeating lines of codes which describe fundamentally identical phenomenological processes that can reoccur in different parts of the physical system. The application of the general transport equation therefore inherently lends itself well to the OMT approach. From the users perspective, the OMT approach results in a much more intuitive modelling framework as well, where modelling elements correspond to physical components of the fuel cell and boundaries between elements reflect interfacial boundary conditions between physical components.

The channel model is applied to determine the thermodynamic conditions in the gas supply channels and to determine the boundary conditions at interfaces A1 and C1. The model is therefore applied twice to simulate two objects; the anode and cathode gas channels.

The porous layer model is applied to determine the concentration and phase pressure profiles through the thicknesses of the GDLs and MPLs. The model can be applied twice initially to simulate two objects; the anode and cathode GDLs. This provides the boundary conditions at interfaces A2 and C2. The model can then be applied once or twice more to simulate two more objects if they appear in the structure of the simulated cell; the anode and/or cathode MPL. Accordingly, this provides the boundary conditions at interfaces A2b and/or C2b. The differential equations in the porous layer model are solved by treating them as initial value problems using the Runge-Kutta scheme.

The quasi-porous layer model is applied to determine the water content profile and the pressure profile of the intruding liquid phase through the PEM. Because the PEM is a non-repeating object in a single-cell, the quasi-porous layer model is applied once. The quasi-porous layer model is also solved as an initial value problem using the Runge-Kutta scheme from the anodic boundary to the cathodic boundary.

Each fuel cell layer is discritised into fifty data points. The overall simulation iterates the net water flux across the cell until the end result at interface C2 or C2b from the quasi-porous layer model for the PEM is the same as the end result at interface C2 or C2b from the porous layer model for the cathode GDL or MPL, again depending on whether or not the MPL is present. If two-phase conditions exist in the PEM, then convergence is judged by comparing liquid phase pressures at interface C2 or C2b. If single-phase conditions exist, then convergence is judged by comparing the PEM water content at interface C2 or C2b as obtained from the quasi-porous layer model to that calculated from the local activity from the porous layer model for the cathode. The general scheme is similar to that applied in the previous chapters and shown in Figure 7-2.

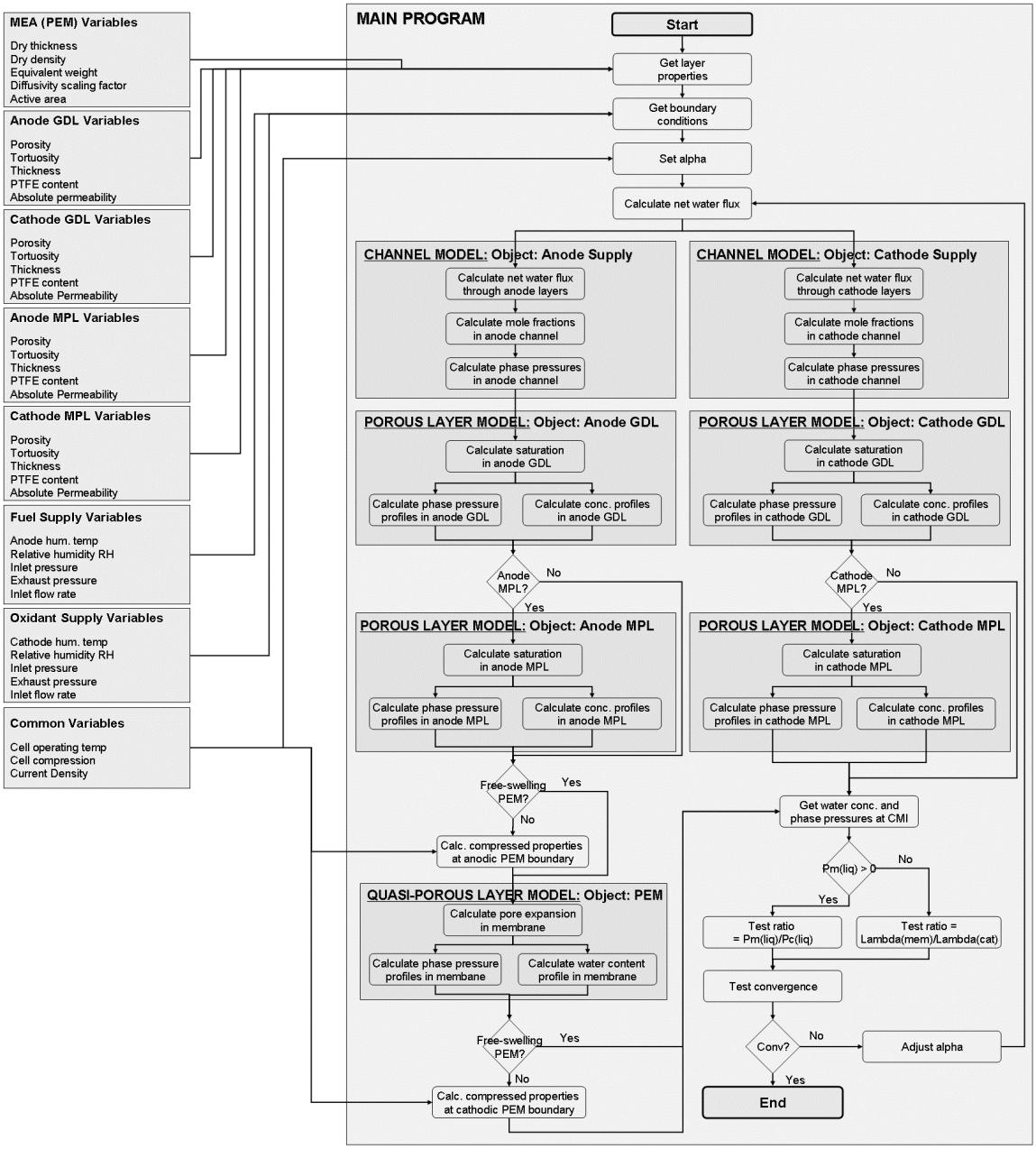

Figure 7-2 Simulation flowchart for the object-orientated single-cell, two-phase multi-layer one-dimensional PEFC model

7.5 Experimental Validation

7.5.1 Net water transport per proton

In order to validate the net water transport calculations of the model, eighteen test cases are taken from previously published experimental data for a Nafion-based single cell tested with E-TEK GDEs [49,54]. The active cell area is 50 cm^2 and the porosity, tortuosity and uncompressed thickness of the gas diffusers are taken as 0.4, 7 and 250 μm respectively [49]. Four operating parameters and two parameters associated with the PEM are altered in the study; operating current density, cell temperature, relative humidity (RH) (anode supply and cathode supply), stoichiometry (anode supply and cathode supply), PEM thickness and PEM equivalent weight. The first sixteen results correspond to a cell operated with Nafion 105 (equivalent weight of 1000 C/equiv. and dry thickness of 127.0 μm) and the remaining two to Nafion 112 (equivalent weight of 1100 C/equiv. and dry thickness of 50.8 μm).

The model is validated by comparing the simulated net water flux per proton to that calculated from experimental measurements for each test case. Since the net water flux ratio α is defined relative to the rate at which hydrogen is oxidised, the net water flux per proton is $\beta = 0.5\alpha$. Figure 7-3 compares the simulated and experimental values of the net water flux per proton.

A positive value of β corresponds to net water flux in the direction of the cathode channel, whereas a negative value corresponds to net water flux in the direction of the anode channel. The results show that the model correctly predicts the direction of net water transport in all eighteen test cases. The results also show that in all test cases, the predicted net water transport from the model is in the same order of magnitude and within reasonable agreement of the experimental value.

Cases 1, 2 and 9-16 demonstrate that with both supplies fully humidified, the net water transport occurs in the direction of the cathode. This holds true for both non-isobaric conditions as evident in cases 1 and 2 and isobaric conditions as evident in cases 9-16. By removing anode humidification, the net water flux switches direction and occurs in the direction of the anode, as evident in cases 3 and 4. If the cathode humidification is removed

		J	T	An RH	Cath RH	P(An)	P(Cath)	st(An)	st(Cath)	beta	beta
		A/cm^2	K	%	%	bar	bar	-	-	(exp.)	(sim.)
N105	Case 1	0.6	333.15	100	100	1.50	3.00	4	2	0.05	0.05
	Case 2	0.6	333.15	100	100	3.00	1.50	4	2	0.05	0.06
	Case 3	0.6	333.15	0	100	1.50	3.00	4	2	-0.23	-0.17
	Case 4	0.6	333.15	0	100	3.00	1.50	4	2	-0.07	-0.07
	Case 5	0.6	333.15	100	0	1.50	3.00	4	2	0.06	0.06
	Case 6	0.6	333.15	100	0	3.00	1.50	4	2	0.06	0.08
	Case 7	0.6	333.15	0	0	1.50	3.00	4	2	-0.20	-0.22
	Case 8	0.6	333.15	0	0	3.00	1.50	4	2	-0.06	-0.07
	Case 9	0.6	353.15	100	100	1.50	1.50	4	2	0.21	0.19
	Case 10	0.4	353.15	100	100	1.50	1.50	4	2	0.20	0.19
	Case 11	0.4	353.15	100	100	3.00	3.00	4	2	0.08	0.07
	Case 12	0.6	353.15	100	100	3.00	3.00	4	2	0.07	0.08
	Case 13	0.6	333.15	100	100	1.50	1.50	4	2	0.07	0.07
	Case 14	0.4	333.15	100	100	1.50	1.50	4	2	0.07	0.07
	Case 15	0.6	333.15	100	100	1.50	1.50	1.5	2	0.06	0.07
	Case 16	0.4	333.15	100	100	1.50	1.50	1.5	2	0.06	0.07
N112	Case 17	0.4	333.15	100	100	1.50	1.50	4	2	-0.09	-0.09
	Case 18	0.4	333.15	100	100	1.50	1.50	1.5	2	-0.08	-0.08

Table 7-3 Test cases for model validation

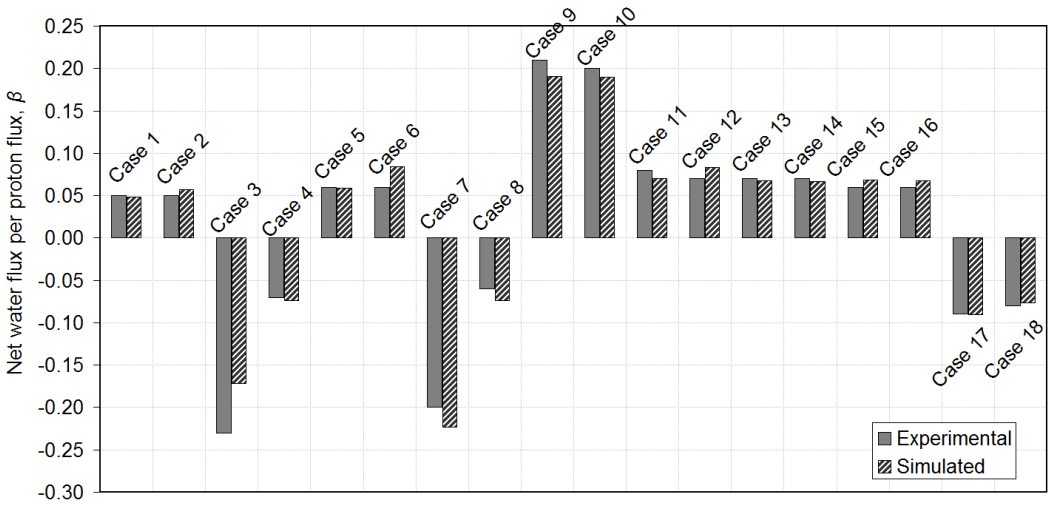

Figure 7-3 Comparison of simulated and experimental values of net water flux per proton for the 18 test cases

instead, the net water flux continues to occur in the direction of the cathode, as evident in cases 5 and 6. Cases 7 and 8 show that when neither supply is humidified, the natural tendency is for the net water flux to occur in the direction of the anode. For these test conditions therefore the direction of net water flux across the Nafion 105 PEM is more sensitive to anode humidification than cathode humidification, applied pressure differentials, current density and hydrogen stoichiometry. Under the isobaric conditions of cases 17 and 18 where the Nafion 112 PEM is used, the net water flux occurs in the direction of the anode even with both supplies fully humidified. This indicates that for the test conditions

considered, the net effect of water back-transport can be retarded when a thicker PEM with a longer transport path is used.

7.5.2 Ohmic Resistance across the PEM

In addition to validating the net water transport per proton across the cell, it is also necessary to predict the water uptake across the PEM and the effect that this has on membrane performance. This is performed in two steps in the current study. The first step is presented here which focuses on validating the specific resistance across the PEM against experimental data under vapour-equilibrated conditions. The second step is presented in section 7.5.3 and focuses on the direct validation of water content per charge site across the PEM against experimental data obtained from magnetic resonance imaging (MRI) under vapour- and liquid-equilibrated conditions.

For a given set of operating conditions, the model can determine the distribution of water across the membrane in terms of water content per charge site. By using equation 7-44, it is possible to translate this distribution into a profile of proton conductivity across the PEM. Conductivity can be inversed to give specific resistance ρ, which has units Ohm-cm.

In the current study, we use the specific resistance profiles presented by Takaichi *et al*. [73] obtained for a 5cm^2 active area PEFC with a 200 μm PEM, SGL-25BC based GDL and MPL assemblies and operated at 353K with 20% RH. Hydrogen and oxygen are fed to the anode and cathode sides of the cell respectively under ambient conditions both at a flow rate 0.2 slpm. The 200 μm PEM is fabricated with seven embedded Pt potential probes between eight 25.4 μm Nafion NRE211 PEMs, which is then hot-pressed to give a total thickness of 200 μm. The potential probes enable the specific resistance profile to be determined *in-situ*. The validation is carried out at four current densities under steady-state conditions; 0.2 mA/cm^2, 0.1 A/cm^2, 0.2 A/cm^2 and 0.3 A/cm^2. The results are presented in Figure 7-4.

Figure 7-4 (a) shows that the model is able to reproduce the experimental results under these single-phase conditions. The results suggest that the specific resistance at the anode increases with current density, while that at the cathode decreases. Figure 7-4 (b)

shows the simulated water content profile across the PEM for the simulated profiles of specific resistance given in Figure 7-4 (a). These results show that the gradient in water content increases with increasing current density; at low current, the distribution in water content is generally uniform and linear. However, as current density increases, the anode side of the PEM dehydrates while the hydration at the cathode side increases. The water content is generally within the band of 3 to 5 water molecules per charge site, demonstrating that under these operating conditions the PEM operates well within the vapour-equilibrated limit of 14/

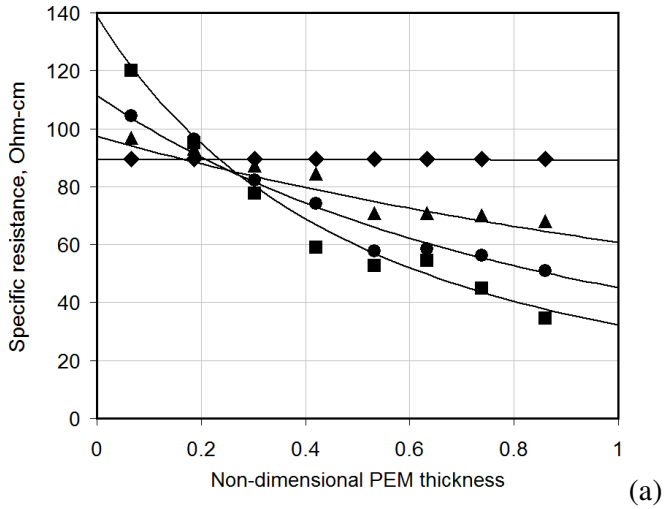

Figure 7-4 (a) Specific resistance profile across the PEM for simulated (line) and measured (points) results at 0.2 mA/cm^2 (♦), 0.1 A/cm^2 (▲), 0.2 A/cm^2 (●) and 0.3 A/cm^2 (■); (b) simulated water content

7.5.3 Water Content across the PEM

The purpose of this sub-section is to validate the simulated water content per charge site across the PEM when liquid water infiltrates the PEM. This is done by using the water content profiles presented by Ikeda *et al.* [74] deduced from magnetic resonance imaging (MRI) scans of a 6cm^2 active cell area PEFC operated at 70˚C and 0.2 A/cm^2 with a 254 μm thick Nafion-1110 PEM and Toray GDLs. The flow rates of the hydrogen and oxygen supply gases are both set to 0.1 slpm at 1 bar. The relatively large thickness of the PEM is necessitated in part by the spatial resolution of the MRI system. The results are however relevant for the validation of the current modelling framework. Three levels of relative humidity (RH) for the supply gases are considered; 40%, 80% and 92%. These particular MRI-generated results were chosen because the operating conditions explicitly invoke vapour- and liquid-equilibrated water uptake across the PEM. The results are presented in Figure 7-5.

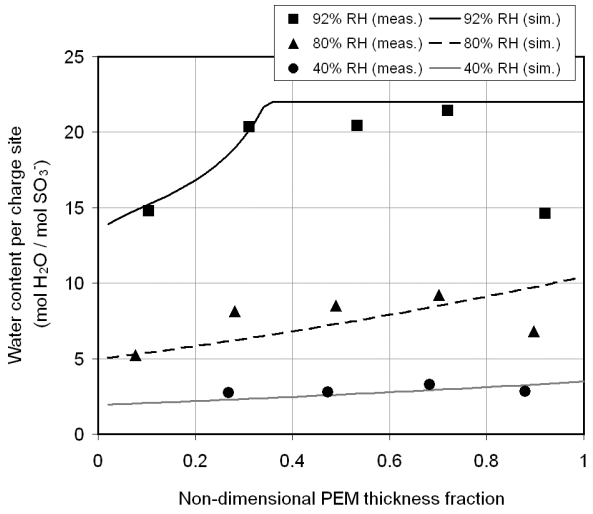

Figure 7-5 Simulated and measured water content profiles as a function of non-dimensional PEM thickness for three levels of supply gas relative humidity; 92%, 80% and 40% [74].

Figure 7-5 demonstrates that for the test cases considered, the 40% and 80% RH states invoke vapour-equilibrated transport across the PEM, whereas the 92% RH state invokes vapour- and liquid-equilibrated transport. With 92% RH, the water content per charge site exceeds the vapour-equilibrated limit of 14 and approaches the liquid-equilibrated limit of 22. With 80% RH, the water content stays below the vapour-equilibrated limit

throughout the thickness of the PEM and confined to the range of 5-11 water molecules per charge site. With 40% RH, the water content profile is the flattest throughout the thickness of the PEM and limited to the range of 2-4 water molecules per charge site.

The simulated results show that the water content generally increases from the anodic boundary to the cathodic boundary. In the case of 92% RH, the simulated results suggest that the water content exceeds the vapour-equilibrated limit in the vicinity of the anodic boundary and reaches the liquid-equilibrated limit half-way through the PEM. From this point, the simulations suggest that all the pores of the PEM are forcibly expanded by the intruding liquid water right the way up to the cathodic boundary. In the case of 40% and 80% RH, the simulated results suggest a gradual increase in water content from the anodic boundary to the cathodic boundary. For all three test cases, the model correctly predicts the magnitude of the water content per charge site, and the predicted profiles in all three cases also follow the general trend captured by the MRI-based measurements.

There is a noticeable discrepancy between the simulated and measured results in the final data point for the 92% and 80% RH cases. It is possible that these final points could occur as an artefact of the experimental setup and measurement system. The experimental and simulated results from the previous sub-section and Figure 6-2 also suggest that the water content should increase continuously through the PEM from the anodic boundary.

It is noted that the measurement of water content profiles through *in-situ* techniques is generally an under-developed area of fuel cell science and engineering, as discussed by St-Pierre [75]. In order to effectively validate fuel cell models, it is beneficial to augment cost-effective *in-situ* measurement techniques by which reproducible water content profiles can be determined for experimental fuel cells that employ representative fuel cell materials.

7.6 Conclusions

The literature identifies that the movement of water in the porous layers of a PEFC is described by forms of Fick's law and Darcy's law to describe diffusion and convection respectively. Diffusion is used to describe the effect of concentration gradients mainly on vapour phase transport while convection is mainly used to describe the effect of phase

pressure gradients on liquid and vapour phase transport. The local difference in phase pressures is used to define the local level of saturation in the porous medium using experimental capillary pressure-saturation curves. The literature also shows that water movement across the PEM is modelled primarily using dilute solution theory and occasionally using concentrated solution theory. The common underlying assumption is that transport across the PEM is mainly governed by a vapour-equilibrated state, but this does not consider the internal change in structure when the boundaries of the PEM come into contact with liquid water.

In the current work, a common fundamental modelling approach is presented based on the previously-developed general transport equation which is used with Darcy's law to describe two-phase transport across both porous and quasi-porous layers of a PEFC. The purpose of the two-phase GTE treatment developed in the current work is to demonstrate a simple yet theoretically consistent and effective method to predict water uptake and transport through the different layers of the PEFC.

The GDL and MPL are treated as porous but deformable structures with predetermined levels of hydrophobic fill material. The PEM is treated as a quasi-porous layer which contains internal channels that can be forcibly expanded by capillary action when a boundary comes into contact with liquid water. This quasi-porous treatment is based on a previously presented physical model and directly accounts for Schroeder's paradox [52]. Cell compaction and membrane constraint are also explicitly modelled in the current framework; the compaction pressure is used to characterise the capillary pressure-saturation relationship for the porous layers and translated into a degree of constraint for the quasi-porous layer to characterise water uptake and transport across it relative to its free-swelling equivalent state.

In the context of a simple object-orientated 1D two-phase fuel cell model, the calculated results using the GTE treatment are shown to be consistent with the experimentally-obtained net water flux data for 18 test cases published in the literature for an E-TEK/Nafion configured cell [49,54]. Calculated profiles of water content across the PEM under a range of current densities and RH conditions that induce vapour- and liquid-equilibrated water uptake are also consistent with data measured for SGL/Nafion configured cells using embedded potential probes [73] and MRI scanning [74]. The agreement in

magnitude - and direction of flow in the validation of net water flux - between calculation and measurement confirms the validity of the two-phase GTE treatment.

The current modelling framework successfully demonstrates that multi-component two-phase transport in the porous and quasi-porous layers of a PEFC can be effectively simulated using the GTE, which is derived directly from fundamental transport theory. The object-orientated modelling framework enables a ready assessment of the overall water transport and water uptake that occurs through the cell, and also allows a detailed look at the constituent transport modes. The theoretical technique therefore demonstrates the common nature of electrochemical transport in fuel cell materials and provides a fundamentally common mechanistic approach that can be readily applied in order to simulate it.

7.7 References

1 **Wang CY.** Fundamental Models for Fuel Cell Engineering. *Chem. Rev.*, 2004, **104**(10), 4727-4766

2 **Weber AZ, Newman J.** Modeling Transport in Polymer-Electrolyte Fuel Cells. *Chem. Rev.*, 2004, **104**(10), 4679-4726

3 **Springer T, Zawodzinksi T, Gottesfeld S.** Polymer Electrolyte Fuel Cell Model. *J. Electrochem. Soc.*, 1991, **138**, 2334-2342

4 **Bernardi D, Verbrugge M.** A Mathematical Model of the Solid-Polymer-Electrolyte Fuel Cell. *J. Electrochem. Soc.*, 1992, **139**, 2477-2491

5 **Fuller T, Newman J.** Water and Thermal Management in Solid-Polymer Electrolyte Fuel Cells. *J. Electrochem. Soc.*, 1993, **140**, 1218–1225.

6 **Wang CY, Cheng P.** Multiphase Flow and Heat Transfer in Porous Media. *Adv. Heat Transfer*, 1997, **30**, 93-182

7 **Wang ZH, Wang CY, Chen KS.** Two-Phase Flow and Transport in the Air Cathode of Proton Exchange Membrane Fuel Cells. *J. Power Sources*, 2001, **94**, 40-50

8 **Pasaogullari U, Wang CY.** Two-Phase Transport and the Role of Micro-Porous Layer in Polymer Electrolyte Fuel Cells. *Electrochim. Acta*, 2004, **49**, 4359-4369

9 **Pasaogullari U, Wang CY.** Liquid Water Transport in Gas Diffusion Layer of Polymer Electrolyte Fuel Cells. *J. Electrochem. Soc.*, 2004, **151**(3), A399-A406

10 **Pasaogullari U, Wang CY.** Two-Phase Modeling and Flooding Prediction of Polymer Electrolyte Fuel Cells. *J. Electrochem. Soc.*, 2005, **152**(2), A380-A390

11 **Pasaogullari U, Wang CY, Chen KS.** Two-Phase Transport in Polymer Electrolyte Fuel Cells with Bilayer Cathode Gas Diffusion Media. *J. Electrochem. Soc.*, 2005, **152**(8), A1574-A1582

12 **Luo G, Ju H, Wang CY.** Prediction of Dry-Wet-Dry Transition in Polymer Electrolyte Fuel Cells. *J. Electrochem. Soc.*, 2007, **154**(3), B316-B321

13 **Wang Y, Wang CY.** Two-Phase Transients of Polymer Electrolyte Fuel Cells. *J. Electrochem. Soc.*, 2007, **154**(7), B636-B643

14 **Birgersson E, Noponen M, Vynnycky M.** Analysis of a Two-Phase Non-Isothermal Model for a PEFC. *J. Electrochem. Soc.*, 2005, **152**(5), A1021-A1034

15 **Djilali N, Lu D.** Influence of Heat Transfer on Gas and Water Transport in Fuel Cells. *Int. J. Therm. Sci.*, 2002, **41**, 29-40

16 **Berning T, Djilali N.** A 3D, Multiphase, Multicomponent Model of the Cathode and Anode of a PEM Fuel Cell. *J. Electrochem. Soc.*, 2003, **150**(12), A1589-A1598

17 **Acosta M, Merten C, Eigenberger G, Class H, Helmig R, Thoben B, Muller-Steinhagen H.** Modeling Non-Isothermal Two-Phase Multicomponent Flow in the Cathode of PEM Fuel Cells. *J. Power Sources*, 2006, **159**, 1123-1141

18 **Ziegler C, Hellmann T, Gerteisen D.** Experimental Study of Two-Phase Transients in a PEMFC. *J. Electrochem. Soc.*, 2008, **155**(4), B349-B355

19 **Ziegler C, Yu HM, Schumacher JO.** Two-Phase Dynamic Modeling of PEMFCs and Simulation of Cyclo-Voltammograms. *J. Electrochem. Soc.*, 2005, **152**(8), A1555-A1567

20 **Natarajan D, Van Nguyen T.** A Two-Dimensional, Two-Phase, Multicomponent, Transient Model for the Cathode of a Proton Exchange Membrane Fuel Cell Using Conventional Gas Distributors. *J. Electrochem. Soc.*, 2001, **148**(12), A1324-1335

21 **Nam JH, Kaviany M.** Effective Diffusivity and Water-Saturation Distribution in Single- and Two-Layer PEMFC Diffusion Medium. *Int. J. Heat Mass Tran.*, 2003, **46**, 4595-4611

22 **Hanamura K, Kaviany M.** Propagation of Condensate Front in Steam Injection into Dry Porous Media. *Int. J. Heat Mass Tran.*, 1995, **38**(8), 1377-1386

23 **Mazumader S, Cole JV.** Rigorous 3-D Mathematical Modeling of PEM Fuel Cells I. Model Predictions without Liquid Water Transport. *J. Electrochem. Soc.*, 2003, **150**(11), A1503-A1509

24 **Mazumader S, Cole JV.** Rigorous 3-D Mathematical Modeling of PEM Fuel Cells II. Model Predictions with Liquid Water Transport. *J. Electrochem. Soc.*, 2003, **150**(11), A1510-A1517

25 **Ye Q, Van Nguyen T.** Three-Dimensional Simulation of Liquid Water Distribution in a PEMFC with Experimentally Measured Capillary Functions. J. Electrochem. Soc., 2007, **154**(12), B1242-B1251

26 **Wang X, Van Nguyen T.** Modelling the Effects of Capillary Property of Porous Media on the Performance of the Cathode of a PEMFC. *J. Electrochem. Soc.*, 2008, **155**(11), B1085-B1092

27 **McKay D, Siegel JB, Ott W, Stefanopoulou AG.** Parameterization and Prediction of Temporal Fuel Cell Voltage Behaviour During Flooding and Drying Conditions. *J. Power Sources*, 2008, 207-222

28 **Leverett MC.** Capillary Behaviour in Porous Solids. *Transactions of the AIME*, 1941, **142**, 159-172

29 **Gostick JT, Fowler MW, Ioannidis MA, Pritzker MD, Volfkovich YM, Sakars A.** Capillary Pressure and Hydrophilic Porosity in Gas Diffusion Layers for Polymer Electrolyte Fuel Cells. *J. Power Sources*, 2006, **156**, 375-387

30 **Weber AZ, Darling RM, Newman J.** Modeling Two-Phase Behaviour in PEFCs. *J. Electrochem. Soc.*, 2004, **151**(10), A1715-A1727

31 **Harkness IR, Hussain N, Smith L, Sharman JDB.** The use of a novel water porosimeter to predict the water handling behaviour of gas diffusion media used in polymer electrolyte fuel cells. *J. Power Sources*, 2009, ***193**, 122-129*

32 **Lin G, Van Nguyen T.** Effect of Thickness and Hydrophobic Polymer Content of the Gas Diffusion Layer on Electrode Flooding Level in a PEMFC. *J. Electrochem. Soc.*, 2005, **152**(10), A1942-A1948

33 **Malevich D, Halliop E, Peppley BA, Pharoah JG, Karan K.** Investigation of Charge-Transfer and Mass-Transfer Resistances in PEMFCs with Microporous Layer Using Electrochemical Impedance Spectroscopy. *J. Electrochem. Soc.*, 2009, **156**(2), B216-B224

34 **Pisani L, Valentini M, Murgia G.** Analytical Pore Scale Modeling of the Reactive Regions of Polymer Electrolyte Fuel Cells. *J. Electrochem. Soc.*, 2003, **150**(12), A1549-A1559

35 **Lin G, He W, Van Nguyen T.** Modeling Liquid Water Effects in the Gas Diffusion and Catalyst Layers of the Cathode of a PEM Fuel Cell. *J. Electrochem. Soc.,* 2004, **151**(12), A1999-A2006

36 **Eikerling M, Kornyshev AA.** Modelling the Performance of the Cathode Catalyst Layer of Polymer Electrolyte Fuel Cells. *J. Electroanal. Chem.*, 1998, **453**, 89-106

37 **Eikerling M, Kornyshev AA.** Proton Transfer in a Single Pore of a Polymer Electrolyte Membrane. *J. Electroanal. Chem.*, 2001, **502**, 1-14

38 **Wang Q, Eikerling M, Song D, Liu Z.** Structure and Performance of Different Types of Agglomorates in Cathode Catalyst Layers of PEM Fuel Cells. *J. Electroanal. Chem.*, 2004, **573**, 61-69

39 **Berg P, Promislow K, St. Pierre J, Stumper J, Wetton B.** Water Management in PEM Fuel Cells. *J. Electrochem. Soc.*, 2004, **151**(3), A341-A353

40 **Ge S, Li X, Yi B, Hsing IM.** Absorption, Desorption, and Transport of Water in Polymer Electrolyte Membranes for Fuel Cells. *J. Electrochem. Soc.,* 2005, **152**(6), A1149-A1157

41 **Sinha PK, Wang CY, Beuscher U.** Transport Phenomenon in Elevated Temperature PEM Fuel Cells. *J. Electrochem. Soc.,* 2007, **154**(1), B106-B116

42 **Bashchuk JJ, Li X.** A Comprehensive, Consistent and Systematic Mathematical Model of PEM Fuel Cells. *Applied Energy*, 2009, **86**, 181-193

43 **Verbrugge MW, Hill RF.** Ion and Solvent Transport in Ion-Exchange Membranes I. A Macrohomogeneous Mathematical Model. *J. Electrochem. Soc.*, 1990, **137**(3), 886-893

44 **Verbrugge MW, Hill RF.** Ion and Solvent Transport in Ion-Exchange Membranes II. A Radiotracer Study of the Sulfuric-Acid, Nafion-117 System. *J. Electrochem. Soc.*, 1990, **137**(3), 893-899

45 **Verbrugge MW, Hill RF.** Transport Phenomena in Perfluorosulfonic Acid Membranes during the Passage of Current. *J. Electrochem. Soc.,* 1990, **137**(4), 1131-1138

46 **Bernardi DM, Verbrugge MW.** Mathematical Model of a Gas-Diffusion Electrode Bonded to a Polymer Electrolyte. *AIChE J.*, 1991, **37**, 1151-1163

47 **Singh D, Lu DM, Djilali N.** A Two-Dimensional Analysis of Mass Transport in Proton Exchange Membrane Fuel Cells. *Int. J. Eng. Sci.*, 1999, **37**, 431-452

48 **Berg P, Promislow K, St Pierre J, Stumper J, Wetton B.** Water Management in PEM Fuel Cells. *J. Electrochem. Soc.*, 2004, **151**(3), A341-A353

49 **Janssen GJM.** A Phenomenological Model of Water Transport in a Proton Exchange Membrane Fuel Cell. *J. Electrochem. Soc.,* 2001, **148**(12), A1313-A1323

50 **Bass M, Freger V.** An Experimental Study of Schroeder's Paradox in Nafion and Dowex Polymer Electrolytes. *Desalination*, 2006, **199**, 277-279

51 **Vallieres C, Winklemann D, Roizard D, Favre E, Scharfer P, Kind M.** On Schroeder's Paradox. *J. Membrane Sci.*, 2006, **278**, 357-364

52 **Weber AZ, Newman J.** Transport in Polymer-Electrolyte Membranes I. Physical Model. *J. Electrochem. Soc.*, 2003, **150**(7), A1008-A1015

53 **Weber AZ, Newman J.** Transport in Polymer-Electrolyte Membranes II. Mathematical Model. *J. Electrochem. Soc.*, 2004, **151**(2), A311-A325

54 **Weber AZ, Newman J.** Transport in Polymer-Electrolyte Membranes III. Model Validation in a Simple Fuel-Cell Model. *J. Electrochem. Soc.*, 2004, **151**(2), A326-A339

55 **Weber AZ, Darling RM, Newman J.** Modeling Two-Phase Behaviour in PEFCs. *J. Electrochem. Soc.*, 2004, **151**(10), A1715-A1727

56 **Weber AZ, Newman J.** A Theoretical Study of Membrane Constraint in Polymer-Electrolyte Fuel Cells. *AIChE Journal*, 2004, **50**(12), 3215-3226

57 **Newman J.** *Electrochemical Systems*, 1973 (Prentice-Hall, Inc. Englewood Cliffs, New Jersey)

58 **Zawodzinski TA, Derouin C, Radzinski S, Sherman RJ, Smith VT, Springer TE, Gottesfeld S.** Water Uptake by and Transport Through Nafion 117 Membranes. *J. Electrochem. Soc.*, 1993, **140**(4), 1041-1047

59 **Slade S, Campbell SA, Ralph TR, Walsh FC.** Ionic Conductivity of an Extruded Nafion 1100 EW Series of Membranes. *J. Electrochem. Soc.,* 2002, **149**(12), A1556-A1564

60 **Kumbur EC, Sharp KV, Mench MM.** Validated Leverett Approach for Multiphase Flow in PEFC Diffusion Media III. Temperature Effect and Unified Approach. *J. Electrochem. Soc.*, 2007, **154**(12), B1315-B1324

61 **Zeigler C, Gerteisen D.** Validity of two-phase polymer electrolyte membrane fuel cell models with respect to the gas diffusion layer. *J. Power Sources*, 2009, **188**, 184-191

62 **Lyons WC, Plisga GS.** *Standard Handbook of Petroleum & Natural Gas Engineering*, 2009 (Gulf Professional Publishing, Houston)

63 **Ye X, Wang CY.** Measurement of Water Transport Properties Through Membrane-Electrode Assemblies I. Membranes. *J. Electrochem. Soc.,* 2007, **154**(7), B676-B682

64 **Meier F, Kerres J, Eigenberger G.** Characterisation of Polyaryl-Blend-Membranes for DMFC Applications. *J. New Mater. Elect. Syst.*, 2002, **5**, 91-96

65 **Meier F, Eigenberger G.** Transport Parameters for the Modelling of Water Transport in Ionomer Membranes for PEM Fuel Cells. *Electrochim Acta*, 2004, **49**, 1731-1742

66 **Volfkovich YM, Bagotzky VS, Sosenkin VE, Blinov IA.** The Standard Contact Porosimetry. *Colloid. Surface. A*, 2001, **187-188**, 349-365

67 **Divisek J, Eikerling M, Mazin V, Schmitz H, Stimming U, Volfkovich YM.** A Study of Capillary Porous Structure and Sorption Properties of Nafion Proton-Exchange Membranes Swollen in Water. *J. Electrochem. Soc.*, 1998, **145**(8), 2677-2683

68 **Hsu WY, Barkley JR, Meakin P.** Ion Percolation and Insulator-to-Conductor Transition in Nafion Perfluorosulfonic Acid Membranes. *Macromolecules*, 1980, **13**(1), 198-200

69 **Lehtinen T, Sundholm G, Holmberg S, Sundholm F, Bjornbom P, Bursell M.** Electrochemical Characterization of PVDF-based Proton Conducting Membranes for Fuel Cells. *Electrochemica Acta*, 1998, **43**(12-13), 1881-1890

70 **Thampan T, Malhotra S, Tang H, Datta R.** Modeling of Conductive Transport in Proton-Exchange Membranes for Fuel Cells. *J. Electrochem. Soc.*, 2000, **147**(9), 3242-3250

71 **Rumbaugh J, Blaha M, Premerlani W, Eddy F, Lorensen W.** *Object-Oriented Modeling and Design*, 1991 (Prentice-Hall, Inc., Englewood Cliffs)

72 **Meyer B.** *Object-oriented Software Construction,* 1988 (Prentice-Hall International Ltd, UK)

73 **Takaichi S, Uchida H, Watanabe M.** Response of Specific Resistance Distribution in Electrolyte Membrane to Load Change at PEFC Operation. *J. Electrochem. Soc.*, 2007, **154**(12), B1373-B1377

74 **Ikeda T, Koido T, Tsushima S, Hirai S.** MRI Investigation of Water Transport Mechanism in a Membrane under Elevated Temperature Condition with Relative Humidity and Current Density Variation. *Electrochemical Society Transactions*, 2008, **16**(2), 1035-1040

75 **St-Pierre J.** PEMFC In Situ Liquid-Water-Content Monitoring Status. *J. Electrochem. Soc.*, 2007, **154**(7), B724-B731

8 Water Transport Studies

In this chapter, the electrochemical PEFC model developed in chapter 7 is applied to investigate a number of practical factors that affect water transport across the PEM in a PEFC. The effects of PEM thickness, anode humidification and PEM constraint on two-phase water transport for a cell with a non-reinforced PEM are investigated. The effect of structural reinforcement within the PEM on water transport is also investigated.

8.1 Introduction

To test the mechanistic equations developed in chapters five and six, the models generated therewith were applied to simulate transport characteristics across the PEFC under vapour-phase conditions. However, water transport characteristics across the cell are likely to change when the operating conditions and cell configuration invoke two-phase conditions at the cathodic PEM boundary and single-phase conditions at the anodic PEM boundary. This is a commonly-observed phenomenon in operational fuel cells. The aim of this chapter is to generate a basic understanding of how water distributes within the non-reinforced PEM under these conditions and how the distribution relates to the underlying transport processes using the two-phase model developed in chapter seven. Three rudimentary parameters are considered individually in the two-phase study initially; PEM thickness, anode humidification and cell compression. The study then holistically considers the effect of all three parameters on the Ohmic resistance of the PEM.

The final part of this chapter focuses on structurally-reinforced membranes and aims to elucidate the effect that structural reinforcement has on water transport. The model is applied to simulate measured data points for resistance across the polymer electrolyte, which are obtained using electrochemical impedance spectroscopy (EIS). For each simulated data point, the model reveals the magnitude of the underlying transport mechanisms and the water content, which is collected and discussed.

8.2 Non-Reinforced Membranes

To carry out water transport studies for a PEFC with a non-reinforced PEM, a number of simulations were run to determine a general set of representative fuel cell operating conditions where two-phase transport within the layers of the cell can be achieved without completely flooding the cathodic porous layers. These parameters are summarised in Table 8-1. These parameters were used for all simulations in this chapter unless stated otherwise.

Parameter	**Value**
Anode supply conditions	
Anode inlet pressure	1 bar
H_2 supply flow rate	0.5 slpm
Anode RH	0%
Cathode supply conditions	
Cathode inlet pressure	1.5 bar
Air supply flow rate	0.5 slpm
Air humidification temperature	363.15 K
Cathode RH	100%
Cell Parameters	
Active cell area	25cm^2
Cell temperature	333.15 K
Cell compression	0 MPa
GDL Properties – Anode and Cathode [1]	
GDL porosity	0.9
GDL thickness	300 μm
GDL tortuosity	1.5
GDL PTFE content	5%
GDL permeability	1×10^{-8} cm^2
MPL Properties – Anode and Cathode [1,2]	
MPL porosity	0.4
MPL thickness	25 μm
MPL tortuosity	1.5
MPL PTFE content	23%
MPL permeability	1×10^{-9} cm^2

Table 8-1 Base operating conditions & material properties used in the PEFC model for the water transport studies, unless otherwise stated.

8.2.1 PEM Thickness

The PEM is characterised by two fundamental properties that can be set through material selection, namely the equivalent weight and the thickness of the PEM. Early PEFCs commonly employed Nafion 117 which has an equivalent weight of **11**00 g/mol and thickness of **7** mils (178 μm). However modern PEMs are typically much thinner and can be structurally reinforced. Examples include Gore-18 and Gore-25 which have 18 and 25 μm thicknesses respectively. Non-reinforced membranes include DuPont-manufactured Nafion 1135, NRE-211 and NRE-212 which have 89, 25 and 51 μm thicknesses respectively. The equivalent weight of the reinforced membranes is typically 950 g/mol whereas the non-reinforced membranes have the same equivalent weight as Nafion 117. The structural reinforcement can limit the diffusivity of water across the polymer electrolyte, which affects net water transport. This will be investigated separately in section 8.3. This sub-section will focus on the effects of PEM thickness at an equivalent weight of 1100 g/mol.

The transition towards thinner PEMs has occurred because the thinness of the PEM can enhance its hydration and therefore its proton conductivity under working fuel cell conditions, as shown by single-phase simulations [3]. The precise effect that the thickness of the PEM has on two-phase transport across it is relatively less well-defined. The effect of five PEM thicknesses are considered in the current study; 25.4, 36.8, 50.8, 63.5 and 76.2 μm.

Figure 8-1 shows the expanded thickness of the unconstrained PEM according to the simulated water uptake. Figure 8-1 also shows that in all five cases, the thickness of the free-swelling PEM increases by over 10% of its original value. The percentage expansion falls as a function of PEM thickness suggesting that the thinner membranes are most susceptible to dimensional change as a consequence of water uptake for the simulated conditions. For the conditions given in Table 8-1, the anodic porous layers do not experience liquid phase transport; however, the cathodic porous layers do which results in a liquid phase boundary pressure at the cathodic PEM interface. The single phase boundary conditions at the anode interface and two phase boundary condition at the cathode interface result in a transitional regime across the PEM where both vapour- and liquid- equilibrated networks co-exist. Figure 8-2 shows the water content profile across the PEM while Figure 8-3 shows the liquid pressure and corresponding pore expansion profiles.

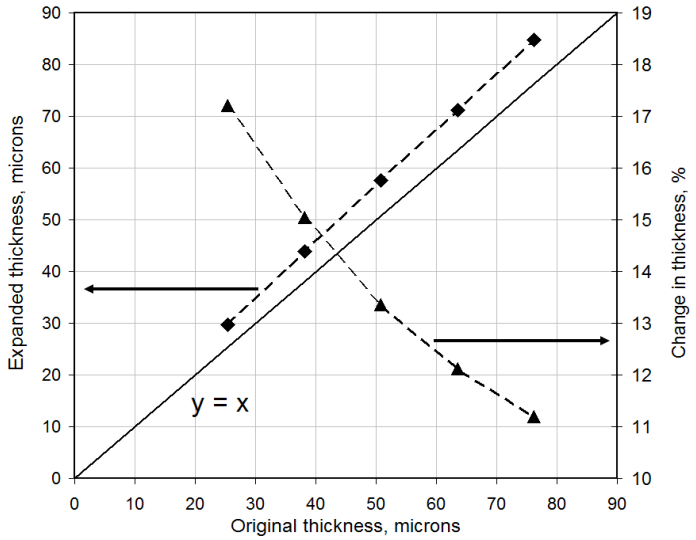

Figure 8-1 Expanded membrane thickness and percentage change in thickness as a function of the original thickness for five simulated PEM thicknesses

Figure 8-2 shows that for all five cases the water content through the PEM increases above 14 water molecules per charge site. Because of the single-phase boundary conditions at the anode, the local water content at this interface is well below 14 for all cases. In the case of the 25.4 μm PEM, the interfacial water content approaches 10. From Figure 8-2, it can be seen that the λ=14 limit is reached within a short distance from the anodic boundary in the thinner PEMs. The liquid phase therefore penetrates a greater proportion of its thickness from the cathode interface than in the thicker PEMs, as evident in Figure 8-3 (a).

Figure 8-3 (b) shows the pore expansion that results from the intrusion of the liquid phase. For the boundary conditions considered here, the pore expansion occurs gradually, increasing steadily from zero where the vapour-only regime ends towards unity at the cathodic PEM boundary. The actual depth of liquid penetration is between 14 μm and 17 μm for all five cases as shown in Figure 8-4 which indicates that the thickness of the PEM does not significantly control the absolute depth of liquid water intrusion.

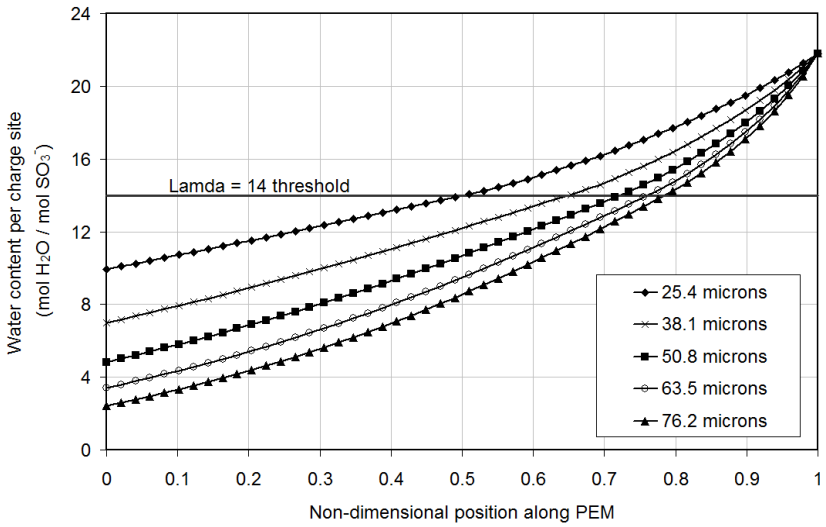

Figure 8-2 Water content profile as a function of non-dimensional position along the expanded PEM thickness for the five different PEM thicknesses

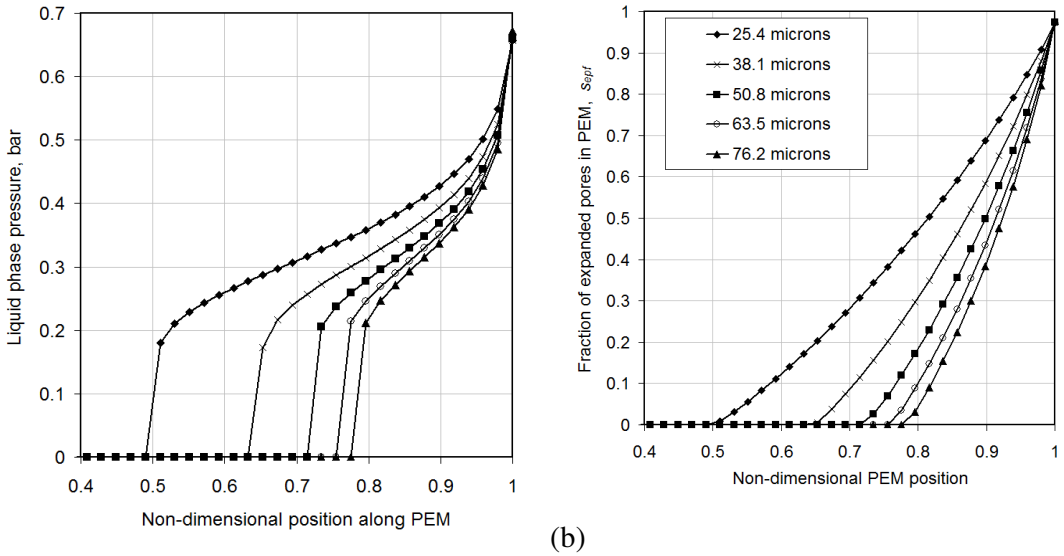

(a) (b)

Figure 8-3 Liquid intrusion profiles for five different PEM thicknesses as a function of non-dimensional position along the expanded PEM thickness. (a) Liquid pressure; (b) pore expansion profile. Note that the x-axis starts at 0.4.

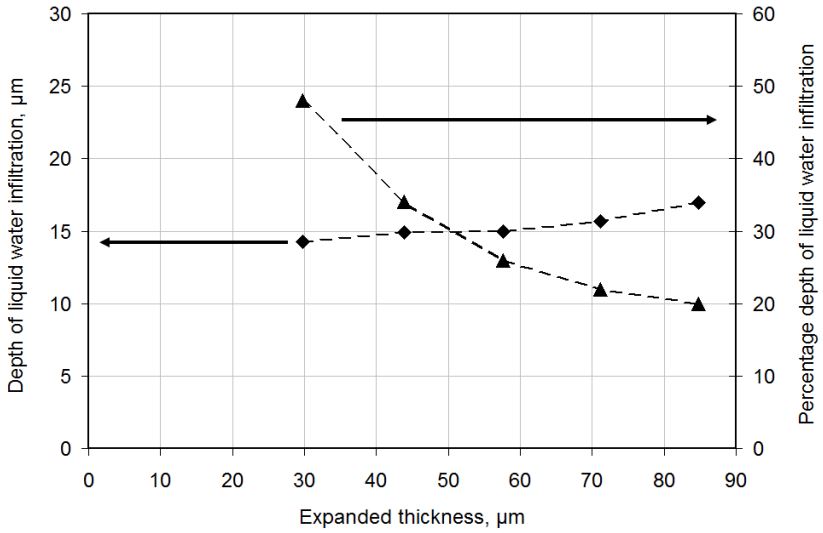

Figure 8-4 Depth of liquid water penetration from cathodic PEM boundary for five PEM thicknesses.

Figure 8-5 shows the direction and magnitude of the net water transport per proton, β, across the PEM and Figure 8-6 resolves the vapour and gas phase components of net water transport within the PEM as a function of thickness for the five thicknesses considered. The components of net water transport per proton in the vapour- and liquid- equilibrated networks can be calculated as;

$$\beta_{vap} = (1 - s_{epf})\beta = (1 - s_{epf})\frac{\alpha}{2} \tag{8-1}$$

$$\beta_{liq} = s_{epf}\beta = s_{epf}\frac{\alpha}{2} \tag{8-2}$$

The calculated results given in Figure 8-5 show that for the simulated conditions, the net water flux occurs in the direction of the anode and is mainly dominated by vapour phase transport. It should be noted that the magnitude of the average vapour and liquid phase components of net water flux do not reflect the continuous flow of water in their respective phases from one boundary of the PEM to the other, but the thickness-averaged fluxes that occurs in the collapsed and expanded regions of the PEM. Figure 8-5 indicates that the contribution of liquid phase flow generally remains unchanged as the thickness of the PEM is increased and that its average flux always occurs in the direction of the cathode.

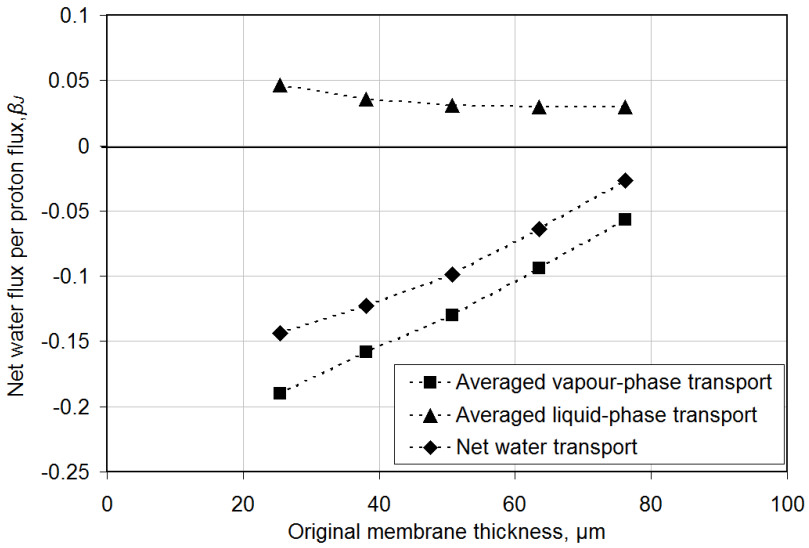

Figure 8-5 Net water transport per proton and average vapour and liquid phase components for five PEM thicknesses

Figure 8-6 shows that in all five cases, there is a steady vapour-phase flux across the PEM in the regions where there is no liquid water intrusion and no corresponding liquid phase flux. However, in the regions where liquid water does intrude the PEM, both vapour and liquid phase fluxes change non-linearly in the shape of two opposing arcs. The liquid phase flux increases from zero heading in the direction of the cathode, peaks, and then decreases. The vapour phase flux increases in magnitude from the steady-state value for the vapour-only regime heading in the direction of the anode, peaks and then decreases. In the case of the thinner PEMs, because the relative depth of liquid infiltration is greater, the bi-modal non-linear transport develops at a much closer distance to the anode than in the case of the thicker PEMs where it is retarded towards the cathode. In order to understand the nature of the non-linearity, attention has to be turned to the underlying phenomenological transport processes.

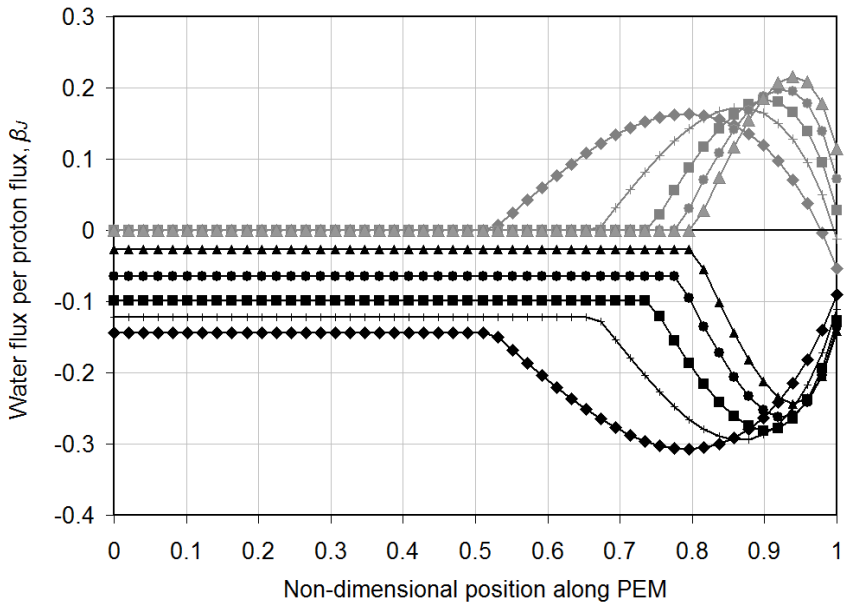

Figure 8-6 Water flux per proton as a function of non-dimensional position along PEM thickness. Grey - liquid phase; black – vapour. (♦) 25.4 μm; (+) 38.1 μm; (■) 50.8 μm; (●) 63.5 μm; (▲) 76.2 μm.

Theoretically, the general transport equation given in equation (7-15) can be resolved into six components of net water transport, namely that due to proton movement, convection and diffusion each in liquid phase and vapour phases. The magnitude of each component can be derived as:

$$\beta_{H+,vap} = \left(1 - s_{epf}\right)\frac{\Phi_{2,vap}}{2\Phi_1};\ \beta_{H+,liq} = s_{epf}\frac{\Phi_{2,liq}}{2\Phi_1} \tag{8-3}$$

$$\beta_{conv,vap} = \left(1 - s_{epf}\right)\frac{\Phi_{3,vap}}{2I\Phi_1};\ \beta_{conv,liq} = s_{epf}\frac{\Phi_{3,liq}}{2I\Phi_1} \tag{8-4}$$

$$\beta_{diff,vap} = \left(1 - s_{epf}\right)\frac{c_{tot}}{2I\Phi_1}\nabla c_w;\quad \beta_{diff,liq} = s_{epf}\frac{c_{tot}}{2I\Phi_1}\nabla c_w \tag{8-5}$$

and by definition

$$\beta_J = \beta_{H+,J} + \beta_{conv,J} + \beta_{diff,J} \tag{8-6}$$

where J denotes phase. The water flux due to proton movement occurs as a combination of proton diffusion and electro-osmotic proton flux due to the electric field. The net water transport per proton flux is defined as;

$$\beta = \sum \beta_{\text{mode},vap} + \sum \beta_{\text{mode},liq} \tag{8-7}$$

Based on these parameters, it is possible to resolve the liquid and vapour curves for the 25.4 μm PEM given in Figure 8-6 into constituent parts. Figure 8-7 shows the corresponding water transport curves as a function of PEM thickness fraction. Convection in the vapour-equilibrated network is assumed to be negligible according to the assumptions of the model, and so $\beta_{conv,vap} = 0$.

From the results in Figure 8-7 it becomes immediately evident that water transport across the PEM is mainly dominated by its diffusion through the PEM and its interaction with proton movement. Along the first 50% of the thickness of the PEM, water transport is dominated by diffusion and proton-induced flux in the vapour-equilibrated network in the absence of liquid water infiltration. The diffusive flux occurs in the direction of the anodic boundary where there is less water than the cathode boundary, as evident in Figure 8-2. The proton flux occurs in the opposite direction, which causes the proton-induced water flux in the vapour-equilibrated network to occur in the direction of the cathode as well. From these two transport modes, it is the diffusive flux which is greater in magnitude and therefore results in a net water flux in the direction of the anode. Along the latter 50% of the thickness of the PEM, both vapour- and liquid-equilibrated transport modes occur, which results in additional diffusive and a proton-induced water flux in the liquid-equilibrated network. As the infiltration of liquid water and the pore expansion increases towards the cathodic boundary, the magnitude of the fluxes in the vapour-equilibrated networks tail-off, while the liquid phase fluxes in the liquid-equilibrated networks become more dominant and increase in magnitude. These characteristics explain the non-linear nature of the liquid and vapour components of the net water flux described in Figure 8-6. In an identical manner to the vapour phase fluxes, the liquid phase diffusive flux occurs in the direction of the anode, whereas the proton-induced flux occurs in the direction of the cathode. The interesting observation here for liquid phase transport is that it is the proton-induced flux which marginally dominates over the diffusive flux and results in an average liquid phase flux that

occurs in the direction of the cathodic boundary, as indicated by Figure 8-5. This can be attributed to equation 7-45 which reflects the fact that the electro-osmotic drag coefficient in a liquid-infiltrated region will be higher than in the collapsed regions. These basic characteristics are generally true for the remaining four membrane thicknesses as well, and so do not need to be discussed individually.

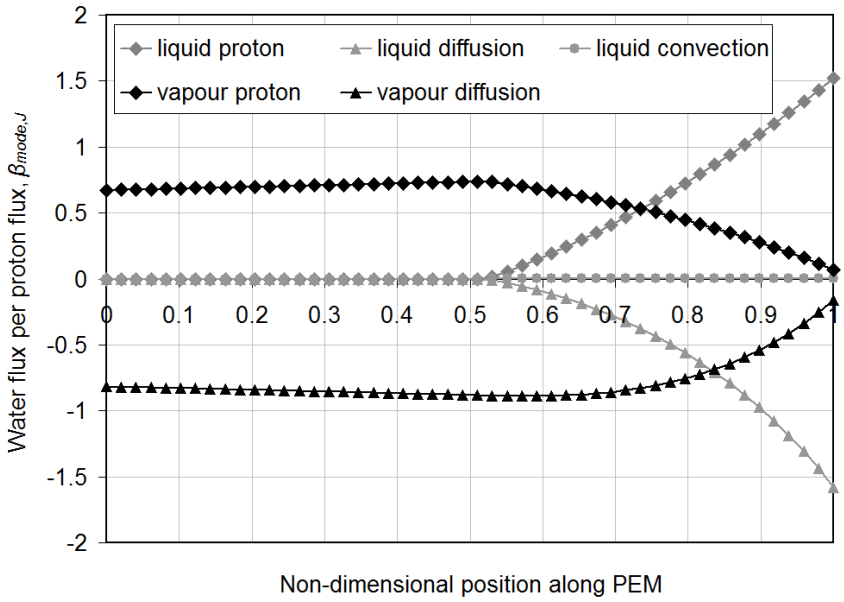

Figure 8-7 Vapour and liquid phase components of net water transport as a function of position along PEM thickness for the 25.4 µm PEM case.

Figure 8-8 confirms that the gradient in water content throughout the thickness of the PEM is greatest in the thinner membranes, which invokes a large diffusive component of net water transport towards the anode, particularly in the dominant vapour-equilibrated network as observed in Figure 8-5 – Figure 8-7. As the thickness increases, the gradient in water content reduces, which will reduce the diffusive component of net water transport for both phases. Interestingly, for the five thicknesses considered the gradient in water content in general increases quite suddenly in the liquid-infiltrated region. The large consequent diffusive flux created towards the anode in the liquid phase as shown in Figure 8-7 is however not sufficient to overcome the proton induced flux in the opposite direction.

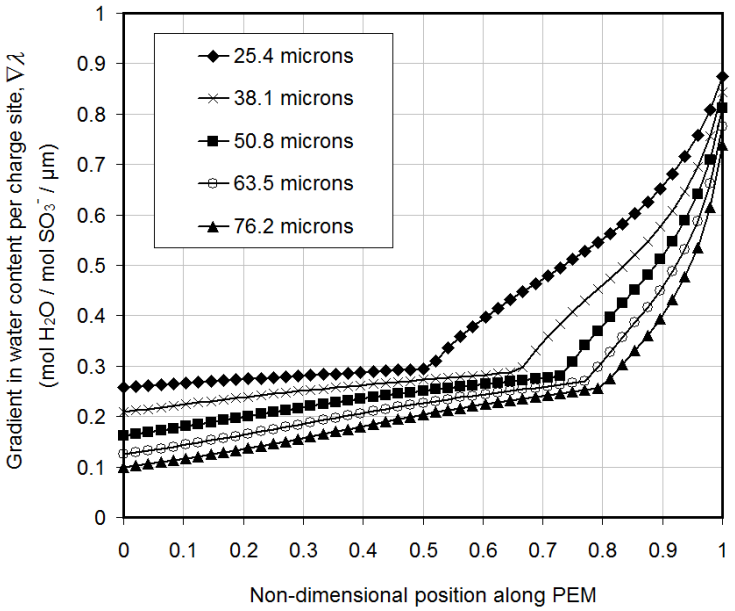

Figure 8-8 PEM water content profile as a function of the non-dimensional membrane position for five PEM thicknesses. The gradient in water content λ' is defined as the local change in water molecules per charge site divided by the length increment in μm.

8.2.2 Anode Humidification

One way of improving the hydration of the PEM from the anodic boundary is to humidify the fuel supply, although there is a system-level penalty to be paid for the increased complexity. Although the implications of anode humidification on water uptake has been well defined for single-phase vapour-equilibrated conditions, it is less well defined for when liquid water intrudes the PEM. Figure 8-9(a) shows the calculated water content as a function of PEM thickness fraction for the five thicknesses considered in the previous subsection; all operating conditions are the same as those given in Table 8-1 apart from the anode RH which is now set to 100%. Compared to Figure 8-2, it is evident that fuel humidification directly improves the hydration of the PEM from the anodic boundary. In the case of the 25.4 µm PEM, the water content at the anodic boundary has increased from around 10 water molecules per charge site to 13. In the case of the 76.2 µm PEM, the water content at the same interface has increased from above 2 molecules per charge site to around 6. Figure 8-9(b) shows that the additional humidity affects the liquid water network in the PEM. Compared to Figure 8-3, it can be seen that the liquid network intrudes a much larger

proportion of the membrane thickness. For the 25.4 μm PEM, the liquid water network now intrudes around 85% of its thickness and over 35% in the case of the 76.2 μm PEM.

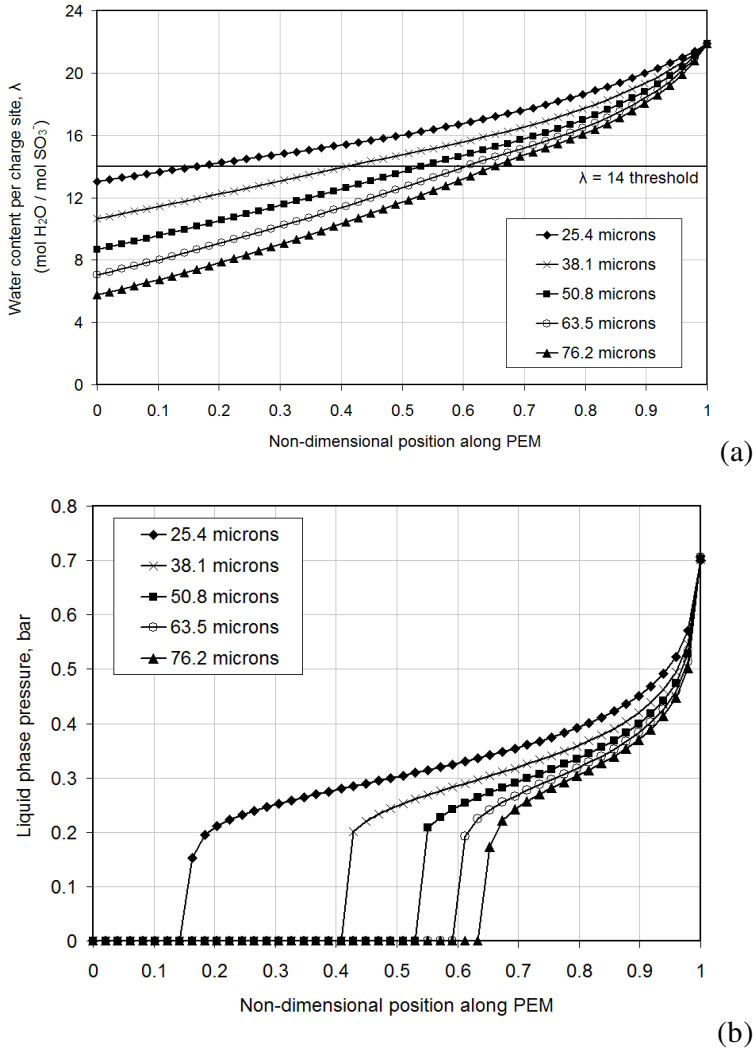

Figure 8-9 Liquid intrusion profiles for five different PEM thicknesses as a function of non-dimensional position along the expanded PEM thickness. (a) Water content; (b) liquid intrusion pressure profile.

Figure 8-10 shows the net water flux per proton across the PEM for each of the five cases, and the constituent average parts in vapour- and liquid- equilibrated networks. The results here are different to those in Figure 8-5. The average water transport per proton in the liquid network occurs in the direction of the anodic boundary, as observed previously. However, with the addition of anode humidification, the average vapour phase transport occurs in the direction of the cathodic boundary. This can be explained by Figure 8-11,

which shows the diffusion and proton-induced components of the vapour-equilibrated flux for the 38.1 μm PEM. The results suggest that with anode humidification, because the PEM is inherently better hydrated, the magnitude of the drag component induced by proton flux towards the cathodic boundary is greater relative to the magnitude of the diffusive component in the opposite direction. The net vapour phase component is therefore positive. The exception to this observation is the 25.4 μm PEM, which suggests a dependence on membrane thickness.

For the 25.4 μm PEM, Figure 8-11 (a) shows that the proton-induced flux is greater than the diffusive flux in the vapour-only region closest to the anode. However, the proton-induced vapour phase flux decreases in magnitude more abruptly than the diffusive vapour phase flux as liquid infiltration increases towards the cathode. Overall, therefore, the diffusive flux dominates in the vapour-equilibrated network and results in a net vapour phase flux occurring in the direction of the anode, as shown in Figure 8-10. The proton-induced flux is continuously greater in magnitude than the diffusive flux in the liquid-equilibrated network, which explains the observation of Figure 8-10 and results in a large net liquid-phase flux occurring in the direction of the cathode.

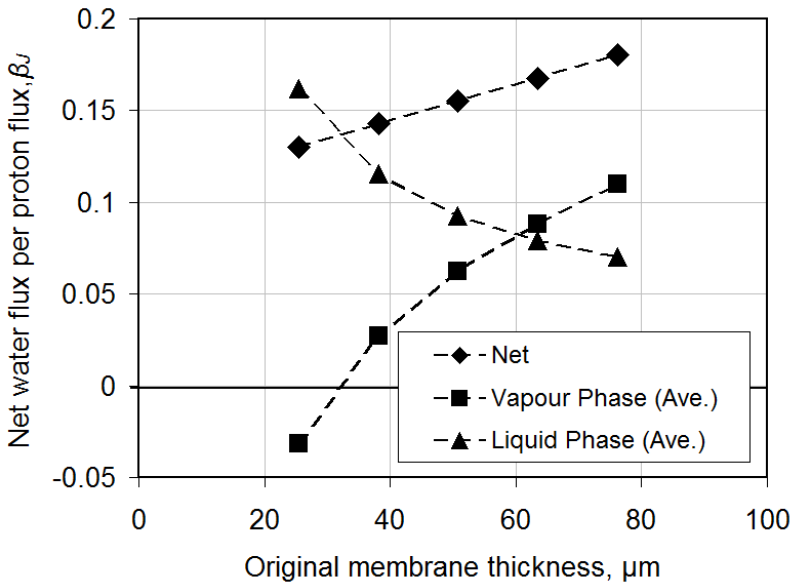

Figure 8-10 Net water transport per proton and average vapour and liquid phase components for five PEM thicknesses. Anode and cathode supplies are saturated

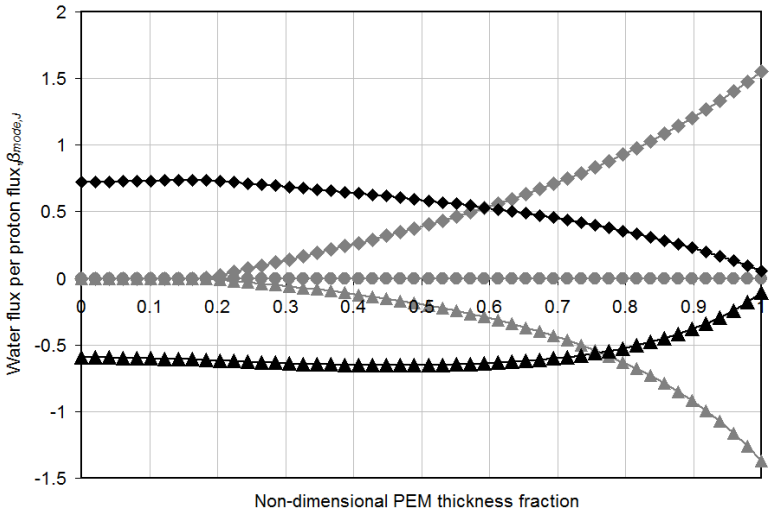

(a)

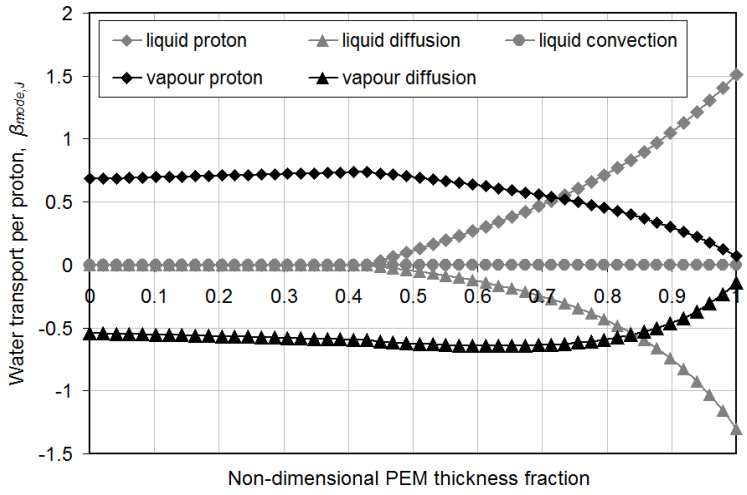

(b)

Figure 8-11 Vapour and liquid phase components of net water transport as a function of position along PEM thickness with both fuel supplies fully humidified. (a) 25.4 μm case; (b) 38.1 μm case.

8.2.3 PEM Constraint

Operational fuel cells are typically compressed to minimise reactant leaks from the peripheries and to ensure good contact between the electron-conducting layers of the cell. In an unconstrained state, the PEM has a natural tendency to swell with water uptake. If the compressive force applied to the cell is sufficiently high, the PEM may also become physically compressed under certain operating conditions. If on the other hand the

compressive force is relatively low, it may allow the PEM to swell and may subsequently impart a compressive force onto the adjacent layers of the cell. By limiting the natural tendency of the PEM to swell, there is a reduction in the amount of water that the polymer end groups can hold. This may affect water management strategies and could affect cell performance. The purpose of this part of the study therefore is to examine what role membrane constraint has on net water transport and water uptake when the PEM is subjected to two-phase conditions at the cathodic boundary.

Figure 8-12 (a) shows the effects of compression on the thickness of the 25.4 μm PEM. In the unconstrained state, the thickness of the PEM increases by over 15% of its dry-state value. However, as constraint is increased, the expansion is curtailed. The point of zero dimensional change occurs in this case when the degree of constraint is just above 0.4. In the fully constrained state, the thickness of the PEM is reduced by around 25% of its dry-state value. The effect on the average water content is shown in Figure 8-12 (b). Figure 8-12b shows the average water content within the PEM and also the average water content within the PEM normalised to the thickness of the free-swelling PEM. The average water content within the PEM increases with constraint, suggesting that compression causes water molecules to become packed much closer together. However, when normalised to the thickness of the free-swelling PEM, the results confirm that the PEM holds much less water when it is compressed than when it swells freely, as would be reasonably expected. Relative to the free-swelling PEM which holds 14.6 molecules per charge site, a fully constrained PEM holds 10.6 molecules per charge site. The effect on net water transport is shown in Figure 8-12c. The average water content is calculated relative to the thickness of the free-swelling PEM. The results show that the average water content drops with increasing constraint from a free-swelling value of 14.6 to a fully constrained value of 10.6. The net water transport occurs in the direction of the anodic boundary regardless of constraint, but its magnitude marginally increases with respect to increasing constraint. Considering the average vapour- and liquid-equilibrated transport components of net water transport shows that both diverge with constraint. The liquid-equilibrated component increases in magnitude in the direction of the cathodic boundary with increasing constraint and the vapour-equilibrated component also increases in magnitude but in the direction of the anodic boundary. These changes in water transport are attributed to the effect of constraint on the thickness of the PEM. A reduction in overall thickness causes the gradient in water content

and extent of liquid infiltration within the PEM to increase causing the diffusive and electro-osmotic drag components to increase respectively.

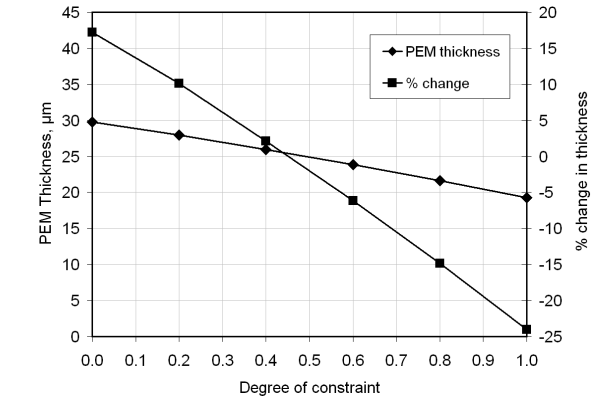

(a)

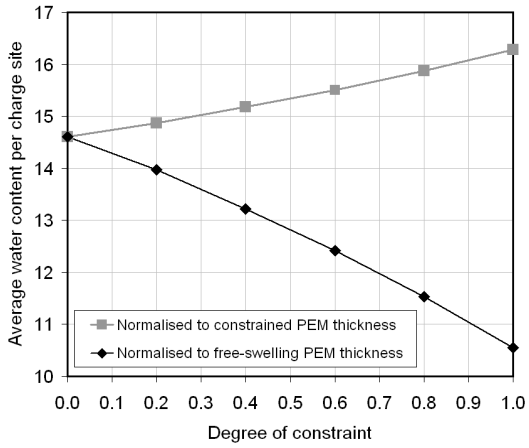

(b)

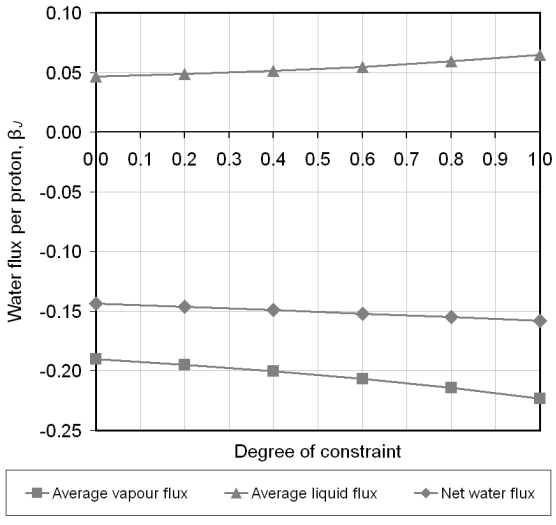

(c)

Figure 8-12 Compression effects on PEM thickness, water content and water transport; (a) change in PEM thickness as a function of degree of constraint; (b) change in average water content; (c) water flux profiles.

Figure 8-13 (a) shows the superficial gradient in water content as a function of constraint, calculated as;

$$\nabla\bar{\lambda} = \frac{\lambda_{A-2b} - \lambda_{C-2b}}{t_{mem,c}} \tag{8-8}$$

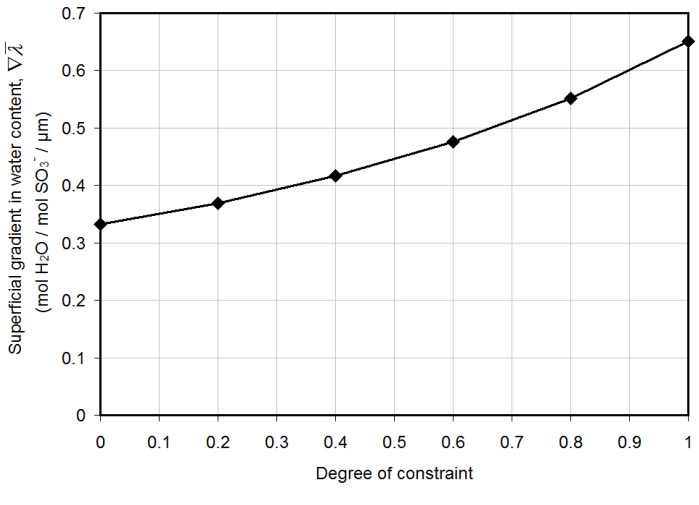

(a)

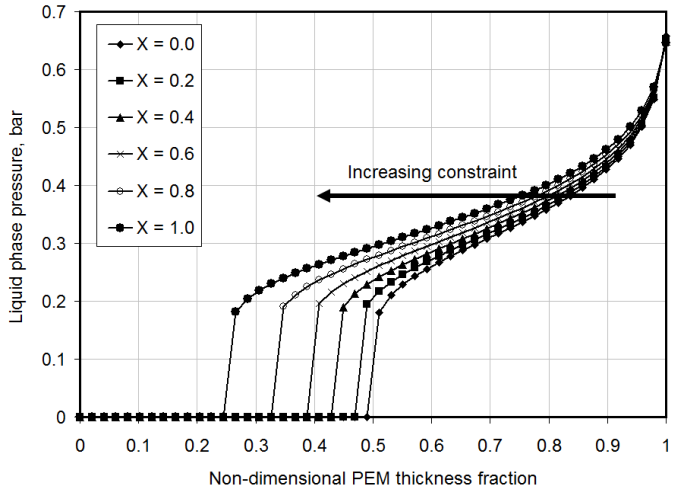

(b)

Figure 8-13 Effect of PEM constraint on PEM water content and liquid infiltration. (a) Superficial gradient in water content as a function of degree of constraint; (b) liquid network intrusion pressure as a function of non-dimensional PEM thickness for different degrees of constraint.

The gradient increases with constraint, which allows the magnitude of the diffusive component of net water transport to increase. Because the diffusive flux is more dominant in the vapour phase, it causes the vapour component of net water transport to increase in magnitude with constraint, as shown in Figure 8-12(c). Figure 8-13 (b) shows the intrusion pressure of the liquid water network for different levels of constraint. The results suggest that greater constraint allows the liquid water network to penetrate a greater proportion of the thickness of the PEM. As a result, the increase in local water content allows more water to be electro-osmotically dragged back to the cathode. This causes the liquid component of net water transport to increase with constraint as shown in Figure 8-12(b) because the water flux due electro-osmotic drag is most dominant in the liquid phase.

8.2.4 Parameter Effects on PEM Resistance

It is possible to generate a holistic understanding of the combined effects of PEM thickness, compression and anode humidification by considering the resistance across the PEM. The proton conductivity at each mesh point across the PEM can be calculated using equation 7-44 as a function of the local volume fraction of water, which itself is calculated as a function of the local water content using equation 7-19. The resistance across the constrained PEM is then calculated as [3];

$$r^{proton} = \int_{0}^{t_{mem,cons}} \frac{1}{\sigma} \cdot dz \tag{8-9}$$

In this part of the study, all five thicknesses are considered with increasing degrees of constraint and three states of inlet humidification. All other conditions are kept the same as those given in Table 8-1. The following three states are considered in Figure 8-14 (a) – (c):

- Figure 8-14 (a): anode saturated to 60℃, cathode saturated to 90℃
- Figure 8-14 (b): anode dry, cathode saturated to 90℃
- Figure 8-14 (c): anode dry, cathode saturated to 60℃

The first two states ensure a partial pressure of liquid water at the cathodic interface. The third state ensures that water only exists in vapour phase at the cathodic interface.

Figure 8-14 (a) shows that by humidifying both supplies and by ensuring that the cathodic boundary of the PEM is in contact with liquid water, the Ohmic resistance of the PEM can be kept generally lower than 0.1 Ohm-cm^2. Figure 8-14 (b) shows that by removing the anode humidification, the Ohmic resistance increases. For the thicker membranes, the effect is more drastic but generally speaking the Ohmic resistance is well below 1 Ohm-cm^2. Figure 8-14 (c) shows that by removing the anode humidification and by reducing the saturation temperature of the cathode supply from 90°C by 30°C - thereby invoking a vapour-equilibrated only transport mode - the Ohmic resistance increases furthermore and can be well above 1 Ohm-cm^2 in the thicker membranes. Figure 8-14 (a) – (c) also show that for all the cases considered, it is the thinnest membranes have the least Ohmic resistance. Overall, the results suggest that the liquid water at the cathodic boundary can help to reduce the resistance across the PEM. The simulated phenomenon can be attributed to the increase in local water content that occurs throughout the thickness of the PEM when liquid water intrudes the PEM from the cathode boundary, and results in a corresponding increase in local conductivity.

Another observation from all three graphs in Figure 8-14 is that the resistance of the PEM decreases with increasing membrane constraint. Referring back to the previous discussion on membrane constraint, it has been established that by constraining the membrane, the PEM will hold less water than its free-swelling equivalent state and also that by increasing constraint the PEM is less likely to expand beyond its dry state and more likely to shrink in thickness. The results of Figure 8-14 suggest that the decrease in water content with respect to constraint is less severe than the simultaneous decrease in thickness. This means that the net effect of membrane constraint is to tighten the distribution of water clusters within it because even though the water content drops slightly, the overall volume of the PEM decreases more substantially and causes the volume fraction of water to increase. This is shown in Figure 8-12b. Consequently under these conditions, it is feasible for the pathways for proton conduction to improve because the charged end groups are packed closer together. These results are consistent with discussions in the literature [4].

From a molecular viewpoint, it is well known that proton movement can be orientated by two mechanisms, namely vehicular transport and Grottus hopping [5,6]. In the first of these, it is assumed that protons bind with water to form hydronium complexes (H_3O^+) which diffuse as molecular ions down a concentration gradient [7]. In the second, it is assumed that

the protons essentially hop from one water molecule to the other independently without relying upon water as a vehicle. In both of these mechanism, there is a clear dependence on the local water content and the closeness of water clusters throughout the PEM. Based on the dependence of conductivity on the volume fraction of water the modelling results suggest that the net proton transport mechanism is improved particularly when liquid water infiltrates the PEM. The results have already shown that depending upon the thickness of the PEM, the infiltration of liquid water can indeed increase the water content markedly. The results also suggest that by constraining the membrane, there is an effect on the arrangement of the hydrophilic domains within the PEM whereby water clusters are forced closer together even though the total amount of water that the PEM holds can be forcibly reduced. Membrane constraint therefore also appears to improve the net proton transport mechanism. In conclusion, therefore, the best scenario for proton conductivity appears to be in a regime where liquid water is allowed to infiltrate the PEM in order to proliferate local water content, and which is also constrained in order to tighten the distribution of water clusters within it. The modelling results suggest that this can be achieved with a thin PEM which is constrained and operated with a cathodic boundary that is in contact with liquid water.

There are a number of clear limitations to this conclusion. First, it has to be acknowledged that the repeated infiltration and expulsion of liquid water in and out of the PEM could hasten the onset of performance degradation and cell failure as discussed in Chapter 3. Figure 8-1 would suggest that this is especially true for thin PEMs which are most prone to aggressive dimensional change. Second, it also has to be acknowledged that the thickness of the PEM limits the rate of fuel and contaminant crossover as shown in Chapters 5 and 6 respectively, although both are also inversely proportional to current density. Third, the liquid water at the cathodic boundary has to be established without flooding the porous layers. Although the flooding of porous layers has not been explored explicitly in the current study, it can be controlled by the physical parameters of the GDL and MPL.

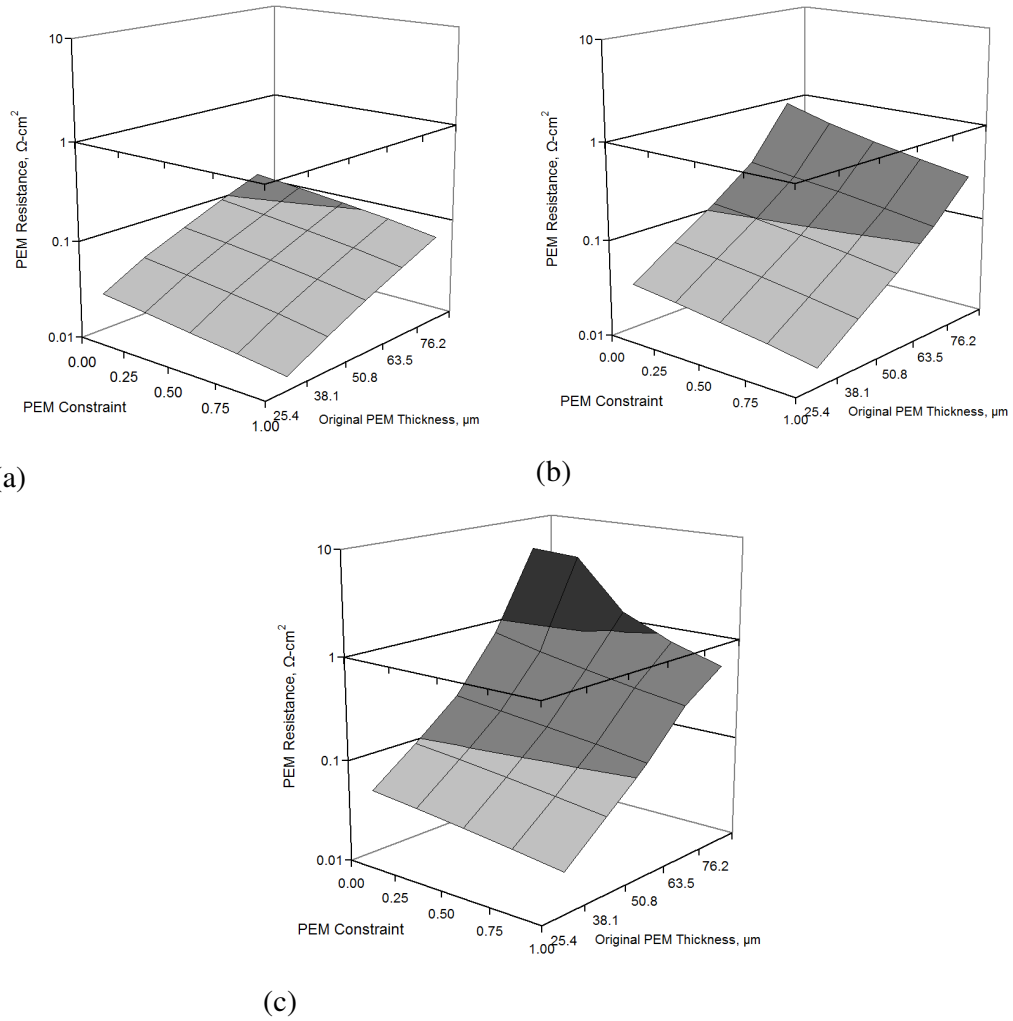

(a) (b)

(c)

Figure 8-14 Resistance maps for different levels of constraint and PEM thicknesses. (a) anode saturated to 333.15 K and cathode saturated to 363.15K (P(liq) > 0 at the cathode); (b) dry anode and cathode saturated to 363.15 K (P(liq) > 0 at the cathode); (c) dry anode, cathode saturated to 333.15 K (P(liq) = 0 at the cathode)

8.3 Structurally-Reinforced Membranes

Structurally-reinforced PEMs are being increasingly used in modern PEFCs. As discussed in the preceding chapter, these membranes contain an inert matrix which is impregnated with polymer electrolyte in order to achieve electrochemical and mechanical properties that the polymer electrolyte cannot provide on its own. The two predominant characteristics that are sought are:

i. low shrinkage upon hydration

ii. high mechanical strength

These properties ensure dimensional stability and therefore durability under PEFC operation conditions. It is the inert matrix - which is typically based on PTFE - that provides the structural reinforcement. The PTFE can take the form of a porous sheet (20-30% wt.% reinforcement), an embedded yarn (10 wt. % reinforcement) or as a fibril dispersion (2-5 wt. %). The reinforcement can allow the thickness of structurally-reinforced membranes to be as low as 5 – 20 μm [8]. While the literature demonstrates that structurally reinforced membranes can exhibit a life-time that is one order of magnitude longer than non-reinforced membrane of comparable thickness [9], what is not so clear is the effect that reinforcement has on water transport characteristics. Ye and Wang [10] determined the transport properties of water through structurally-reinforced membranes and noted the following based on high-frequency response measurements:

1. electro-osmotic drag coefficient: the drag coefficient held a value of around 1.07 over a large relative humidity range between 40% and 95%
2. diffusion coefficient: the diffusion coefficient of water was likely to be anywhere between a factor of 0.1 and 0.9 of that for a non-reinforced Nafion membrane over a large range of water contents (it was inferred that measurements were carried between 4 and 15 water molecules per charge site).

The electro-osmotic drag coefficient is consistent with that measured for Nafion (preceding section) for vapour equilibrated conditions. This therefore suggests that the reinforcement does not affect the mechanism by which water is dragged due to proton migration. The diffusivity of water, however, is clearly affected. One possible mechanism could be the hydrophobic nature of the PTFE, which may be limiting the mobility of water molecules within the PEM and therefore restricting its diffusivity. The purpose of this investigation is to simulate and understand the measured proton conductivity of a PEFC employing a structurally-reinforced PEM over a range of operating conditions.

8.3.1 Experimental

Materials

For the purposes of the current study, an 18 µm **s**tructurally-**r**einforced PE**M** which is **c**oated with anode and cathode **c**atalyst (SR-CCM) is employed with an equivalent weight of 950 g/mol, dry density of 2 g/cm^3 and footprint of 193.67 cm^2. Two sets of results are considered in the present study to reveal the characteristic behaviour of the SR-CCM. In the first case (case 1), two standard GDL-MPL assemblies were employed on both sides of the SR-CCM; characteristic properties are estimated from the literature [1,11]. The standard material contains a carbon-paper GDL with a bulk porosity of 0.9, nominal thickness of 300 µm and PTFE content of 5 wt%. The bulk porosity of the MPL is 0.4 and has a nominal thickness of 25 µm and PTFE content of 40 wt %. In the second case (case 2), the standard GDL-MPL assembly employed for the cathode is replaced with a similar GDL-MPL assembly that contains no PTFE in the GDL.

Experimental Setup

A single-cell fixture with a serpentine flow channel was used as the test cell. A bespoke system with digital mass flow controllers, data acquisition and an RBL-100-300-2000 programmable load bank was used for gas supply, humidity control and electronic load control. An Autolab 302N frequency response analyser and potentiostat were used for in-situ proton conductivity measurements based on electrochemical impedance spectroscopy (EIS). Zview software (Scribner Associates, Inc.) was used to analyse the collected AC impedance data.

Experimental Procedure

The compaction pressure applied to the cell is 1.5 MPa. Figure 20 provides the flow rates and equivalent calculated stoichiometries of the anode and cathode as a function of current density when operated with humidified hydrogen and dry air respectively. The

cathode is operated open-ended while the anode is dead-ended and purged periodically to remove any condensate in the anode flow fields. The anode inlet pressure is set to 1.5 bar while the cathode inlet pressure is increased from around 1.0 bar to around 1.1 bar with current density. The EIS measurements are taken from the cell over a range of operating current densities (0.5 – 0.9 A/cm^2). It is assumed that the x-intercept on the Nyquist plot of the PEFC frequency response reflects the total resistance of the cell, i.e., the sum of resistance to the flow of protons and electrons. The resistance to the flow of electrons in the electron-conducting parts of the cell such as the end plates and carbon substrate porous layers were measured *ex-situ* (at nominal thicknesses where appropriate) and determined to be 42 mΩ-cm^2 for the standard case and 40 mΩ-cm^2 for the second case. It is assumed that these values are not likely to change *in-situ* and therefore assumed to be constant. Subtracting these figures from the measured x-intercept gives the value of Ohmic resistance to proton flow, which is characterised primarily by the proton conductivity of the PEM. This is likely to change *in-situ* due to the operating conditions of the cell and the water uptake that occurs as a result. In this investigation, the resulting resistance of the PEM is simulated using the model developed in the previous chapter.

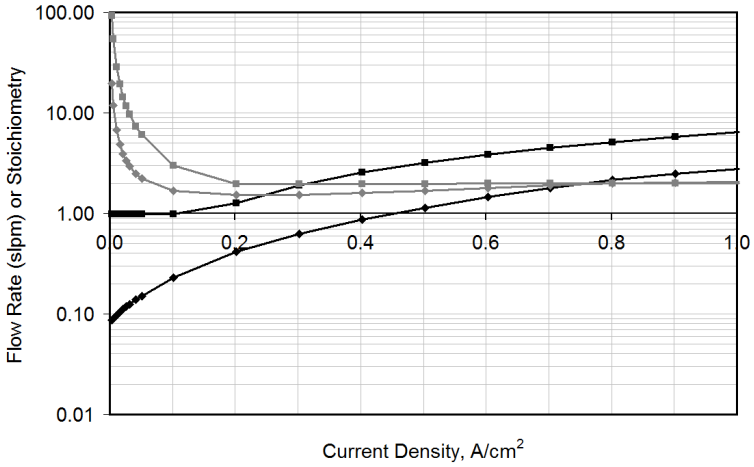

Figure 8-15 Applied anode (♦) and cathode (■) flow rates in standard litres per minute (black) and calculated stoichiometries (grey)

8.3.2 Results and Discussion

In order to investigate the effect of SR-CCMs on water transport, the diffusivity scaling factor in the PEFC model is tuned until the simulated resistance to proton flow

predicted by the model agrees with that obtained from measurement. In doing so, each current density is simulated turn-by-turn using the measured boundary conditions of the channel gases (flow rates, pressures, inlet gas temperatures), and the average cell temperature which is estimated from the measured inlet and outlet temperatures of both anode and cathode supplies. Figure 8-16 shows the membrane resistance from measurement, the simulated membrane resistance and the tuned diffusivity scaling factor for both test cases. Interestingly, the tuned values for the scaling factor result in an almost straight-line relationship with current density intersecting the origin for both test cases yet generate very close correlations between the simulated and measured membrane resistance, which have a non-linear dependence on current density. The simulations suggest that for test conditions considered, the diffusivity scaling factor lies in the range of 0.02 – 0.4.

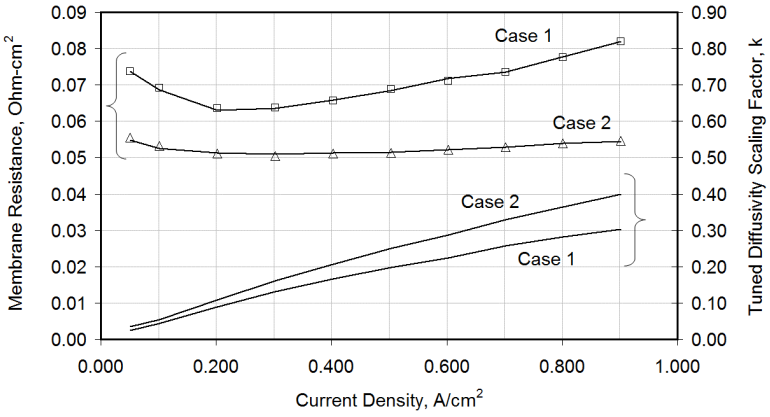

Figure 8-16 Membrane resistance and tuned diffusivity scaling factor as a function of current density. (□) measured case 1 (aGDL/cGDL: 5/5 wt. % PTFE); (△) measured case 2 (aGDL/cGDL: 5/0 wt.% PTFE); (——) simulated values.

Figure 8-17 shows the simulated thickness-averaged water content curves which correspond to the results of Figure 8-16. The results show that the water content is initially low for both cases but rises sharply and peaks in the 0.2 – 0.25 A/cm^2 band. This results in the initial fall in membrane resistance observed in Figure 8-16. Thereafter, the water content gradually falls, which results in the high membrane resistance observed in Figure 8-16 for both cases up to 0.9 A/cm^2. The low initial water content can be explained by the drying effect that is caused by the high initial stoichiometries of the cathode supplies, noting that the cathode gas is supplied dry. This causes the cell to loose the small amounts of moisture

generated in the form of product water in the cathode catalyst layer. As the stoichiometry settles to around 2 for both supplies after 0.2 A/cm^2, the subsequent changes in water content are less abrupt.

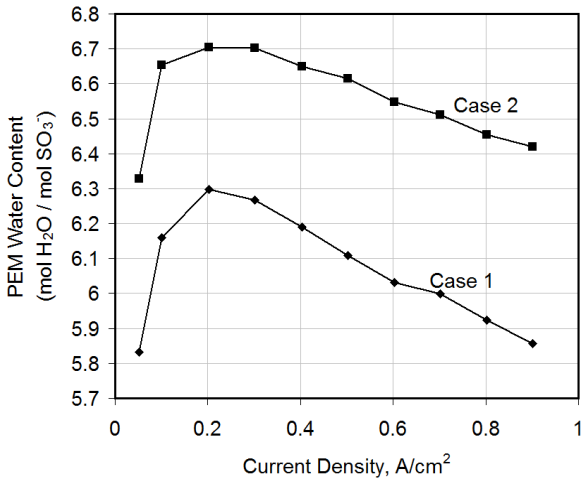

Figure 8-17 Simulated thickness-averaged water content as a function of current density for case 1 and case 2 as a function of current density.

Figure 8-18 shows the electro-osmotic drag and diffusive components of net water flux across the PEM. Figure 8-18(a) shows that the electro-osmotic drag component increases in almost direct proportion to current density. Figure 8-18(b) however shows that the diffusive component has a non-linear dependence on current density. The initial diffusive flux is high in magnitude, which demonstrates that the concentration gradient is sufficiently high to drive transport across the PEM from the cathodic boundary to the drier anodic boundary even though the scaling factor is limiting the diffusion coefficient. Because the stoichiometry of the cathode supply is high up to 0.25 A/cm^2, the drying effect begins to limits the concentration of water at the cathodic PEM boundary and therefore reduces the diffusive flux. As current density increases to 0.9 A/cm^2, the production of water increases while the cathode stoichiometry decreases, which has the net effect of increasing the concentration of water at the cathodic PEM boundary. This has the effect of increasing the water content gradient across the PEM and therefore increases the magnitude of the diffusive flux. Overall, therefore, the non-linearities observed in Figure 8-16 – Figure 8-18 occur as a result of the operational setup in terms of reactant supply and the subsequent effect on membrane hydration.

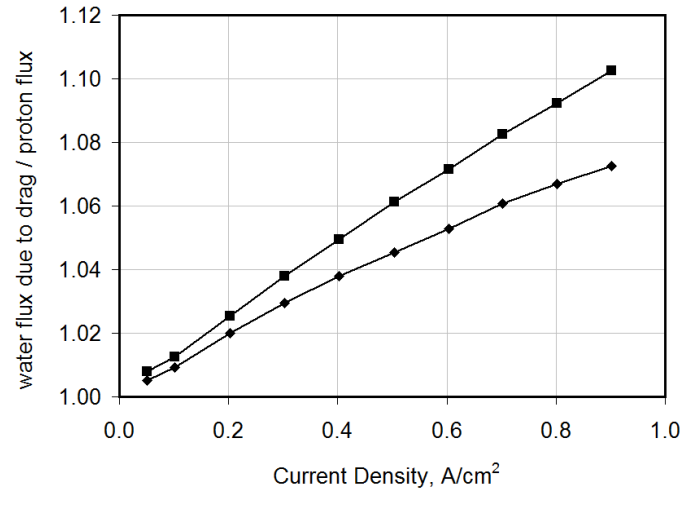

(a)

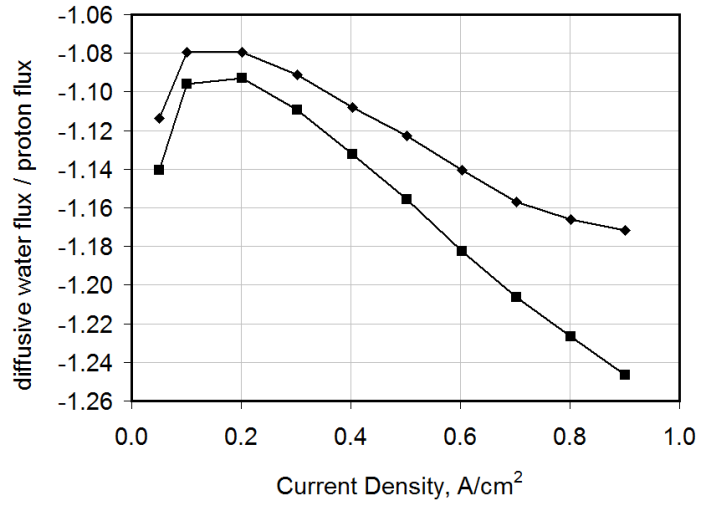

(b)

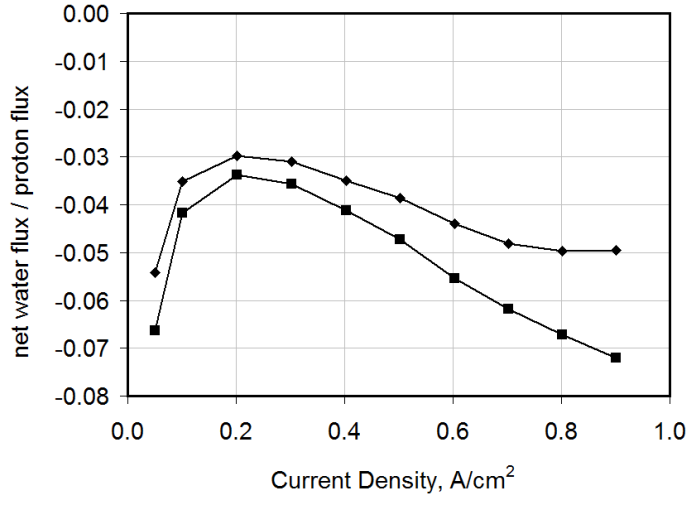

(c)

Figure 8-18 (a) Electro-osmotic drag (b) and diffusive components of (c) net water flux across the PEM as a function of current density. Test case 1 (♦); test case 2 (■).

What remains to be explained is the difference in the tuned diffusivity scaling factor between cases 1 and 2 which appears to enhance both electro-osmotic and diffusive fluxes across the PEM, as shown in Figure 8-16. In order to explain this, attention is turned to Figure 8-19 which shows the calculated membrane thickness for each case. The results show that the highly-constrained PEMs do not undergo aggressive dimensional change. For both cases the simulations suggest that the change in thickness between the two cases is around 0.1% of the nominal thickness of 18 microns. However, the results reveal that from the two cases, it is the second which allows the greatest amount of expansion; case 1 allows a 1.7% expansion whereas case 2 allows a 1.8% expansion. This marginal difference can be attributed to the difference in PTFE contents in the cathode GDLs. For case 2, there is no PTFE in the cathode GDL which appears to allow slightly more expansion than for case 1 where the cathode GDL is arguably more rigid due to the 5 %wt. PTFE content. The results therefore suggest that the diffusivity scaling factor may have a dependence upon the compressed state of the SR-CCM. Even though the difference in expansion is only 0.1% of the nominal thickness, the effect on the scaling factor is more profound; at 0.9 A/cm^2 the diffusivity scaling factor is limited to 0.3 for case 1 whereas it increases to 0.4 for case 2. Therefore, because the water is more mobile in case 2, the magnitude of its diffusive flux ratio is greater in magnitude than case 1 (in the direction of the anode from the cathode). This improves the hydration of the PEM but also allows a slight increase in the electro-osmotic drag (in the opposite direction from anode side to cathode side).

Interestingly, Figure 8-18(b) suggests that it is the diffusive flux that is greater in magnitude than the electro-osmotic drag flux under the test cases considered, bearing in mind that the cathode supply is at a lower pressure than the dead-ended anode supply. The results suggest that the structural reinforcement that naturally curtails the diffusive flux and limits the water content of the PEM also therefore retards the amount of water that can be electro-osmotically dragged back. Therefore water is allowed to travel in the direction of the anode, which may assist in delaying the onset of mass transport limitations due to cathode flooding. This phenomenon could be inherent to most low-pressure applications of SR-CCMs in PEFCs.

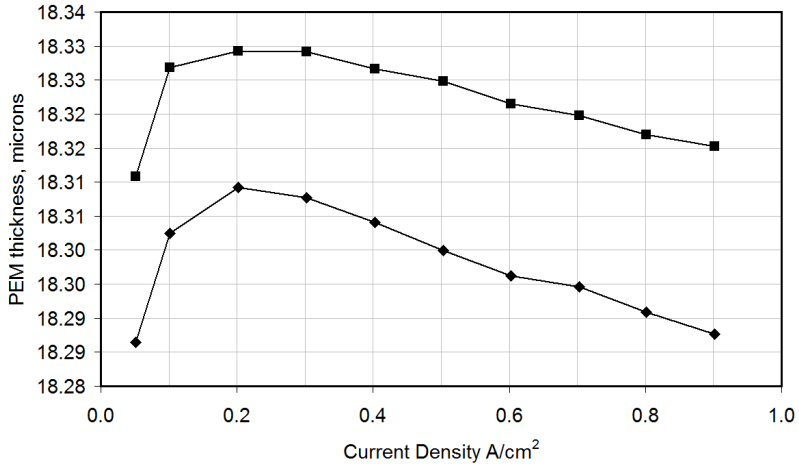

Figure 8-19 Change in PEM thickness as functions of current density. (♦) Case 1; (■) case 2.

8.4 Conclusions

The multi-layer 1D two-phase fuel cell model developed in Chapter 8 has been applied to examine water transport and water uptake characteristics through the PEM when the cathodic PEM boundary is in contact with liquid water. The conclusions are:

1. The effect of PEM thickness - The simulated results show that for a given set of operating conditions, the depth of liquid water penetration from the cathodic boundary is largely unaffected by the thickness of the PEM when unconstrained. The results show that the net water flux per proton in the liquid network of the PEM also remains largely unaffected by the thickness of the PEM, but that the same does not hold true for transport in the vapour-equilibrated mode. The magnitude of the net water flux in the vapour-equilibrated mode decreases with increasing PEM thickness, suggesting that a longer transport path can retard the vapour-phase transport across the PEM. Overall, therefore, net water transport decreases in magnitude with PEM thickness. The results from this first set of simulations where the anode gas is supplied dry also show for all simulated thicknesses that the diffusive water flux dominates over the proton-induced flux in the vapour phase, but that the proton-induced flux dominates over the diffusive flux in the liquid phase.

2. The effects of anode inlet gas humidification - The results suggest that by humidifying the anode supply, the hydration of the anode side of the PEM improves and can also allow a

more extensive liquid water network to form which reaches deeper towards the anodic side of the PEM from the cathodic boundary. The results also suggest that the proton-induced water flux in vapour- and liquid-equilibrated networks are greater in magnitude than the diffusive components because of the increased water content throughout the thickness of the PEM, which causes the net water transport to occur in the direction of the cathode for the thicker membranes. However, the results also suggest that the effect of electro-osmotic drag flux in the vapour region can be sensitive to the thinness of the PEM and the depth of liquid water penetration.

3. The effects of cell compression on membrane constraint - The results demonstrate that PEM constraint can easily restrict its water content relative to its free-swelling state and can also be accompanied by a decrease in the thickness of the PEM. If the change in thickness with constraint is more severe than the change in water content, the gradient in water content can indeed increase, which can hasten both liquid and vapour phase transport. However, for the test conditions considered, a substantial change in net water transport was not observed. The results also suggest that PEM constraint can cause water molecules to become packed closer together. The results also demonstrate that cell compression may allow the liquid water network to infiltrate deeper into the polymer matrix from the cathodic boundary towards the anodic boundary.

4. Combined effects of PEM thickness, humidification and compression - For the simulated conditions, the results suggest that low Ohmic resistance can be achieved for thin membranes which are operated in a constrained state and with a cathodic boundary that is in contact with liquid water. The limitation of this conclusion is that reducing the thickness of the PEM will cause a greater crossover of hydrogen, as shown in chapter 6.

5. Effects of structurally-reinforced membranes **-** The experimental results obtained from *in-situ* impedance data and simulation suggest that for a highly-compressed PEFC, the diffusivity scaling factor for structurally reinforced membranes can be as low as 0.02 – 0.4 (i.e., the diffusivity of water in a structurally-reinforced PEM could be less than 40% of that typically measured in an non-reinforced PEM such as Nafion). The results suggest that the diffusivity scaling factor depends upon the compressed state of the PEFC and the structural rigidity of surrounding layers. For the two test cases considered in the current study where the PEFC is operated in a highly-compressed state, the results from simulation show that the

SR-CCM will still tend to swell but that its change in thickness is limited to less than 2%. The simulated results however suggest that the constrained state of the PEM has an effect on the diffusivity scaling factor; a 0.1% difference in the change in thickness allows the maximum diffusivity scaling factor at 0.9 A/cm^2 to increase from 0.3 to 0.4.

8.5 References

1 **Krewer U, Yoon HK, Kim HT.** Basic model for membrane electrode assembly design for direct methanol fuel cells. *J. Power Sources*, 2008, **175**, 760-772

2 **Yang WW, Zhao TS.** Numerical investigation of effect of membrane electrode assembly structure on water crossover in a liquid-feed direct methanol fuel cell. *J. Power Sources*, 2009, **188**, 433-446

3 **Springer T, Zawodzinksi T, Gottesfeld S.** Polymer Electrolyte Fuel Cell Model. *J. Electrochem. Soc.*, 1991, **138**, 2334-2342

4 **Weber AZ, Newman J.** A Theoretical Study of Membrane Constraint in Polymer-Electrolyte Fuel Cells. *AIChE Journal*, 2004, **50**(12), 3215-3226

5 **Moilanen DE, Pitelic IR, Fayer MD.** Water Dynamics in Nafion Fuel Cell Membranes, the Effects of Confinement and Structural Changes on the Hydrogen Bond Network. *J. Phys. Chem. C*, 2007, **111**(25), 8884-8891

6 **Zawodzinski TA, Derouin C, Radzinski S, Sherman RJ, Smith VT, Springer TE, Gottesfeld S.** Water Uptake by and Transport Through Nafion 117 Membranes. *J. Electrochem. Soc.*, 1993, **140**(4), 1041-1047

7 **Pei H, Hong L, Lee JY.** Polymer Electrolyte Membrane Based on 2-Acrylamido-2-Methyl Propanesulfonic Acid Fabricated by Embedded Polymerization. *J. Power Sources*, 2006, **160**, 949-956

8 **Savadogo O.** Emerging Membrane for Electrochemical Systems, Part I High Temperature Composite Membarnes for Polymer Electrolyte Fuel Cell (PEFC) Applications. *J. Power Sources*, 2004, **127**, 135-161

9 **Liu W, Ruth K, Rusch G.** Membrane Durability in PEM Fuel Cells. *J. New. Mat. Electrochem. Systems*, 2001, **4**, 227-231

10 **Ye X, Wang CY.** Measurements of Water Transport Properties Through Membrane-Electrode Assemblies, I. Membranes. *J. Electrochem. Soc.*, 2007, **154**(7), B676-B682

11 **Ihonen J, Mikkola M, Lindbergh G.** Flooding of Gas Diffusion Backing in PEFCs. *J. Electrochem. Soc.*, 2004, **151**(8), A1152-A1161

9 Conclusions and Future Work

The aim of this thesis was to develop a universal electrochemical theory to describe the mechanisms of electrochemical transport in PEFCs, which reconciles the benchmark modelling philosophies in the literature and demonstrably predicts single-phase and two-phase flow phenomenon. It is known that electrochemical transport is influenced by cell configuration, material composition and operating conditions in a fuel cell and therefore governs fuel cell performance, cost and longevity. As such, the development and application of the general transport equation in this thesis has established a means of understanding the mechanisms of electrochemical transport in porous and quasi-porous layers in the PEFC.

This study is the first to provide a structured understanding of how transport across all porous and quasi-porous layers of the PEFC can be mechanistically modelled and demonstrates a common fundamental approach for both porous and quasi-porous electrochemical systems. The verification of simulated predictions with experimental data establishes confidence in the described information provided by the general transport equation. It is therefore believed that the verified modelling framework can be used directly to support the design process of PEFCs.

9.1 Conclusions

The following principal conclusions can been drawn from the thesis.

Fundamental Concepts:

- The fundamental concepts of fuel cell performance and the factors that affect thermodynamic efficiency have been described in the early part of this thesis.
- A thorough review of the practical factors that affect the performance of the PEFC has also been presented, which provides a comprehensive understanding of the technical challenges and state-of-the-art concepts for PEFC technology and the significance of electrochemical transport.

- The review identified that the PEFC is susceptible to twenty-two common faults which can be induced by forty-eight general causes. These twenty-two common faults can pertain to the PEM, CL, GDL, BPP and sealing material.
- The review has been used to construct a system of fault trees for the PEFC which provides a valuable insight into the mechanisms by which modes of performance degradation can propagate and result in significant performance loss (through increases in activation, mass transport, Ohmic or efficiency losses) or cell failure [1].
- The review identifies that electrochemical transport and water management in particular is crucial to understanding how PEFC technology can be designed for performance, longevity and cost.

Benchmark Modelling Techniques:

- The benchmark modelling approaches for electrochemical transport in the fuel cell modelling literature have been described, including how they have been applied to simulate transport across the various layers of the cell. The discussion identifies dilute solution theory and concentrated solution theory as the main modelling branches for transport in porous and quasi-porous layers.
- The theory of electrode kinetics has also been discussed and a semi-empirical approach based on the thin interface assumption has been developed to describe the processes that occur in the anode and cathode catalyst layers.

Multi-Layer Modelling with Multi-Species Input:

- The modelling work carried out in this thesis began with the development of a multi-species input model which is demonstrably coupled to a one-dimensional modelling framework based on dilute solution theory.
- The multi-species input model establishes the capability to handle multi-component input gases and directly couples the boundary conditions in the supply channels with the cross-flow that occurs through the PEFC. The composition of the reactant supply gases in the channels of the PEFC is calculated based on the initial dry gas composition, stoichiometry, pressure and relative humidity of the supply gases, the cell operating current density and fluid cross-flow through the cell.
- The model has been implemented and validated against experimental data for the Ballard Mark IV PEFC in the open literature.

- The model has been applied to simulate the effect of CO poisoning in the cathode catalyst layer due to contamination in the anode supply. The simulation results confirm that when a PEFC is operated on a 30% carbon dioxide / 70% hydrogen fuel supply with up to 50 ppm carbon monoxide, the crossover of CO across the PEM can reduce the cathode potential at 1 A/cm^2 by up to 15%. The results also show that by increasing the CO content of the fuel supply from 10 ppm to 100 ppm, there is a corresponding increase in the rate of CO crossover by one order of magnitude for all current densities tested (0 to 1 A/cm^2).

Fundamental Theory of Electrochemical Transport in PEFCs:

- This thesis has considered how the fundamental theory of molecular transport can be applied to simulate multi-component flow through PEFC media; the underlying philosophy has focused on establishing a unifying mechanistic treatment for multi-component electrochemical transport across the multi-layer PEFC, initially paying attention to single-phase systems and then two-phase systems.
- In Chapter 6 a general transport equation has been developed from the molecular theory of gases and liquids [2] and can account for thermal diffusion, molecular diffusion, convection and electro-osmotic drag in multi-species form in porous and potentially quasi-porous media.
- The theoretical validity of the general transport equation has been proven by deriving the key transport equations in the literature developed by Bernardi *et al.*, Springer *et al.*, and Newman *et al.*
- The general transport equation can be merged with the multi-component input model as described in Chapter 5 to study the factors affecting single-phase multi-component electrochemical transport though the PEM.
- The numerical validity of the general transport equation has thus been proven by simulating a PEFC in 1D with a three-species PEM system (water, electrolyte, protons) under single-phase conditions. The numerical validity has been demonstrated by comparing the generated results against benchmark water content curves published in the open literature. The results show that for simulations based on dilute solution theory, a c_j/c_T factor is inherently assumed to be equal to unity, which consequently leads to an over-prediction in the spatial concentration distribution of a species. This

is most noticeable at current densities exceeding 0.5 A/cm^2 for the test cases considered.

- The application of the general transport equation through a multi-layer 1D model in Chapter 6 has elucidated the dependence of hydrogen crossover on the thickness of the PEM, cell operating temperature and current density. The results reveal that at 80℃, 1 *atm* reactant supply pressure and 1 *A/cm*^{2}, the nominal membrane thickness for less than 5 *mA/cm*^{2} equivalent crossover current density is 30 μm.
- The relationship between hydrogen crossover with current density identified in this thesis has been used recently to explain fluoride release rates measured in chemically degraded operational PEFCs by other researchers [3,4,5].

The Mechanisms of Two-Phase Transport in PEM Fuel Cells

- The final part of the thesis has extended the application of the GTE to model two-phase multi-component flow through a multi-layer PEFC. It has been demonstrated that the general transport equation developed in Chapter 6 can been applied with Darcy's law to simulate two-phase flow through the porous (GDL, MPL) and quasi-porous layers (PEM) of a PEFC. Multi-component input gases can be handled using a modified form of the multi-component input model developed in Chapter 5.
- It has been demonstrated that liquid infiltration in porous layers can be accounted for by employing the standard and validated Leverett J-functions. To account for liquid infiltration in the quasi-porous layer and therefore Schroeder's paradox, a physical model described elsewhere has been adopted [6]. The model assumes that liquid water can forcibly create a liquid network through the partially hydrophobic and partially hydrophilic PEM when it comes into contact with a boundary.
- The modelling treatment has considered the porous layers of the PEFC such as the GDL and MPL to be compressible under fuel cell compaction forces. It is shown that compression effects on the PEM can be handled using a mechanical sub-model which calculates the water uptake profile across the membrane based on its compressed thickness and thermodynamic boundary conditions.
- The model can be implemented using the object-oriented modelling technique, which enhances the usability and adaptability of the code for future work.
- Simulation results have been validated against experimental water transport and water uptake data for both single- and two-phase operating conditions from the open

literature [7,8,9,10]. The model confirms the measurements taken from water balance tests, specific resistance profiles across the PEM from embedded probe tests and water content profiles obtained through MRI scanning.

- The results show that the thickness of the PEM, anode gas humidification and cell constraint can all contribute towards reducing the resistance to proton transport by allowing liquid water to penetrate a greater proportion of its thickness, thereby improving proton conductivity.

9.2 Future Work

The modelling work presented here represents a significant step towards representative simulations of the complete PEFC under a range of design and operating conditions. The results presented in this thesis demonstrates the capability of the present modelling framework to provide insights to physical processes occurring within a fuel cell. It is anticipated that the macroscopic treatment developed in the thesis is one modelling tool that can interface with a range of capabilities in order to establish a comprehensive PEFC development system for the purposes of PEFC design, *in-situ* characterisation and diagnostics. The following provides a discussion of future work in order to exploit the work of this thesis.

The current macroscopic modelling framework is implemented through a one-dimensional treatment. This allows the bulk processes across all relevant layers of the PEFC to be considered in a single simulation, accounting for cross-flow through the PEM by treating it as an electrochemical system. Fundamentally, because the porous and quasi-porous layers of the PEFC exhibit complex collapsible structural characteristics, it is difficult to capture the behaviour that occurs within them comprehensively using multi-dimensional approaches based on computational fluid dynamics (CFD) or the lattice Boltzmann (LB) technique, for example, in isolation. Therefore, the modelling work described in this thesis serves a purpose that is not rigorously satisfied by such approaches. However, in doing so, the current modelling framework is reduced to a one-dimensional treatment which neglects to consider the macroscopic channel effects in the reactant supply channels and the inlet and exit manifolds of the PEFC. In addition, it does not elucidate how multi-component and potentially multi-phase flow propagates through the actual heterogeneous three-dimensional

porous structures of the PEFC. The overall solution therefore lies in harnessing the relative merits of all three approaches in order to comprehensively simulate both macroscopic and microscopic processes occurring within the PEFC.

9.2.1 Microscopic Modelling

The lattice-Boltzmann (LB) modelling technique is a statistical method that can simulate multi-species, multi-phase and reactive flows through a pre-defined model of a three-dimensional porous structure with prescribed surface properties. It has the potential to simulate the precise movement of gas components and liquid water through representative geometric models of heterogeneous porous structures in the PEFC such as the GDL, MPL and CL. However, in order for the LB model to work correctly the physical boundary conditions at opposing faces of the three-dimensional structural model of a given PEFC layer have to be specified, which are impossible to measure experimentally. These boundary conditions (phase pressures and partial pressures of gas constituents at layer interfaces, flow rates through individual layers) can be generated by the theoretical treatment developed in this thesis.

To date, a multi-dimensional LB model has been specifically developed and applied with representative three-dimensional digital models of a carbon-paper GDL obtained from X-ray computed micro-tomography in order to validate the simulated gas-phase permeability through its porous structure [11]. The next step is to apply representative fuel cell boundary conditions between fuel cell layers from the model described in chapter 7 to simulate multi-species transport through the porous structure of the GDL. Figure 9-1 is an initial single-phase LB simulation of oxygen infiltration through a carbon paper cathode GDL as part of a multi-component mixture comprised additionally of nitrogen and water vapour. The simulation is carried out using boundary conditions generated directly by the model presented in chapter 7.

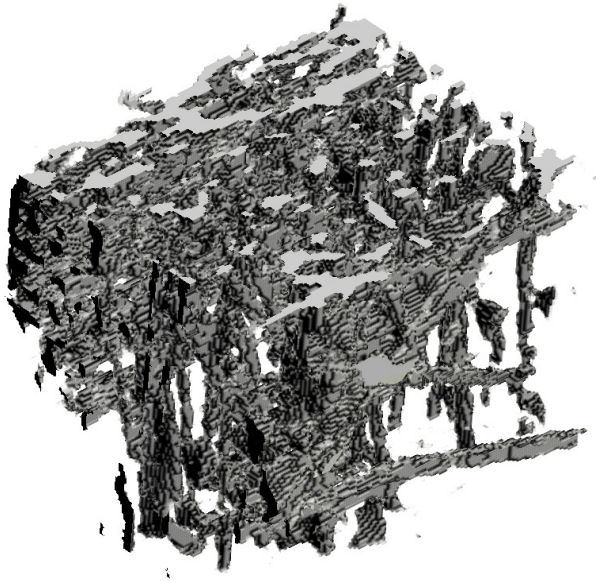

(a)

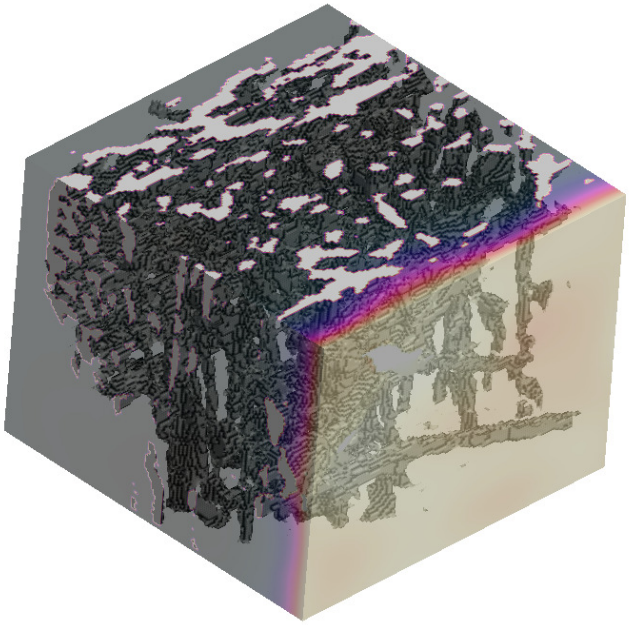

(b)

Figure 9-1 Single-phase multi-component Lattice Boltzmann simulation of oxygen permeation through a carbon paper GDL; (a) X-ray tomography model of a carbon paper GDL; (b) simulated infiltration of oxygen using boundary conditions from the model presented in chapter 7

9.2.2 Macroscopic Modelling

Computational Fluid Dynamics

CFD modelling is a powerful tool that can predict the behaviour of laminar and non-laminar flows through complex three-dimensional geometries such as bipolar plate channels, fuel cell inlet manifolds and exit manifolds. Existing CFD codes readily deal with multi-phase flows and heat transfer, which as discussed can both be dominant factors in the performance of operational PEFC systems.

As discussed in Chapter 3, as the partial pressure of water exceeds the saturation vapour pressure for a given temperature in the channels of the cells, water vapour will start to condense. Subsequent flooding will have an impact on the planar current density distribution across the cell hence cell performance. In addition, planar temperature differences can also develop across the footprint area of a cell, depending on the heat generated due to electrical loses, the thermal conductivity of the hardware components of the PEFC and the thermal conductivity of the coolant and reactant supplies. All of these factors can affect heat loss to cooling environments. If as a result the local cell temperature is excessively high, water in the cell will evaporate leading to membrane dehydration. This results in a drop in local current density and therefore cell performance.

In order to locally resolve the cross-flow through the compressible porous and quasi-porous layers of the PEFC as a function of the local thermo-fluidic conditions in the channels, it is possible to interface the model described in Chapter 7 with a multi-phase three-dimensional CFD treatment that accounts for heat transfer. CFD models cannot readily predict the cross-flow through the PEFC and have to fix the net water flux ratio *a-priori* [12,13]. They do not consider two-phase effects on the performance of the PEM or compression effects either [14]. By combining models, however, a comprehensive assessment of cell configuration and design can be carried out to determine how performance in operational fuel cells can be sustained in spite of the development of planar non-uniform two-phase transport and thermal gradients.

Figure 9-2 demonstrates the principal of multi-scale modelling based on the GTE, LB and CFD techniques discussed above. The LB model is used to determine bulk properties of the visualised PEFC material sample, which in the first instance are supplied to the GTE and CFD models. Existing CFD models can determine the distribution of reactants in the flow fields of the anode and cathode bi-polar plates. The GTE model determines the phase pressures and boundary conditions between layers within the PEFC, which can be supplied back to the LB model to visualise how the flow actually behaves within the porous structure of the material (i.e., the GDL, MPL or CL) under representative fuel cell operating conditions. This therefore provides vital information about the porous structure which can assist the next iteration of material design.

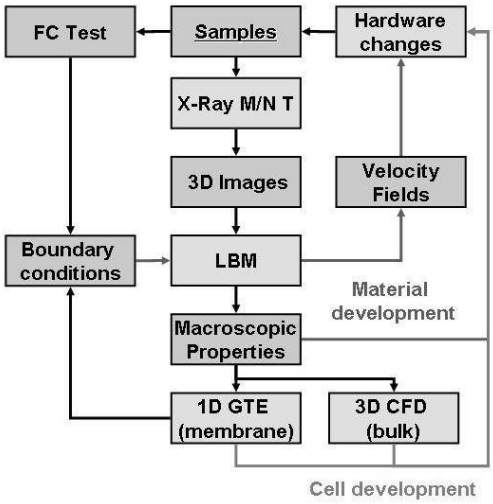

Figure 9-2 Multi-Scale PEFC Modelling

The Hardy-Cross Method

Implementation of numerical techniques based on CFD often result in computationally-intensive models that require days or weeks to generate results. It can be more advantageous to strategically employ less computationally-intensive models at difference stages of cell/stack development which may not be as highly-accurate as CFD models, but able to generate a qualitative and quantitative assessment of macroscopic fuel cell performance in terms of flow field configuration in a relatively short space of time.

In previous work which is not presented here [15], a pseudo two dimensional flow network approach has been developed to determine the pressure losses within a fuel cell stack using the Hardy-Cross method [16] and empirical relations for pressure drops along straight sections, bends and junctions for joining and separating flows [17,18,19]. The Hardy-Cross technique was originally designed to predict pressure losses around pipe networks with distributed sink and source points for civil engineering problems. However, the previous research demonstrated the feasibility to link the model developed in Chapter 6 with the Hardy-Cross method for fuel cell engineering at stack-level; the Hardy-Cross method can predict the pressure loss around the anode and cathode flow networks, which comprise of inlet and exit manifolds that are connected by channel sections of variable geometry and configuration, and multiple sink and source terms for cross-flow through the cell. The single-cell model is applied to determine the amount of cross-flow between the two networks based on the channel conditions predicted by the flow network model.

The Hardy-Cross method simplifies the flow network into a one-dimensional network with prescribed cross-sectional geometries and sub-models to determine the pressure drop around bends depending on bend geometry. Preliminary results from the study demonstrated the ability to solve the pressure trace of a 25-cell stack within 25 minutes [15].

Figure 9-3 illustrates preliminary results obtained by the Hardy-Cross method with the single-phase model developed in chapter 5. The resulting model is applied to simulate a 25-cell stack with a footprint area of 35.5 cm^2 and bipolar plates with single-serpentine flow fields of 1mm by 1mm cross-sectional geometry. For the simulation, the gas supply pressures are set to 2 bar and the cell is operated at 80°C at 0.5A/cm^2. The results in figures 9-3 (a) and (b) suggest a pressure drop of 350 Pa and 50 Pa respectively along the length of the cathode and anode inlet manifolds respectively and 31 kP and 6 kPa pressure rises in the respective exit manifolds. Figures 9-3 (c) and (d) demonstrate the ability to simulate cell-to-cell variations in cross-flow through the cell and stoichiometric conditions as a function of the pressure drop along the anode and cathode flow fields within the stack.

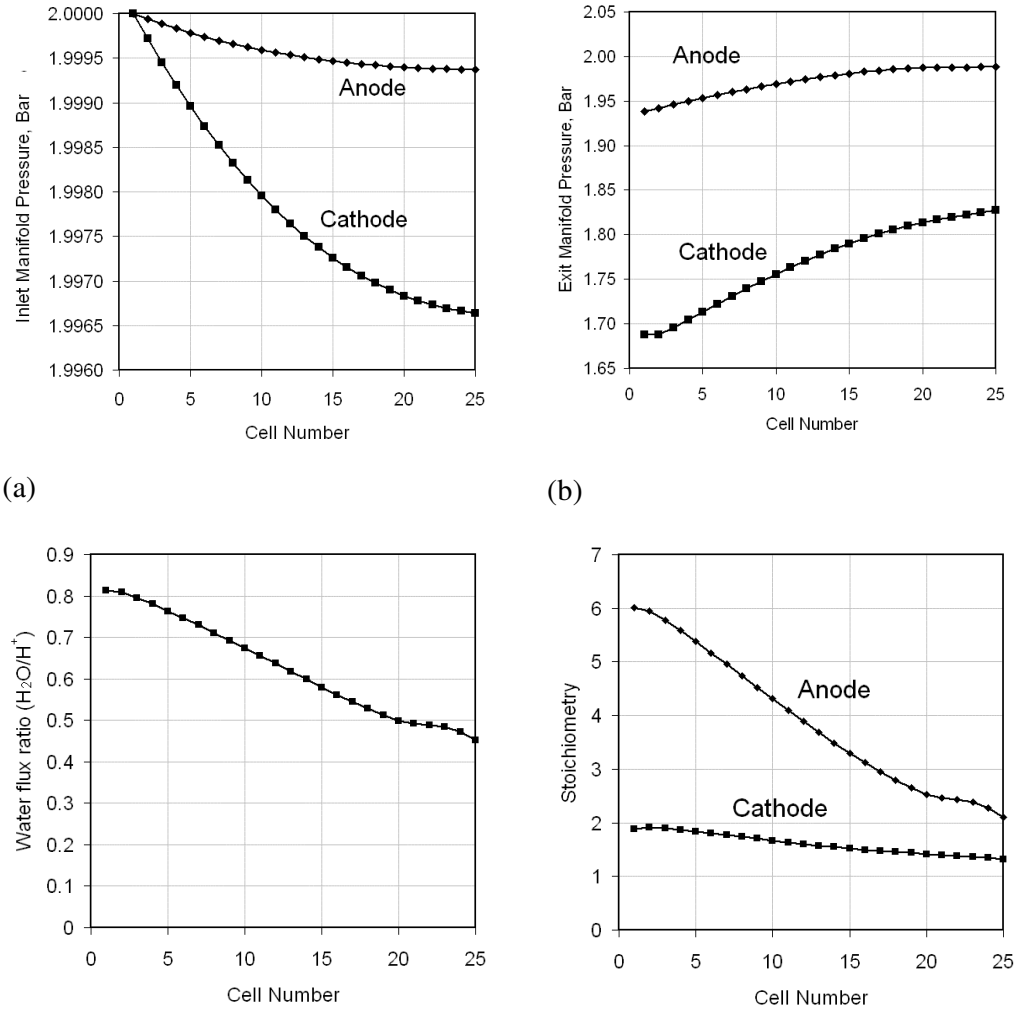

Figure 9-3 Simulated pressure drops in a 25-cell stack using the Hardy-Cross method and the single-phase electrochemical transport model developed in chapter 6; (a) inlet manifolds; (b) exit manifolds; (c) cell-to-cell net water flux ratio; (d) cell-to-cell stoichiometry.

9.3 References

1 **Rama P, Chen R, Andrews J.** Failure Analysis of Polymer Electrolyte Fuel Cells. *SAE*, **2008**, 2008-01-0634

2 **Hirshfelder JO, Curtiss CF, Bird RB.** *Molecular Theory of Gases and Liquids*, 1964 (John Wiley & Sons, Inc., New York)

3 **Kundu S, Karan K, Fowler M, Simon LC, Peppley B, Halliop E.** Influence of micro-porous layer and operating conditions on the fluoride release rate and degradation of PEMFC membrane electrode assemblies. *J. Power Sources*, 2008, **179**, 693-699

4 **Kundu S, Fowler M, Simon LC, Abouatallah R.** Reversible and irreversible degradation in fuel cells during Open Circuit Voltage durability testing. *J. Power Sources*, 2008, **182**, 254-258

5 **Kundu S, Fowler MW, Simon LC, Abouatallah R, Beydokhti N.** Degradation analysis and modelling of reinforced catalyst coated membranes operated under OCV conditions. *J. Power Sources*, 2008, **183**, 619-628

6 **Weber AZ, Newman J.** Transport in the Polymer-Electrolyte Fuel Membranes, I, Physical Model. *J. Electrochem. Soc.*, 2004, **150**(7), A1008-A1015

7 **Janssen GJM.** A phenomenological model of water transport ina aproton exchange membrane fuel cell. *J. Electrochem. Soc.*, 2001, **151**(3), A341-A353

8 **Weber AZ, Newman J.** Transport in the Polymer-Electrolyte Fuel Membranes, III, Model Validation in a Simple Fuel-Cell Model. *J. Electrochem. Soc.*, 2004, **151**(2), A326-A339

9 **Takaichi S, Uchida H, Watanabe M.** Response of Specific Resistance Distribution in Electrolyte Membrane to Load Change at PEFC Operation. *J. Electrochem. Soc.*, 2007, **154**(12), AB1373-1377

10 **Ikeda T, Koido T, Tsushima T, Hirai S.** MRI Investigation of Water Transport Mechanism in a Membarne under Elevated Temperature Condition with Relative Humidity and Current Density Variation. *ECS Trans.*, 2008, **16**(2), 1035-1040

11 **Rama P, Liu Y, Chen R, Ostadi H, Jiang K, Zhang X, Fisher R, Jeschke M.** An X-ray Tomography Based lattice-Boltzmann Simulation Study on Gas Diffusion Layers of Polymer Electrolyte Fuel Cells. *J. Fuel Cell Sci. Technol. ASME*, 2009 (*article in press*)

12 **Wang ZH, Wang CY, Chen KS.** Two-Phase Flow and Transport in the Air Cathode of Proton Exchange Membrane Fuel Cells. *J. Power Sources*, 2001, **94**, 40-50

13 **Lum KW**. *Three Dimensional Computational Modelling of a Polymer Electrolyte Membrane Fuel Cell*, 2003 (Doctoral Thesis, Loughborough University)

14 **Wang CY.** Fundamental Models for Fuel Cell Engineering. *Chem. Rev.*, 2004, **104**(10), 4727-4766

15 **Rama P, Chen R, Thring RH**. PEFC Stack Modelling. *International Energy Agency Annex XVI*, June 2006, ECN Petten, Holland

16 **Street RL, Watters GZ, Vennard KJ.** *Elementary Fluid Mechanics*, 1996 (John Wiley & Sons, New York)

17 **Maharudrayya S, Jayanti S, Deshpande AP.** Pressure losses in laminary flow through serpentine channels in fuel cell stacks. *J. Power Sources*, 2004, **138**, 1-13

18 **Maharudrayya S, Jayanti S, Deshpande AP.** Pressure drop and flow distribution in multiple parallel-channel configurations used in proton-exchange membrane fuel cell stacks. *J. Power Sources*, 2006, **157**, 358-367

19 **Benedict RP.** *Fundamentals of Pipe Flow*, 1980 (John Wiles & Sons, New York)

A Appendices

A.1 Sub-models for the Inlet and Channel Regions of a PEFC

Calculation of electrode stoichiometry

Using the dry mole fraction of the inlet gas y_i^o, the concentration of species *i* can be calculated through the ideal gas law as;

$$c_i^o = y_i^o \frac{p}{RT} \tag{A-1}$$

where p is the inlet pressure in Pascal and T is the temperature of the heated gas in Kelvin. The molar flow of species *i* supplied to the electrode in the un-humidified state in mol/s can then be calculated as;

$$\dot{N}_i^{E-in} = c_i^o v_{E-in} \tag{A-2}$$

where v_{E-in} is the volumetric flow rate of the un-humidified gas supplied to the electrode, i.e., air to the cathode or neat hydrogen to the anode. The reactant flux through the channel/GDL interface is;

$$\dot{N}_i^{E-1} = \frac{IA_c}{n} \tag{A-3}$$

where A_c is the active area of the cell and n is equal to either 1 or 2 for anode or cathode supplies respectively. Finally, the electrode stoichiometry can be calculated as;

$$\upsilon_i = \frac{\dot{N}_i^{E-\text{in}}}{\dot{N}_i^{E-1}} \tag{A-4}$$

The molar flow rates in mol/cm^2-s are then calculated as;

$$\dot{n}_i^{E-1} = \frac{I}{n} \tag{A-5}$$

$$\dot{n}_i^{E-in} = \upsilon_i \dot{n}_i^{E-1} \tag{A-6}$$

Phase Pressures at the channel-GDL surface interface

In order to determine the transport across the GDL, the phase pressures and concentrations of the gas-phase constituents are required for the boundary of the GDL that interfaces with the channel. It is assumed in the current study that liquid water in the channels is entrained in the gas in the form of small droplets. Using the previously developed multi-component channel model described in chapter 5, the boundary pressures at the channel-GDL interface can be calculated as follows;

$$p_{gas} = y_{gas} p_{channel} \tag{A-7}$$

$$p_{liq} = P_{channel} - p_{gas} \tag{A-8}$$

where the gas-phase mole fraction is calculated as;

$$y_{gas} = 1 - y_{liq} \tag{A-9}$$

$$y_{liq} = y_w - y_{sat} \tag{A-10}$$

$$y_{sat} = \frac{p_w^{sat}}{p_{channel}} \tag{A-11}$$

In Equation (A-10), x_w is determined from the multi-component input model. The gas-phase concentration of species *i* for the GDL boundary is calculated as;

$$c_i = y_i \frac{p_{gas}}{RT} \tag{A-12}$$

and for water calculated as;

$$c_{w,sat} = \frac{p_w^{sat}}{RT} \quad \text{for } 0 < y_{liq} < 1 \tag{A-13}$$

The concentration of liquid water can be calculated as;

$$c_{w,liq} = \frac{\rho_{liq}}{M_w} \tag{A-14}$$

A.2 Key equations for the effects of cell compression on the water uptake and thickness of the quasi-porous PEM

It is assumed that cell compression has an equivalent effect of constraining the membrane. The polymer electrolyte membrane contains charged hydrophilic end groups that have a strong affinity to water. This affinity causes water clusters to form around the end groups, which enlarge and cause the polymer chains to spread out. The total volume of the polymer system therefore increases with water uptake.

When a membrane is constrained, the affinity between the hydrophilic end groups and water still remains, but the energy required to deform the polymer matrix increases. As such, the water clusters that form around the end groups play a limited role in pushing out the polymer chains and instead become nested closer together.

In the current modelling framework, we adopt an existing approach to evaluate the water content of a constrained membrane as a function of its equivalent free-swelling state [1]:

$$\lambda_{cons} = \lambda_{fs}\left[\frac{V_{cons}}{V_{fs}}\right]^{\frac{GV_w}{RT}} \tag{A-15}$$

where the total free volume of the membrane system V_{fs} is calculated as using equation 7-48 and the total constrained volume V_{cons} is calculated as;

$$V_{cons} = V_{mem} + V_w(1-\chi)\lambda_{fs} \tag{A-16}$$

In the current study, the volumetric compression ratio V_{cons}/V_{fs} is also used to recalculate the constrained thickness of the PEM as a function of its free-swelling value using

$$t_{mem,cons} = t_{mem}\left(V_{cons}/V_{fs}\right)^{1/3} \tag{A-17}$$

The bulk modulus of the membrane system, G, can be expressed as [2]:

$$G = \frac{\boldsymbol{E}}{3(1-2\nu)} \tag{A-18}$$

where ν is the Poisson ratio. For an incompressible material, the Poissons ratio is 0.5. Choi *et al.* accordingly assumed a value of 0.5 in their study [3] however the more recent experimental observations of Solasi *et al.* suggest a value of 0.4 [4]. The latter is therefore applied in the current model. The Youngs Modulus E for Nafion below the glass transition temperature is calculated as [1]:

$$\boldsymbol{E} = 273\left(\frac{T_{ref}}{T}\right)\exp\left[-0.1655\left(\frac{\lambda M_w}{EW} + \frac{1200-EW}{100}\right)\right] \tag{A-19}$$

The Youngs Modulus for structurally reinforced membranes is estimated as 500 MPa [5].

In the current modelling framework, the degree of constraint χ is defined relative to the maximum compressive pressure applicable to the working cell;

$$\chi = \frac{C}{C_{\max}} \tag{A-20}$$

In the current work, $C_{\max} = 1.6$ MPa.

For the initial assumption of a free-swelling membrane, the thickness of the membrane is calculated as a function of the average water content across it [1];

$$t_{mem} = t_{mem,u/c}\left(1 + x\frac{\bar{\lambda}V_w}{V_m}\right) \tag{A-21}$$

where the maximum dimensional change x is dependant upon the type of PEM. For Nafion, the value is taken as 0.360 [6]. The literature suggests that for structurally reinforced membranes the dimensional change is around 20% that of non-reinforced membranes [5]. As such, it is assumed that the dimensional change for reinforced membranes is a maximum of 0.072. Because the average water content of the membrane is initially unknown, a series of iterations have to be carried out in order to converge on the proper value of PEM thickness. The modelling work in chapter 5 determined that five iterations are sufficient and this conclusion is directly applied to the current model.

A.3 References

1 **Weber AZ, Newman J.** A Theoretical Study of Membrane Constraint in Polymer-Electrolyte Fuel Cells. *AIChE Journal*, 2004, **50**(12), 3215-3226

2 **Solecki R, Conant RJ.** *Advanced Mechanics of Materials*, 2003 (Oxford University Press, Inc. New York)

3 **Choi P, Jalani NH, Datta R.** Thermodynamics and Proton Transport in Nafion I. Membrane Swelling, Sorption, and Ion-Exchange Equilibrium. *J. Electrochem. Soc.*, 2005, **152**(3), E84-E89

4 **Solasi R, Zou Y, Huang X, Reifsnider K, Condit D.** On mechanical Behaviour and In-Plane Modeling of Constrained PEM Fuel Cell Membrane Subjected to Hydration and Temperature Cycles. *J. Power Sources*, 2007, **167**, 366-377

5 **Tang Y, Kusoglu A, Karlsson AM, Santare MH, Cleghorn S, Johnson WB.** Mechanical Properties of a Reinforced Composite Polymer Electrolyte Membrane and its Simulated Performance in PEM Fuel Cells. *J. Power Sources*, 2008, **175**, 817-825

6 **Weber AZ, Newman J.** Transport in Polymer-Electrolyte Membranes II. Mathematical Model. *J. Electrochem. Soc.*, 2004, **151**(2), A311-A325

B List of Publications

Rama P, Chen R, Andrews J. A Review of Performance Degradation and Failure Modes for Hydrogen-Fuelled Polymer Electrolyte Fuel Cells. *Proc. Inst. Mech. Eng., Part A*, 2008, 222, 421-441 (**Chapter 3**)

Rama P, Chen R, Andrews J. Failure Analysis of Polymer Electrolyte Fuel Cells. *SAE*, 2008-01-0634 (**Chapter 3**)

Rama P, Chen R, Thring R. A Polymer Electrolyte Membrane Fuel Cell Model with Multi-Species Input. *Proc. Inst. Mech. Eng., Part A,* 2005, 219, 255-271 (**Chapter 5**)

Rama P, Chen R, Thring R. Polymer Electrolyte Fuel Cell Transport Mechanisms: A Universal Modelling Framework from Fundamental Theory. *Proc. Inst. Mech. Eng., Part A,* 2006, 220, 353-350 (**Chapter 6**) [*]

Rama P, Liu Y, Chen R. Polymer Electrolyte Fuel Cell Transport Mechanisms: Simulation Study of Hydrogen Crossover and Water Content. *SAE*, 2008-01-1802 (**Chapter 6**)

Rama P, Chen R. Polymer Electrolyte Fuel Cell Transport Mechanisms: A Universal Approach to Multi-Layer Two-Phase Modelling through the General Transport Equation. *ASME J. Fuel Cell Sci. Technol., 2010* (*article in press*), DOI: 10.1115/1.4001004 (**Chapter 7**)

Rama P, Liu Y, Chen R, Ostadi H, Jiang K, Zhang X, Fisher R, Jeschke M. An X-ray Tomography Based lattice-Boltzmann Simulation Study on Gas Diffusion Layers of Polymer Electrolyte Fuel Cells. *ASME J. Fuel Cell Sci. Technol.,* 2010 (*article in press*), DOI: 10.1115/1.3211096 (**Chapter 9**)

[*] Selected by the Editor and a panel of Editorial Board Members to receive the PE Publishing Award for the best paper published in the Journal in 2006